Development of interface based damage-plasticity constitutive model and its application in the simulation of masonry structures under monotonic and cyclic loads

A Thesis Submitted for the Degree of Doctor of Philosophy

School of Civil, Environmental and Mining Engineering, the University of Adelaide

THE UNIVERSITY of ADELAIDE

By

Yu Nie

BEng (Civil Engineering), MEng (Structural Engineering)

May 2022

Principal supervisor

A/Prof. Abdul Sheikh

School of Civil, Environmental and Mining Engineering

The University of Adelaide

Co-supervisor

Prof. Michael Griffith

School of Civil, Environmental and Mining Engineering

The University of Adelaide

Co-supervisor

A/Prof. Phillip Visintin

School of Civil, Environmental and Mining Engineering

The University of Adelaide

Acknowledgements

Firstly, I would like to thank my principal supervisor, Associate Professor Abdul Sheikh, for his wholehearted support and encouragement. I also want to express my sincere gratitude to co-supervisors Professor Michael Griffith and Associate Professor Phillip Visintin. They provided comprehensive encouragement and support which allowed me to overcome research difficulties faced in the last four years. Thanks to my supervisors' significant contributions and guidance, I obtained a series of research skills including theoretical analysis and academic writing, and successfully applied these skills to solve practical engineering problems for masonry structures. Also thanks go to Dr. Jaroslav Vaculik and Mr. Chris Burton who introduced me to the experimental study of masonry, I had the privilege to work with them in my early research.

Many thanks for the financial support of the University of Adelaide who awarded me an Adelaide Graduate Research Scholarship (AGRS). At the same time, thanks to the School of Civil, Environmental & Mining Engineering (CEME), Faculty of Engineering, Computer & Mathematical Sciences (ECMS) and Phoenix HPC Research Technology Support Team for their extensive administrative and technical support.

I also greatly appreciate Dr. Tianyu Xie, Dr. Chengfeng Fang, Dr. Linh Anh Le, Dr. Shahin Mahdi, Dr. Azizul Islam, Dr. Zhongcun Zuo, and other senior PhDs in the University of Adelaide who provided me with lots of advice and help when I was stuck and confused.

Declaration

I certify that this work contains no material which has been accepted for the award of any other degree or diploma in my name, in any university or other tertiary institution and, to the best of my knowledge and belief, contains no material previously published or written by another person, except where due reference has been made in the text. In addition, I certify that no part of this work will, in the future, be used in a submission in my name, for any other degree or diploma in any university or other tertiary institution without the prior approval of the University of Adelaide and where applicable, any partner institution responsible for the joint-award of this degree.

I acknowledge that copyright of published works contained within this thesis resides with the copyright holder(s) of those works.

I also give permission for the digital version of my thesis to be made available on the web, via the University's digital research repository, the Library Search and also through web search engines, unless permission has been granted by the University to restrict access for a period of time.

I acknowledge the support I have received for my research through the provision of an Australian Government Research Training Program Scholarship.

May 10th 2022

Yu Nie

Abstract

Simulation of masonry structures at the mesoscale level to capture cracking failure is a challenging topic due to both the complexity of masonry materials and numerical difficulties in solving nonlinear problems. Within the framework of finite element method, cohesive elements with an interfacial constitutive model are commonly utilized as brick-mortar joints to simulate the nonlinear response of masonry structures, including simulation of mechanical behaviour and cracking patterns. This modelling strategy provides effective prediction of the strength-deformation relationship and failure modes of materials/structures, but is highly computationally expensive and convergence issues are frequently encountered during the numerical implementation process.

In this thesis, interfacial constitutive models are proposed and developed in conjunction with advanced numerical implementation methods to avoid or overcome convergence difficulties. Constitutive criteria for masonry joints are established based on damage mechanics and plasticity principals which define the nonlinear behaviour of interface model in traction-separation scheme (stress-relative deformation relation). Another critical problem, divergence, is solved by improving numerical implementation method at both the global (FE solver) and local (material algorithm) level. The accuracy and robustness of the proposed interfacial models are validated at the elemental and structural level by comparing the load-displacement response and failure modes of finite element models with experimental results obtained from literature.

Initially, the finite element method is investigated by using a general numerical software (Abaqus) which provides built-in interfacial models based on damage mechanics (cohesive zone model, CZM). A surface based cohesive technique is applied to model the connection between bricks and mortar joints. Since the built-in interfacial model can only determine the tension-shear mixed mode of joints, solid elements are defined with a continuum nonlinear material model (concrete damage plasticity model, CDP) to predict the compressive failure of bricks. To achieve most efficient and stable computational results, different numerical solvers are compared and the Implicit Dynamic solver with linear search option is adopted as the most proper numerical technique.

After developing an understanding of the finite element modelling process, a plasticity based interfacial model is developed for the zero-thickness cohesive element. The plasticity model includes a hyperbolic yield surface which can define the tension-shear mix-mode failure of joints. An energy dissipation/plastic work based evaluation law is applied to determine the variation of internal variables, including strength softening, dilation and frictional change. Robustness of the numerical implementation is enhanced by subdividing large increments of deformation (relative displacements) into smaller sizes to increase the convergence of Newton-Raphson iteration in implicit integration.

Regarding the cyclic behaviour of masonry structures, stiffness degradation of brick-mortar joints is often observed in experimental tests under unloading/reloading path. To improve the plasticity model, damage parameters are induced into the constitutive formula. In this way, a comprehensive interface model with inelastic deformation, strength reduction and stiffness degradation (considering the cracking closure) is presented in this study. A consistent tangent

stiffness matrix for this coupled damage-plasticity model is also derived in a recursive format in sub-stepping scheme to achieve quadratic convergence rate.

Despite the robustness and accuracy of the above described damage-plasticity model, it's computational efficiency is limited by the complication of stress return mapping, thus application when simulating masonry structures under cyclic loadings requires significant computational resources. A simplified damage-plasticity model is proposed by using a similar constitutive formulation, but it is implemented in a more efficient numerical strategy where damage mechanics is separated from plasticity. By transferring stresses between effective and nominal stress spaces, the computation of damage mechanics and plasticity are completed in two individual progresses which are connected by the state dependent variable (plastic work). Furthermore, effects of the dilation coefficient on the constitutive behaviour and numerical modelling are investigated in the study by using a softening dilation function. Compared with the constant coefficient with a small magnitude, the proposed changeable dilation function can reflect physical phenomenon of masonry joints more realistically, and it is also helpful in enhancing the stress return mapping procedure.

In addition to tension and shear failures, compressive crushing is another critical failure mode when masonry walls under in-plane loadings. By adding a compressive cap model into the interfacial based constitutive criteria, the crushing failure of masonry is represented by using cohesive elements. Therefore, all nonlinear behaviours are concentrated in the cohesive element with an interfacial multi-surface model and bricks are assumed as an elastic material. Even though this simplification has been widely accepted in mesoscale modelling of quasi-brittle materials, existing interfacial models usually ignore the compressive behaviour of cohesive element for convenience. To make the present interfacial model capable of simulating compressive failure, an elliptical yield surface is combined with the hyperbolic yield surface to form a multi-surface elastoplastic model. In effective stress space, tension-shear mixed hyperbolic yield surface follows a perfectly-plastic rule where no deformation or variation is allowed, while the compressive cap yield surface controlled by a hardening-plastic rule is allowed to extend in limited region until the interface reaches ultimate compressive strength of the masonry.

In the aspect of damage mechanics, a series of polynomial equations relying on plastic work is adopted in the constitutive criteria to control the evaluation of internal variables, including the growth of damage parameters and the decrease of other internal variables (e.g. dilation effects). Configuration coefficients are considered in polynomial equations to help calibrate curves of internal variables along with plastic works/inelastic deformations. With the aid of a piecewise function, the hardening-softening relationship of the interface under monotonic/cyclic compressive loadings can be properly simulated, including the variation of normal stiffness which keeps constant during strength hardening stage but degrades in the strength softening process. Concerning the intricacy of numerical convergence in multi-surface model, a more advanced adaptive sub-stepping technique is adopted in the algorithm of numerical implementation where the sub-dividing size of large deformations can be automatically adjusted based on converging performance in each sub-steps.

List of publications

Nie Y, Sheikh A, Griffith M, Visintin P. A damage-plasticity based interface model for simulating in-plane/out-of-plane response of masonry structural panels. Computers & Structures. 2022 Feb 1;260:106721.

Nie Y, Sheikh A, Visintin P, Griffith M. An interfacial damage-plastic model for the simulation of masonry structures under monotonic and cyclic loadings. Submitted to Engineering Fracture Mechanism (under review).

Nie Y, Sheikh A, Visintin P, Griffith M. Simulation of masonry structures under monotonic/cyclic loading conditions with an interfacial based multi-surface damage-plastic model. Submitted to Computer Methods in Applied Mechanics and Engineering (submitted).

Table of Contents

Chapter 1: Introduction

Historical and residual buildings with masonry walls are extremely vulnerable in seismic loads. Investigation of masonry structures is an attractive and challenging work in the research area of earthquake and structural dynamics (Derakhshan et al. 2020). Numerical methodologies are widely utilized in simulating masonry structures considering is advantages in solving complex nonlinear problems, such as finite element method (Kujawa et al. 2020), discrete element method (Malomo and DeJong, 2021), discrete-finite element method (Deb et al. 2021) and meshless method (Giambanco et al. 2018; LM Ribolla et al. 2020). Among these numerical methods, finite element (FE) analysis has the longest history and most mature application in the analysis of masonry structures since 1978 (Page, 1978). Pioneering works conducted by Lofti and Shing (1994) and Lourenco and Rots (1997) illustrated that developing interface/cohesive constitutive model for mortar/brick joints is one of the most practical strategy for masonry simulation within FE frameworks.

According to the classification of Lourenco (1997), modelling approaches of masonry structures can be divided into three strategies based on different treatments of bricks and mortar joints: 1) detailed micro-modelling strategy (Andreotti, 2018) simulates masonry in a straightforward concept where bricks and mortars are created by solid elements and the de-bonding in brick-mortar interface is defined by zero thickness cohesive elements or contact pairs; 2) simplified macro-modelling strategy (Ravichandran et al, 2021; Panto et al, 2019) homogenize the masonry wall as a continuum model where the mechanical behaviour of bricks and mortars are uniformed into continuum representative volume element (RVE); 3) simplified micro-modelling strategy (Lourenco and Rots, 1997) includes mortar joints defined by constitutive models with non-linear behaviours while bricks are set as elastic with inserted artificial/fake joints. Among above modelling strategies, detailed micro-modelling strategy requires a huge computational cost that is impractical in engineering application for large scale masonry buildings, while simplified macro-modelling strategy has no capability to predict the cracking pattern or failure modes of masonry accurately. Only simplified micro-modelling strategy can keep a well balance between computational efficiency and accuracy, and it is widely adopted in existing literature introduced below.

The primary interest of simplified micro-modelling method is to develop interface model for mortar/artificial joints. Considering the anisotropic behaviours of masonry joints in normal and shear directions, the constitutive criteria of interface models is commonly developed based on traction-separation rule where the joint has different properties under normal (Mode I), shear (Mode II) and tension-shear mixed loadings. Furthermore, the normal behaviour of interface is different under tension and compression in simulating the failure of quasi-brittle materials (Dragon et al. 2000). Therefore, a proper theoretical framework is required to be established based on the anisotropic characteristic of masonry joints. In existing literature, damage mechanics and the theory of plasticity are two popular frameworks to model the nonlinear mechanical behaviours of interfaces.

Interfacial damage models are widely investigated in studies on composite materials (Turon et al. 2007; De Morais, 2013) and it becomes popular in the application of masonry (Abdulla et al. 2017; Zeng et al. 2021) recently because it has been widely built-in commercial

FE software (Abaqus, 2015). By adding frictional coefficient into the contact based cohesive model, damage mechanism can simulate the mode I/tension and mode II/shear failure of mortar joints roughly. However, the determination of mixed-mode parameters for damage model under complex loading scenario is problematic due to the lack of experimental evidence. The current mix-mode criteria, Benzeggagh-Kenane fracture criterion (Benzeggagh and Kenane, 1996), is initially proposed based on the experimental observation from composite materials rather than masonry joints. Besides, the dilation characteristics of mortar bed joints, which has been proved to play an important role in masonry structures by experimental evidence (Andreotti et al. 2019), is not considered in the damage framework interface model (Alfano and Sacco, 2006). Most importantly, pure damage model has no capability to simulate the hysteretic behaviour of interfaces when irreversible deformation generates.

Plastic models are earlier developed for interface/cohesive element and they are commonly applied in masonry wall modellings. Based on the difference of yield surfaces, plastic models can be classified as: 1) single hyperbolic yield surface (Lofti and Shing, 1994) which defines the tension-shear mixed mode failure; 2) multi-straight yield surfaces model (Scimemi et al. 2014) composed by tension cut-off and Coulomb frictional surface; 3) multi-straight yield surfaces model with compression cut-off (Minga et al. 2018; Xie et al, 2021) or diagonal flat compressive surface (Sutcliffe et al. 2001; Chaimoon and Attard, 2007); 4) multi-hyperbolic yield surfaces model (Macorini and Izzuddin, 2011) where the compressive region is also defined be a hyperbolic curve; 5) single closed form smooth yield surface (Citto, 2008; Kumar et al. 2014) which defines the elastic domain by using one formulation; and 6) the most well-known multi-yield surfaces model proposed by Lourenco and Rots (1996) who defined the elastic domain by using tension cut-off, Coulomb frictional surface and an elliptical compressive cap. Despite the commonly adoption of plasticity framework, it has limitation in modelling the stiffness degradation of material under unloading-reloading path.

An interfacial model merging damage mechanics and plasticity should be capable of modelling the physical behaviour of masonry joints more realistically, because the combined model considers both irreversible deformation and stiffness degradation that are two most distinctly physical phenomena of masonry joints under cyclic loadings. In recent researches, the development and application of damage-plasticity models for masonry joints is rising. For instance, Spada et al. (2009) developed a damage-plasticity model within thermodynamic framework, but its numerical implementation is relatively complicated since they defined 16 different cases (active constraints) for stress updating. Yuen et al (2019) proposed a damage-plasticity model with a hyperbolic tension-shear yield surface, but its computational cost is expensive since the authors only provide explicit (forward Euler) implementation solution. Compared with them, the damage-plasticity model proposed by Minga et al. (2018) is more efficient and concise because the damage procedure is algorithmically decoupled with plasticity which enhances the stability of stress updating by fixing the evaluation of yield surfaces in effective stress space. Similar concept is also adopted in modelling concrete material based on continuum mechanism (Valentini and Hofstetter, 2013; Simo and Ju, 1987; Ju 1989). However, the model proposed by Minga et al. (2018) has no capable of simulating the hardening behaviour of masonry joints under compression. To improve it, Xie et al. (2021) proposed a new damage-plasticity model which can model the compressive hardening strength by using an elastic-secant combined normal stiffness. Nevertheless, the concept of elastic-secant combined normal stiffness is unrealistic if the interface is subjected to unloading path

from compression to tension, and the softening behaviour of their interface under uniaxial loads can only be represented by bilinear curves.

In addition to propose a proper constitutive model, the numerical implementation of interface model is another challenge because of converging difficulties which is frequently occurs in implicitly numerical computation. A fully implicit integration system with closed point projection method (CPPM) is commonly utilized in plastic models due to the unconditionally stability (Ortiz and Popov, 1985) and high accuracy (Chaboche and Cailletaud, 1996). However, in implicit integration system the stress return mapping procedure is usually attained by using Newton-Raphson iterative technique which has diverging issues in some situations, such as the hyperbolic yield/potential surface with high curvatures (Wilkins et al. 2020) and large strain/deformation increment (Sloan et al. 2001). Furthermore, multi-surface model with corners increase the difficulty of convergence since the active yield surfaces need to be updated iteratively based on Karush–Kuhn–Tucker (KKT) conditions (Simo and Hughes, 2006). To solve these numerical issues, numerical tools from the region of convex optimization (Arora, 2004; Boyd and Vandenberghe, 2004) are adopted by studies on geo-material modelling (Abreu et al, 2021), such as line search method (Adhikary et al. 2017; Pérez‐Foguet and Armero; 2002; Lee et al. 2021) which can help enlarge the converging region of minimum functions (Lester and Scherzinger, 2017). In studies related to wood simulation, brutal force technique is utilized by Pech et al. (2021) in timber constitutive model composed by a number of yield surfaces (Lukacevic et al. 2017). The idea of sub-stepping scheme is firstly proposed by Sloan (1987) to enhance the stability of forward Euler integration, and then Pérez-Foguet et al. (2001) proposed the new scheme applicable for backward Euler integration.

The aim of this study is to propose an interfacial based constitutive model within the theoretical framework of damage mechanics and plasticity. By using cohesive element built-in FE software Abaqus, the proposed constitutive model (denoting mortar joints) is used in interface element and cooperated with solid element (denoting bricks) to simulate the different levels of masonry structures under complex loading conditions.

Firstly, in **Chapter 2** the damage based interfacial model (Abaqus) is combined with the surface based frictional contact (Abaqus) to simulate the failure of masonry walls under monotonic in-plane and out-of-plane loads for gaining initial confidence. Then a pure plasticity based interfacial model is employed in **Chapter 3** by implementing the model in the form of a user defined material model (UMAT) as an external subroutine to simulate the nonlinear behaviour of zero-thickness cohesive element. To reproduce the phenomenon of stiffness degradation, damage parameters are incorporated into a plastic model in **Chapter 4**. In addition, an enhancement technique known as sub-stepping scheme is adopted in the numerical implementation to improve robustness. To improve the computational efficiency, an effective stress based formulation is adopted to separating damage and plasticity components of the model algorithmically in **Chapter 5** where a more detail treatment of dilation effects is included. A damage-plasticity based model is developed specifically for investigating the behaviour of masonry under compression in **Chapter 6**, and the cap model is finally combined with a smooth hyperbolic surface based model in **Chapter 7**. To improve the accuracy of stress return mapping path and the stabilization of numerical implementation, an innovative technique is adopted for detection of active yield surfaces to implement an adaptive sub-stepping scheme.

Reference

Abdulla KF, Cunningham LS, Gillie M. Simulating masonry wall behaviour using a simplified micro-model approach. Engineering Structures. 2017 Nov 15;151:349-65.

Abreu R, Mejia C, Roehl D. A comprehensive implicit substepping integration scheme for multisurface plasticity. International Journal for Numerical Methods in Engineering. 2021 Sep 27.

Adhikary DP, Jayasundara CT, Podgorney RK, Wilkins AH. A robust return-map algorithm for general multisurface plasticity. International Journal for Numerical Methods in Engineering. 2017 Jan 13;109(2):218-34.

Alfano G, Sacco E. Combining interface damage and friction in a cohesive-zone model. International Journal for Numerical Methods in Engineering. 2006 Oct 29;68(5):542-82.

Andreotti G, Graziotti F, Magenes G. Detailed micro-modelling of the direct shear tests of brick masonry specimens: the role of dilatancy. Engineering Structures. 2018 Aug 1;168:929-49.

Andreotti G, Graziotti F, Magenes G. Expansion of mortar joints in direct shear tests of masonry samples: implications on shear strength and experimental characterization of dilatancy. Materials and Structures. 2019 Aug;52(4):1-6.

Arora J. Introduction to optimum design. Elsevier; 2004 Jun 2.

B Valentini, G Hofstetter. Review and enhancement of 3D concrete models for large-scale numerical simulations of concrete structures. International Journal for numerical and analytical Methods in Geomechanics. 2013 Feb 25;37(3):221-46.

Benzeggagh ML, Kenane MJ. Measurement of mixed-mode delamination fracture toughness of unidirectional glass/epoxy composites with mixed-mode bending apparatus. Composites science and technology. 1996 Jan 1;56(4):439-49.

Boyd SP, Vandenberghe L. Convex optimization. Cambridge university press; 2004 Mar 8.

Caballero A, Willam KJ, Carol I. Consistent tangent formulation for 3D interface modeling of cracking/fracture in quasi-brittle materials. Computer Methods in Applied Mechanics and Engineering. 2008 Jun 1;197(33-40):2804-22.

Chaboche JL, Cailletaud G. Integration methods for complex plastic constitutive equations. Computer methods in applied mechanics and engineering. 1996 Jun 15;133(1-2):125-55.

Chaimoon K, Attard MM. Modeling of unreinforced masonry walls under shear and compression. Engineering structures. 2007 Sep 1;29(9):2056-68.

Chaimoon, K. R. I. T. "Numerical simulation of fracture in unreinforced masonry." PhD diss., Ph. D thesis, 2007.

Citto C. Two-dimensional interface model applied to masonry structures (Doctoral dissertation, University of Colorado at Boulder).

Chang LZ, Rots JG, Esposito R. Influence of aspect ratio and pre-compression on force capacity of unreinforced masonry walls in out-of-plane two-way bending. Engineering Structures. 2021 Dec 15;249:113350.

Crouch RS, Askes H, Li T. Analytical CPP in energy-mapped stress space: application to a modified Drucker–Prager yield surface. Computer methods in applied mechanics and engineering. 2009 Jan 15;198(5-8):853-9.

D'Altri AM, de Miranda S, Castellazzi G, Sarhosis V. A 3D detailed micro-model for the in-plane and out-of-plane numerical analysis of masonry panels. Computers & Structures. 2018 Aug 15;206:18-30.

De Morais AB. Mode I cohesive zone model for delamination in composite beams. Engineering Fracture Mechanics. 2013 Sep 1;109:236-45.

Deb T, Yuen TY, Lee D, Halder R, You YC. Bi-directional collapse fragility assessment by DFEM of unreinforced masonry buildings with openings and different confinement configurations. Earthquake Engineering & Structural Dynamics. 2021 Dec;50(15):4097-120.

Derakhshan H, Walsh KQ, Ingham JM, Griffith MC, Thambiratnam DP. Seismic fragility assessment of nonstructural components in unreinforced clay brick masonry buildings. Earthquake Engineering & Structural Dynamics. 2020 Mar;49(3):285-300.

DIANA, FEABV. "DIANA Finite Element Analysis User's Manual Release 10.3 Delft." (2019).

Dragon A, Halm D, Désoyer T. Anisotropic damage in quasi-brittle solids: modelling, computational issues and applications. Computer methods in applied mechanics and engineering. 2000 Mar 17;183(3-4):331-52.

Giambanco G, Ribolla EL, Spada A. Meshless meso-modeling of masonry in the computational homogenization framework. Meccanica. 2018 May;53(7):1673-97.

Grassl P, Jirásek M. Damage-plastic model for concrete failure. International journal of solids and structures. 2006 Nov 1;43(22-23):7166-96.

Grassl P, Rempling R. A damage-plasticity interface approach to the meso-scale modelling of concrete subjected to cyclic compressive loading. Engineering Fracture Mechanics. 2008 Nov 1;75(16):4804-18.

Grassl P, Xenos D, Nyström U, Rempling R, Gylltoft K. CDPM2: A damage-plasticity approach to modelling the failure of concrete. International Journal of Solids and Structures. 2013 Nov 1;50(24):3805-16.

Griffith MC, Vaculik J, Lam NT, Wilson J, Lumantarna E. Cyclic testing of unreinforced masonry walls in two-way bending. Earthquake Engineering & Structural Dynamics. 2007 May;36(6):801-21.

Ju JW. On energy-based coupled elastoplastic damage theories: constitutive modeling and computational aspects. International Journal of Solids and structures. 1989 Jan 1;25(7):803-33.

Kaushik HB, Rai DC, Jain SK. Stress-strain characteristics of clay brick masonry under uniaxial compression. Journal of materials in Civil Engineering. 2007 Sep;19(9):728-39.

Koiter WT. Stress-strain relations, uniqueness and variational theorems for elastic-plastic materials with a singular yield surface. Quarterly of applied mathematics. 1953;11(3):350-4.

Kujawa M, Lubowiecka I, Szymczak C. Finite element modelling of a historic church structure in the context of a masonry damage analysis. Engineering Failure Analysis. 2020 Jan 1;107:104233.

Kumar N, Amirtham R, Pandey M. Plasticity based approach for failure modelling of unreinforced masonry. Engineering structures. 2014 Dec 1;80:40-52.

La Malfa Ribolla E, Giambanco G, Spada A. Mesoscopic aspects of the computational homogenization with meshless modeling for masonry material. International Journal for Numerical Methods in Engineering. 2020 Aug 30;121(16):3610-35.

Lee J, Bong HJ, Lee MG. Return mapping with a line search method for integrating stress of the distortional hardening law with differential softening. Computers & Structures. 2021 Dec 1;257:106652.

Lester BT, Scherzinger WM. Trust‐region based return mapping algorithm for implicit integration of elastic‐plastic constitutive models. International Journal for Numerical Methods in Engineering. 2017 Oct 19;112(3):257-82.

Lourenço PB, Rots JG. Multisurface interface model for analysis of masonry structures. Journal of engineering mechanics. 1997 Jul;123(7):660-8.

Lukacevic M, Lederer W, Füssl J. A microstructure-based multisurface failure criterion for the description of brittle and ductile failure mechanisms of clear-wood. Engineering Fracture Mechanics. 2017 May 1;176:83-99.

Macorini L, Izzuddin BA. A non‐linear interface element for 3D mesoscale analysis of brick‐masonry structures. International Journal for numerical methods in Engineering. 2011 Mar 25;85(12):1584-608.

Malomo D, DeJong MJ. A Macro-Distinct Element Model (M-DEM) for out-of-plane analysis of unreinforced masonry structures. Engineering Structures. 2021 Oct 1;244:112754.

Messali F, Esposito R, Ravenshorst GJ, Rots JG. Experimental investigation of the in-plane cyclic behaviour of calcium silicate brick masonry walls. Bulletin of Earthquake Engineering. 2020 Jun;18(8):3963-94.

Messali F, Ravenshorst G, Esposito R, Rots JG. Large-scale testing program for the seismic characterization of Dutch masonry walls. InProceedings of 16th world conference on earthquake (WCEE), Santiago, Chile 2017 Jan.

Minga E, Macorini L, Izzuddin BA. A 3D mesoscale damage-plasticity approach for masonry structures under cyclic loading. Meccanica. 2018 May;53(7):1591-611.

Ng CL. Experimental and theoretical investigation of the behaviour of brickwork cladding panel subjected to lateral loading (Doctoral dissertation, University of Edinburgh).

Ortiz M, Popov EP. Accuracy and stability of integration algorithms for elastoplastic constitutive relations. International journal for numerical methods in engineering. 1985 Sep;21(9):1561-76.

Panto B, Silva L, Vasconcelos G, Lourenço PB. Macro-modelling approach for assessment of out-of-plane behavior of brick masonry infill walls. Engineering Structures. 2019 Feb 15;181:529-49.

Pech S, Lukacevic M, Füssl J. A robust multisurface return-mapping algorithm and its implementation in Abaqus. Finite Elements in Analysis and Design. 2021 Aug 1;190:103531.

Pérez-Foguet A, Armero F. On the formulation of closest-point projection algorithms in elastoplasticity—part II: Globally convergent schemes. International Journal for numerical Methods in Engineering. 2002 Jan 20;53(2):331-74.

Pérez-Foguet A, Rodríguez-Ferran A, Huerta A. Consistent tangent matrices for substepping schemes. Computer methods in applied mechanics and engineering. 2001 Jun 8;190(35-36):4627-47.

Pluijm R. Non-linear behaviour of masonry under tension. HERON-ENGLISH EDITION-. 1997;42:25-54.

Pluijm RV. Shear behaviour of bed joints. InProceedings of the 6th North American Masonry Conference. Drexel University, Philadelphia, Pennsylvania, USA 1993 Jun 6 (pp. 125-136).

Ravichandran N, Losanno D, Parisi F. Comparative assessment of finite element macro-modelling approaches for seismic analysis of non-engineered masonry constructions. Bulletin of Earthquake Engineering. 2021 Oct;19(13):5565-607.

Salmanpour AH, Mojsilović N, Schwartz J. Displacement capacity of contemporary unreinforced masonry walls: an experimental study. Engineering Structures. 2015 Apr 15;89:1-6.

Scimemi GF, Giambanco G, Spada A. The interphase model applied to the analysis of masonry structures. Computer Methods in Applied Mechanics and Engineering. 2014 Sep 1;279:66-85.

Simo JC, Hughes TJ. Computational inelasticity. Springer Science & Business Media; 2006 May 7.

Simo JC, Ju J. Strain-and stress-based continuum damage models—I. Formulation. International journal of solids and structures. 1987 Jan 1;23(7):821-40.

Sloan SW, Abbo AJ, Sheng D. Refined explicit integration of elastoplastic models with automatic error control. Engineering Computations. 2001 Feb 1.

Sloan SW. Substepping schemes for the numerical integration of elastoplastic stress–strain relations. International journal for numerical methods in engineering. 1987 May;24(5):893-911.

Sutcliffe DJ, Yu HS, Page AW. Lower bound limit analysis of unreinforced masonry shear walls. Computers & Structures. 2001 Jun 1;79(14):1295-312.

Systemes D. Abaqus 6.14 documentation–theory guide. Providence, RI. 2015.

Tao Y, Chen JF. Concrete damage plasticity model for modeling FRP-to-concrete bond behavior. Journal of composites for construction. 2015 Feb 1;19(1):04014026.

Turon A, Davila CG, Camanho PP, Costa J. An engineering solution for mesh size effects in the simulation of delamination using cohesive zone models. Engineering fracture mechanics. 2007 Jul 1;74(10):1665-82.

Vermeltfoort, A. Th, Theo Raijmakers, and H. J. M. Janssen. "Shear tests on masonry walls." (1993): 1183-1193.

Wilkins A, Spencer BW, Jain A, Gencturk B. A method for smoothing multiple yield functions. International Journal for Numerical Methods in Engineering. 2020 Feb 15;121(3):434-49.

Xie Z, Sousamli M, Messali F, Rots JG. A sub-stepping iterative constitutive model for cyclic cracking-crushing-shearing in masonry interface elements. Computers & Structures. 2021 Dec 1;257:106654.

Yuen TY, Deb T, Zhang H, Liu Y. A fracture energy based damage-plasticity interfacial constitutive law for discrete finite element modelling of masonry structures. Computers & Structures. 2019 Aug 1;220:92-113.

Zeng B, Li Y, Noguez CC. Modeling and parameter importance investigation for simulating in-plane and out-of-plane behaviors of un-reinforced masonry walls. Engineering Structures. 2021 Dec 1;248:113233.

Chapter 2: A pure damage based model

Nie, Y, Sheikh, A., Griffith, M., Visintin, P. and Vaculik, J. (2019, Nov 29- Dec 1). The application of mixed-mode de-cohesion criteria in masonry finite element analysis. Australian Earthquake Engineering Society 2019 Conference, Newcastle City Hall, New South Wales.

Abstract

This chapter introduces a novel finite element modelling approach for masonry structures. The mixed-mode de-cohesion criteria is applied on a detailed and a simplified finite element model separately to predict the behaviour of masonry walls under different loading conditions, including the in-plane load and the out-of-plane load. The joint in the detailed model is composited by interfaces and mortar layer, whilst in the simplified model it is represented by a pair of interfaces. The interfacial constitutive model includes damage initiation and damage involution that can simulate the post-failure behaviour of masonry joints under tensile, shear, compressive and their combined loads. The failure of masonry structure under high compression can be represented by brick failure with concrete damage plasticity criteria. Performance of the detailed modelling approach is evaluated by comparing modelling results with experimental results.

2.1 Introduction

The application of finite element model (FEM) in analysing masonry structures has been widely acceptable, especially for some historical buildings that are not allowed to conduct destructive tests. The failure of unreinforced masonry wall (URM) includes both interaction de-bonding and brick material damage, thus it is necessary to make use of proper interaction criteria and material criteria simulating the behaviour of masonry wall.

Common used simulation strategies of masonry walls are: 1) detailed micro-modelling strategy; 2) simplified micro-modelling strategy as well as 3) macro-modelling strategy (Lourenco, 1997). The detailed model is most close to real masonry structure geometry but its running cost is relatively high, and sometimes only explicit algorithm can overcome the convergence difficulties (Andreotti et.al, 2018). In contract, the macro-model without mortar joints has highest computation efficiency but it has to scarify accuracy to some extent (Lofti & Shing, 1991; Anthoine, 1995). A compromised method is using simplified micro-model that simplifies mortar joints as a non-thickness interface, which is also the most popular modelling approach (Lourenco & Rots, 1997; Lofti & Shing, 1994; Abdulla et.al 2017).

(a) wall collapse under out-of-plane load

(b) wall failure under in-plane load

Fig. 2-1 Building collapse under seismic loads (Gautam et.al 2016)

A masonry structure is extremely sensitive to seismic force, so it is common that masonry buildings collapsing occur in earthquake disasters. A seismic load has two horizontal waves that are perpendicular to and parallel to masonry walls respectively, resulting in in-plane loads and out-of-plane loads on structures. As shown in **Fig. 2-1**, the whole wall in the building fall down due to the seismic load being perpendicular to the wall surface as shown in **Fig. 2-1a**, whereas the lateral wall under a parallel seismic load has inclined cracks as shown in **Fig. 2-1b**.

This paper evaluates the performance of masonry walls under in-plane loads and out-of-plane loads by applying a de-cohesive mixed constitutive model in expended brick-brick interface (simplified model) and mortar-brick interface (detailed model). The interaction constitutive model is proposed by Camanho & Davila (2002) to simulate the delamination of composite material. A more detailed discussion of interaction behaviour is presented in the next section.

2.2 Interaction Behaviour

Pluijm (1992) investigated the tensile and shear behaviours of masonry by a series of tests and summarized their behaviours as shown in **Fig. 2-2**. In the pre-failure stage, both the normal and shear behaviour of masonry joints are elastic, so elastic modulus or elastic stiffness can describe the traction-separation relationship. In the post-failure stage, the stress-displacement curve has a non-linear softening relation which can be expressed by exponential equations (Nazir, 2014) or a damage model (D'Altri, 2018). This paper adopts damage mechanism to describe the post-failure behaviour of masonry joints.

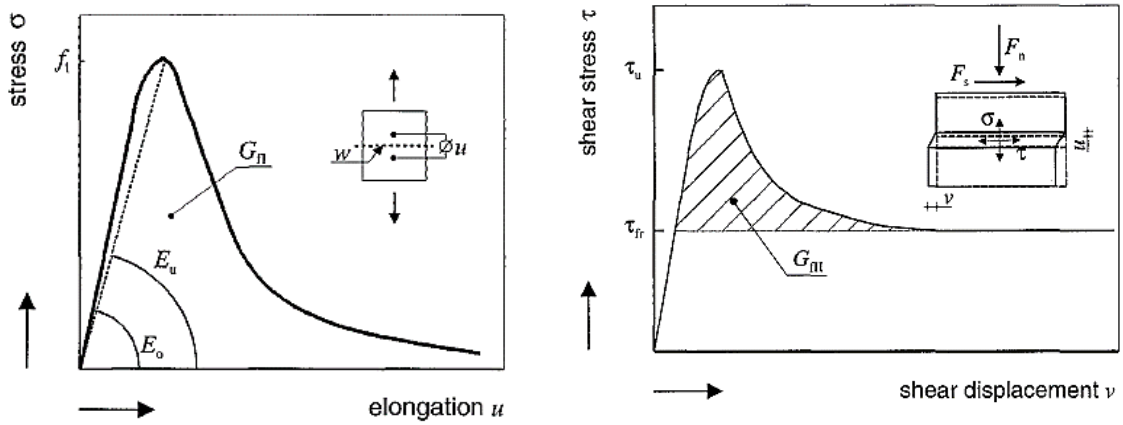

(a) normal tensile behaviour (b) shear behaviour

Fig. 2-2 Masonry joint behaviour in normal and shear direction (Pluijm, 1992)

The connections between brick-brick or brick-mortar are simulated by zero-thickness de-cohesion element as shown in **Fig. 2-3**. The de-cohesive element comprises of 8 nodes and its

constitutive behaviour is described by the relation between separations (displacements) and tractions (stresses) across the interface.

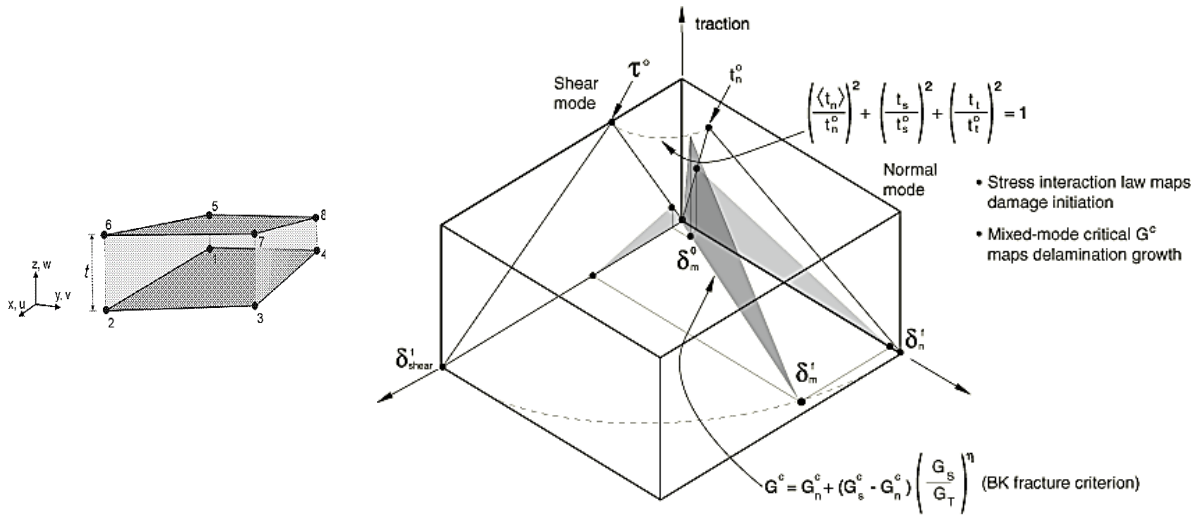

Fig. 2-3 De-cohesive element and its mix-mode response (Abaqus Users' Manual, 2014)

The linear elastic traction-separation behaviour is expressed by an uncoupled equation:

$$\begin{bmatrix} t_n \\ t_s \\ t_t \end{bmatrix} = \begin{bmatrix} K_{nn} & 0 & 0 \\ 0 & K_{ss} & 0 \\ 0 & 0 & K_{tt} \end{bmatrix} \begin{bmatrix} u_n \\ u_s \\ u_t \end{bmatrix} \tag{2.1}$$

where: t_n, t_s and t_t are the traction stress in tensile, shear I and shear II directions; K_{nn}, K_{ss} and K_{tt} are the elastic stiffness in the tensile, shear I and shear II directions; u_n, u_s and u_t are the separation displacement in tensile, shear I and shear II directions respectively.

The material properties of brick is elastic and the linear elastic stiffness of interaction is defined based on the modelling strategies. For detailed micro-model, the contact elastic stiffness is equal to 500 times the stiffness of the under-laying elements (D'Altri, 2018), whilst for the simplified micro-model, the contact elastic stiffness is defined as:

$$K_{nn} = \frac{E_b\, E_j}{h_j\,(E_b\, -\, E_j)}, \qquad K_{tt} = K_{ss} = \frac{G_b\, G_j}{h_j\,(G_b\, -\, G_j)} \tag{2.2}$$

where: E_b and E_j are the Young's modulus of brick and mortar joint respectively; G_b and G_j are the shear modulus of brick and mortar joint respectively; h_j is the height of the mortar joints. It should be noted that **Eq (2.2)** is only suitable for simplified modelling strategy which allowing the interpenetration happened, as shown in **Fig. 2-4**.

As shown in **Fig. 2-4**, the brick-mortar couplet with two half bricks and one mortar layer can be transferred to a composite model with one brick and one mortar joint, similarly to the expended brick couplet. The expended brick couplet has one zero thickness interface spring with stiffness *kn*. To ensure the deformation of the real and simplified couplet equal,

$$\frac{P}{ku}+\frac{P}{km}=\frac{P}{ku}+\frac{P}{ku,\exp}+\frac{P}{K_{nn}} \tag{2.3}$$

Substitute expressions in **Fig 2-4** into **Eq (2.3)**

$$\frac{t_m}{E_m}=\frac{t_m}{E_u}+\frac{1}{K_{nn}} \tag{2.4}$$

And then K_{nn} can be derived has the same expression as **Eq (2.2)**, similar to the derivation of shear stiffness.

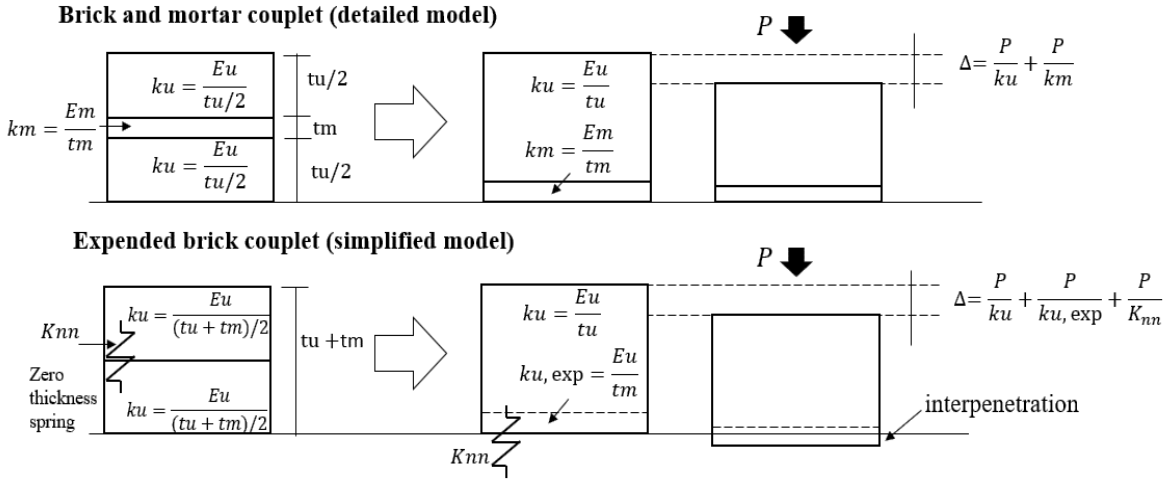

Fig. 2-4 Derivation of elastic normal stiffness for zero thickness interface element

The initiation of damage degradation of interaction can be activated by either maximum stress criterion or quadratic stress criteria. In this paper, the maximum stress criterion is applied in the detailed model while quadratic stress criteria is applied in the simplified model:

$$\text{Max}\left\{\frac{\langle t_n\rangle}{f_n},\frac{t_s}{f_s},\frac{t_t}{f_t}\right\}=1 \tag{2.5a}$$

$$\left(\frac{\langle t_n\rangle}{f_n}\right)^2+\left(\frac{t_s}{f_s}\right)^2+\left(\frac{t_t}{f_t}\right)^2=1 \tag{2.5b}$$

where f_n, f_s and f_t are the maximum stress in tensile, shear I and shear II directions measured by direct tensile test and direct shear test, as the peak values shown in **Fig. 2-2**. Macaulay bracket function $\langle t_n\rangle = (|t_n|+t_n)/2$.

The damage evolution process is controlled by the damage variable *D* and the predicted contact stress $(\bar{t}_n, \bar{t}_s, \bar{t}_t)$ calculated by elastic stiffness:

$$t_n=(1-D)\bar{t}_n,\qquad t_s=(1-D)\bar{t}_s,\qquad t_t=(1-D)\bar{t}_t \tag{2.6}$$

The damage variable *D* is calculated by a linear softening equation:

$$D = \frac{u_m^f(u_m^{max} - u_m^0)}{u_m^{max}(u_m^f - u_m^0)} \tag{2.7}$$

where u_m^f, u_m^{max} and u_m^0 are the total failure displacement, maximum effective displacement and initial damage displacement respectively, as shown in **Fig. 2-5**.

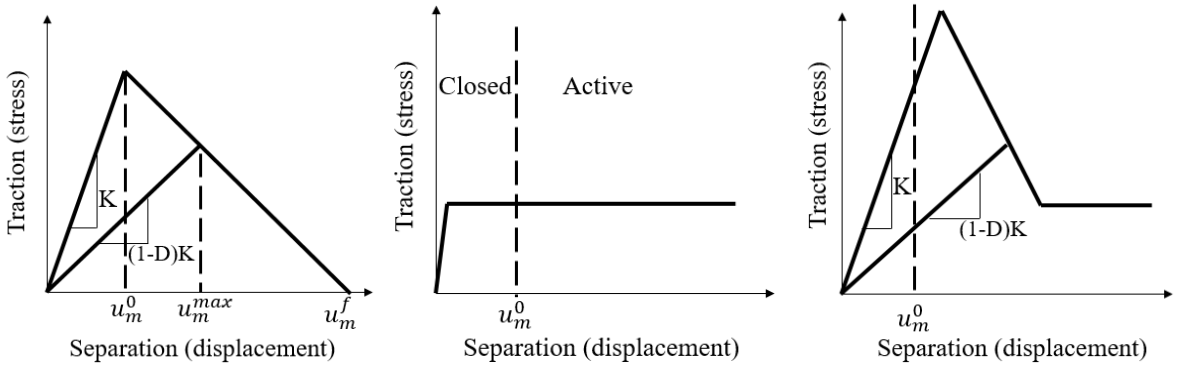

(a) traction-separation behaviour

(b) penalty friction behaviour

(c) combined behaviour with traction-separation law and penalty friction behaviour

Fig. 2-5 Combined interaction constitutive model

In the damage evolution process the total failure displacement u_m^f is calculated by the mixed fracture energy G_{mixed}^C:

$$u_m^f = 2G_{mixed}^C / f_{eff} \tag{2.8}$$

where: f_{eff} is the effective traction stress at damage initiation which is combined by shear mode and normal mode traction stresses. G_{mixed}^C is the mixed energy obtained Benzeggagh-Kenane (B-K) fracture criterion (Benzeggagh & Kenane, 1996):

$$G_{mixed}^C = G_n^f + \left(G_s^f - G_n^f\right)\left(\frac{G_s + G_t}{G_s + G_t + G_n}\right)^m \tag{2.9}$$

where: G_n^f and G_s^f are the fracture energy determined from direct tensile test and direct shear test respectively; G_n, G_s and G_t are the effective energy in the tensile, shear I and shear II direction respectively. m is the cohesive property parameter for the material, the author recommends m =2 for masonry joints here.

It is common that implicit constitutive model with softening and damage degradation behaviour has convergence problems. To overcome the potential convergence difficulties, a viscosity coefficient, μ, is adopted for the stabilization of the FE model. The value of μ is recommend as 0.002 based on Abdulla's (2017) parametric study for masonry finite element models. Surface based cohesive behaviour is applied in this project to simulate the brick-brick interface (simplified micro-model) or brick-mortar interface (detailed micro-model). Compared with element based cohesive behaviour, surface based behaviour has an advantage that it allows the

combination of traction-separation behaviour (**Fig. 2-5a**) with compressive-fractional behaviour (**Fig. 2-5b**). If the masonry specimen is under compressive and shear loading simultaneously, the interface has the composited behaviour in shear direction as shown in **Fig. 2-5c**. For the shear behaviour, if the traction-separation is undamaged, the cohesive is active but penalty friction is closed. Once the traction-separation start damaging, the penalty becomes active and contributes to the shear stress, so the shear stress is the combination of traction-separation and penalty friction.

2.3 Material Non-liner Behaviour

As a typical quasi-brittle material, clay bricks have typically granular-like characteristics that could be simulated by pressure-dependent yield constitutive model. Besides, their experimental results indicated that brick has much stronger compressive strength than its tensile strength under uniaxial loading condition (Chaimoon & Attard, 2009). Drucker-Prager model (1952) and Concrete Damage Plasticity (CDP) model proposed by Lee and Fenves (1998) are commonly used to simulate the quasi-brittle behaviour for pressure sensitive material with different uniaxial characteristics.

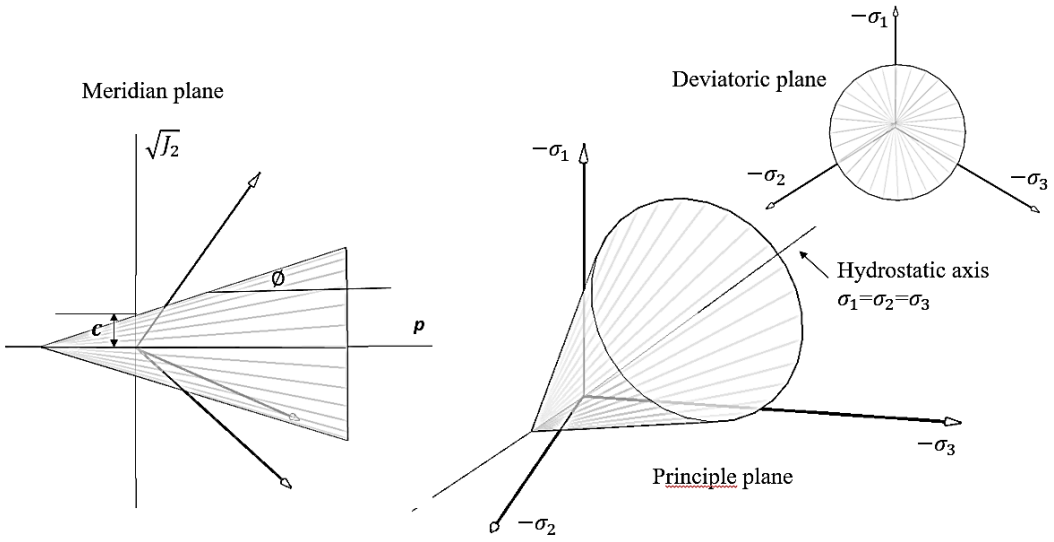

Fig. 2-6 Drucker-Prager criteria presented in meridian plane, principle plane and deviatoric plane

As shown in **Fig. 2-6**, Drucker-Prager model is a smooth surface cone in the 3D principle plane, and its cone tip is located in the tensile region while the bottom base is lie on the compressive region and has endless extension. In the deviatoric plane, Drucker-Prager model is an isotropic circle with a centre in the hydrostatic axis. The pressure-dependent characteristic can be represented in the meridian plane with yield equation:

$$f = \sqrt{J_2} - p\ tan\emptyset - c(\widetilde{\varepsilon_c^{pl}}) = 0 \tag{2.10}$$

where $\emptyset$ and $c(\widetilde{\varepsilon_c^{pl}})$ are frictional angle and cohesive strength in the meridian plane respectively, and the cohesive strength has hardening or softening characteristics with the increase of equivalent plastic strain. $\sqrt{J_2}$ is the root value of stress invariant which can be expressed in the principle plane as:

$$J_2 = \frac{1}{6}[(\sigma_1 - \sigma_2)^2 + (\sigma_2 - \sigma_3)^2 + (\sigma_3 - \sigma_1)^2] \tag{2.11}$$

Or a more common expression in the ordinate system:

$$J_2 = \frac{1}{6}[(\sigma_x - \sigma_y)^2 + (\sigma_y - \sigma_z)^2 + (\sigma_z - \sigma_x)^2] + \tau_{xy}^2 + \tau_{yz}^2 + \tau_{zx}^2 \tag{2.12}$$

And the horizontal axis ***p*** is the pressure or hydrostatic stress which has the expression as:

$$p = \frac{-(\sigma_1 + \sigma_2 + \sigma_3)}{3} \tag{2.13}$$

For quasi-brittle material, the dilation angle is usually not equal to the frictional angle, and the phenomenon requires the constitutive model obey non-associate flow rule with flow potential as:

$$G = \sqrt{J_2} - p\ tan\psi \tag{2.14}$$

where ψ is the dilation angle in the meridian plane, as shown in **Fig. 2-7**. The two functions f and G define the yield criteria and plastic flow direction respectively. Usually, the dilation angle is relatively smaller than frictional angle. The plastic strain increment vector $\{d\varepsilon^p\}$ is obtained from flow rule as:

$$\{d\varepsilon^p\} = d\lambda\ \frac{\partial G}{\partial\{\sigma\}} \tag{2.15}$$

In the above equation, $d\lambda$ is a scalar called the increment of plastic multiplier which determines the magnitude of plastic strain increment vector, while $\frac{\partial G}{\partial\{\sigma\}}$ is a vector which defines the direction of plastic strain increment vector. If the frictional angle $\emptyset$ equals to the dilation angle ψ, the direction vector derived from yield function $\frac{\partial f}{\partial\{\sigma\}}$ will be the same as the direction vector derived from potential function $\frac{\partial G}{\partial\{\sigma\}}$, which is called associate plastic flow rule.

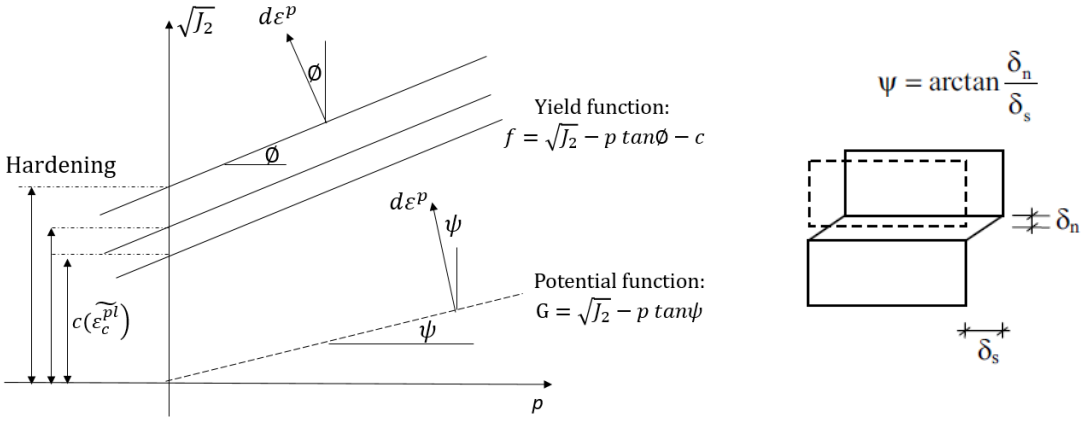

Fig. 2-7 Flow direction in yield surface and potential surface

The damage plasticity model for concrete developed by Lee and Fenves (1998) described the nonlinear behaviour of quasi-brittle materials by combining the isotropic damage elasticity with isotropic tensile and compressive plasticity. Uniaxial tensile and compressive behaviour of CDP model is illustrated in the **Fig. 2-8** with stress-strain relationship:

$$\sigma_t = (1 - d_t)\, E_0\, \widetilde{\varepsilon_t^{el}} = (1 - d_t)\, E_0 \left(\varepsilon_t - \widetilde{\varepsilon_t^{pl}}\right) \tag{2.16}$$

$$\sigma_c = (1 - d_c)\, E_0\, \widetilde{\varepsilon_c^{el}} = (1 - d_c)\, E_0 \left(\varepsilon_c - \widetilde{\varepsilon_c^{pl}}\right) \tag{2.17}$$

where E_0 is the elastic modulus, d_t and d_c are damage variables for tension and compression respectively with range $0 \le d_t \le 1$ and $0 \le d_c \le 1$. The damaged plastic tensile strain and compressive strain can be calculated as:

$$\widetilde{\varepsilon_t^{pl}} = \varepsilon_t^{pl} - \frac{d_t}{(1 - d_t)} \frac{\sigma_t}{E_0} \tag{2.18}$$

$$\widetilde{\varepsilon_c^{pl}} = \varepsilon_c^{pl} - \frac{d_c}{(1 - d_c)} \frac{\sigma_c}{E_0} \tag{2.19}$$

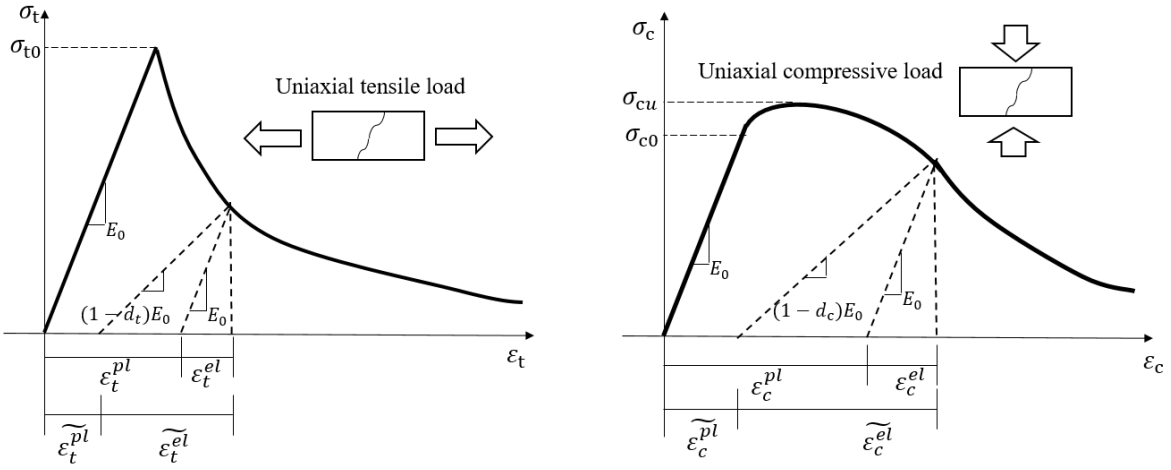

Fig. 2-8 Response of material under uniaxial test

Lubliner et.al (1989) firstly proposed a yield function for the plastic damage model as:

$$f = \frac{1}{1-\alpha}\left(\alpha I_1 + \sqrt{3J_2} + \beta\langle\bar{\sigma}_{max}\rangle - \gamma\langle\bar{\sigma}_{max}\rangle\right) \tag{2.20}$$

And then Lee and Fenves (1998) modified the above equation as:

$$f = \frac{1}{1-\alpha}\left(\alpha I_1 + \sqrt{3J_2} + \beta\langle\bar{\sigma}_{max}\rangle - \gamma\langle\bar{\sigma}_{max}\rangle\right) - \sigma_c(\widetilde{\varepsilon_c^{pl}}) \tag{2.21}$$

where α, β and γ are dimensionless constants, and they can be expressed as:

$$\alpha = \frac{\frac{f_{bc0}}{f_{c0}} - 1}{2\left(\frac{f_{bc0}}{f_{c0}}\right) - 1}; \qquad 0 \le \alpha \le 0.5 \tag{2.22}$$

$$\beta = \frac{\sigma_c\left(\widetilde{\varepsilon_c^{pl}}\right)}{\sigma_t\left(\widetilde{\varepsilon_t^{pl}}\right)}(1-\alpha) - (1+\alpha) \tag{2.23}$$

$$\gamma = \frac{3(1-K)}{2K-1}; \quad 0.5 < K \le 1.0 \tag{2.24}$$

Other components in **Eq (2.21)** such as I_1 is the stress invariant and $I_1 = \sigma_1 + \sigma_2 + \sigma_3$; $\bar{\sigma}_{max}$ is the maximum principal effective stress. In **Eq (2.22)**, f_{bc0} is the biaxial compressive strength and f_{c0} is the uniaxial compressive strength. **Fig. 2-9** describes the position of stress points for single element in different loading conditions in $\boldsymbol{\sigma_1 - \sigma_2}$ plane. CDP constitutive model has a closed symmetrical configuration when $\boldsymbol{\sigma_3} = 0$, and the yield surface is composited by three functions in different biaxial loading conditions. The intersections between axis and the yield surface present the uniaxial loading conditions. **Fig. 2-10** represents the projection of CDP model in deviatoric plane and meridian plane.

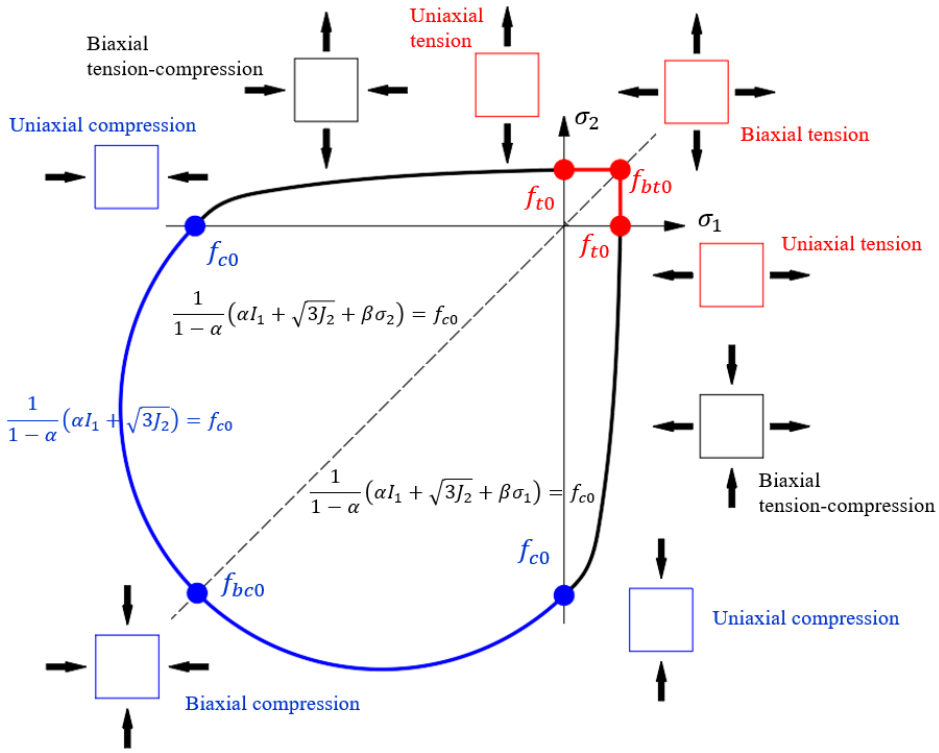

Fig. 2-9 Yield surface in $\boldsymbol{\sigma_1 - \sigma_2}$ plane ($\boldsymbol{\sigma_3 = 0}$)

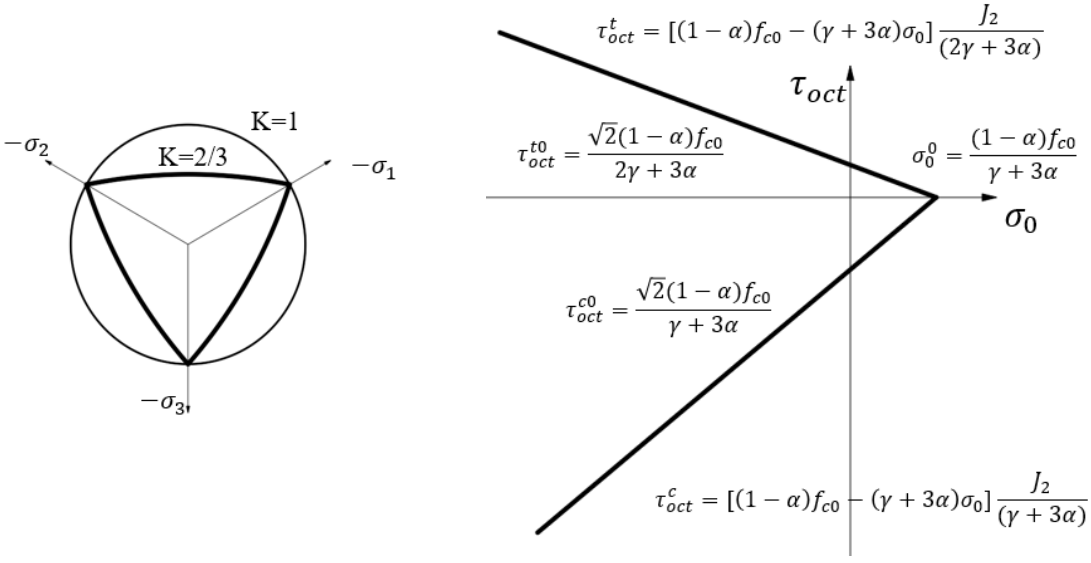

Fig. 2-10 Yield function of CDP constitutive model in deviatoric plane (left) and meridian plane (right)

2.4 Viscous Regulation

It is common that implicit constitutive model with softening and damage degradation behaviour has convergence problems. Davila et.al (2001) mentioned that serious convergence problem usually found in the analysis of interface element with softening behaviour. To overcome the potential convergence difficulties, a widely accepted method called viscous regularization schemes is applied in the FE models with a viscosity coefficient, μ. The viscous regulation scheme allow cohesive stress calculated from traction-separation law can be beyond the yield surface, and the tangent stiffness operator become positive.

The regulation theory is established based on the assumption of energy balance where extra energy dissipation is dependent on the velocity of separation (Yu et.al 2016). In **Section 2**, **Eqs (2.6)** and **(2.7)** introduce the relationship of traction stress and separation displacement by damage way. The true stresses (t_n, t_s, t_t) are calculated by multiplying $(1-D)$ with trial elastic stress $(\bar{t}_n, \bar{t}_s, \bar{t}_t)$ from **Eq (2.1)**. The regulation process involves a viscos damage variable D_v, which is defined as:

$$\dot{D_v} = \frac{\partial D_v}{\partial t} = \frac{1}{\mu}(D - D_v) \tag{2.25}$$

where $\dot{D_v}$ is a differential of D_v about the time step increment. Then the traction stress should be calculated (t_n, t_s, t_t) could be obtained by:

$$t_n = (1-D_v)\bar{t}_n, \qquad t_s = (1-D_v)\bar{t}_s, \qquad t_t = (1-D_v)\bar{t}_t \tag{2.26}$$

The value of μ is recommend as 0.002 based on Abdulla's (2017) parametric study for masonry finite element models.

2.5 Finite Element Model

2.5.1 Small scale masonry couplet specimen

To verify the reliability of the interaction model introduced above, a small scale masonry FE model coupled by two bricks and a mortar layer is built for comparing its modelling results with experimental results under pure tensile load and combined shear-compressive load, as shown in **Fig. 2-11**. **Table 2-1** lists all input data used for FE model of the small scale masonry couplet FE model. It can be seen from **Fig. 2-11** that the stress contours for tensile and shear loading is not symmetric during the final softening stage. This phenomenon may be caused by the unsymmetrical geometry of the FE model where mortar joint is connected with the upper brick.

Table 2-1 Damage parameters for nonlinear couplet models

	Normal strength f_t (N/mm^2)	Cohesive parameter c (N/mm^2)	Friction coefficient **μ**	Shear strength f_s (N/mm^2)	Tensile fracture energy (Nmm/mm^2)	Shear fracture energy (Nmm/mm^2)

Tension	0.28	0.3	0	0.3		0.188
Shear -0.1MPa pressure	0.3	0.87	0.75	0.945	0.012	0.071
Shear -0.5MPa pressure		0.87	0.75	1.245		0.123
Shear -1.0MPa pressure		1.2	1	2.2		0.188

.

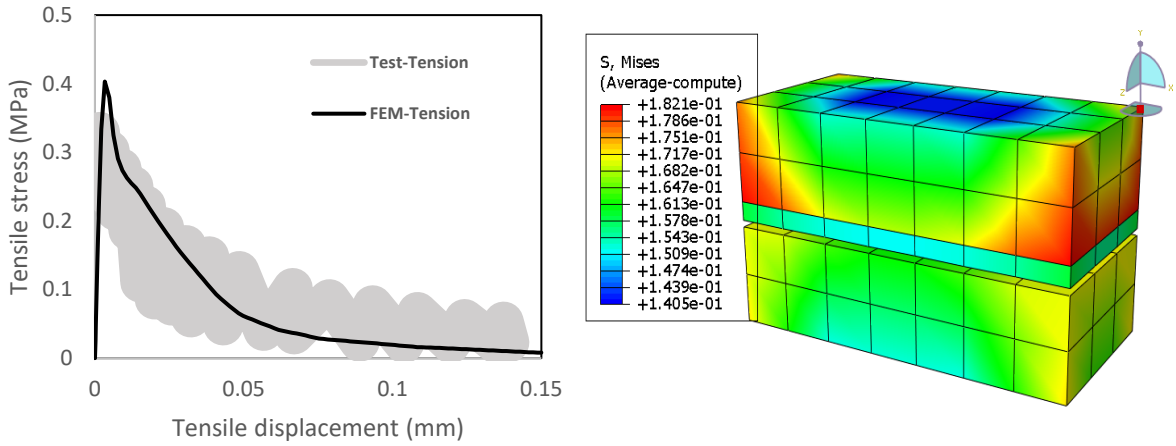

(a) Tensile behaviour

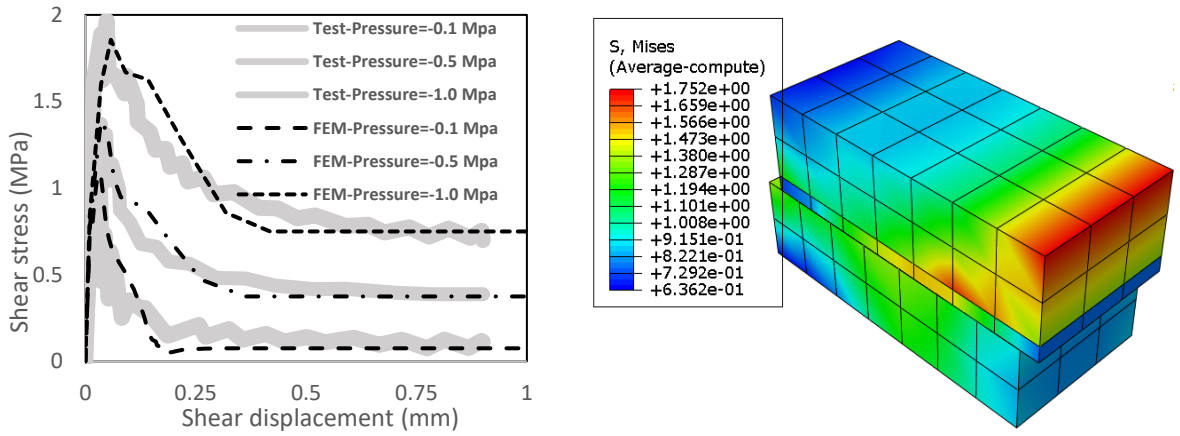

(b) Shear behaviour

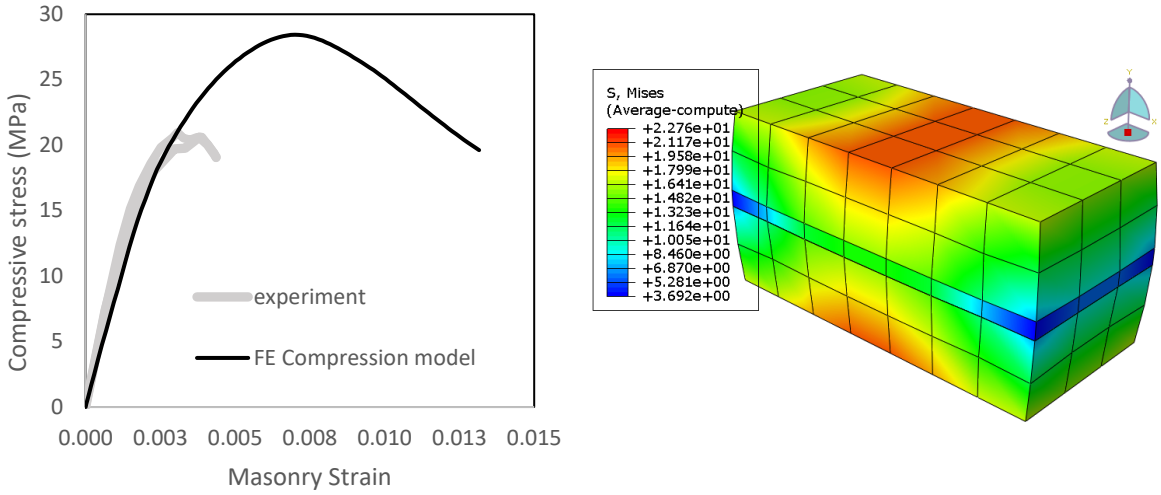

(c) Compressive behaviour

Fig. 2-11 Comparison of the damage behaviour between experimental results (Pluijm 1999; Pluijm and Vermeltfoort 1991) and proposed FE models

2.5.2 Detailed Micro-Model (In plane load)

A finite element model for the masonry under pre-compression and in-plane shear load is built as shown in **Fig 2-12**. The FE model technique proposed by D'Altri et.al (2018) used "texture units", a composite unit including both brick and mortar, to assembly masonry wall, which reduces the number of interfaces and improves the computing efficiency. The nonlinear behaviour of both brick and mortar are simulated by concrete damage plasticity (CDP) constitutive model (Lee & Fenves, 1998). **Table 2-2** and **Table 2-3** list all input data for the detailed micro FE model for masonry wall under in-plane load. The modelling results are compared with experiments conducted by Vermeltfoort and Raijmakers (1993). **Fig. 2-13** shows the failure pattern of FE models. Comparison between modelling results and experimental results is shown in **Fig. 2-14**.

Table 2-2 Interface properties of the in-plane wall model

	Tensile strength f_t (N/mm^2)	Shear strength f_s (N/mm^2)	Tensile fracture energy G_I^f (Nmm/mm^2)	Shear fracture energy G_{II}^f (Nmm/mm^2)
Pressure= -0.3	0.1	0.3	0.01	0.2
Pressure= -1.21	0.12	0.2	0.012	0.1
Pressure= -2.12	0.1	0.2	0.01	0.1

Table 2-3 Non-linear properties of bricks and mortar for CDP model of in-plane wall

Mortar				Brick			
Elastic modulus (MPa) 850; 1200		Poisson's ratio 0.15		Elastic modulus (MPa) 16700		Poisson's ratio 0.15	
Tensile nonlinear uniaxial behaviour		Compressive nonlinear uniaxial behaviour		Tensile nonlinear uniaxial behaviour		Compressive nonlinear uniaxial behaviour	
Stress (MPa)	Inelastic strain	Stress (MPa)	Inelastic strain	Stress (MPa)	Inelastic strain	Stress (MPa)	Inelastic strain
1.5	0	7	0	3.5	0	9	0
0.1	0.002	7.5	0.002	0.3	0.002	9.5	0.001
		0.4	0.015			0.6	0.007

(FE model of masonry walls under 0.3MPa and 2.12MPa pre-pressure have 850 MPa Elastic modulus mortar, while FE model of masonry wall under 1.21MPa pre-pressure has 1200 MPa Elastic modulus mortar.)

Fig. 2-12a shows the in-plane wall finite element model geometry and different textured units distribution, and **Fig. 2-12b** shows the loading conditions for the experimental specimen and its general failure patterns. There totally four masonry wall specimens were tested, two walls under 0.3 MPa vertical pre-pressure, one wall under 1.21 MPa vertical pre-pressure and one wall under 2.12MPa pre-pressure. Both experimental results and modelling results found a diagonal crack as the failure patterns for in-plane wall specimens. Firstly, there were short horizontal cracks appear on the top and bottom corners, and then tensile and shear failure happens on some head and bed joints. Finally, a continuum diagonal crack presented in the wall.

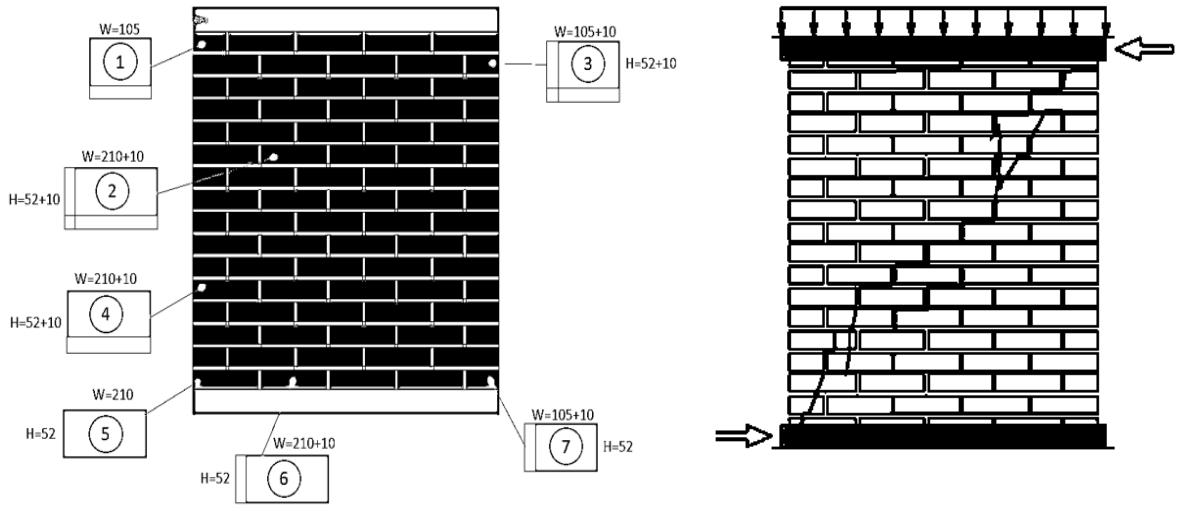

(a) finite element model assembly

(b) experiment specimen with cracking pattern

Fig. 2-12 In-plane masonry wall geometry

In **Fig. 2-13a,c,e**, minimum principle stress contour can help predict the next cracks happening position where negative stress concentrated due to the reason that interface tensile stress reduced. Similar to the experimental results, horizontal cracks found in corners initially, and then diagonal cracks appeared in the wall centre. It can be seen that the maximum magnitude of minimum principal stress contour plot has variation in stress (0.08, 0.225, 0.104), which is mainly caused by the different level of compressive failure of bricks. Some bricks in **Fig. 2-13e** have been softening while those in **Fig. 2-13a,b** are still in hardening stage.

In **Fig. 2-7b,d,f**, Concrete damage plasticity (CDP) model predicted the location of brick cracks occurs as well as the compressive crushing failure.it can be seen that the most critical compressive crushing exists on the corners.

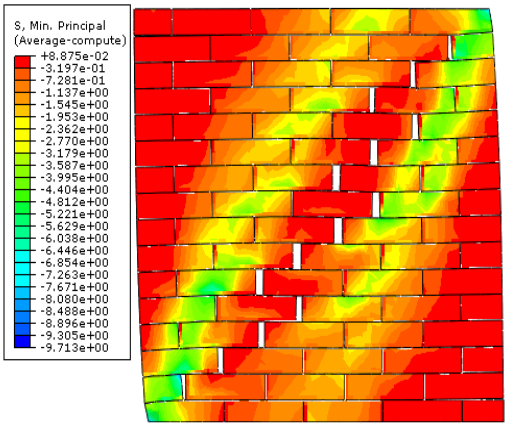

(a) Minimum principle stress contour (0.3MPa pre-pressure)

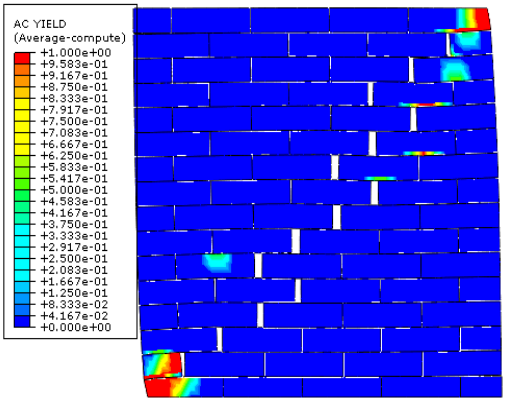

(b) brick yield patterns (0.3MPa pre-pressure)

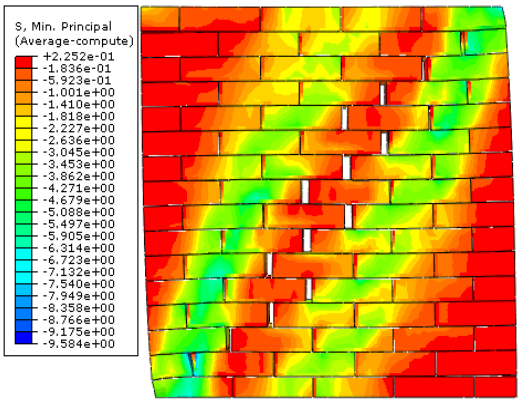

(c) Minimum principle stress contour (1.21MPa pre-pressure)

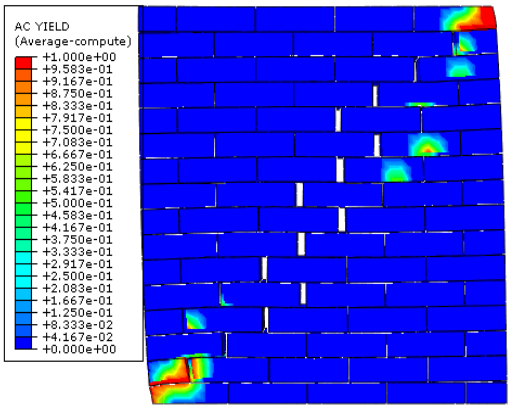

(d) brick yield patterns (1.21MPa pre-pressure)

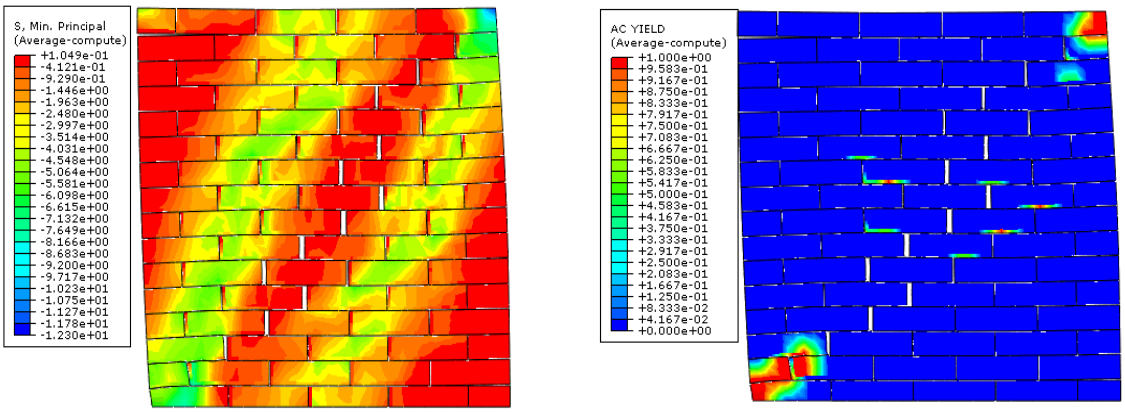

(e) Minimum principle stress contour (2.12MPa pre-pressure)

(f) brick yield patterns (2.12MPa pre-pressure)

Fig. 2-13 Failure patterns of modelling walls for specimens

In the **Fig. 2-14**, finite element models can predict the pre-failure and post-failure behaviour of masonry walls under in-plane shear loads effectively, but modelling results relatively overestimate the peak load of each wall. For walls under low pre-pressure (0.3 MPa), their non-linear behaviour includes a hardening part and a long consistent load plateau, while the plateau will decrease finally with the displacement increment. For walls under high pre-pressure (1.21 MPa and 2.12 MPa), their non-linear behaviour includes a short hardening and a followed long softening. It can be seen for the curves in **Fig. 2-8** that, the difference of final post-failure loads is relatively smaller than the difference of peak loads. The reason is that peak load is supported by shear and tensile capacity of joints, so different pre-pressures will result in different shear frictional capacities. However, with the increment of displacement, joint failure happened and lose their cohesive capacity, the failure load of masonry structures will be determined by wall's overturning capacity, namely, the compressive capability of bricks in corners.

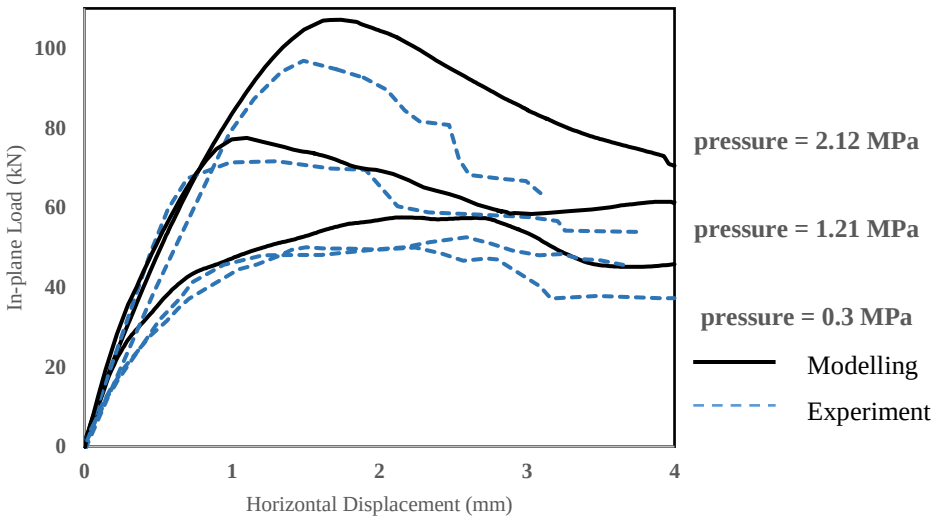

Fig. 2-14 Load-displacement relation of in-plane wall testing

2.5.3 Simplified Micro-Model (Out-of-plane load)

To estimate the performance of masonry wall under out-of-plane pressure load, two FE models with different configurations are simulated. One model is created based on single leaf masonry panel tested by Ng (1996) with 1190 mm height, 795 mm width and 53 mm thickness, so the height-width (H/W) ratio is about 1.5, as shown in **Fig. 2-15a**. Another model is created for the clay brick wall (Griffith's & Vaculik, 2007) with 2500 mm height, 4000 mm width and 110 mm thickness, so the height-width (H/W) ratio is around 0.63, as shown in **Fig. 2-15b**. **Table 2-4** lists the input interfacial properties used for FE models of two type out-of-plane walls. **Table 2-5** presents input data for FE model based on CDP material model of Ng' (1996) single leaf panel and **Table 2-6** lists input data for FE model using Drucker-Prager material model of the clay brick wall test by Griffith's & Vaculik's (2007).

Since the sizes of out-of-plane walls are much larger than in-plane walls sizes, the simplified micro-modelling strategy is more suitable for the simulation of out-of-plane wall. Besides, a quasi-static implicit dynamic analysis procedure is used to accelerate analysis time and save data storage. The analysis needs inertia parameters, such as density of the masonry wall, to solve motion equations.

Table 2-4 Interface properties of the out-of-plane wall model

	Tensile strength f_t (N/mm^2)	Shear strength f_s (N/mm^2)	Tensile fracture energy G_I^f (Nmm/mm^2)	Shear fracture energy G_{II}^f (Nmm/mm^2)
H/W=1.5	0.24	0.44	0.01	0.022
H/W=0.63	0.09	0.13	0.009	0.03

Table 2-5 Properties of expended bricks for CDP model (out of plane wall with 1.5 H/W ratio)

Elastic modulus (MPa)		Poisson's ratio		Density kg/m^3	
16700		0.15		2500	
Tensile nonlinear uniaxial behaviour		Compressive nonlinear uniaxial behaviour		Dilation angle	10
Stress (MPa)	Inelastic strain	Stress (MPa)	Inelastic strain	Eccentricity	0.1
3.5	0	11	0	f_{b0}/f_{c0}	1.16
0.3	0.002	11.5	0.001	K	0.667
		0.6	0.007	Viscosity parameter	0.002

Table 2-6 Properties of expended bricks for DP model (out of plane with 0.63 H/W ratio)

Elastic modulus (MPa)	Poisson's ratio	Angle of friction	Flow Stress Ratio	Dilation angle
3540	0.15	36	1	11.3

.

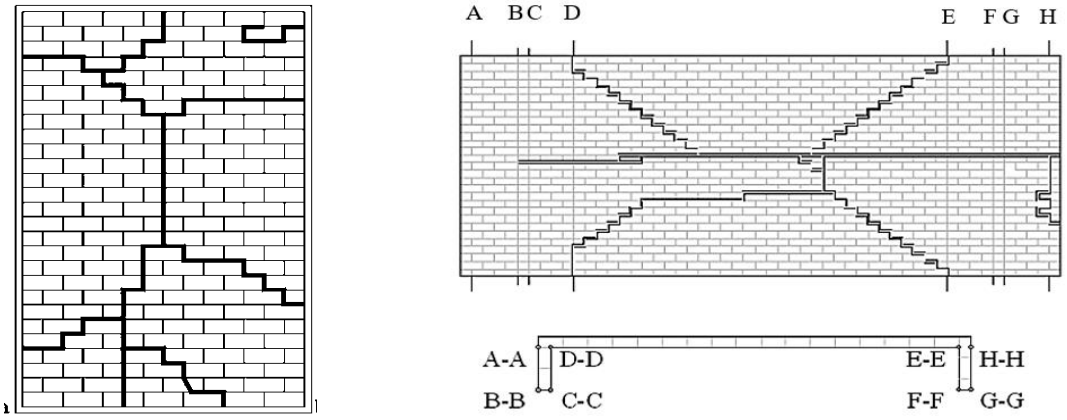

(a) H/W = 1.5 (left, Ng 1996) (b) H/W = 0.63 (right, Griffith & Vaculik 2007)

Fig. 2-15 Masonry wall with different geometry and corresponding failure modes

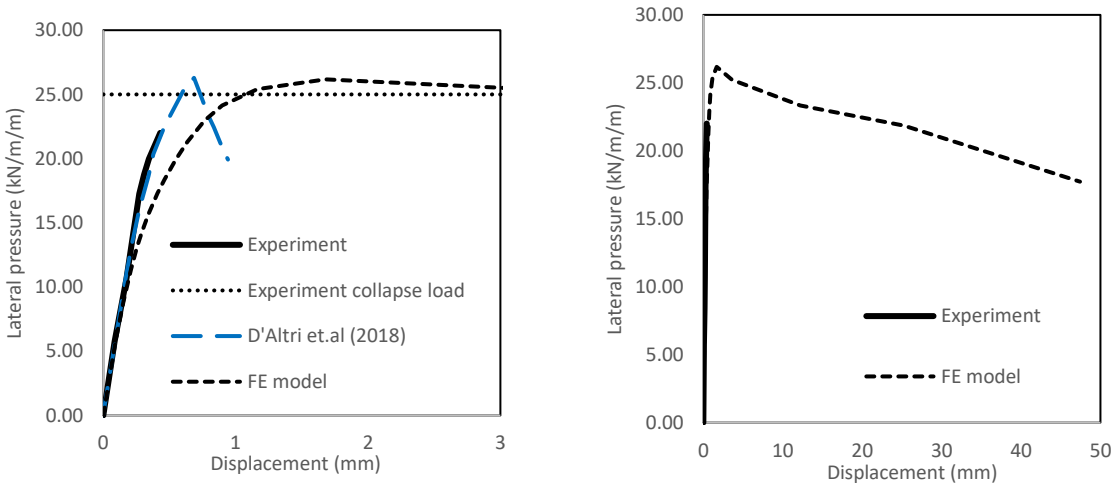

(a) displacement range 0-3mm (b) displacement range 0-50mm

Fig. 2-16 Load-displacement relation for H/W=1.5 masonry wall

In **Fig. 2-16**, the experimental result provided maximum load capacity and load-pressure relation from 0 to 0.5mm displacement. **Fig. 2-16a** compares the modelling results with

experimental results as well as D'Altri et.al (2018) modelling results. The experimental results did not capture the post-failure behaviour of the masonry wall but it provided the peak load which can be predicted by the FE model. Difference with the modelling result from D'Altri et.al (2018) which shows the masonry will be collapsed suddenly after the peak load, the FE model proposed by this paper predicts the masonry wall has much longer post-failure behaviour with a gradually softening curve, as shown in **Fig. 2-16b**. The FE model estimates the load-pressure relation over 50mm, and it predicts a softening process for the masonry wall.

The cracking pattern and stress contour of FE model are shown in **Fig. 2-17**. **Fig. 2-17a,b** show the maximum stress contour for bricks compressive failure, **Fig. 2-17c,d** show minimum stress contour for bricks tensile failure, **Fig. 2-17e,f** show the interface opening contour for masonry joint failure and **Fig. 2-17g,h** show the deformation of masonry in vertical middle and horizontal middle respectively. The cracking pattern includes four diagonal cracks caused by two-way bending moment and one vertical crack caused by horizontal bending moment. The air-bag pressure firstly resulted in the two-way bending deformation and then the four diagonal crack happened, which is followed by a vertical crack caused by horizontal bending moment. The maximum principal stress contour shows that four corners experienced the most critical damage. In contrast, other positions have relatively lower stress concentration.

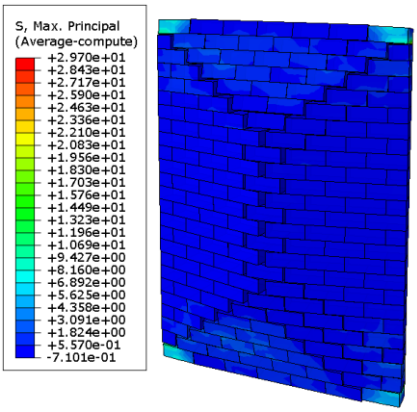

(a) Maximum stress contour (Front)

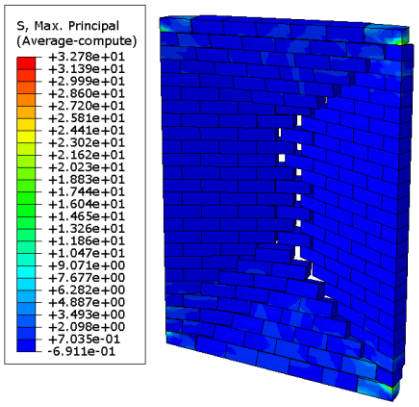

(b) Maximum stress contour (Back)

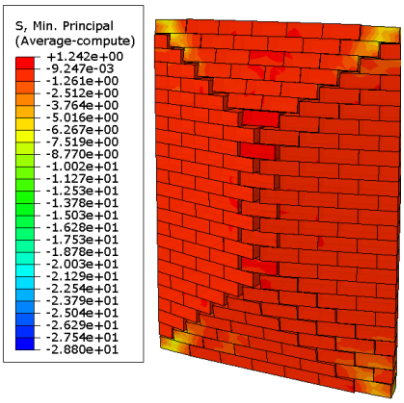

(c) Minimum stress contour(Front)

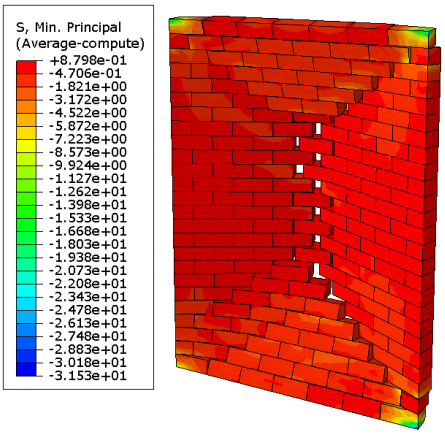

(d) Minimum stress contour(Back)

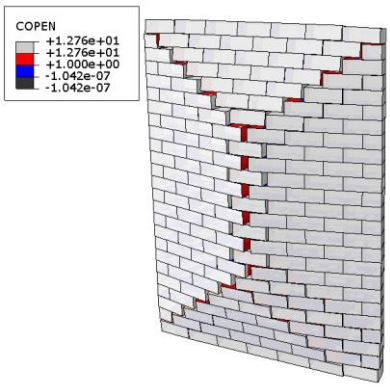

(e) cracking pattern (Front)

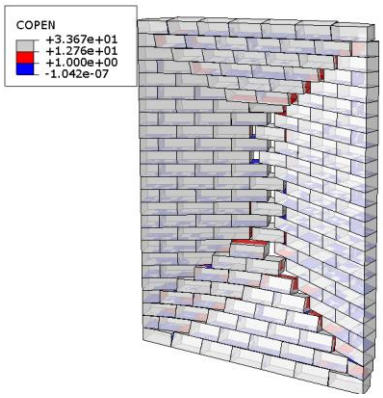

(f) cracking pattern (Back)

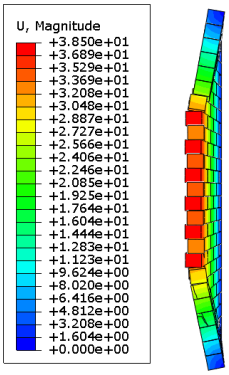

(g) Half FE model deformation Vertical direction

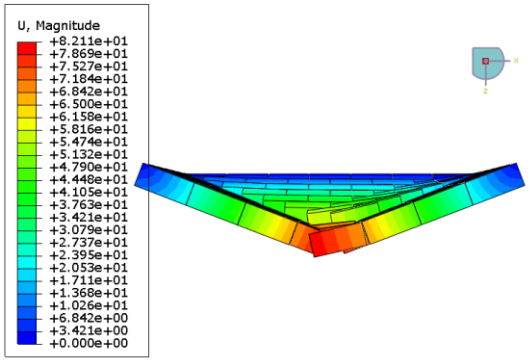

(h) Half FE model deformation Horizontal direction

Fig. 2-17 Failure patterns of H/W = 1.5 wall FE models

Difference with the H/W=1.5 wall FE model using CDP as material constitutive model, the nonlinear material constitutive model for simulating H/W=0.63 wall FE model is Drucker-Prager (DP) plasticity model. The material parameters are summarized in the Table 6, and the hardening behaviour of expended brick is obtained based on Kaushik et.al (2007) analytical model as shown in **Fig. 2-18a**. Another difference is the analysis procedure for H/W=0.63 wall is implicit static rather than implicit dynamic, because the author obtained a better failure pattern for the masonry from implicit static procedure.

Fig. 2-18a shows the relationship between yield stress and plastic strain for expanded bricks under uniaxial compressive load modelled with Drucker-Prager material model. The expanded brick can bear nearly 16MPa peak uniaxial compression with a linear softening response. The air bag pressure - lateral displacement relationships for the FE model and the experiment specimen are compared in **Fig. 2-18b**, which shows the pressure increased gradually and then kept a constant value with the increase of lateral displacement. Initially, the pressure was resisted by the wall until it reached the maximum two-way bending capacity where diagonal cracks, then the horizontal cracks happened means only vertical bending capacity resist the pressure.

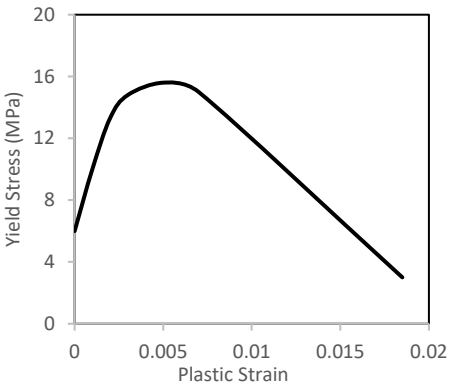

(a) Hardening behaviour of a brick under uniaxial compression obtained from analytical model

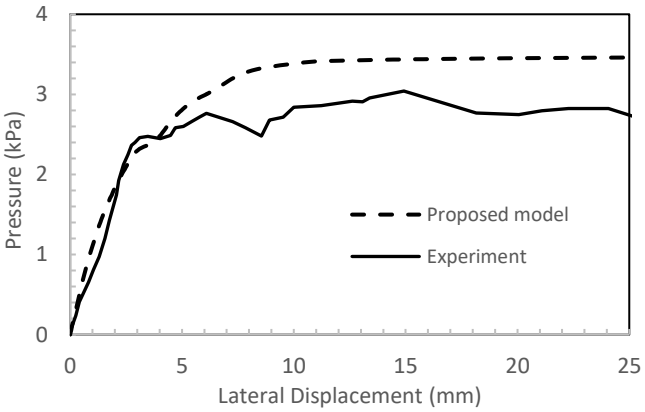

(b) Pressure – lateral displacement relation for a masonry wall (H/W = 0.63)

Fig. 2-18 Material behaviour and structure response

Maximum principle stress contour (**Fig. 2-19a, b**), minimum principle stress contour (**Fig. 2-19c, d**), cracking patterns (**Fig. 2-19e, f**) and deformation shapes (**Fig. 2-19g,h**) are shown in **Fig. 2-19**. The cracking pattern includes four diagonal cracks caused by two-way bending moment and two horizontal cracks caused by vertical bending moment. It can be seen from **Fig. 2-19a, b** that the distribution of maximum principle stress has highly consistence with the crack patterns, which means the tensile failure may happen not only in the joint, but also in the brick near the cracked joint. In **Fig. 2-19**, damage contours are not displayed since there is no damage parameters are used in the Drucker-Prager model.

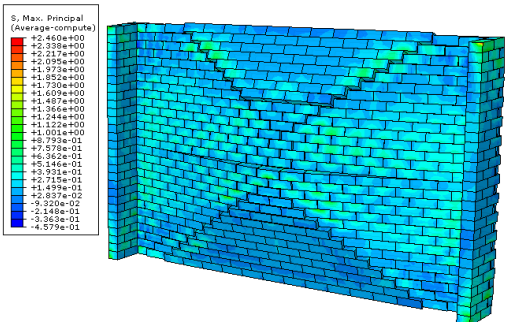

(a) Maximum stress contour (front)

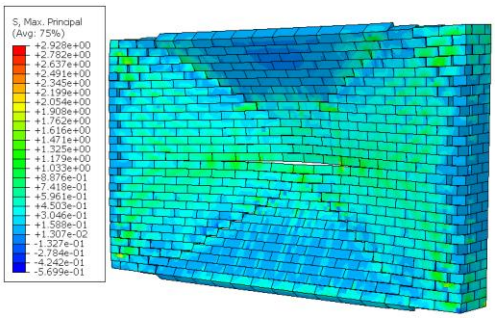

(b) Maximum stress contour (back)

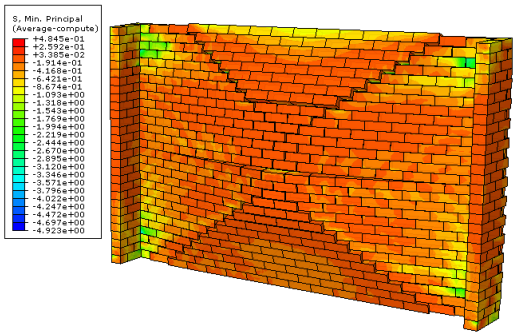

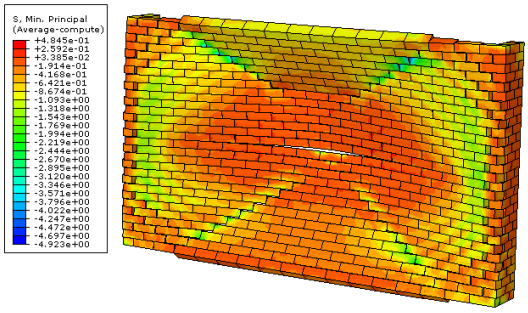

(c) Minimum stress contour (front)

(d) Minimum stress contour (back)

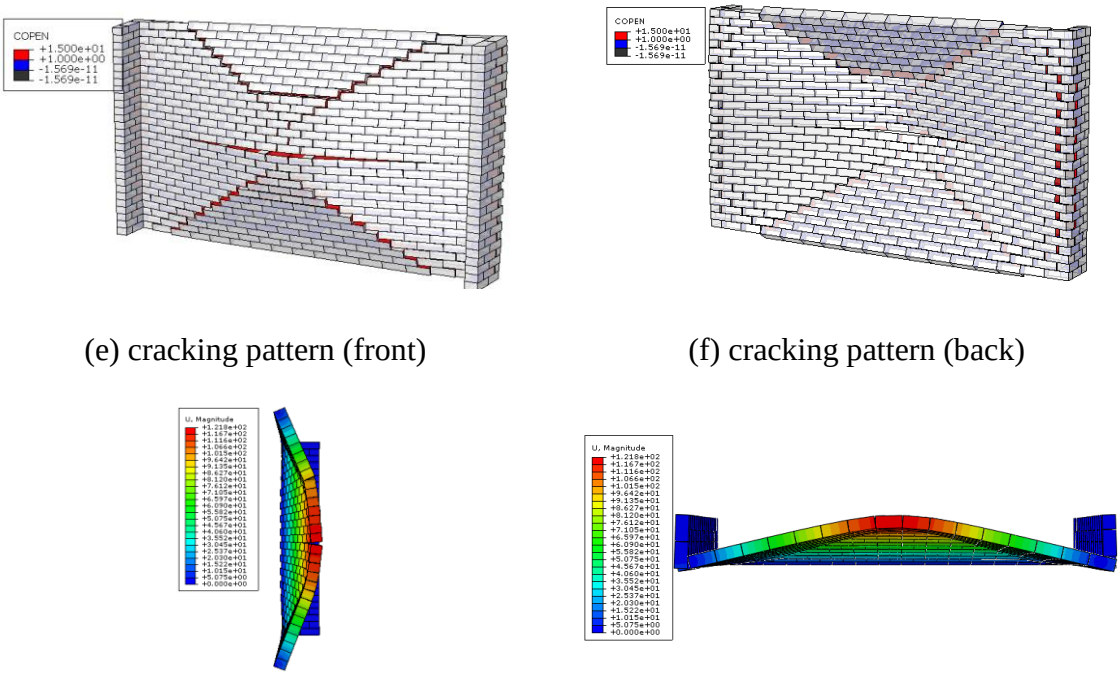

(e) cracking pattern (front)

(f) cracking pattern (back)

(g) Half FE model deformation Vertical direction

(h) Half FE model deformation Horizontal direction

Fig. 2-19 Failure patterns of H/W = 0.63 wall FE models

2.6 Conclusion

In this paper, a mix-mode damage interaction constitutive model is applied in both detailed micro-modelling strategy for in-plane masonry walls and simplified micro-modelling strategy for out-of-plane masonry walls. Concrete damage plasticity material model and Drucker-Prager material model are used to simulate the nonlinear behaviour of expended bricks in different geometry walls under out-of-plane pressure.

The proposed interfacial modelling approach can avoid convergence difficulty with the help of the viscosity coefficient, which also improves the computing efficiency by the acceptable cost of accuracy. Compared with existing finite element models, the proposed model presented in this paper has the ability to predict the post-failure behaviour of masonry wall under different loading conditions exactly. Besides, the failure patterns of finite element wall models have quite well agreement with experimental results.

However, the complex mechanism of interface shear behaviour is still needed to be investigated. The combination of normal pressure and shear movement will result in frictional force that plays a critical role in the post failure behaviour in the shear direction. Another flaw of the proposed models is that neither the shear capacity nor the shear fracture energy is sensitive to the normal stress in the contact faces. According to Pluijm's (1992) study both shear strength

and shear fracture energy have a positive linear relation with normal stress. Therefore, the authors will focus on a more functional interaction constitutive model in the future study.

2.7 Reference

Abdulla, K. F., Cunningham, L. S., & Gillie, M. (2017). Simulating masonry wall behaviour using a simplified micro-model approach. Engineering Structures, 151, 349-365.

Andreotti, G., Graziotti, F., & Magenes, G. (2018). Detailed micro-modelling of the direct shear tests of brick masonry specimens: the role of dilatancy. Engineering Structures, 168, 929-949.

Anthoine, A. (1995). Derivation of the in-plane elastic characteristics of masonry through homogenization theory. International journal of solids and structures, 32(2), 137-163.

Benzeggagh, M. L., & Kenane, M. J. C. S. (1996). Measurement of mixed-mode delamination fracture toughness of unidirectional glass/epoxy composites with mixed-mode bending apparatus. Composites science and technology, 56(4), 439-449.

Camanho, P. P., & Dávila, C. G. (2002). Mixed-mode decohesion finite elements for the simulation of delamination in composite materials.

Chaimoon, K. and Attard, M.M., 2009. Experimental and numerical investigation of masonry under three-point bending (in-plane). Engineering Structures, 31(1), pp.103-112.

Davila, C., Camanho, P., & de Moura, M. (2001, April). Mixed-mode decohesion elements for analyses of progressive delamination. In 19th AIAA applied aerodynamics conference (p. 1486).

D'Altri, A. M., de Miranda, S., Castellazzi, G., & Sarhosis, V. (2018). A 3D detailed micro-model for the in-plane and out-of-plane numerical analysis of masonry panels. Computers & Structures, 206, 18-30.

Drucker, D.C. and Prager, W., 1952. Soil mechanics and plastic analysis or limit design. Quarterly of applied mathematics, 10(2), pp.157-165.

Gautam, D., Rodrigues, H., Bhetwal, K. K., Neupane, P., & Sanada, Y. (2016). Common structural and construction deficiencies of Nepalese buildings. Innovative Infrastructure Solutions, 1(1), 1.

Kaushik, H. B., Rai, D. C., & Jain, S. K. (2007). Stress-strain characteristics of clay brick masonry under uniaxial compression. Journal of materials in Civil Engineering, 19(9), 728-739.

Lee, J. and Fenves, G.L., 1998. Plastic-damage model for cyclic loading of concrete structures. Journal of engineering mechanics, 124(8), pp.892-900.

Lee, J., & Fenves, G. L. (1998). Plastic-damage model for cyclic loading of concrete structures. Journal of engineering mechanics, 124(8), 892-900.

Lotfi, H. R., & Shing, P. B. (1991). An appraisal of smeared crack models for masonry shear wall analysis. Computers & structures, 41(3), 413-425.

Lotfi, H. R., & Shing, P. B. (1994). Interface model applied to fracture of masonry structures. Journal of structural engineering, 120(1), 63-80.

Lourenço, P. B., & Rots, J. G. (1997). Multisurface interface model for analysis of masonry structures. Journal of engineering mechanics, 123(7), 660-668.

Lourenço, P. J. B. B. (1997). Computational strategies for masonry structures.

Lubliner, J., Oliver, J., Oller, S. and Oñate, E., 1989. A plastic-damage model for concrete. International Journal of solids and structures, 25(3), pp.299-326.

Manual, A. U. (2014). Version 6.14-4. Dassault Syste'mes Simulia Corp, Providence.

Ng, C. L. (1996). Experimental and theoretical investigation of the behaviour of brickwork cladding panel subjected to lateral loading.

Van der Pluijm, R. (1992). Material properties of masonry and its components under tension and shear.

Vermeltfoort, A. T., & Raijmakers, T. M. J. (1993). Deformation controlled meso shear tests on masonry piers. The Netherlands: Building and Construction Research, Eindhoven, Report B-92-1156, TNO-BOUWrrU Part, 2.

Yu, H., Olsen, J. S., Olden, V., Alvaro, A., He, J., & Zhang, Z. (2016). Viscous regularization for cohesive zone modeling under constant displacement: An application to hydrogen embrittlement simulation. Engineering Fracture Mechanics, 166, 23-42.

Chapter 3: A pure plasticity based model

Nie, Y, Sheikh, A., Griffith, M., Visintin, P. and Vaculik, J. (2020, Nov 18 - 29). An interface constitutive model for predicting masonry structural failure by finite element method. Australian Earthquake Engineering Society Virtual Conference

Chapter 3: A pure plasticity based model

Abstract

This chapter introduces an interface model which can be used to predict the failure modes of masonry walls under in-plane loads. The interface constitutive model is developed for a cohesive element that simulates the cracking behaviour in mortar joints and brick potential cracking area based on a 2D traction-separation law in the framework of plasticity. Interfacial characteristics, including dilation, friction and mixed mode cohesive failure, are considered in the interface model which can simulate the tensile-shear failure of masonry interface. A concrete damage plasticity model is applied to simulate the compressive crushing behaviour of bricks. A fully backward Euler method with consistent tangent operator is adopted for the implementation of the zero thickness interface model, while an adaptive sub-stepping scheme is adopted for the algorithm to improve the robustness of numerical models. Performance of the interface constitutive model is evaluated by comparing modelling results with experimental results. The comparisons show that the proposed model can effectively predict the load capacity and nonlinear response of masonry walls under in-plane loading. In the further work, the interface elastoplastic model would be extended to damage-plasticity model which has a wider application in simulating masonry walls under cyclic and seismic loads.

3.1 Introduction

Masonry structures and materials were widely used in historical buildings (eg. construction age over 100 years) which are sensitive to the external loads, such as earthquake and foundation settlement. To protect these buildings from external dangers and reduce potential loss, predicting the failure modes for masonry is necessary as it can provide useful information for reinforcement and repairing work. The analysis of masonry structure is relatively complex Compared with steel or concrete buildings due to its composite material characteristics and the different mechanics of brick and mortar. Thus, predicting the cracking propagation and crushing failure in masonry structures is a challenging task. To analyse masonry structures the use of empirical formula is a common methodology which can provide necessary engineering information including load capacity, deformation in certain position and stiffness degradation (Griffith et.al, 2007; Vaculik & Griffith, 2017). While analytical methods are concise and practical in masonry construction, its performance in detecting the post-failure modes of aging masonry buildings is limited. In the early stage of repairing historical architectures, determining potential cracking or crushing regions in the masonry structure is a key step for further reinforcement work (Vaculik et.al 2018). Compared with traditional analytical methods, numerical modelling can offer more comprehensive details on the post-failure response of masonry structures by presenting the cracking contours in mortar joints and compression failure contours in bricks. Clear identification of failure modes is helpful in reducing reinforcement cost and improving repairing efficiency (Su et.al, 2011).

Plasticity theory and damage mechanics are two popular frameworks for creating the constitutive criterion for the interface of masonry and other quasi-brittle materials (D'Altri et.al 2019). Both frameworks establish the fracture criterions of interface in tension (Mode I) and shear (Mode II) by using a traction-separation law in the cohesive element (Camanho & Dávila, 2002).

Damage mechanics simulate the nonlinear behaviour of material using a stiffness degradation assumption which has a specified advantage in cyclic loading simulations (Smoljanović et.al,

2015). However, two critical characteristics of quasi-brittle materials, frictional and dilation effects, are not considered in the damage constituents. Thus, plasticity theory including Coulomb frictional criterion with non-associated flow rule is a more proper framework for masonry structure modelling. The idea of applying plasticity theory in cohesive element for cracking modes simulation is not only using in masonry structures (Macorini & Izzuddin, 2011; Giambanco et.al, 2001), but also widely accepted in rock (Linh et.al 2017), concrete (Linh et.al 2019) and geotechnical material modelling (DeBorst et.al, 2012). Although plasticity theory includes comprehensive characteristics of masonry nonlinear behaviour, its accuracy and robustness meets difficulties during implementation stage. To ensure the accuracy, backward Euler integration method with Newton-Raphson iteration (Trapp & Öchsner, 2018) is adopted as the stress return mapping strategy but it may lead to diverging problem, thus adaptive sub-stepping scheme (Pérez et.al, 2001; Abbo 1997) is considered in the implementation algorithm for enhancing the modelling robustness.

In this paper, a hyperbolic yield surface (Caballero et.al, 2008) considering a tension-shear mixed mode failure is proposed for simulation of masonry joint cracking while a concrete damage plasticity model is used to predict brick compressive crushing. This modelling combination provide a comprehensive and detailed failure model for masonry structures and avoids the convex problem in multi-surface constitutive models. Implicit integration approach and sub-stepping scheme at the material level ensure both accuracy and robustness of modelling results.

3.2 Finite element modelling

There are three main categories for finite element modelling and each of them have pros and cons regarding their computing costs and accuracy, there are: (1) detailed micro-modelling which contains all detailed instances including brick element, mortar element and brick-mortar interface; (2) simplified micro-modelling where mortar layers are simplified as zero-thickness interface connecting bricks and (3) macro-modelling where the brick and mortar are combined and regarded as one material. The simplified modelling strategy is a common approach assumes the masonry structure is mainly composed of extended bricks, while the mortar joints are lumped into a series of horizontal and vertical zero-thickness interfaces between the extended bricks, as shown in the **Fig. 3-1**.

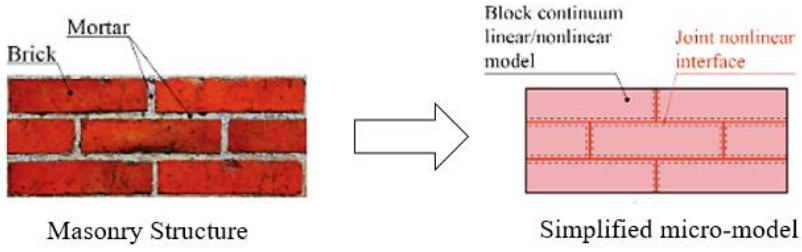

Fig. 3-1. Simplified micro-modelling strategies (D'Altri et.al 2018)

3.3 Interface constitutive model

The current interface constitutive model mimics the nonlinear material behaviour in 2D stress space ($\sigma - \tau$) based on a plasticity framework. A typical cohesive element having two parallel surfaces with zero thickness between them is shown in **Fig. 3-2** that has normal (n) and shear (s) displacements or rather relative displacements (u_n, u_s) and corresponding stresses components (σ, τ). The elastic stiffness of the interface in the normal and shear directions can be represented by two springs having stiffness of *Kn* and *Ks* with no coupling between them. With these quantities, the elastic stiffness matrix [*K*], stress vector $\{\sigma\}$ and displacement vector $\{u\}$ are as follows:

$$[K] = \begin{bmatrix} Kn & 0 \\ 0 & Ks \end{bmatrix} \quad \{\sigma\} = \begin{Bmatrix} \sigma \\ \tau \end{Bmatrix} \quad \{u\} = \begin{Bmatrix} u_n \\ u_s \end{Bmatrix} \tag{3.1}$$

.

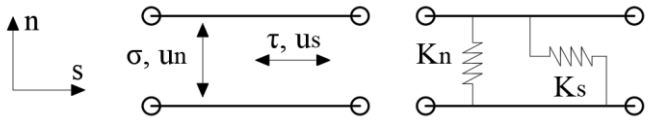

Fig. 3-2 Elastic behaviour

Fig. 3-3 shows the interfacial stress-displacement response with softening, modelled as plastic deformations, where the displacement increment $\{\mathrm{du}\} = [du_n \quad du_s]^T$ can be decomposed in its elastic $\{\mathrm{du^e}\} = \{du_n^e,\ du_s^e\}^T$ and plastic $\{\mathrm{du^p}\} = \{du_n^p,\ du_s^p\}^T$ components i.e. $\{\mathrm{du}\} = \{du^e\} + \{du^p\}$. Figure 3 also helps to write the increment stress–strain relationship as:

$$\{d\sigma\} = [K]\{du^e\} = [K](\{du\} - \{du^p\}) \tag{3.2}$$

It shown the determination of plastic displacement increment $\{du^p\}$ is vital and it can be obtained using the flow rule of plasticity as:

$$\{du^p\} = \dot{\lambda}\frac{\partial Q}{\partial\{\sigma\}} \tag{3.3}$$

where *Q* is the plastic potential which is similar to yield or failure surface *F* as shown in **Fig. 3-4**.

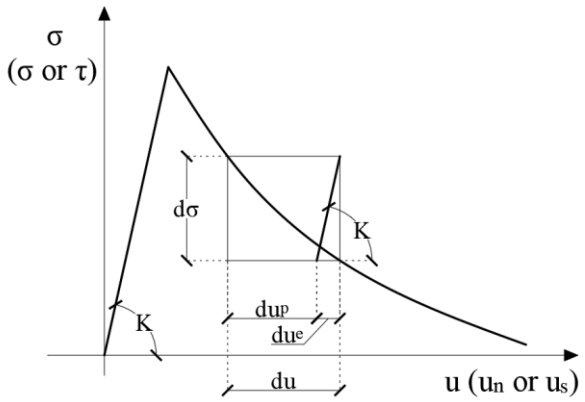

Fig. 3-3 Stress-displacement response

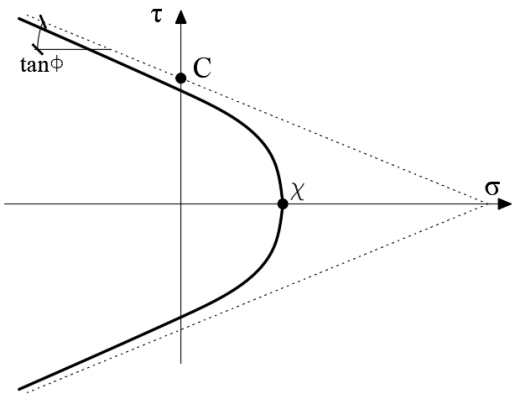

Fig. 3-4 Yield surface of the interface

3.3.1 Plastic potential and failure surfaces

The failure surface (**Fig. 3-4**) is having a hyperbolic shape that can be enveloped considering normal-shear mixed yield behaviour. The hyperbolic failure surface F is defined by three hardening parameters: 1) tensile strength χ, 2) cohesive strength in shear C (asymptotic cohesion in this case), and 3) friction angle ϕ or friction coefficient $tan\phi$ as follows.

$$F(\{\boldsymbol{\sigma}\},\{\Phi\}) = -(C - \sigma\, tan\phi) + \sqrt{\tau^2 + (C - \chi\, tan\phi)^2} = 0 \tag{3.4a}$$

$$\{\Phi\} = \{tan\phi, C, \chi\} \tag{3.4b}$$

Since masonry joints have a quasi-brittle material behaviour, a non-associate flow rule is adopted by taking a plastic potential Q which is different with the yield surface F. The expression of Q can be obtained from that of F (**Eq 3.4**) by replacing friction angle ϕ with dilation angle ϕ_Q and cohesion C with C_Q as follows.

$$Q(\{\boldsymbol{\sigma}\},\{\Phi_Q\}) = -(C_Q - \sigma\, tan\phi_Q) + \sqrt{\tau^2 + (C_Q - \chi\, tan\phi_Q)^2} = 0 \tag{3.5a}$$

$$\{\Phi_Q\} = \{tan\phi_Q, C_Q, \chi\} \tag{3.5b}$$

3.3.2 Plastic work and its evolution

Plastic work is taken as the internal variable that is utilised to characterising the evolution of cracking in the plastic stage. With the growth of cracks, the hardening parameters $(tan\phi, C, \chi)$ show a softening behaviour leading to shrinking of the yield surface. The plastic work increment due to crack growth is defined as:

$$dW = \begin{cases} \sigma du_n^p + \tau\, du_s^p, & \sigma \geq 0 \ \ (Tension) \\ (|\tau| + \sigma\, tan\phi)\, |du_s^p|, & \sigma < 0 \ \ (Compression) \end{cases} \tag{3.6}$$

The effect of σ in the second part of the above equation ($\sigma < 0$) follows the recommendation of Willam et al. (1984). **Fig. 3-5** shows the evolution of hardening parameters ($tan\phi, C, \chi$) where all of them are having a softening behaviour which are defined as follows.

$$\chi = \begin{cases} \chi_0 \left(\frac{1}{2} + \frac{1}{2} cos\left(\frac{\pi W}{G_f^I} \right) \right), 0 < W \leq G_f^I \\ 0, \qquad\qquad W > G_f^I \end{cases} \tag{3.7}$$

$$C = \begin{cases} C_0 \left(\frac{1}{2} + \frac{1}{2} cos\left(\frac{\pi W}{G_f^{II}} \right) \right), 0 < W \leq G_f^{II} \\ 0, \qquad\qquad W > G_f^{II} \end{cases} \tag{3.8}$$

$$tan\phi = \begin{cases} tan\phi_0 - (tan\phi_0 - tan\phi_r) \left(\frac{1}{2} - \frac{1}{2} cos\left(\frac{\pi W}{G_f^{II}} \right) \right), & 0 < W \leq G_f^{II} \\ tan\phi_r \ , & W > G_f^{II} \end{cases} \tag{3.9}$$

It is to be noted that cosine functions are used in the above equations which helps to ensure continuity in the derivatives needed in future calculations. **Fig. 3-5** shows that the hardening parameters varied from their initial values $\chi_0, C_0, tan\phi_0$ to zero except for $\tan\phi_0$ which is having a residual frictional coefficient $tan\phi_r$. The above equations also need G_f^I and G_f^{II} which are fracture energies in normal (tension) mode (Mode I) and shear mode (Mode II) respectively.

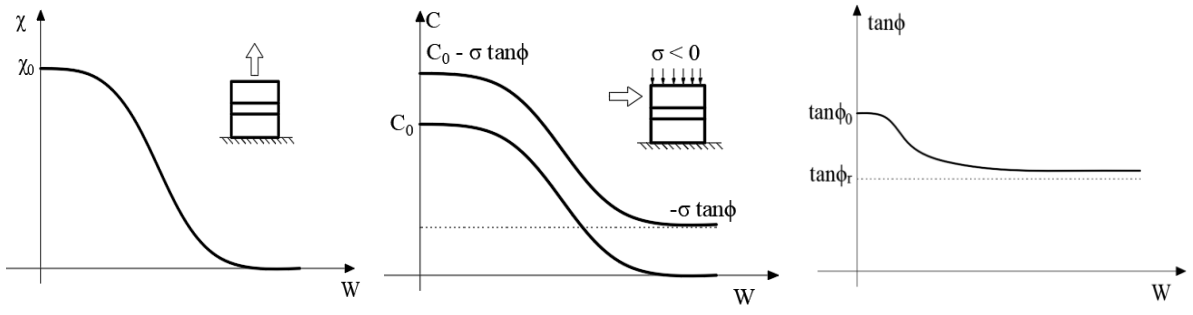

(a) Tensile strength (b) Cohesion in shear (c) Friction coefficient

Fig. 3-5 Evolution of hardening parameters

3.4 Numerical implementation and adaptive sub-stepping scheme

The above formulation for the interface constitutive model is implemented by using an elastic predictor-plastic corrector strategy in a monolithic framework. A system of nonlinear equations containing of stress $\{\sigma\}_{n+1}$, plastic work W_{n+1} and plastic multiplier $d\lambda$ is solved together using a full implicit backward Euler stress updating scheme with the help of Newton-Raphson iteration technique applied at each Gauss point (local level). Moreover, consistent tangent stiffness matrix is derived to support the full Newton-Raphson iteration at the element or global level. Even though the backward Euler technique provides accurate results, convergence is a common issue in many situations for solving complex numerical problems. To improve the robustness of the FE model, an adaptive sub-stepping scheme is adopted in this study.

3.4.1 Stress return mapping

The objective of the time integration technique (backward Euler) for stress return at a local level (Gauss point) is to determine its stress $\{\sigma\}_{n+1}$ and plastic work W_{n+1} corresponding to load step n+1 using their known converged values in the previous load step n and the known displacement increment $\{du\}_{n+1}$ coming from the global analysis. This will be solved iteratively using Newton-Raphson technique due to nonlinearity if yielding occurs.

The first step is to determine the trial stress (elastic predictor) that can be expressed as：

$$\{\sigma^{trial}\}_{n+1} = \{\sigma\}_n + [K]\{du\}_{n+1} \tag{3.10}$$

If the substitution of above trial stress and known plastic work (W_n) in **Eq. (3.4)** gives a negative value of F, there is no yielding occurs and it will lead to $\{\sigma\}_{n+1} = \{\sigma^{trial}\}_{n+1}$ and $W_{n+1} = W_n$. Otherwise, the stress and internal variable need to be updated as follows:

$$\{\sigma\}_{n+1} = \{\sigma^{trial}\}_{n+1} - \dot{\lambda}\,[K]\,\{m(\{\sigma\}_{n+1}, W_{n+1})\} \tag{3.11}$$

$$W_{n+1} = W_n + dW_{n+1}(\{\sigma\}_{n+1}, W_{n+1}, \dot{\lambda}) \tag{3.12}$$

where $m(\{\sigma\}_{n+1}, W_{n+1}) = \{m\}_{n+1} = \partial Q/\partial\{\sigma\}$ is the direction of the flow vector which is function of $\{\sigma\}_{n+1}$ and W_{n+1}. As both **Eqs. (4.2)** and **(4.3)** are having implicit forms in terms of $\{\sigma\}_{n+1}$ and W_{n+1}, the problem is solved by NR iterative technique but it needs one more extra equation due to occurrence of the incremental plastic multiplier $\dot{\lambda}$ as an additional unknown variables. The full consistency condition of the yield function **Eq. (3.4)** i.e. $F(\{\sigma\}_{n+1}, W_{n+1}) = 0$ is for that purpose. In order to solve these equations iteratively in a combined or monolithic form, they are rearranged to express their residuals $\{r\}_{n+1} = \{r\} = [\{r_\sigma\}^T \quad r_W \quad r_F]^T$ (the subscript for the current load step n+1 is omitted for simplification of the presentation) as follows:

$$\begin{cases} \{r_\sigma\} = \{\sigma\}_{n+1} - \{\sigma^{trial}\}_{n+1} + \dot{\lambda}\,[K]\{m\}_{n+1} \\ r_W = W_{n+1} - W_n - dW_{n+1} \\ r_F = F(\{\sigma\}_{n+1}, W_{n+1}) \end{cases} \tag{3.13}$$

For solution of the set of above equations, $\{\sigma\} = \{\sigma\}_{n+1}$, $W = W_{n+1}$ and $\dot{\lambda}$ are taken as the independent unknowns which are expressed in a compact form as $\{\psi\} = [\{\sigma\}^T \quad W \quad \dot{\lambda}]^T$ for the convenience. Now the residual is linearized using Taylors series for the NR iterative solution as follows:

$$\mathrm{r}(\{\psi\}^{j+1}) = \mathrm{r}(\{\psi\}^j + \{\delta\psi\}^{j+1}) = \mathrm{r}(\{\psi\}^j) + \frac{\partial \mathrm{r}(\{\psi\}^j)}{\partial\{\psi\}^j}\{\delta\psi\}^{j+1} + \mathrm{O}[\delta^2] \tag{3.14}$$

where *j* is the iteration number. The gradient expression $\frac{\partial \mathrm{r}(\{\psi\})}{\partial\{\psi\}} = \frac{\partial \mathrm{r}(\{\sigma\},\mathrm{W},\dot{\lambda})}{\partial(\{\sigma\},\mathrm{W},\dot{\lambda})}$ is the Jacobian matrix $[\mathrm{J}] = [\mathrm{J}](\{\psi\}^j)$ which can be expressed as:

$$[\mathrm{J}](\{\psi\}^j) = \frac{\partial \mathrm{r}(\{\psi\}^j)}{\partial\{\psi\}^j} = \frac{\partial \mathrm{r}(\{\sigma\},\mathrm{W},\dot{\lambda})}{\partial(\{\sigma\},\mathrm{W},\dot{\lambda})} = \begin{bmatrix} [\mathrm{I}] + \dot{\lambda}\,[\mathrm{K}]\,\dfrac{\partial\{\mathrm{m}\}}{\partial\{\sigma\}} & \dot{\lambda}\,[\mathrm{K}]\,\dfrac{\partial\{\mathrm{m}\}}{\partial\{\kappa\}} & [\mathrm{K}]\{\mathrm{m}\} \\ -\dfrac{\partial \mathrm{dW}}{\partial\{\sigma\}} & 1 - \dfrac{\partial \mathrm{dW}}{\partial \mathrm{W}} & -\dfrac{\partial \mathrm{dW}}{\partial\dot{\lambda}} \\ \left\{\dfrac{\partial \mathrm{F}}{\partial\{\sigma\}}\right\}^{\mathrm{T}} & \left\{\dfrac{\partial \mathrm{F}}{\partial \mathrm{W}}\right\}^{\mathrm{T}} & 0 \end{bmatrix} \tag{3.15}$$

Assuming a correct solution of **Eq. (3.14)** at iteration number j+1 i.e. $\mathrm{r}(\{\psi\}^{j+1}) = 0$ and truncation of the equation after its first order terms i.e. $\mathrm{O}[\delta^2] \cong 0$, **Eq. (3.14)** can be rewritten as:

$$[0] = \mathrm{r}(\{\psi\}^j) + \frac{\partial \mathrm{r}(\{\psi\}^j)}{\partial\{\psi\}^j}\{\delta\psi\}^{j+1} = \mathrm{r}\begin{pmatrix} \{\sigma\}^{\mathrm{j}} \\ \mathrm{W}^{\mathrm{j}} \\ \mathrm{d}\lambda^{\mathrm{j}} \end{pmatrix} + [\mathrm{J}](\{\psi\}^j)\begin{Bmatrix} \{\delta\sigma\}^{\mathrm{j+1}} \\ \delta\mathrm{W}^{\mathrm{j+1}} \\ \delta\dot{\lambda}^{j+1} \end{Bmatrix} \tag{3.16}$$

With this equation, the unknown variables can be updated iteratively as:

$$\{\psi\}^{j+1} = \{\psi\}^j + \{\delta\psi\}^{j+1} \tag{3.17}$$

$$\{\delta\psi\}^{j+1} = \begin{Bmatrix} \{\delta\sigma\}^{\mathrm{j+1}} \\ \delta\mathrm{W}^{\mathrm{j+1}} \\ \delta\lambda^{\mathrm{j+1}} \end{Bmatrix} = -[\mathrm{J}]^{-1}(\{\psi\}^j)\ \mathrm{r}\begin{pmatrix} \{\sigma\}^{\mathrm{j}} \\ \mathrm{W}^{\mathrm{j}} \\ \mathrm{d}\lambda^{\mathrm{j}} \end{pmatrix} \tag{3.18}$$

The iteration will continue till the norm of the residual meets the convergence tolerance i.e. $\|\mathrm{r}(\{\psi\}^{j+1})\| < TOL$ (a small number that is taken as 10^{-6} in this study). Once the convergence is obtained, the latest updated values of these variables $\{\psi\}^{j+1}$ will be their final results for the load step n+1 i.e. $\{\psi\}^{j+1} = \{\psi\}_{n+1}$, which can be used as their initial values for the next load step (n+2). The initial values of these variables for the load step n+1 are taken as: $\{\sigma\}^{j=0} = \{\sigma^{\mathrm{trial}}\}_{n+1}$, $W^{j=0} = W_n$, and $\dot{\lambda}^{j=0} = 0$.

3.4.2 Consistent tangent stiffness

For the FE solution at the global (structural) level, the formulation of elements needs a consistent tangent stiffness matrix at Gauss points if full Newton iteration technique is used for the global level solution to minimise the unbalanced load vector of the whole structure. For this purpose, derivative of **Eq. (3.13)** with respect to displacement increment {du} and a rearrangement of the equation can be made as follows:

$$\frac{\partial}{\partial\{du\}}\begin{bmatrix}\{\sigma\}_{n+1} + \dot{\lambda}\,[K]\{m\}_{n+1} \\ W_{n+1} - dW_{n+1} \\ F(\{\sigma\}_{n+1}, W_{n+1})\end{bmatrix} = \frac{\partial}{\partial\{du\}}\begin{bmatrix}\{\sigma\}_n + [K]\{du\}_{n+1} \\ W_n \\ 0\end{bmatrix} \tag{3.19}$$

By using chain rule for the left hand side of **Eq (3.19)** consisting of unknown variables at the current load step (n+1) along with initial knowns values of these variables ($\{\sigma\}_n$, W_n) from previous load step on the right hand side of the equation, it can be expressed in terms of Jacobian (see **Eq. 3.15**) as:

$$[J\,](\{\psi\}_{n+1})\begin{bmatrix}\left[\frac{\partial\{\sigma\}_{n+1}}{\partial\{du\}}\right] \\ \left[\frac{\partial W_{n+1}}{\partial\{du\}}\right] \\ \left[\frac{\partial d\lambda_{n+1}}{\partial\{du\}}\right]\end{bmatrix} = \begin{bmatrix}[K] \\ 0 \\ 0\end{bmatrix} \tag{3.20}$$

The above equation is rewritten by inverting the Jacobian as:

$$\begin{bmatrix} \left[\frac{\partial\{\sigma\}_{n+1}}{\partial\{du\}}\right] \\ \left[\frac{\partial W_{n+1}}{\partial\{du\}}\right] \\ \left[\frac{\partial d\lambda_{n+1}}{\partial\{du\}}\right] \end{bmatrix} = [J]^{-1}(\{\psi\}_{n+1}) \begin{bmatrix} [K] \\ 0 \\ 0 \end{bmatrix} \tag{3.21}$$

where the portion of the right hand side of **Eq. (3.21)** correspond to $\left[\frac{\partial\{\sigma\}_{n+1}}{\partial\{du\}}\right]$ is the consistent tangent stiffness matrix.

3.4.3 Adaptive sub-stepping scheme

The iterative solution of nonlinear equations using NR technique often encounters convergence problem in both local and global level if the load or displacement increment are not small. The global level problem can usually be controlled automatically by adjusting the size of global load increment in commercial FE codes (such as ABAQUS) with in-built options, but the local level problem need be addressed specifically by using our own material model UMAT. For this purpose, the sub-stepping scheme is adopted in the present study (Perez-Foguet et al. 2001) which divides a larger displacement increment in small sub-increments as $\{du\} = \sum_{i=1}^{ns}\{du\}_i = \sum_{i=1}^{ns}\alpha_i\{du\}$ where *ns* is the number of sub-steps and α_i is the scaling parameter of *i*th sub-step.

Fig. 3-6 illustrates the general concept used in the sub-stepping strategy where a typical displacement increment is divided into six small sub-increments. The initial value of the stress for the 1st sub-step is defined as $\{\sigma\}_{i=0}$ which is equal to the known converged stress values obtained at the end of previous load step $\{\sigma\}_n$. In this case, the trial stress for the first sub-step $\{\sigma^{trial}\}_{i=1} = \{\sigma\}_{i=0} + [K]\{du\}_1$ is the final stress at the end of this sub-step i.e. $\{\sigma^{trial}\}_{i=1} = \{\sigma\}_{i=1}$ as it is located within the yield surface $F(\{\sigma\}_n,\ \chi_n, C_n, tan\phi_n)$. This is similarly applicable for next two sub-steps (i = 2 and 3) to get $\{\sigma\}_{i=2}$ and $\{\sigma\}_{i=3}$. However, the trial stress for the 4th sub-step $\{\sigma^{trial}\}_{i=4}$ is outside the yield surface, which will require NR iteration to return back to the correct yield surface $F(\{\sigma\}_{i=4},\ \chi_{i=4}, C_{i=4}, tan\phi_{i=4})$ from $\{\sigma^{trial}\}_{i=4}$ using the procedure stated in **Section 3.4.1** for this sub-step. It should be noted that the value of plastic work $W_{i=4}$ will be updated in this sub-step along with the stress $\{\sigma\}_{i=4}$ while $W_{i=1} = W_{i=2} = W_{i=3} = W_{i=0} = W_n$. This process will be repeated up to last sub-step ($i = 6$ in this case) to get $\{\sigma\}_{i=6}$ and $W_{i=6}$, which are the final values of stress and plastic work at the end of this load increment (n+1) i.e. $\{\sigma\}_{n+1} = \{\sigma\}_{i=6}$ and $W_{n+1} = W_{i=6}$. The hardening parameters can be determined using the value of W_{n+1} which will help to get the new yield surface $F(\{\sigma\}_{n+1},\ \chi_{n+1}, C_{n+1}, tan\phi_{n+1})$.

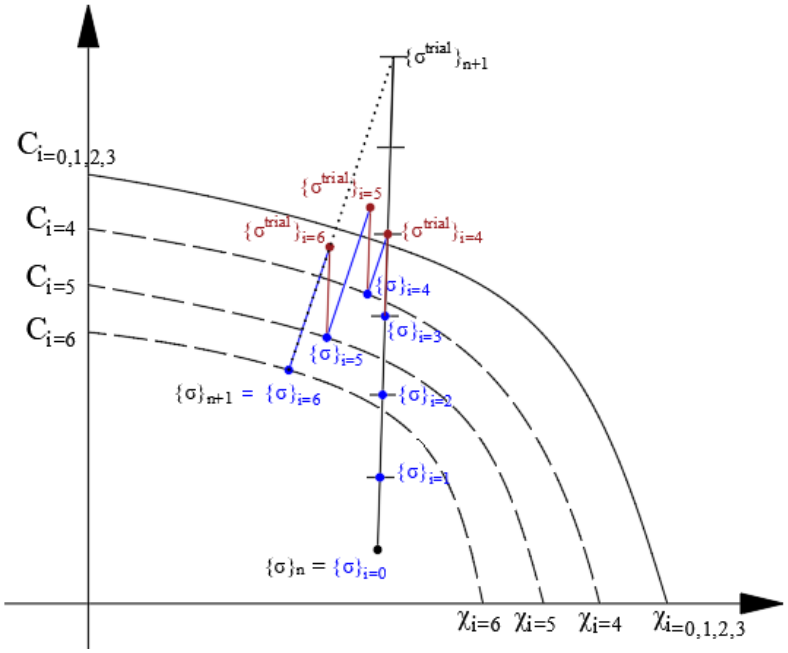

Fig. 3-6 Sub-stepping iteration scheme for stress return mapping

The procedure for getting the consistent tangent stiffness in this scheme is more complex than that illustrated in **Eq. (3.19)** as it should be updated in every sub-step. For a sub-step (say *i*th sub-step), **Eq. (3.19)** can be expressed as:

$$\frac{\partial}{\partial\{du\}}\begin{bmatrix}\{\sigma\}_{i+1} + d\lambda\,[K]\{m\}_{i+1} \\ W_{i+1} - dW_{i+1} \\ F(\{\sigma\}_{i+1}, W_{i+1})\end{bmatrix} = \frac{\partial}{\partial\{du\}}\begin{bmatrix}\{\sigma\}_i + [K]\{du\}_{i+1} \\ W_i \\ 0\end{bmatrix} \tag{3.22}$$

Using $\{\mathrm{du}\}_i = \alpha_i\{\mathrm{du}\}$, the procedure used for deriving the left hand side of **Eq. (3.20)** is applied to both sides of **Eq. (3.20)** to expressed the equation in the following form.

$$[J\,](\{\psi\}_{i+1})\begin{bmatrix}\left[\frac{\partial\{\sigma\}_{i+1}}{\partial\{du\}}\right] \\ \left[\frac{\partial W_{i+1}}{\partial\{du\}}\right] \\ \left[\frac{\partial d\lambda_{i+1}}{\partial\{du\}}\right]\end{bmatrix} = \begin{bmatrix}\frac{\partial\{\sigma\}_i}{\partial\{du\}} + \alpha_{i+1}[K] \\ \frac{\partial W_i}{\partial\{du\}} \\ 0\end{bmatrix} \tag{3.23}$$

The above equation can be rearranged in a similar manner as of **Eq. (3.21)** as follows to get the consistent tangent stiffness matrix.

$$\begin{bmatrix} \left[\frac{\partial\{\sigma\}_{i+1}}{\partial\{du\}}\right] \\ \left[\frac{\partial W_{i+1}}{\partial\{du\}}\right] \\ \left[\frac{\partial d\lambda_{i+1}}{\partial\{du\}}\right] \end{bmatrix} = [J]^{-1}(\{\psi\}_{i+1}) \begin{bmatrix} \frac{\partial\{\sigma\}_i}{\partial\{du\}} + \alpha[K] \\ \frac{\partial W_i}{\partial\{du\}} \\ 0 \end{bmatrix} \tag{3.24}$$

3.5 Numerical examples

In this section, the response of two unreinforced masonry walls under in-plane loads has been simulated using a well-regarded FE code ABAQUS. For an accurate prediction of the response of the masonry walls, a new interface model developed in this study is implemented with ABAQUS using a user defined material model (UMAT) in the form a subroutine developed in FORTRAN. Both walls have the same geometry but different pre-pressures (*p*) as shown in **Fig. 3-7**. The dimension of the shear wall is 1000mm (height) × 990mm (width) × 100 mm (thick) made of 18 courses (layers) of solid clay bricks each having a size of 210mm (length) × 52mm (height) ×100mm (thick). The top course of bricks is connected to a steel beam which provide lateral shear displacement while another steel beam is connected to the bottom course of bricks to provide a fixed boundary condition (Raijmakers, 1992).

Table 3-1 Material properties of bricks

Elastic modulus (MPa)		Poisson's ratio		Density (Ns^2/mm^4)	
16700		0.18		19×10^{-9}	
Tensile nonlinear uniaxial behaviour		Compressive nonlinear uniaxial behaviour		Dilation angle	10
Stress (MPa)	Inelastic strain	Stress (MPa)	Inelastic strain	Eccentricity	0.1
3.5	0	11	0	f_{b0}/f_{c0}	1.12
0.3	0.002	11.5	0.001	K	0.667
		0.6	0.007	Viscosity parameter	0.0002

In this section, the response of two unreinforced masonry walls under in-plane loads has been simulated using a well-regarded FE code ABAQUS. For an accurate prediction of the response of the masonry walls, a new interface model developed in this study is implemented with ABAQUS using a user defined material model (UMAT) in the form a subroutine developed in FORTRAN. Both walls have the same geometry but different pre-pressures (*p*) as shown in **Fig. 3-7**. The dimension of the shear wall is 1000mm (height) × 990mm (width) × 100 mm (thick) made of 18 courses (layers) of solid clay bricks each having a size of 210mm (length) × 52mm (height) ×100mm (thick). The top course of bricks is connected to a steel beam which provide lateral shear displacement while another steel beam is connected to the bottom course of bricks to provide a fixed boundary condition (Raijmakers, 1992).

The simplified micro-modelling strategy (Lourenco and Rots, 1996) that lumps mortar joints as zero thickness interfaces is adopted in the present study for improving the computational efficiency and obtaining a reasonable cracking pattern. The bricks are modelled using plane stress rectangular elements (CPS4R) while cohesive elements (COH2D4) are used for mortar

joints. As the vertical mid-plane of brick units is one of the potential failure plane, cohesive elements (COH2D4) are also used for that by treating this plane as an artificial (fake) joint for all brick units. The damage-plasticity model (CDP) is used for simulating the material behaviour of bricks which can also simulate cracking and crushing of bricks indirectly. The parameters used in the nonlinear modelling of bricks and interfaces are listed in the **Table 3-1** and **Table 3-2**. Geometry of the specimens are shown in **Fig. 3-7**.

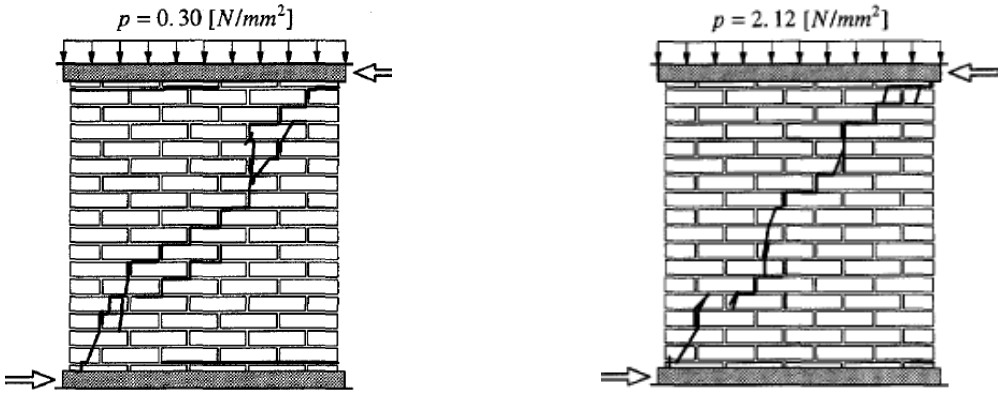

(a) shear wall under 0.3MPa pressure (b) shear wall under 2.12MPa pressure

Fig. 3-7 Loading conditions and failure modes of experimental walls (Raijmakers, 1992)

Table 3-2. Interface properties

Mortar interface (0.3MPa ; 2.12MPa)			
Normal stiffness Kn (N/mm^3)	Shear stiffness Ks (N/mm^3)	Tensile strength χ (N/mm^2)	Shear strength C (N/mm^2)
82; 82	36; 36	0.25; 0.16	0.375; 0.224
Tensile fracture energy G_f^i (N/mm^2)	Shear fracture energy G_f^{ii} (N/mm^2)	Friction coefficient $\tan\phi$	Dilation coefficient $\tan\phi_Q$
0.018; 0.018	0.125; 0.05	0.75	0.001
Fake joint for brick (0.3MPa and 2.12MPa)			
Normal stiffness Kn (N/mm^3)	Shear stiffness Ks (N/mm^3)	Tensile strength χ (N/mm^2)	Shear strength C (N/mm^2)
500	500	2	2.8
Tensile fracture energy G_f^i (N/mm^2)	Shear fracture energy G_f^{ii} (N/mm^2)	Friction coefficient $\tan\phi$	Dilation coefficient $\tan\phi_Q$
0.08	0.5	1	1

Load-displacement relations shown in **Fig. 3-8** compares the numerical results and experimental results. The wall under 0.3MPa pre-pressure has in-plane loading capacity around 50kN and it shows a long plateau in the nonlinear response, while the wall under 2.12MPa pre-pressure has approximated 100kN peak load capacity followed by a softening response until the load capacity reduces to 60kN. Besides the experimental data, the ABAQUS built-in damage model (Camanho, P.P. and Dávila, C.G., 2002) is utilized by the authors (2019) and its modelling results of in-plane walls are also presented in the **Fig. 3-8**.

Experimental results indicate that the pre-pressure can influence the cracking patterns in corners of the walls. In **Fig. 3-7a**, the wall under 0.3MPa pressure has two significant horizontal cracks in the top left corner and bottom right corner, while in **Fig. 3-7b** there is no similar cracks occur in the corner. The reason resulting in different cracking patterns is that higher pressure (2.12MPa) provides more compression on the horizontal bed interfaces thus the opening cracks in wall left top and right bottom corners would be restrained. The difference of carking growth is captured by FE models clearly from **Fig. 3-9a** to **9c**.

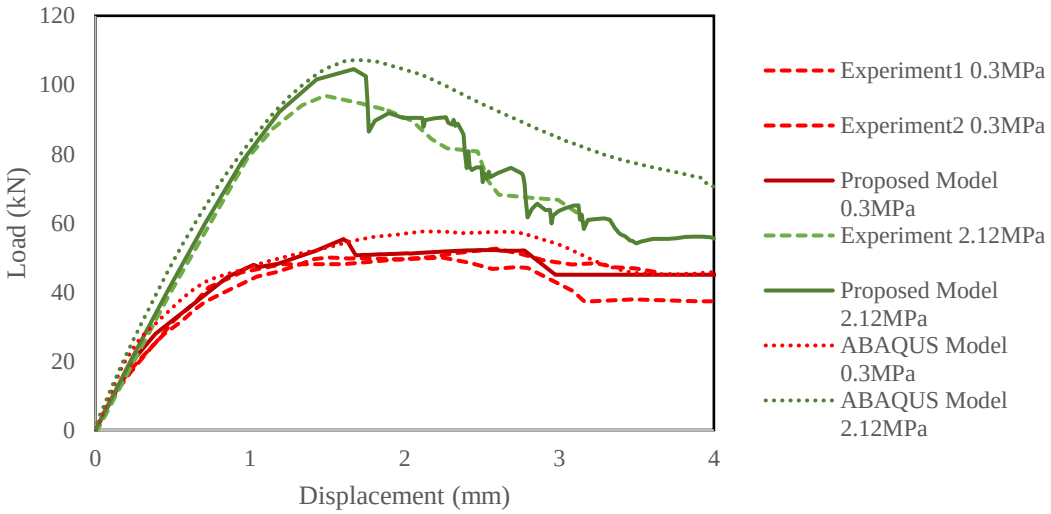

Fig. 3-8 Load-displacement relations

The initial cracks (in **Fig. 3-9a**) for 0.3MPa wall are firstly found in top and bottom corners as horizontal opening, while that for 2.12MPa wall are found in the wall central area as vertical opening. After that, cracks continue developing (in **Fig. 3-9b**) in the 0.3MPa Wall and 2.12MPa wall. For the former, corner cracks keep growing and meanwhile cracks in the wall centre begin to form, while for the latter the initial central cracks gradually extend to the corner along the dialog path and some vertical opening become more obvious. **Fig. 3-9c** shows the final failure modes of both walls, the 0.3MPa wall has a continued jogged pattern dialog cracks and two horizontal cracks in the top and bottom corners, while the 2.12MPa wall presents a dialog cracking pattern with several vertical cracks. The applied horizontal displacements corresponding to different cracking stages are also commented in the **Fig. 3-9a** to **3.9c**. Some bricks in the central region have rotations happen with the development of cracks, which is due to the dilation behaviour of the wall.

Fig. 3-9d use ABAQUS built in concrete damage plasticity (CDP) model to detect the compressive failure of bricks during the in-plane loading process, and the crushing failures are determined by the material yield contour in the wall toes.

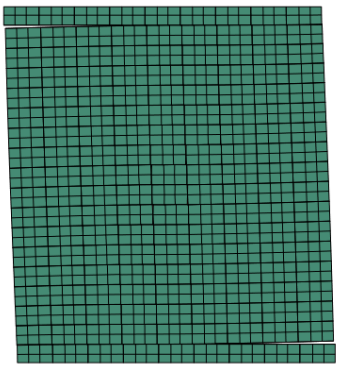

Wall under 0.3MPa pressure

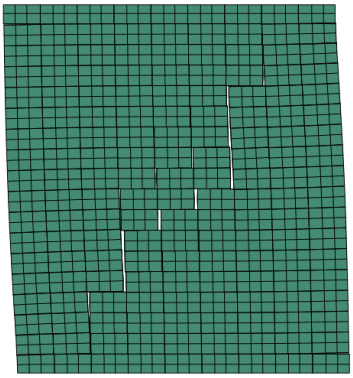

Wall under 2.12MPa pressure

(a) Deformation & failure patterns (initial cracking, around 1.5mm)

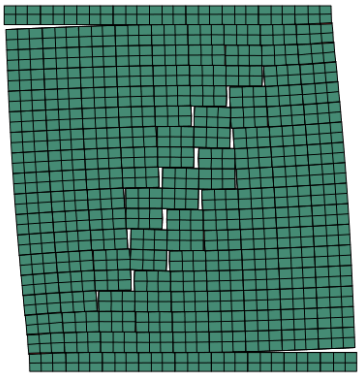

Wall under 0.3MPa pressure

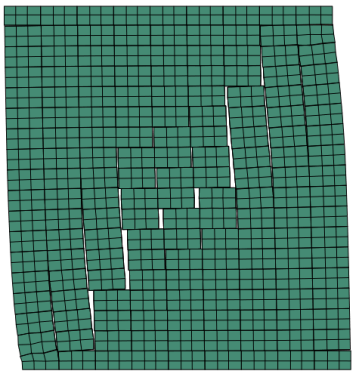

Wall under 2.12MPa pressure

(b) Deformation & failure patterns (cracking growth, around 2mm)

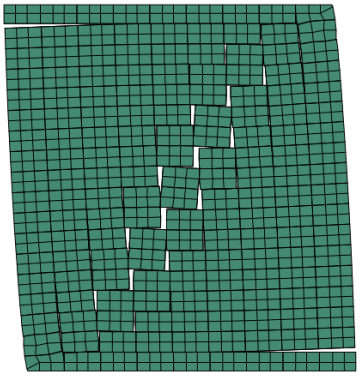

Wall under 0.3MPa pressure

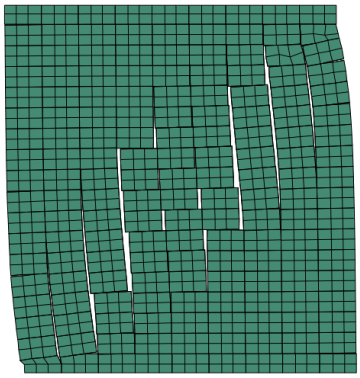

Wall under 2.12MPa pressure

(c) Deformation & failure patterns (fully cracking, around 3.5mm)

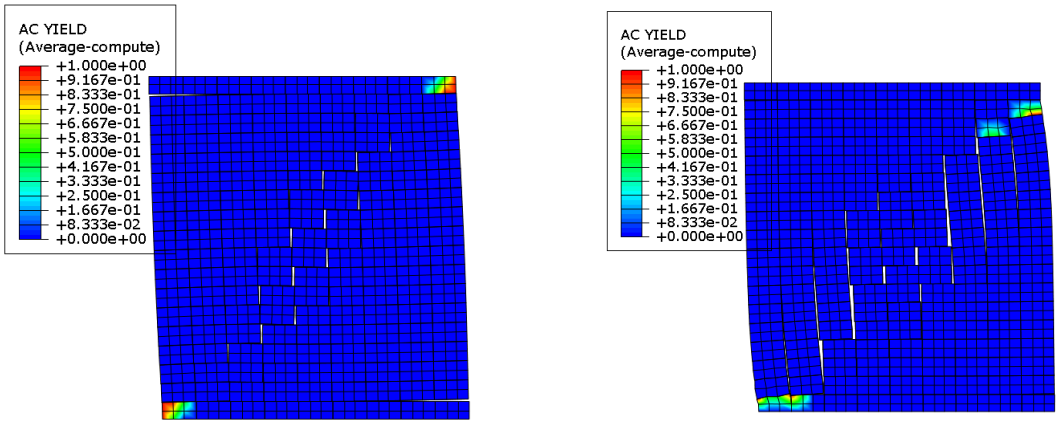

Wall under 0.3MPa pressure Wall under 2.12MPa pressure

(d) Brick crushing (yield area contour)

Fig. 3-9 Masonry wall cracking and crushing failure modes

3.7 Conclusion

This paper proposes an interface model which is applied in predicting the nonlinear response and cracking patterns of unreinforced masonry walls under in-plane loads. Simplified micro-modelling strategy with extended brick and zero-thickness mortar is adopted for running finite element models considering is computational efficiency and proper failure modes visualization. An interface model is proposed in 2D/3D stress space based on the plasticity theory, and an adaptive sub-stepping approach is adopted for improving the convergence performance of FE model in local level. The backward Euler integration method with consistent tangent operator ensures the accuracy of modelling results. Softening evolution laws define the softening process of strength variables with the energy dissipation in interface area. Comparison between experimental and numerical results demonstrated that the proposed interface model performs well in simulating the nonlinear behaviour and cracking failure of masonry walls under in-plane loading conditions. Load-displacement relations have a satisfied agreement in both experimental and numerical results. Diagonal cracking are cleared captured by FE models and the influence of pre-pressure on the failure modes are well reflected in the modelling progress.

3.7 Reference

Abbo, A.J., (1997). Finite element algorithms for elastoplasticity and consolidation (Doctoral dissertation, University of Newcastle).

Caballero, A., Willam, K.J. and Carol, I., (2008). Consistent tangent formulation for 3D interface modeling of cracking/fracture in quasi-brittle materials. Computer Methods in Applied Mechanics and Engineering, Vol 197(33-40), pp.2804-2822

Camanho, P.P. and Dávila, C.G., (2002). Mixed-mode decohesion finite elements for the simulation of delamination in composite materials. NASA report.

D'Altri, A.M., Sarhosis, V., Milani, G., Rots, J., Cattari, S., Lagomarsino, S., Sacco, E., Tralli, A., Castellazzi, G. and de Miranda, S., (2019). Modeling strategies for the computational

analysis of unreinforced masonry structures: review and classification. Archives of Computational Methods in Engineering, pp.1-33.

De Borst, R., Crisfield, M.A., Remmers, J.J. and Verhoosel, C.V., (2012). Nonlinear finite element analysis of solids and structures. John Wiley & Sons.

Giambanco, G., Rizzo, S. and Spallino, R., (2001). Numerical analysis of masonry structures via interface models. Computer methods in applied mechanics and engineering, Vol 190(49-50), pp.6493-6511.

Griffith, M.C., Vaculik, J., Lam, N.T.K., Wilson, J. and Lumantarna, E., (2007). Cyclic testing of unreinforced masonry walls in two-way bending. Earthquake Engineering & Structural Dynamics, Vol 36(6), pp.801-821.

Le, L.A., Nguyen, G.D., Bui, H.H., Sheikh, A.H. and Kotousov, A., (2019). Incorporation of micro-cracking and fibre bridging mechanisms in constitutive modelling of fibre reinforced concrete. Journal of the Mechanics and Physics of Solids, Vol 133, p.103732.

Le, L.A., Nguyen, G.D., Bui, H.H., Sheikh, A.H., Kotousov, A. and Khanna, A., (2017). Modelling jointed rock mass as a continuum with an embedded cohesive-frictional model. Engineering Geology, Vol 228, pp.107-120.

Nie, Y, Sheikh, A., Griffith, M., Visintin, P. and Vaculik, J. (2019). The application of mixed-mode de-cohesion criteria in masonry finite element analysis, Australian Earthquake Engineering Society 2019 Conference, Nov 29- Dec 1, Newcastle City Hall, New South Wales

Pérez-Foguet, A., Rodríguez-Ferran, A. and Huerta, A., (2001). Consistent tangent matrices for substepping schemes. Computer methods in applied mechanics and engineering, Vol 190(35-36), pp.4627-4647.

Raijmakers, T.M.J. and Vermeltfoort, A.T., (1992). Deformation controlled tests in masonry shear walls. holandés), Report B-92-1156, TNO-Bouw, Delft, Países Bajos.

Smoljanović, H., Nikolić, Ž. and Živaljić, N., (2015). A combined finite–discrete numerical model for analysis of masonry structures. Engineering fracture mechanics, Vol 136, pp.1-14.

Su, Y., Wu, C. and Griffth, M.C., (2011). Modelling of the bond–slip behavior in FRP reinforced masonry. Construction and Building Materials, Vol 25(1), pp.328-334.

Vaculik, J. and Griffith, M.C., (2017). Probabilistic analysis of unreinforced brick masonry walls subjected to horizontal bending. Journal of Engineering Mechanics, Vol 143(8), p.04017056.

Vaculik, J., Visintin, P., Burton, N.G., Griffith, M.C. and Seracino, R., (2018). State-of-the-art review and future research directions for FRP-to-masonry bond research: Test methods and techniques for extraction of bond-slip behaviour. Construction and Building Materials, Vol 183, pp.325-345.

Chapter 4: A coupled damage-plasticity based model

Nie, Y., Sheikh, A., Griffith, M., & Visintin, P. (2022). A damage-plasticity based interface model for simulating in-plane/out-of-plane response of masonry structural panels. Computers & Structures, 260, 106721.

Statement of Authorship

Title of Paper	A damage-plasticity based interface model for simulating in-plane /out-of-plane response of masonry structural panels
Publication Status	☑ Published ☐ Accepted for Publication ☐ Submitted for Publication ☐ Unpublished and Unsubmitted w ork w ritten in manuscript style
Publication Details	Nie Y, Sheikh A, Griffith M, Visintin P. A damage-plasticity based interface model for simulating in-plane/out-of-plane response of masonry structural panels. Computers & Structures. 2022 Feb 1;260:106721.

Principal Author

Name of Principal Author (Candidate)	Yu Nie
Contribution to the Paper	Proposed the constitutive model and implement it by numerical method. Validate the proposed model by comparing numerical models with experimental results. Write and modify the manuscript.
Overall percentage (%)	70%
Certification:	This paper reports on original research I conducted during the period of my Higher Degree by Research candidature and is not subject to any obligations or contractual agreements with a third party that would constrain its inclusion in this thesis. I am the primary author of this paper.
Signature	Date: 10 May 2022

Co-Author Contributions

By signing the Statement of Authorship, each author certifies that:

i. the candidate's stated contribution to the publication is accurate (as detailed above);
ii. permission is granted for the candidate in include the publication in the thesis; and
iii. the sum of all co-author contributions is equal to 100% less the candidate's stated contribution.

Name of Co-Author	Abdul Sheikh
Contribution to the Paper	Proposed the general concept and gave guidance of the methodology Supervised the technical development. Evaluate and revised the manuscript.
Signature	Date: 10 May 2022

Name of Co-Author	Michael Griffith
Contribution to the Paper	Supervised the technical development. Evaluate and revised the manuscript.
Signature	Date: 10 May 2022

Name of Co-Author	Phillip Visintin
Contribution to the Paper	Supervised the technical development. Evaluate and revised the manuscript.
Signature	Date: 10 May 2022

Please cut and paste additional co-author panels here as required.

Chapter 4: A coupled damage-plasticity based model

Abstract

A coupled damage-plastic based constitutive model using a traction-separation law is developed in this study to simulate the behaviour of mortar joints in masonry structural panels subjected to in-plane (2D) and out-of-plane (3D) loading. A smooth hyperbolic failure surface is used to develop the interface material model, which is implemented numerically using a fully implicit backward Euler integration technique is unconditionally stable. To further improve the accuracy and robustness of the interface model, an adaptive sub-stepping scheme and associated consistent tangent operator are formulated considering the effects of damage and plastic deformations. This is beneficial for simulating full-scale masonry structures because the size of load step for some locations with higher deformations can be significantly larger than other locations. The model is first validated using a single cohesive element within a finite-element modelling platform, to assess its behaviour under all possible deformation modes: tensile, compressive with shear and tensile-shear mix-mode behaviour. The cyclic response of a masonry couplet is then simulated to assess model performance in the unloading scenario. Finally, the model is applied to masonry structural walls for simulating their failure response under in-plane and out-of-plane loads, and a good correlation with the experimental results is observed.

4.1 Introduction

Unreinforced masonry structures have been widely used in historic buildings, architecturally driven modern buildings of significant size and in residential construction. In general, masonry structures have good load bearing capacity under gravity actions, which result in compression, but they are vulnerable to lateral loads such as earthquake actions, which result in bending. In order to design retrofits for the key components of the structure to prevent its premature failure, it is necessary to be able to predict the response of the structure (Vaculik et al. 2018).

Analysis of masonry structures is often based on analytical approaches (Griffith et al. 2007; Vaculik and Griffith. 2017) utilising simplifying assumptions, to provide predictions of load carrying capacity with a reasonable level of accuracy. The use of a concise analytical form is convenient, but in general, these simplified approaches cannot provide a complete understanding of failure including post-peak behaviour, and the locations and nature of failure modes, particularly for structures with arbitrary geometries and loading.

Comprehensive numerical modelling strategies can provide detailed prediction of failure, including information of the cracking pattern in mortar joints and bricks and locations of brick unit crushing (Milani and Lourenco. 2012). Clear identification of failure modes and their locations are helpful in reducing retrofit cost and improving repairing efficiency (Su et al. 2011).

The development of numerical modelling techniques with different degrees of sophistications for a credible simulation of the behaviour of masonry structures has therefore drawn a considerable research interest. The major focus of these studies is on the development of material models and implementation within a reliable Finite Element (FE) code such as Abaqus (Systèmes, 2014) or an in-house FE code. In this context, the simplified micro model introduced by Lourenco and Rots (1997) for simulating masonry structures has become popular. This approach requires a continuum based material model for bricks and an interface model based on a traction-separation law to characterise tensile (Mode I) and shear (Mode II) failures

(Camanho and Dávila. 2002) of mortar joints. In many studies, the brick blocks are treated as elastic bodies to minimise computational demand, while due to the inherent weakness of the mortar joints, an inelastic material model based on different modelling frameworks (Citto 2008; Kumar et al. 2014; Kumar and Barbato. 2019; Giambanco et al. 2001; Macorini and Izzuddin; 2011; Milani 2011; Nazir and Dhanasekar. 2014) is used. The interface model used by a group of investigators (Alfano and Sacco 2006; Abdulla et al. 2017; D'Altri et al. 2018; D'Altri et al. 2019; Lotfi and Shing. 1994; Parrinello et al. 2009; Sacco and Lebon. 2012; Smoljanović et al. 2015) for mortar joints are pure damage mechanics based modelling framework. Such a model is also available in a Finite Element (FE) code such as Abaqus, but importantly, it does not have the ability to accommodate frictional resistance provided by mortar joints during sliding (Mode II) displacements. Abdulla et al. (2017) addressed this issue by simply adding the Abaqus frictional contact model to the Abaqus interface model for their simulation. This approach represents a simple solution, but the determination of the damage parameter and its correlation with other quantities in a mixed-mode fracture scenario is problematic. To address these limitations researchers (Alfano and Sacco 2006) have developed new interface models combing damage and frictional components. However, these models do not consider the effect of some critical characteristics of mortar joint such as permanent plastic deformations and dilation (Andreotti et al. 2019).

This has inspired a group of researchers to develop plasticity-based models considering non-associated flow rules for correct representation of dilation and the Coulomb frictional criterion, which has been found to be a more suitable framework for modelling mortar joints because they are considered as interfaces in a simplified micro model based simulation of masonry. In this context, one of the initial attempts was made by Lotfi and Shing (1994) who proposed a single yield surface in the form of a smooth hyperbolic curve to combine tension and shear for mixed mode failure of masonry joints. In contrast, Lourenco and Rots (1997) proposed a multi-surface interface model, which consists of a More-Coulomb type friction surface with tension cut-off and a compression cap for simulating crushing failure. This is a popular model developed by Lourenco and Rots (1997), which has been used by many other researchers, e.g. Chaimoon and Attard (2007) who simplified the elliptic shape of the compressive cap into a diagonal flat surface for the convenience of numerical implementation. While a multi-surface yield surface can give a better physical representation, its computation implementation is challenging because the stress return algorithm may encounter convergence issue near the corners (intersection of two surfaces) due to singularity. It is to be noted that Simo and Hughes (2006) proposed an effective approach for multi-surface failure models with corners to address the convergence issue. They adopted two different implementation strategies for considering the right number and combination of active surfaces, which have been defined as: a) exact method and b) optimised method. Although these methods performed successfully in many situations, they faced convergence issue in some scenarios found in geo-mechanics problem (Adhikary et al. 2017), composite materials (Pech et al. 2021), and soil mechanics problem (Abreu et al. 2021). Thus the implementation technique of Simo et al. (2006) has been subsequently enhanced by some researchers such as Pech et al. (2021) who introduced a concept defied as brute force method for accommodating larger active surfaces to improve robustness. Similarly, Abreu et al. (2021) used line search and adaptive sup-stepping techniques while Adhikary et al. (2017) used line search and brutal force method for improving the robustness of their implementations.

In order to avoid these challenges in numeric implementation of the constitutive model, some researchers (Citto 2008) used a single smooth yield surface (without corners) for modelling all failure modes (tension, shear and compression) of masonry joints with the single yield function to have a relatively simple model. While advantageous in removing the corners from the yield surface, these models (Citto 2008) involve relatively complex formulations and the convergence performance is also not encouraging as reported by Kumar and Barbato (2019). A pure plasticity based model became popular but it does not consider damage to accommodate stiffness degradation due to micro cracking of mortar joints, which is crucial under cyclic loading having a loading-unloading-reloading scenarios.

An ideal interface model for masonry joint should therefore consider damage and plasticity, which has motivated some researches to develop such models, these are however limited in number and having some issues. The models proposed by Minga et al. (2018) and Spada et al. (2009) used multi-surfaces yield functions with flat surfaces that produced sharp corners with discontinuity. This is avoided in the work of Yuen et al. (2019) by taking a smooth hyperbolic yield surface, but the model is implemented by forward Euler integration technique which requires very small load steps leading to high computational costs in large scale structural simulation, and may lead to divergence as this integration technique is not unconditionally stable. Therefore, there is a need for the development of a credible interface model for masonry joints considering the effects of damage, plasticity and their coupling, which is attempted in this investigation.

The proposed interface model utilised the key concepts of the pioneering interface model developed by Carol's research group (Caballero et al. 2006; Caballero et al. 2008; Carol et al. 2001) who used a smooth hyperbolic yield surface for simulating concrete cracking. Carol's model has been used by many researches due to its good predicting capability with robust performance in numerical simulations. However, Carol's model is based on a pure plasticity framework with no stiffness degradation. To address this issue, the model proposed here incorporated damage and its coupling with plasticity. For the purpose, the treatment used for accommodating damage followed the approach adapted by Nguyen et al. (2017) and Le et al. (2017; 2018) for modelling rock fracturing. For numerical implementation of the proposed material model at an integration point, a fully implicit backward Euler integration technique is adopted as it is unconditionally stable. Despite this, the model may experience convergence difficulty for a complex mixed mode loading such as tension-shear loading scenario and the problem can magnify for a relatively large displacement increment. This issue is addressed by incorporating a robust adaptive sub-stepping strategy for the numerical integration of the proposed constitutive model following the concept introduced by Perez-Foguet et al. (2001). This sub-stepping strategy has been used by other researchers (Caballero et al. 2008) in implementing models but all these models are based on a plasticity framework and hence this is likely the first attempt to implement the sub-stepping scheme in a damage-plasticity based interface model for masonry joints. However, our formulation is restricted to single surface model to make it relatively simple.

4.2 Constitutive model of the interface

The constitutive model for the 3D interface proposed in this paper contains characteristics from both damage mechanisms and plastic deformations and their couplings. As the interface has

zero thickness, a traction-separation relationship is used, where the traction/stress vector consists of normal and shear components as $\{\sigma\} = \{\sigma_n,\ \sigma_s\}^{\mathrm{T}}$, while separation or relative displacement (not strain) is $\{u\} = \{u_n,\ u_s\}^{\mathrm{T}}$. For a 3D interface, the shear stress has two components but they are combined as $\sigma_s = \sqrt{(\sigma_{s1})^2 + (\sigma_{s2})^2}$ to have a single shear stress component. Similarly, two components of the shear displacement (relative) are combined as $u_s = \sqrt{(u_{s1})^2 + (u_{s2})^2}$.

Following the uniaxial behaviour, the relative displacement vector for a generic case (2D or 3D) {u} can be split in terms of elastic $\{u^e\}$ and in-elastic/plastic $\{u^p\}$ components:

$$\{u\} = \{u^e\} + \{u^p\}; \qquad \begin{Bmatrix} u_n \\ u_s \end{Bmatrix} = \begin{Bmatrix} u_n^e \\ u_s^e \end{Bmatrix} + \begin{Bmatrix} u_n^p \\ u_s^p \end{Bmatrix} \tag{4.1}$$

where u_n and u_s are normal and shear components of {u} respectively.

Based on the traction-separation law, the stresses at any point within a masonry joint can be written:

$$\sigma_n = (1 - D_n)\, K_n^0\, u_n^e - D_n\, K_n^0\, \langle -u_n^e \rangle \tag{4.2}$$

$$\sigma_s = (1 - D_s)\, K_s^0\, u_s^e + D_s\, tan\phi\, \langle -\sigma_n \rangle\, \mathrm{sign}(u_s^e) \tag{4.3}$$

where K_n^0 and K_s^0 are initial stiffness parameters for the interface, $tan\phi$ is the frictional coefficient, and D_n and D_s are the damage parameters under normal and shear mode, which will be defined in the next section. The Macaulay bracket for a parameter x $(\langle x \rangle = (|x| + x)/2)$ is used to distinguish the tensile or compressive nature of the normal stress/displacement (relative) while the Sign function *sign*(*x*) is used to make the shear behaviour symmetric in case of reversible loading.

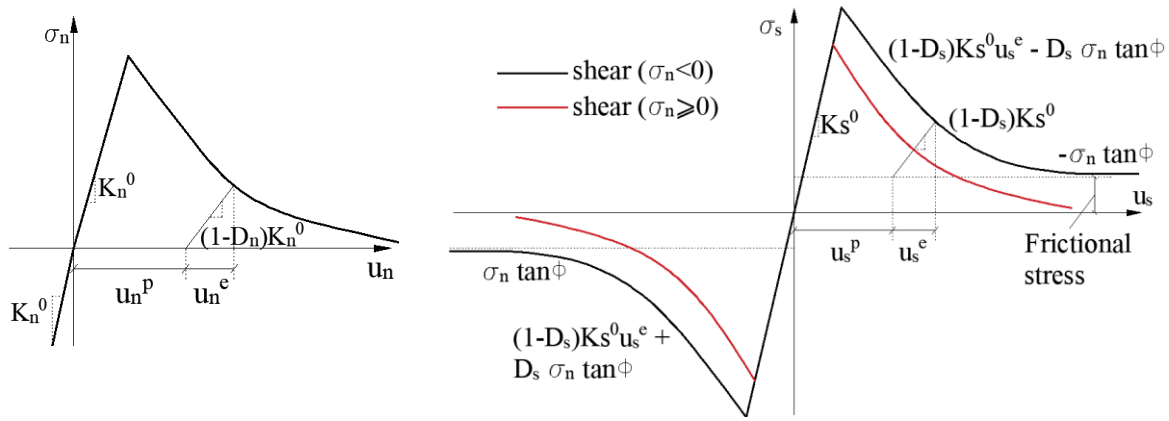

(a) under pure normal stress (b) under shear stress with normal stress

Fig. 4-1 Stress-relative displacement relationship of the interface

Fig. 4-1 shows the stress-relative displacement relationship of the interface, where **Fig. 4-1a** demonstrates **Eq. (4.2)** and **Fig. 4-1b** shows **Eq. (4.3).** The first part of **Eq. (4.3)** i.e. $(1 - D_s)\, K_s^0\, u_s^e$ contributes the cohesive component of the interfacial shear behaviour, while its second part $D_s\, tan\phi\, \langle -\sigma_n \rangle\, \text{sign}(u_s^e)$ represents the frictional component.

4.3. Internal variable - evolution of damage and hardening parameters

When an interface undergoes inelastic deformations, the energy dissipation due to irreversible relative displacements is used to define the evolution laws for the hardening (softening in the present case) and damage parameters used for defining the yield and potential surfaces presented in the next section. Compared with inelastic deformations which has to be defined according to normal and shear directions, energy dissipation is a more unified variable that includes both nonlinear normal and shear behaviours of materials. The dissipated energy $W^p = \int dW^p$ caused by the work done by the plastic displacements (relative) is taken as the internal variable where the integral form is used to accommodate the nonlinear variations of stress with plastic relative displacement as shown in the **Fig. 4-2**.

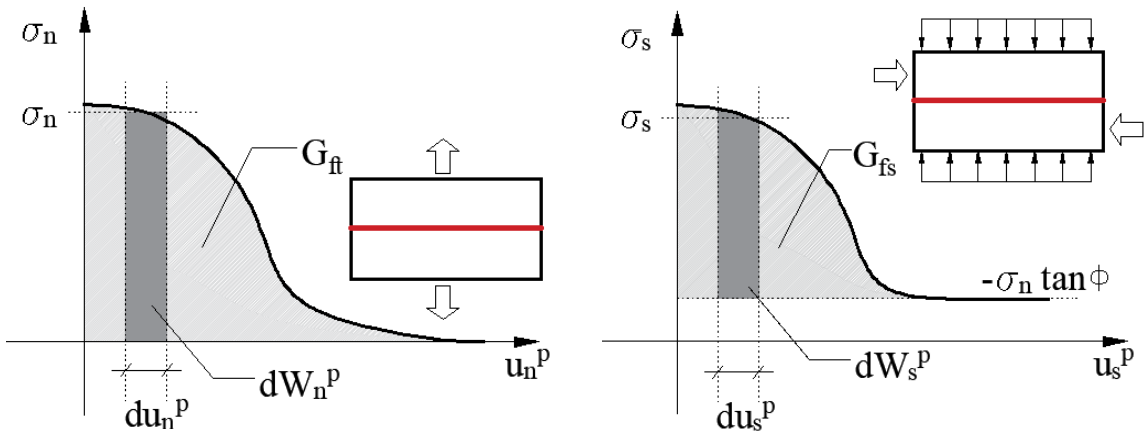

(a) tensile mode of deformation (b) shear mode of deformation

Fig. 4-2 Plastic work and fracture energies of the interface

With the progression of plastic deformations, the dissipation energy will be increased and its capacity will be exhausted when the plastic work will be reaching the value of fracture energy G_f (material property), which is equal to the area under the stress-plastic displacement (relative) curve (**Fig. 4-2**). The fracture energy for the tensile mode G_{ft} and shear mode G_{fs} along with the incremental plastic works are shown in **Fig. 4-2a** and **Fig. 4-2b** respectively. It should be noted that the energy dissipated by the frictional component of the shear stress will not be counted in estimating W^p as the measurement of the shear mode of fracture energy G_{fs} does not include frictional resistance (**Fig. 4-2b**). Based on these considerations, the incremental plastic work can be expressed as:

$$dW^p = \begin{cases} \sigma_n\, du_n^p + \sigma_s\, du_s^p, & \sigma_n \geq 0 \\ \left|du_s^p\right|(|\sigma_s| + \sigma_n tan\phi), & \sigma_n < 0 \end{cases} \tag{4.4}$$

The model has employed two damage parameters corresponding to normal and shear modes of deformations. These are defined in terms of plastic work and fracture energy as:

$$\mathrm{D}_n(W^p) = \begin{cases} \left(\frac{1}{2} - \frac{1}{2}\cos\left(\frac{\pi W^p}{G_{ft}}\right)\right) & W^p < G_{ft} \\ 1 & W^p \geq G_{ft} \end{cases} \tag{4.5}$$

$$\mathrm{D}_s(W^p) = \begin{cases} \left(\frac{1}{2} - \frac{1}{2}\cos\left(\frac{\pi W^p}{G_{fs}}\right)\right) & W^p < G_{fs} \\ 1 & W^p \geq G_{fs} \end{cases} \tag{4.6}$$

where, the above expressions in the form of *cosine* functions help to avoid any discontinuous slope at the ends of their evaluation range (i.e. D = 0, D = 1) and therefore minimize convergence issue as recommended by Caballero et al. (2008). The above equations introduce the coupling of damage and plasticity. The damage parameters are used to define the evolution of hardening parameters as follows:

$$\chi = (1 - D_n)\chi_0 \tag{4.7}$$

$$\mathrm{C} = (1 - D_s)\mathrm{C}_0 \tag{4.8}$$

$$\tan\phi = (1 - D_s)\tan\phi_0 + D_s \tan\phi_r \tag{4.9}$$

where, χ_0, C_0 and $\tan\phi_0$ are initial undamaged values of tensile strength, shear strength, and frictional coefficient respectively, while $\tan\phi_r$ is the residual frictional coefficient. This approach is similar to that is typically followed in a pure plasticity based formulation. These damage parameters will also be utilised for stiffness degradation in the following sections. As the degradation of frictional coefficient is not found to be significant in many physical shear tests (Yuen et al. 2019), the present model have not consider degradation of this hardening parameter.

4.4 Yield surface and potential surface

The yield surface provides the envelope of elastic domain which can be represented for the interface model in terms of normal stress and shear stress shown in **Fig. 4-3**. The proposed yield criteria is based on the concept of Caballero et.al (2008) which has a hyperbolic profile and after accommodating the damage parameters can be expressed as:

$$F(\{\sigma\}, \mathrm{D}_n, \mathrm{D}_s) = -(\mathrm{C}_0(1-\mathrm{D}_s) - \sigma_n tan\phi) + \sqrt{\sigma_s{}^2 + (\mathrm{C}_0(1-\mathrm{D}_s) - \chi_0(1-\mathrm{D}_n)\, tan\phi)^2} = 0 \qquad (4.10)$$

Fig. 4-3 shows three typical key states of the yield surface during its evolution from the initial position when the interface has no damage i.e. $D_n = D_s = 0$. The tensile strength will be fully exhausted when $D_n = 1$ but the shear capacity (apparent cohesion) will still be present (partially) at that time and D_s will be less than one. The yield surface will shrink further and come to its final stage when $D_n = D_s = 1$, at which point both the tensile and shear strengths will be exhausted. For numerical analysis, the maximum value of damage parameters is taken as 0.9999 so as to avoid computational issues. **Fig. 4-4** shows the hyperbolic yield surface with its evolution in 3D stress space for a better visualisation, while **Fig. 4-3** shows a sectional view of the 3D yield surface passing through the normal stress axis.

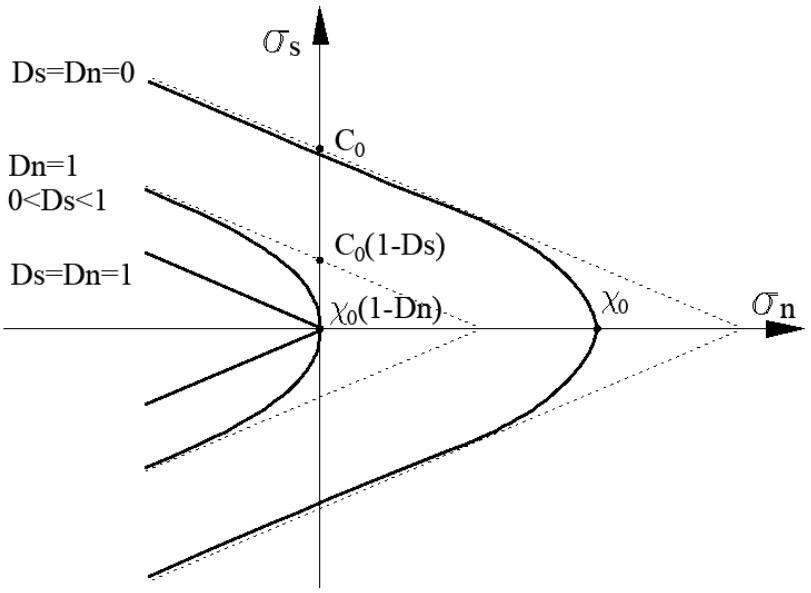

Fig. 4-3 Yield surface and its evolution with damage growth

Quasi-brittle materials such as masonry or concrete exhibit dilation under shear loading due to surface roughness, the dilation angle ϕ_Q is however always less than the friction angle ϕ. Thus, a different potential function is needed for the evaluation of plastic deformations, which makes the proposed model non-associated as potential and yield functions are different. The proposed potential function has followed similar format to the yield function (with the replacement of friction angle ϕ by the dilation angle ϕ_Q and the replacement of the apparent cohesion C with a corresponding parameter C_Q) and it expressed as:

$$Q(\{\sigma\}, \mathrm{D}_n) = -\left(\mathrm{C}_Q - \sigma_n tan\phi_Q\right) + \sqrt{\sigma_s{}^2 + \left(\mathrm{C}_Q - \chi_0(1-\mathrm{D}_n)\, tan\phi_Q\right)^2} = 0 \qquad (4.11)$$

Also, it is to be noted that the potential function does not need D_s as the value of C_Q as will not be changed during loading.

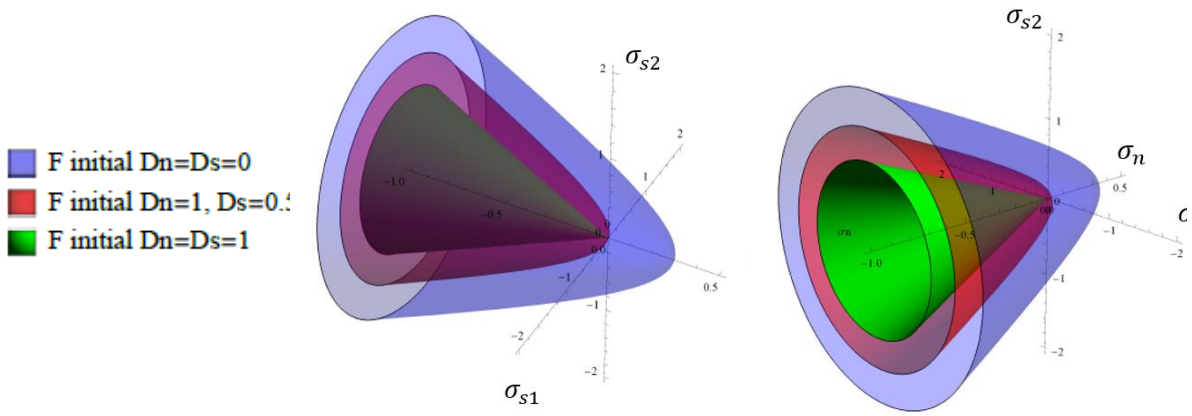

Fig. 4-4 Hyperbolic yield surface ($\chi_0 = 0.3MPa,\ C_0 = 0.87MPa,\ tan\phi = 1$)

The yield surface is a physical entity obtained using experimental test data, but the potential surface is a conceptual object utilised for controlling the plastic displacement in the right direction with the introduction of dilation angle. As the value of ϕ_Q is notably smaller than ϕ, the hyperbolic potential surface becomes narrow if the shear strength parameter is not changed i.e. $C_Q = C$, which will produce a large gap between the shear stress values obtained from yield and potential surfaces for a given normal stress. In order to minimise this gap, the value of C_Q need to be increased considerably compared to C, and is adopted here as did by other researches.

4.5 Numerical integration technique of constitutive equations

A fully implicit backward Euler integration technique is adopted to numerically implement the proposed constitutive model in an incremental manner. The primary aim of this task is to evaluate the independent variables (stresses, internal variable, and incremental plastic multiplier) at the end of a time step "t+1" (load step in the present case) when the converged values of the independent variables are known at the end of previous time step "t". Once the incremental displacements (relative) $\{du\}^{t+1}$ of an integration point within an interface are obtained from the global structural analysis due to the incremental load of the current time step, the trial stresses $\{^{trial}\sigma\}^{t+1}$ at time t+1 can be evaluated from the known converged stresses $\{\sigma\}^t$ at time t assuming elastic constitutive behaviour at that point as:

$$^{trial}\sigma_n^{t+1} = \begin{cases} \sigma_n^t + (1 - D_n^t)K_n^0 du_n^{t+1}, & \sigma_n^t > 0 \\ \sigma_n^t + K_n^0 du_n^{t+1}, & \sigma_n^t \le 0 \end{cases} \tag{4.12}$$

$$ {}^{trial}\sigma_s^{t+1} = \begin{cases} \sigma_s^t + (1 - D_s^t) K_s^0 du_s^{t+1}, & \sigma_n^t > 0 \\ \sigma_s^t + K_s^0 du_s^{t+1}, & \sigma_n^t \le 0 \end{cases} \tag{4.13} $$

The trial stresses are then substituted in the yield function to check the status of the integration point (elastic or inelastic deformations):

$$ \begin{aligned} &F\left(\{{}^{trial}\sigma\}^{t+1}, W^{p,t}\right) \le 0 \text{ - elastic deformation } \{\sigma\}^{t+1} = \{{}^{trial}\sigma\}^{t+1}, W^{p,t+1} = W^{p,t} \\ &F\left(\{{}^{trial}\sigma\}^{t+1}, W^{p,t}\right) > 0 \text{ - damage-plastic deformation} \\ &\text{(need backward Euler integration)} \end{aligned} \tag{4.14} $$

It is to be noted that the yield function in the above equation is expressed in terms of stress and plastic work W^p only, because all damage and strength parameters can be defined in terms of W^p. The trial stress will be inside the elastic domain if the first condition of **Eq. (4.14)** is satisfied, otherwise the trial stress will be outside the elastic domain shown in **Fig. 4-5,** and needs to be brought back to the yield surface. Here, this has been done by implementing a closed point projection return mapping approach for backward Euler integration. **Fig. 4-5** also shows the movement of the yield surface from *t* to *t*+1, which is due to the change of W^p caused by additional plastic deformation occurred within the current time step.

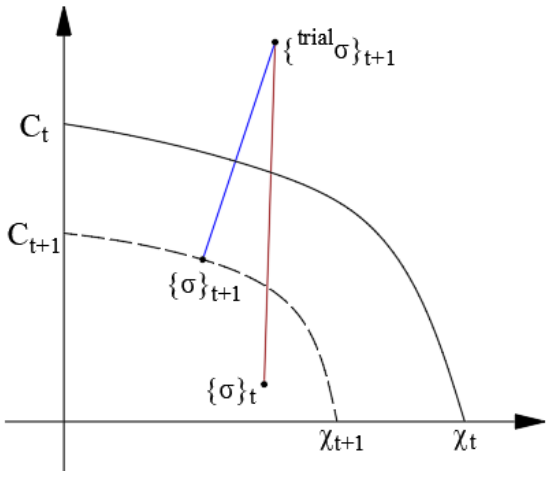

Fig. 4-5 Stress return mapping for backward Euler integration process

.

4.5.1 Backward Euler integration

When the incremental displacement (relative) $\{du\}^{t+1}$ is not entirely elastic, it can be split into its elastic and plastic components $\{du\}^{t+1} = \{du^e\}^{t+1} + \{du^p\}^{t+1}$ or $\{du^e\}^{t+1} = \{du\}^{t+1} -$

$\{du^p\}^{t+1}$, and this can be used to express the stress at time t+1 according to backward Euler integration technique:

$$\sigma_n^{t+1} = \sigma_n^t + (1 - D_n^{t+1})K_n^0(du_n^{t+1} - du_n^{p,t+1})$$
$$\sigma_s^{t+1} = \sigma_s^t + (1 - D_s^{t+1})K_s^0(du_s^{t+1} - du_s^{p,t+1}) \quad (4.15)$$

The above equation can now be expressed in terms of elastic predictor and plastic corrector as:

$$\sigma_n^{t+1} = \sigma_n^t + (1 - D_n^{t+1})K_n^0 du_n^{t+1} - (1 - D_n^{t+1})K_n^0 du_n^{p,t+1}$$
$$\sigma_s^{t+1} = \sigma_s^t + (1 - D_s^{t+1})K_s^0 du_s^{t+1} - (1 - D_s^{t+1})K_s^0 du_s^{p,t+1} \quad (4.16)$$

Considering the interface under compressive load, where the damage mechanism is not activated due to the crack closure effect, **Eq. (5.5)** can be rewritten as:

$$\sigma_n^{t+1} = \begin{cases} \sigma_n^t + (1 - D_n^{t+1})K_n^0 du_n^{t+1} - (1 - D_n^{t+1})K_n^0 du_n^{p,t+1} & \sigma_n^{t+1} > 0 \\ \sigma_n^t + K_n^0 du_n^{t+1} & \sigma_n^{t+1} \le 0 \end{cases} \quad (4.17)$$

$$\sigma_s^{t+1} = \begin{cases} \sigma_s^t + (1 - D_s^{t+1})K_s^0 du_s^{t+1} - (1 - D_s^{t+1})K_s^0 du_s^{p,t+1} & \sigma_n^{t+1} > 0 \\ \sigma_s^t + K_s^0 du_s^{t+1} - K_s^0 du_s^{p,t+1} & \sigma_n^{t+1} \le 0 \end{cases} \quad (4.18)$$

The above formulation will help to upgrade damage and hardening parameters at the same time within each iteration (details are in the next section) using plastic dissipation energy ($D^{t+1}(W^{p,t+1})$) as done by Nguyen et al. (2017).

Now the incremental plastic displacement $d\{u^p\}^{t+1}$ can be determined based on the non-associated flow rule utilising **Eq. (4.11)** for the potential function as:

$$d\{u^p\}^{t+1} = d\lambda^{t+1}\left(\frac{\partial Q}{\partial\{\sigma\}}\right)^{t+1} = d\lambda^{t+1}\{m\}^{t+1} \quad (4.19)$$

The above equation can be substituted in **Eqs. (4.17)** and **(4.18)** and these two equations can be expressed in a compact matrix form as:

$$\{\sigma\}^{t+1} = \{\sigma\}^{t} + ([I] - [D]^{t+1})[K^0]\{du\}^{t+1} - d\lambda^{t+1}[L]^{t+1}[K^0]\{m\}^{t+1} \tag{4.20}$$

where

$[K^0] = \begin{bmatrix} K_n^0 & 0 \\ 0 & K_s^0 \end{bmatrix}$ $[I] = \begin{bmatrix} 1 & 0 \\ 0 & 1 \end{bmatrix}$ $[L]^{t+1} = \begin{bmatrix} (1 - D_n^{t+1})H(\sigma_n^{t+1}) & 0 \\ 0 & 1 - D_s^{t+1}H(\sigma_n^{t+1}) \end{bmatrix}$

$[D]^{t+1} = \begin{bmatrix} D_n^{t+1}H(\sigma_n^{t+1}) & 0 \\ 0 & D_s^{t+1}H(\sigma_n^{t+1}) \end{bmatrix}$ *H(x)* is the step function

Similarly, the plastic work at time *t*+1 can be expressed according to backward Euler integration technique as:

$$W^{p,t+1} = W^{p,t} + dW^{p,t+1} \tag{4.21}$$

where the incremental plastic work for the time step can be written according to Eq. (3.2) as:

$$dW^{p.t+1} = \begin{cases} \sigma_n^{t+1}\, du_n^{p,t+1} + \sigma_s^{t+1}\, du_s^{p,t+1} & \sigma_n^{t+1} \geq 0 \\ \left|du_s^{p,t+1}\right|(|\sigma_s^{t+1}| + \sigma_n^{t+1} tan\phi) & \sigma_n^{t+1} < 0 \end{cases} \tag{4.22}$$

In order to solve all unknown independent variables ($\{\sigma\}^{t+1}$, $W^{p,t+1}, d\lambda^{t+1}$), another equation is needed in addition to **Eqs. (4.20)** and **(4.21)**. For this purpose, the full consistency condition is employed that can be expressed as:

$$F(\{\sigma\}^{t+1}, W^{p,t+1}) = 0 \tag{4.23}$$

4.5.2 Newton-Raphson (NR) iteration

In **Eqs. (4.20), (4.21)** and **(4.23)**, the unknown variables ($\{\sigma\}^{t+1}$, $W^{p,t+1}, d\lambda^{t+1}$) are dependent on themselves (appear both sides of these equation), which makes these equations implicit due to use of backward Euler integration. Thus, the solution of this system requires an iterative process and Newton-Raphson (NR) technique is employed for that. **Eqs. (4.20), (4.21)** and **(4.23)** are rearranged and their residuals are combined in the form of a vector so as to solve the system of equations monolithically as:

(4.24)

$$\{r\}^j = \begin{Bmatrix} \mathrm{r}_\sigma \\ \mathrm{r}_{Wp} \\ \mathrm{r}_F \end{Bmatrix}^j = \begin{Bmatrix} \{\sigma\}^j - \{\sigma\}^t - \left([I] - [D]^j\right)[K^0]\{du\}^{t+1} + d\lambda^j[L]^j[K^0]\{m\}^j \\ W^{p,j} - W^{p,t} - dW^{p,j} \\ F\left(\{\sigma\}^j, W^{p,j}\right) \end{Bmatrix}$$

where all unknown variables at time t+1 will be iteratively updated. Thus the superscript t+1 of these variables are replaced with j where j indicated the iteration number. All known converged values of the variable obtained at the end of previous time step t will be constant during the iteration. The iterative process is continued until the convergence of variables of the current time step, which is checked by calculating the norm of the residuals and comparing with a predefined small tolerance value (*TOL*) as follows:

$$\|\mathrm{r}\|_\infty = MAX\{\|\mathrm{r}_\sigma\|, |\mathrm{r}_{Wp}|, |\mathrm{r}_F|\} < TOL \tag{4.25}$$

Once the above condition is satisfied for a specific value of j, all independent variables ($\{\sigma\}^j$,$W^{p,j}$, $d\lambda^j$) will be replaced with ($\{\sigma\}^{t+1}$,$W^{p,t+1}$,$d\lambda^{t+1}$) and move forward to the next time step. If converge is not achieved, the independent variables are updated using the Jacobian [*J*], which is the gradient of the residual vector:

$$\begin{Bmatrix} \{\sigma\} \\ W^p \\ d\lambda \end{Bmatrix}^{j+1} = \begin{Bmatrix} \{\sigma\} \\ W^p \\ d\lambda \end{Bmatrix}^j + \begin{Bmatrix} \delta\{\sigma\} \\ \delta W^p \\ \delta d\lambda \end{Bmatrix}^{j+1} = \begin{Bmatrix} \{\sigma\} \\ W^p \\ d\lambda \end{Bmatrix}^j - \left([\mathrm{J}]^j\right)^{-1}\{\mathrm{r}\}^j \tag{4.26}$$

$$[\mathrm{J}]^j = \left(\frac{\partial\{\mathrm{r}\}}{\partial(\{\sigma\}, W^p, d\lambda)}\right)^j = \begin{bmatrix} \frac{\partial\{\mathrm{r}_\sigma\}}{\partial\{\sigma\}} & \frac{\partial\{\mathrm{r}_\sigma\}}{\partial W^p} & \frac{\partial\{\mathrm{r}_\sigma\}}{\partial d\lambda} \\ \frac{\partial \mathrm{r}_{Wp}}{\partial\{\sigma\}} & \frac{\partial \mathrm{r}_{Wp}}{\partial W^p} & \frac{\partial \mathrm{r}_{Wp}}{\partial d\lambda} \\ \frac{\partial F}{\partial\{\sigma\}} & \frac{\partial F}{\partial W^p} & 0 \end{bmatrix}^j \tag{4.27}$$

The implementation algorithm of the backward Euler integration is presented in **Algorithm 4-1**.

Algorithm 4-1. Newton-Raphson (NR) iteration for the backward Euler integration technique

1: *Define initial variables for the NR loop*
$\sigma_n^{j=0} = {}^{trial}\sigma_n^i;\ \sigma_s^{j=0} = {}^{trial}\sigma_s^t;\ W^{p,j=0} = W^{p,i-1};\ d\lambda^{j=0} = 0;\ \|\mathrm{r}\|^{j=0} = 1$

2: *NR loop*
DO WHILE ($\|\mathrm{r}\|^j > TOL$)
j = j+1
IF (j > jMax) **THEN** Flag=0; EXIT Sub-step loop
Compute: $\{D\}^j;\ \{r\}^j;\ \|\mathrm{r}\|^j;\ [\mathrm{J}]^j;\ \left([\mathrm{J}]^j\right)^{-1}$
IF (' NaN ' or ' ±Infinite ' in $\left([\mathrm{J}]^j\right)^{-1}$) **THEN** Flag=0; EXIT Sub-step loop

IF ($\|\mathrm{r}\|^j \leq TOL$) **THEN EXIT** *NR loop*

Compute increment variables, $\begin{Bmatrix} \delta\sigma_n \\ \delta\sigma_s \\ \delta W^p \\ \delta d\lambda \end{Bmatrix}^{j+1} = -\left([\mathrm{J}]^j\right)^{-1}\{\mathrm{r}\}^j$

Compute new variables, $\begin{Bmatrix} \sigma_n \\ \sigma_s \\ W^p \\ d\lambda \end{Bmatrix}^{j+1} = \begin{Bmatrix} \delta\sigma_n \\ \delta\sigma_s \\ \delta W^p \\ \delta d\lambda \end{Bmatrix}^{j+1} + \begin{Bmatrix} \sigma_n \\ \sigma_s \\ W^p \\ d\lambda \end{Bmatrix}^{j}$

IF ($d\lambda^{j+1} < 0$) THEN $d\lambda^{j+1} = 0$

ENDDO *NR loop*

3: *Update variables in " i " sub-step*
$\begin{Bmatrix} \sigma_n \\ \sigma_s \\ W^p \\ d\lambda \end{Bmatrix}^{i} = \begin{Bmatrix} \sigma_n \\ \sigma_s \\ W^p \\ d\lambda \end{Bmatrix}^{j};\ W^{p,i} = W^{p,j};\ \left([\mathrm{J}]^i\right)^{-1} = \left([\mathrm{J}]^j\right)^{-1}$

4.5.3 Consistent tangent operator for global analysis

For the material stiffness matrix at Gauss points (local) needed for calculation of element stiffness matrices utilised for global level finite element analysis, the use of a consistent tangent operator (CTO) is most appropriate when the full Newton-Raphson technique is employed for the global (out of balance load) analysis. This section presents the derivation of the CTO for the proposed interface model consisting of damage and plastic deformations. The CTO $(\partial\{\sigma\}/\partial\{du\})^{t+1}$ will be calculated at the end of local iterations (**Eq. (4.26)**) when convergence (**Eq. (4.25)**) is reached, i.e. the residual tend to zero. The CTO can be obtained by taking derivative of the residual i.e. **Eq. (4.24)** with respect to $\{du\}^{t+1}$ where *j* (last iteration number for achieving convergence) will be replaced with *t*+1. After taking this derivative and keeping terms at time *t*+1 on the left hand side while terms at time *t* on the right hand side as:

$$\frac{\partial}{\partial\{du\}}\begin{Bmatrix}\{\sigma\}^{t+1}+[D]^{t+1}[K^0]\{du\}^{t+1}+d\lambda^{t+1}[L]^{t+1}[K^0]\{m\}^{t+1}\\ W^{p,t+1}-dW^{p,t+1}\\ F(\{\sigma\}^{t+1},W^{p,t+1})\end{Bmatrix} = \frac{\partial}{\partial\{du\}}\begin{Bmatrix}\{\sigma\}^{t}+[I][K^0]\{du\}^{t+1}\\ W^{p,t}\\ 0\end{Bmatrix} \tag{4.28}$$

For the left hand side of the above equation, the derivation can be expressed in terms of independent variables using the chain rule:

$$\frac{\partial}{\partial(\{\sigma\},W^p,d\lambda)}\begin{Bmatrix}\{\sigma\}^{t+1}+[D]^{t+1}[K^0]\{du\}^{t+1}+d\lambda^{t+1}[L]^{t+1}[K^0]\{m\}^{t+1}\\ W^{p,t+1}-dW^{p,t+1}\\ F(\{\sigma\}^{t+1},W^{p,t+1})\end{Bmatrix}\begin{bmatrix}\left[\frac{\partial\{\sigma\}}{\partial\{\mathrm{du}\}}\right]\\ \left[\frac{\partial W^p}{\partial\{\mathrm{du}\}}\right]\\ \left[\frac{\partial d\lambda}{\partial\{\mathrm{du}\}}\right]\end{bmatrix}^{t+1} = \begin{bmatrix}[K^0]\\ [0]\\ [0]\end{bmatrix} \tag{4.29}$$

where the first component of the left hand side of **Eq. (4.29)** is the Jacobian [J] given by **Eq. (4.27)**. Hence, **Eq. (4.29)** can be rewritten as:

$$\begin{bmatrix}\left[\frac{\partial\{\sigma\}}{\partial\{\mathrm{du}\}}\right]\\ \left[\frac{\partial W^p}{\partial\{\mathrm{du}\}}\right]\\ \left[\frac{\partial d\lambda}{\partial\{\mathrm{du}\}}\right]\end{bmatrix}^{t+1} = \left([J]^{-1}\right)^{t+1}\begin{bmatrix}[K^0]\\ 0\\ 0\end{bmatrix} \tag{4.30}$$

Finally, the consistent tangent stiffness can written as:

$$\left[\frac{\partial\{\sigma\}^{t+1}}{\partial\{\mathrm{du}\}^{t+1}}\right] = [P]^T([J]^{-1})^{t+1}[P][K^0] \tag{4.31}$$

where $[P] = \begin{bmatrix} 1 & 0 & 0 & 0 \\ 0 & 1 & 0 & 0 \end{bmatrix}^T$ is the projection matrix.

4.6 Sub-stepping scheme for the integration of constitutive model

For implementation of the constitutive model (**Sections 4.2** to **4.4**) at Gauss integration points with cohesive elements, a fully implicit backward Euler integration technique (**Section 4.5**) is adopted because it is unconditionally stable. However, a complex mixed mode (tension-shear) loading scenario at a Gauss point may convergence difficulty, and this can be a severe issue when the incremental displacement (relative) becomes large. This issue may be addressed by reducing the size of load steps, which may be a solution of a simple test problem such as compression of a cylinder but reducing step size can have a major impact on the overall computational demand since the variation of deformation within a full size structure such as masonry system can be significant. To improve the robustness of numerical implementations in such scenarios, various strategies have been adopted by different investigators, such as defining specific auxiliary surfaces for better initial approximations (Bićanić and Pearce, 1996) and enlarging the convergence region of the NR technique (Armero and Pérez-Foguet. 2002; Pérez-Foguet and Armero 2002). However, these approaches need different formulations for the different constitutive models. A more generic strategy was introduced through a sub-stepping scheme which were successfully applied in both forward Euler formulation (Abbo and Sloan. 1996; Sloan 1987) and backward Euler formulation (Pérez-Foguet et al. 2001). Thus the sub stepping scheme adopted in the present study will be beneficial to solve the present problem with improved convergence performance.

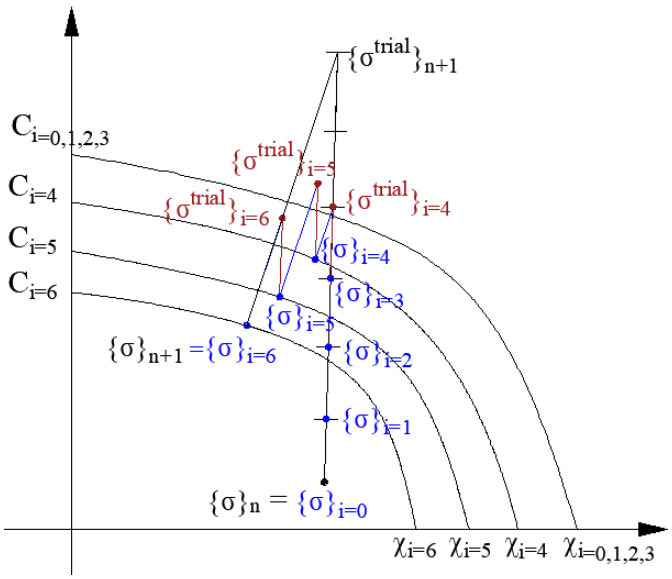

Fig. 4-6 Stress return mapping at an integration point with sub-stepping scheme

Fig. 4-6 illustrates the general concept of the sub-stepping scheme where the displacement increment is divided into small sub-increments $\{du\} = \sum_{i=1}^{n}\{du\}^i$. In a typical case, the first

few sub-steps (i = 1 to m) may cause elastic loading, while plastic loading will occur during subsequent sub-steps (i = m+1 to n). A specific case is shown in **Fig. 4-6** where the values of m and n are taken as 3 and 6 as a sample example. The stress values at the beginning of 1st sub-step defined as $\{\sigma\}^{t+i/n}$ (i=0) is equal to the known converged stress values obtained at the end of previous load step $\{\sigma\}^{t}$. In this case, the trial stress for the first sub-step ${}^{trial}\{\sigma\}^{t+1/n} = \{\sigma\}^{t+0/n} + ([I] - [D]^{t+0/n})[K^0]\{du\}^{i=1}$ is the final stress at the end of this sub-step i.e. $\{\sigma\}^{t+1/n} = {}^{trial}\{\sigma\}^{t+1/n}$ as the trial stress is located within the yield surface. This is similarly applicable for the next two sub-steps (i = 2 and 3) to get $\{\sigma\}^{t+2/n}$ and $\{\sigma\}^{t+3/n}$. However, the trial stress for the 4th sub-step ${}^{trial}\{\sigma\}^{t+4/n}$ is outside of the yield surface, which requires an NR iteration to return the stress point back to the correct yield surface $F(\{\sigma\}^{t+4/n},\ W^{p,t+4/n})$ following the procedure presented in previous section for a full load step without sub-stepping. The value of plastic work $W^{p,t+4/n}$ is updated for this sub-step due to plastic loading while $W^{p,t+3/n} = W^{p,t+2/n} = W^{p,t+1/n} = W^{p,t+0/n} = W^{p,t}$ due to elastic loading for these sub-steps. This process will be repeated up to last sub-step ($i = 6$ in this case) to get $\{\sigma\}^{t+6/n}$ and $W^{p,t+6/n}$, which are the final values of stress and plastic work at the end of this entire load increment (t+1) i.e. $\{\sigma\}^{t+1} = \{\sigma\}^{t+6/n}$ and $W^{p,t+1} = W^{p,t+6/n}$. For an incremental displacement at an integration point within a load step, the number of sub-step is initially taken as one, which is successively doubled until the iterative solution at local level is converged for all sub-steps (see algorithm below).

Algorithm 4-2. Adaptive sub-stepping scheme

1: *Define initial variables for the adaptive loop*
SubN = 1; $\alpha = 1/\text{SubN}$; Flag = 0
2: *Adaptive loop*
DO WHILE (Flag = 0)
3: *Sub-step loop*
DO i=1, subN
4: *NR loop*
DO WHILE ($\|r\|$ > TOL)
j = j+1
IF (j > jMax) **THEN** Flag=0; EXIT Sub-step loop
ENDDO *NR loop*
IF (i=subN) THEN Flag=1
ENDDO Sub-step loop
IF (Flag=1) **THEN**
EXIT *Adaptive loop*
ELSE
subN = 2 × subN;
IF (subN > subNMax) **THEN** $\Delta(t+2) = \Delta(t+1)/2$; Leave $t+1$ step
ENDDO *Adaptive loop*
5: *Update variables in " t+1 " step*
$\{\sigma\}^{t+1} = \{\sigma\}^{i=subN};\ W^{p,t+1} = W^{p,i=subN};\ [K^{tan}]^{t+1} = \left[\frac{\partial\{\sigma\}^{i=sub}}{\partial\{\mathrm{du}\}^{t+1}}\right]$

.

The consistent tangent operator is also used with the sub-stepping based integration strategy for better convergence. The CTO presented in the previous section cannot be used directly because the derivative of the residual (**Eq. (4.28)**) is with respect to the displacement increment of the full load step, while the parameters such as plastic multiplier are available only for sub-steps and hence cannot be used to calculate values for the full load step. Thus the formulation of CTO needs to be modified by employing the basic procedure applied to **Eq. (4.24)** to get **Eq. (4.28)** for a full load step in previous section to a sub-step *i* in the present case. The subscript *t*+1 used in the previous section will be $t + i/n$ in this case, which is written as *i* for convenience:

$$\frac{\partial}{\partial\{du\}}\begin{Bmatrix}\{\sigma\}^i + [D]^i[K^0]\{du\}^i + d\lambda^i[L]^i[K^0]\{m\}^i \\ W^{p,i} - dW^{p,i} \\ F\left(\{\sigma\}^i, W^{p,i}\right)\end{Bmatrix} = \frac{\partial}{\partial\{du\}}\begin{Bmatrix}\{\sigma\}^{i-1} + [I][K^0]\{du\}^i \\ W^{p,i-1} \\ 0\end{Bmatrix} \tag{4.32}$$

Applying the chain rule to express the derivative on left hand side of **Eq. (4.32)** and replacing the incremental displacement of the sub-step in terms that of the full load step $\{du\}^i = (1/n)\{du\}^{t+1}$, **Eq. (4.32)** can be rewritten as:

$$\frac{\partial}{\partial(\{\sigma\}, W^p, d\lambda)}\begin{Bmatrix}\{\sigma\}^i + [D]^i\left[K^0\right]\{du\}^i + d\lambda^i[L]^i\left[K^0\right]\{m\}^i \\ W^{p,i} - dW^{p,i} \\ F\left(\{\sigma\}^i, W^{p,i}\right)\end{Bmatrix}\begin{bmatrix}\left[\frac{\partial\{\sigma\}^i}{\partial\{\mathrm{du}\}}\right] \\ \left[\frac{\partial W^{p,i}}{\partial\{\mathrm{du}\}}\right] \\ \left[\frac{\partial d\lambda^i}{\partial\{\mathrm{du}\}}\right]\end{bmatrix} = \begin{bmatrix}\frac{\partial\{\sigma\}^{i-1}}{\partial\{\mathrm{du}\}} + (1/n)[K^0] \\ \frac{\partial W^{p,i-1}}{\partial\{\mathrm{du}\}} \\ [0]\end{bmatrix} \tag{4.33}$$

It is to be noted that $\{\sigma\}^{i-1}$ and $W^{p,i-1}$ appear on the right hand side of **Eq. (4.33)** will contribute, which was zero in **Eq. (4.29)**. This is because the derivative of the stress $\{\sigma\}^{i-1}$ and plastic work $W^{p,i-1}$ at the end of previous sub-step *i*-1 (not the full load step) are expressed

with respect to the incremental displacement of the full load step {du}. Similar to previous section, the first part of the left hand side of **Eq. (4.33)** is replaced with Jacobin matrix for the sub-step *i* and the equation can be rearranged as:

$$\begin{bmatrix} \left[\frac{\partial\{\sigma\}^i}{\partial\{\mathrm{du}\}}\right] \\ \left[\frac{\partial W^{p,i}}{\partial\{\mathrm{du}\}}\right] \\ \left[\frac{\partial d\lambda^i}{\partial\{\mathrm{du}\}}\right] \end{bmatrix} = ([J]^{-1})^i \begin{bmatrix} \frac{\partial\{\sigma\}^{i-1}}{\partial\{\mathrm{du}\}} + \alpha[K^0] \\ \frac{\partial W^{p,i-1}}{\partial\{\mathrm{du}\}} \\ [0] \end{bmatrix} \tag{4.34}$$

The values of $\left[\frac{\partial\{\sigma\}^i}{\partial\{\mathrm{du}\}}\right]$ and $\frac{\partial W^{p,i}}{\partial\{\mathrm{du}\}}$ are updated recursively while moving through the sub-steps with their zero initial value i.e. $\left[\frac{\partial\{\sigma\}^0}{\partial\{\mathrm{du}\}}\right] = \frac{\partial W^{p,0}}{\partial\{\mathrm{du}\}} = 0$, and the CTO can finally be expressed at the end of last sub-step ($i = n$) i.e. end of the full load step as:

$$\left[\frac{\partial\{\sigma\}}{\partial\{\mathrm{du}\}}\right]^{t+1} = \left[\frac{\partial\{\sigma\}^n}{\partial\{\mathrm{du}\}}\right] = [P]^T([J]^{-1})^n \begin{bmatrix} \frac{\partial\{\sigma\}^{n-1}}{\partial\{\mathrm{du}\}} + \alpha[K^0] \\ \frac{\partial W^{p,ni-1}}{\partial\{\mathrm{du}\}} \\ [0] \end{bmatrix} \tag{4.35}$$

The consistent tangent operator is updated recursively (over all sub-steps). The algorithm for the numerical implementation of the sub-stepping scheme with consistent tangent operator is provided in **Algorithm 4-3**.

Algorithm 4-3. CTO update in sub-stepping scheme

1: *Given initial variables from i=0 sub-step*
$\left[\frac{\partial\{\sigma\}}{\partial\{du\}}\right]^{i=0} = [0];\ \left[\frac{\partial W^p}{\partial\{du\}}\right]^{i=0} = [0];\ \{\sigma\}^{i=0} = \{\sigma\}^t;\ W^{p,i=0} = W^{p,t}$

2: *Sub-step loop*
DO i=1, subN

Compute trial stress ${}^{trial}\{\sigma\}^i$ of " i " sub-step

Define initial variables for NR loop:
$\sigma_n^{j=0} = {}^{trial}\sigma_n^i;\ \sigma_s^{j=0} = {}^{trial}\sigma_s^i;\ W^{p,j=0} = W^{p,i-1};\ d\lambda = 0;\ \|\mathrm{r}\|^{j=0} = 1.0$

3: *NR loop*
Using the NR loop procedure in **Algorithm 1**
IF (Flag =0) THEN EXIT Sub-step loop
Output converged variables: $\{\sigma\}^j;\ W^{p,j};\ \left([\mathrm{J}]^j\right)^{-1};$

4: *Update " i " sub-step variables*
$\{\sigma\}^i = \{\sigma\}^j;\ W^{p,i} = W^{p,j};\ \left([\mathrm{J}]^i\right)^{-1} = \left([\mathrm{J}]^j\right)^{-1}$
Compute CTO $\left[\frac{\partial\{\sigma\}^i}{\partial\{\mathrm{du}\}^{t+1}}\right]$ and $\left[\frac{\partial W^{p,i}}{\partial\{\mathrm{du}\}^{t+1}}\right]$
IF (i=subN) **THEN** converges in "t+1" step, Flag = 1

ENDDO

4.7 Numerical validation

To validate and assess the performance of the proposed nonlinear interface model, numerical tests are conducted by inserting the interface model within a finite element modelling platform. The specific numerical examples undertaken include testing of a single element under uniaxial and bi-axial modes, a masonry couplet under compression-shear mode, two masonry walls subjected to in-plane loading, and a masonry wall under out-of-plane loading. ABAQUS (Version: 6.14), being one of the most reliable finite element programs, is adopted for the FE implementation, where the interface constitutive model is implemented by writing a FORTRAN code as a user defined material subroutine (UMAT). The static-implicit solver is used to conduct the single element testing, and the dynamic-implicit solver with the option of quasi-static analysis is applied to the masonry structures as convergence issues are severe in large scale applications.

4.7.1 Single element test

The 8-node three-dimensional cohesive element (COH3D8) shown in **Fig. 4-7** is used, which is firmly supported at its bottom surface by restraining all degrees of freedom of the four nodes

(bottom surface). The top surface is subjected to different modes of loading by imposing displacements along i) Y axis (tensile mode), ii) X axis (share mode), and iii) X and Y axes (tension-shear mixed mode). In order to have the same displacement of the four top surface nodes, displacements are imposed to a reference point (RP) created for this purpose and are kinematically coupled (connected) to these four nodes. This approach also helps to conveniently capture the total force applied to the top surface in the form of reactive force of the RP. The size of the element is taken as 100mm×100mm with a thickness of 10mm, the value of thickness does not have effect due to the use of a traction-separation constitutive relationship but thickness is needed for creating the geometry. As experimental data for these three modes (i, ii, and iii) for a single material set is not available, experimental data are obtained from different sources with different material properties. The material properties used in the validation are listed in **Table 4-1** .

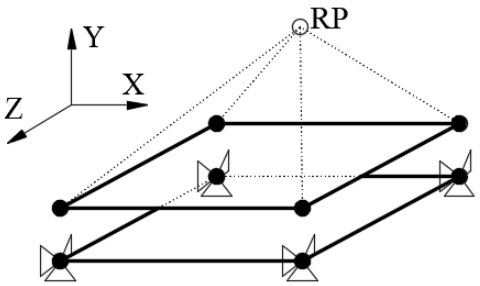

Fig. 4-7 A 3D single cohesive element

Table 4-1 Material properties used for the single element tests

Mode	K_n (N/mm^3)	K_s (N/mm^3)	χ_0 (MPa)	C_0 (MPa)	$\tan\phi$	C_Q (MPa)	$\tan\phi_Q$	G_{ft} (N/mm)	G_{fs} (N/mm)
Tension (i) or shear test (ii)	100	100	0.3	1	0.8	100	0.01	0.012	0.071 0.188
Mix-mode test (iii)	200	200	2.8	6	0.8	60	0.03	0.3	3

Fig. 4-8 shows the response of the cohesive element under pure monotonic tensile load, where a steep linear elastic response is followed by a nonlinear softening behaviour after the interface has reached the tensile strength ($\chi = 0.3$MPa as provided as material property in **Table 4-1)**. The predicted result (Present – FE model) is found to be enveloped within the range of experimental results from Pluijm (1992; 1993) presented as dashed lines (**Fig. 4-8a**). The numerical results produced by Lourenco and Rots (1996) using their model is also included in **Fig. 4-8a** as further comparison. The results predicted by Present – FE model is consistent with the experimental results as well as the existing numerical results.

Now considering the shear mode, the shear test is conducted with a constant pre-pressure of 0.1MPa (low compression) in one case and 1.0MPa (high compression) in the other. It should be noted that two values of shear fracture energy are used following the strategy of Lourenco and Rots (1996) who suggested $G_{fs} = 0.058 - 0.13\sigma_n$ as originally suggested by Pluijm (1992; 1993). **Fig. 4-8b** shows that the predicted results are consistent with the experimental and numerical results from literature. The model has successfully captured both peak shear strength and residual frictional strength, which are influenced by the magnitude of pre-pressure.

For the mixed-mode loading case, the normal (tensile) and shear displacements are imposed simultaneously in order to maintain a constant ratio between them, which is taken as u_n/u_s = tan60° i.e. a load path inclined at 60° with the direction of shear. The results generated by the proposed model are compared with the experimental results reported by Hassanzadeh (1990) and simulated results by Caballero et al. (2008) in **Fig. 4-8c** to show the normal stress vs normal displacement variation, and **Fig. 4-8d** for shear stress vs shear displacement variation. For this mixed-mode loading scenario, the results show that the peak tensile stress is close to the tensile strength ($\chi_0 = 2.8$ MPa) provided as an input, while the peak shear stress is considerably lower than the shear strength ($C_0 = 6$MPa) because tensile failure precedes shear failure.

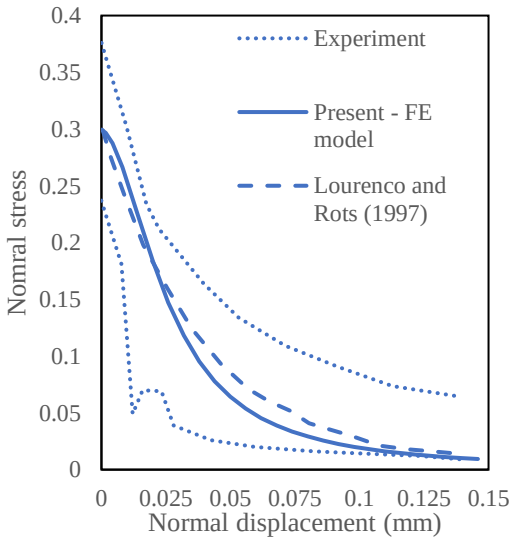

(a) Uniaxial tensile test

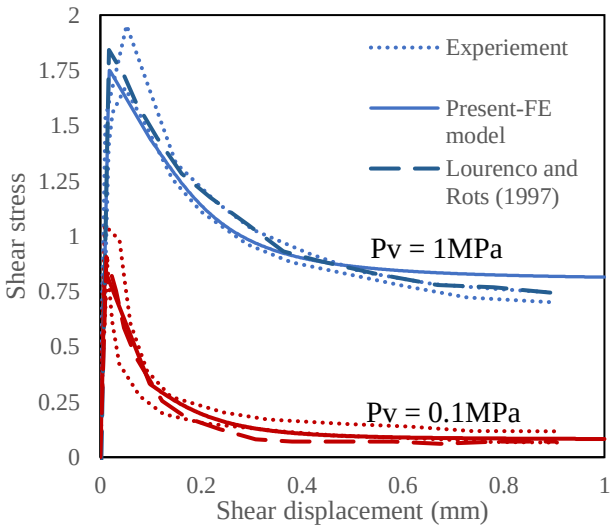

(b) Uniaxial shear test

(Pv is constant vertical compressive pressures applied on the top surface of the cohesive element)

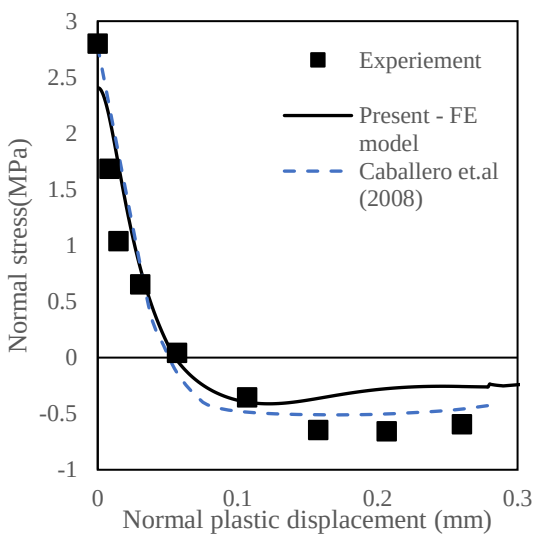

(c) Mixed-mode test (60°): normal result

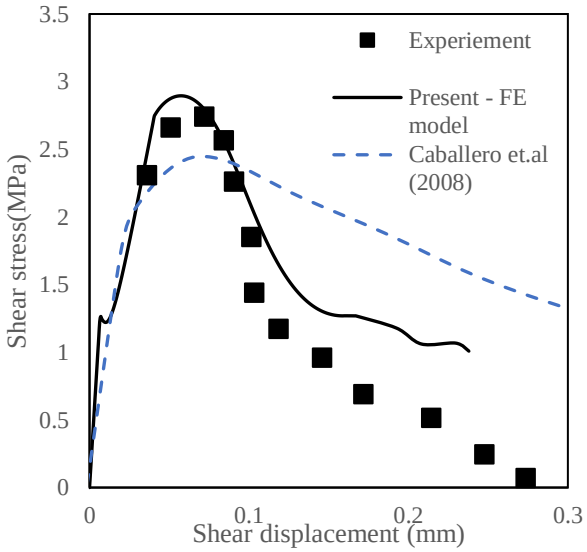

(d) Mixed-mode test (60°): shear result

Fig. 4-8 Loading test of the single element

4.7.2 A masonry couplet under cyclic shear loading under constant pre-pressure

In this section, a masonry couplet (**Fig. 4-9a**), tested by Atkinson et.al (1989) under cyclic shear loading with a constant pre-pressure (Pv = 4.31MPa), is modelled with the FE code ABAQUS. For this purpose, brick units are modelled with 8-node solid elements (C3D8R) while the mortar joints are modelled with 8-node three-dimensional cohesive elements (COH3D8) along with the proposed constitutive model in the form of UMAT. A full size brick unit (193mm×55mm×100mm) is discretised with a course mesh (7×2×3) as well as a fine mesh (19×6×10), and the interface elements follows that discretisation system. The results predicted by the two mesh sizes did not show significant differences. The material properties used for nonlinear interface elements (mortar joints) are given in **Table 4-2**, while the bricks are assumed to have elastic deformations taking their material properties as: elastic modulus E = 16700MPa, Poisson's ration v = 0.2, and density $\rho = 1.9\times10^{-9}$ tonne/mm^3. The density of bricks is needed as the implicit-dynamic solver is used in this case to enhance the convergence stability of the FE simulation.

Table 4-2 Material properties of mortar joints (shear couplet test specimen)

K_n (N/mm^3)	K_s (N/mm^3)	χ_0 (MPa)	C_0 (MPa)	$\tan\phi$	C_Q (MPa)	$\tan\phi_Q$	G_{ft} (N/mm)	G_{fs} (N/mm)
82	36	0.65	1.2	0.67	120	0.01	0.278	2.78

The bottom surface of the shear couplet specimen is fully restrained, and the top surface is subjected to cyclic shear/horizontal displacement using a reference point (RP) where one and a quarter complete cycles (**Fig. 4-9b**) of the shear displacement is applied. The pre-compression is first applied and kept constant (*Pv* = 4.31MPa) before imposing the shear displacement. The response of the shear couplet predicted by the FE model is presented with the experimental results reported by Atkinson et.al (1989) in **Fig. 4-9b**, and a good correlation between the experimental and numerical result is observed. The figure demonstrates that the softening of shear strength starts after reaching the peak at the end of the linear elastic region. The interface resistance then gradually degrades to a constant frictional resistance, which occurs due to the pre-compression. As the fracture energy is fully consumed at this stage, no cohesive strength exists for the mortar joint and its shear strength is provided by only the frictional resistance.

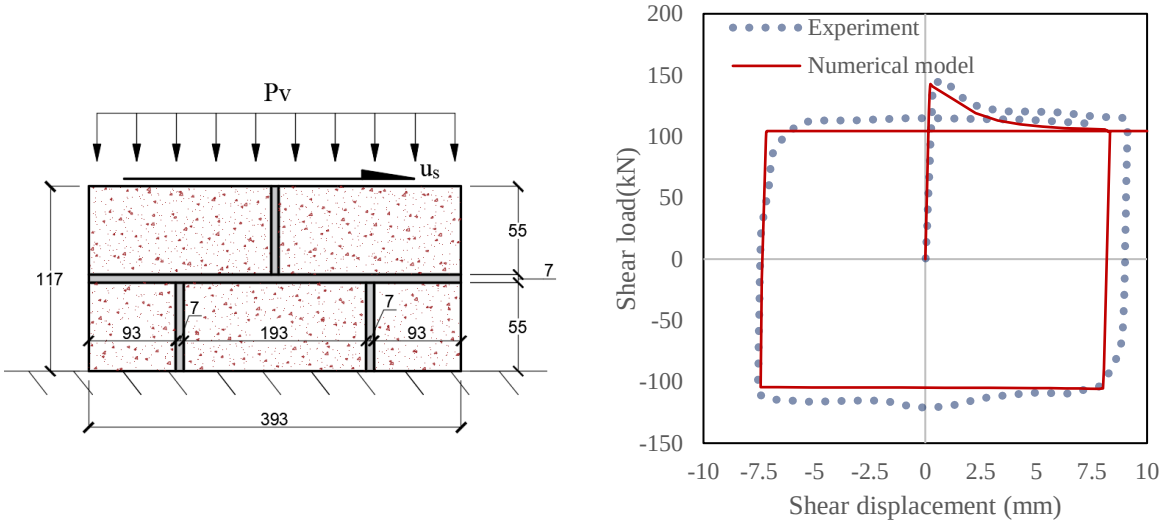

(a) Specimen geometry (b) Shear load vs shear displacement

Fig. 4-9 Shear couplet under 4.31MPa pre-pressure

4.7.3 In-plane (monotonic) response of masonry walls

Three typical cases (**Fig. 4-10a**) from a series of masonry walls tested by Raijmakers and Vermeltfoort (1993) under in-plane loading are modelled in a similar way to the shear couplet specimen in the previous section to investigate the performance of the proposed model in simulating realistic masonry structures. The walls (**Fig. 4-10a**) are supported at the base and subjected to shear displacement at the top surfaces using a steel beam. They (**Fig. 4-10a**) are also subjected to a pre-pressure where the first two walls (J4D and J5D) are under the same pre-compression of 0.3MPa while the pre-pressure is 2.12MPa for the third wall (J7D). All wall specimens have the same geometry (990mm×1000mm×100mm), and consist of 18 courses of solid clay bricks where a full size brick has a dimension of 210mm×52mm×100mm and all mortar joints are 10mm thick.

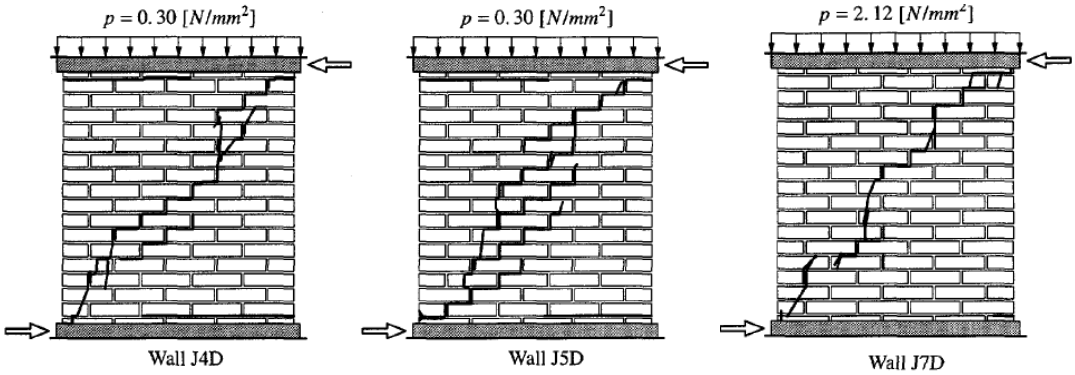

(a) Experimental set-up of the masonry walls and their failure modes (Raijmakers and Vermeltfoort. 1993)

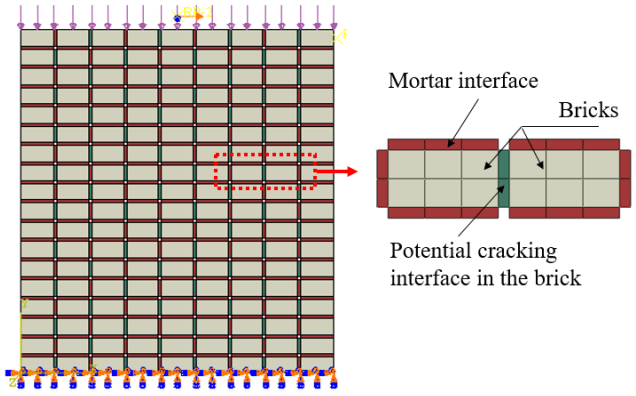

(b) FE model of a typical masonry wall

Fig. 4-10 Masonry walls under in-plane loading

.

As the walls are subjected to in-plane loading, a two-dimensional modelling strategy using Abaqus is adopted in this section for computational efficiency. The bricks are modelled with 2D plane stress elements (CPS4R) and the mortar joints are modelled with 2D interface elements (COH2D4) where a full size brick (210mm×52mm) is discretised with a mesh size of 6×2 and the interface elements followed the meshing arrangement of the bricks. **Fig. 4-10b** shows the FE model of a typical masonry wall with the loading (pre-compression) and boundary conditions along with the reference point (RP) for imposing equal horizontal displacement of all nodes at the wall top surface. As a full-size brick has the potential to crack along its vertical mid-plane aligned with the head joint of adjacent course of bricks, an artificial joint is considered at that plane and is also modelled with the interface element, which is highlighted by magnifying a portion of the wall in **Fig. 4-10b**. For the modelling of these walls, the material properties used for the interfaces and bricks are listed in **Table 4-3** and **Table 4-3** respectively. In order to simulate the inelastic behaviour of bricks including their diffused micro-cracking and crushing behaviour, the concrete damage-plasticity (CDP) material model availably in Abaqus for modelling quasi-brittle materials has been applied.

Table 4-3 Material properties of the interfaces (walls with in-plane loading)

	K_n (N/mm^3)	K_s (N/mm^3)	χ_0 (MPa)	C_0 (MPa)	$\tan\phi$	C_Q (MPa)	$\tan\phi_Q$	G_{ft} (N/mm)	G_{fs} (N/mm)
Mortar joint [a]	82	36	0.25	0.35	0.75	35	0.01	0.018	0.125
Mortar joint [b]	82	36	0.16	0.224	0.75	22.4	0.01	0.012	0.05
Brick joint	500	500	2	2.8	1	280	0.01	0.08	0.5

a: Wall J4D and J5D, b: Wall J7D

.

Table 4-4 Material properties of brick (walls with in-plane loading)

Uniaxial tensile behaviour		Uniaxial compressive behaviour			Other relevant parameters for brick material	
Stress (MPa)	Inelastic strain	Stress* (MPa)		Inelastic strain	E = 16700 MPa	[b] e = 0.1
3.5	0	6	11	0	ν = 0.18	[c] f_{b0}/f_{c0} = 1.12
0.3	0.002	6.5	11.5	0.001	ρ = 1.9×10^{-9} tonne/mm^3	[d] K = 0.667
		0.6	0.6	0.007	Viscosity = 0.0002	[e] $\psi = 10^0$

* First column of stress correspond to Wall J4D and J5D are second column corresponds to Wall J7D

[b] eccentricity, [c] bi-axial ratio, [d] ratio of stress invariant on meridian, [e] dilation angle– needed by material model (CDP)

Fig. 4-11 shows the failure mode of the walls predicted by the FE model, where it is observed that significant diagonal cracks occur along with horizontal cracks near the corners. The diagonal cracks are found to initiate near the central portion of the walls and propagate gradually towards the corners as the lateral load increases. The results shows that the pre-pressure on the walls has significant effect on the degree and pattern of cracking. For example, horizontal cracks near the top left corner and bottom right corner for the walled with lower pre-compression (0.3MPa) are clearly visible, while these cracks are not visible for the walls with higher pre-compression (2.12MPa). This is expected as the higher pre-pressure provides higher vertical compression that resist opening of bed joints.

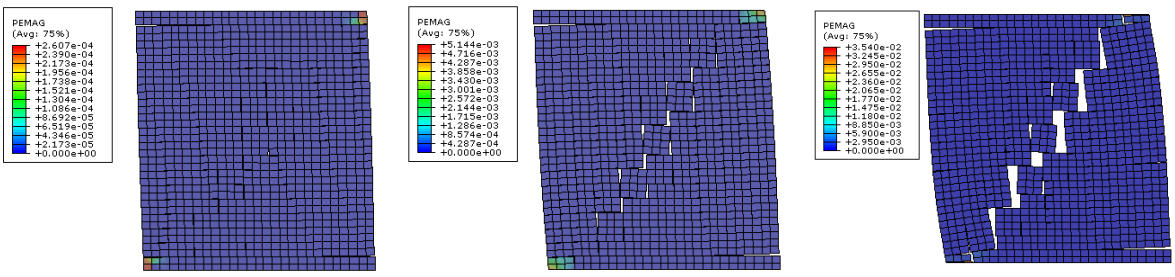

1.12mm 2.2mm 3.71mm

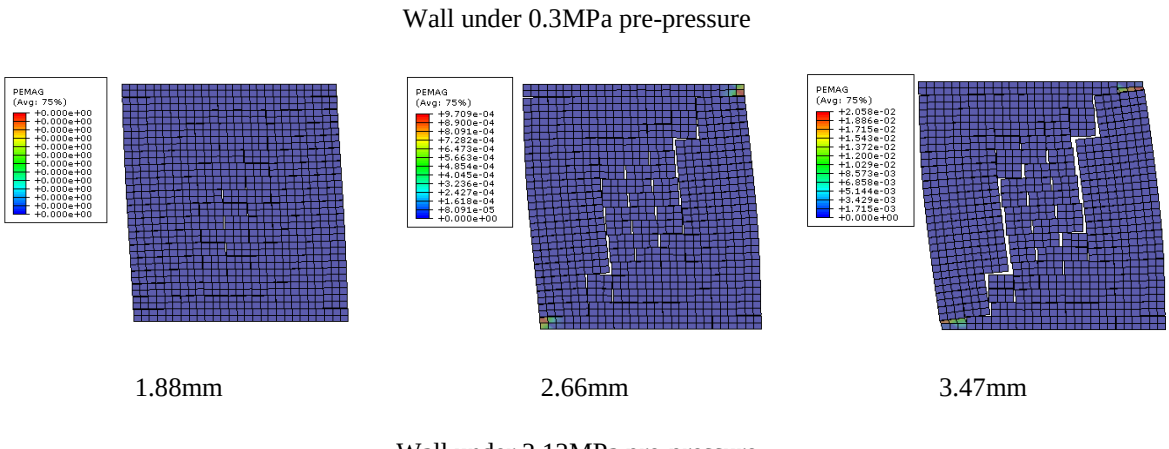

Fig. 4-11 Failure modes of the walls under in-plane loading predicted by the FE model (PEMAG: compressive plastic strain magnitude to quantify crushing)

The load displacement response of the walls extracted from the reference point (RP) of the FE model is plotted along with the experimental results given by Raijmakers and Vermeltfoort (1993) in **Fig. 4-12** and demonstrate the numerical results are in good agreement with the experimental results. The figure also shows that the first two walls (J4D and J5D) could resist a peak load of around 50kN with no significant drop up to 4mm displacement as reported by Raijmakers and Vermeltfoort (1993). The third wall (J7D) provided around 100kN peak load capacity followed by a softening response until the load capacity reduces to 60kN (approximate) at its final collapse.

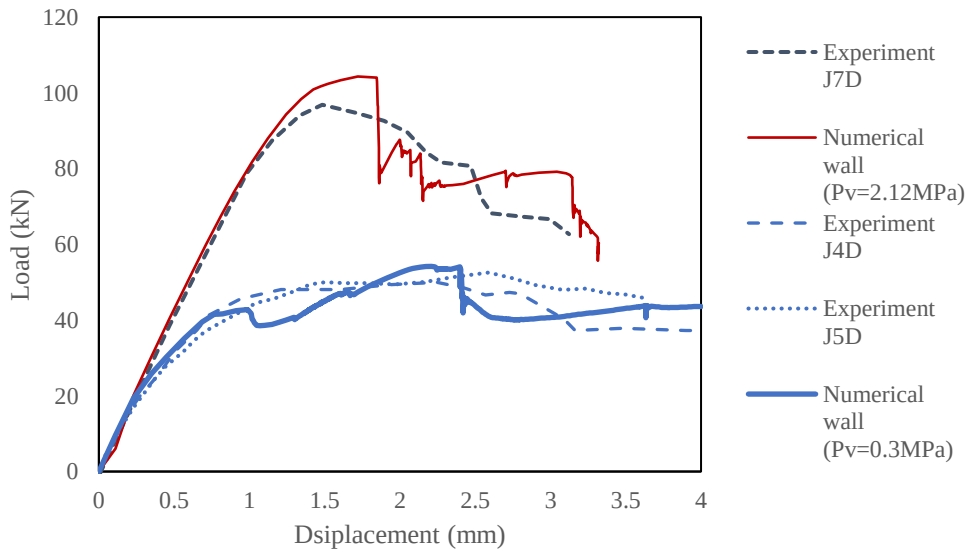

Fig. 4-12 Experimental validation of the load-displacement response of the walls under in-plane loading

4.7.4 A masonry wall supported at four sides under out-of-plane loading causing two-way bending

The experimental validation of the proposed model under a 3D state of stress is undertaken in this section by considering a masonry wall (**Fig. 4-13**) tested by Chee Liang (1996) in which a transverse load is applied on one of the surfaces of the wall, which it is supported along all four edges using a steel frame. The single leaf wall is 795mm wide, 1190mm tall and 53mm thick, which is made with solid clay bricks, each having a dimension of 112mm×36mm×53mm, and all mortar joints are 10mm thick. In the experiment investigation, the wall was subjected to a surface pressure by using an air bag that causes a two-way bending failure of the masonry panel, as shown in the **Fig. 4-13b**. For the present FE modelling of the wall, the material properties used for the interface and bricks are listed in **Table 4-5** and **Table 4-6** respectively.

The bricks are modelled with 8-node hexahedral solid elements (C3D8R) where a mesh size of 4×2×3 is used for a full size brick (112mm×36mm×53mm). The mortar and artificial brick joints are modelled with 8 node 3D cohesive elements (COH3D8), which followed the meshing system of the bricks. In terms of material models, CDP is used for bricks as in the earlier section and the proposed interface model is used for the mortar and brick joints. Assuming a simply supported condition provided by the steel frame (**Fig. 4-13a**) at the four sides of the wall, the DOF (degrees of freedom) for the translational displacements of all nodes on the loaded surface of the wall panel along its four edges are restrained. In order to apply pressure on the wall, a reference point (RP) is assigned and connected to all nodes on the loaded surface but the connection of the RP with the nodes are established with a feature (Abaqus) "structural distributing" instead of "kinematic coupling" used in previous sections. This feature helps to provide uniformly distributed load on all connected nodes by imposing Z-directional (**Fig. 4-13c**) displacement on the RP. In this case, the nodes coupled with the RP will not be required to have same displacement for all nodes as in previous sections. It is interesting to note that the usual load control technique used by Abdulla et al. (2017) fails to simulate the post peak softening behaviour of the wall.

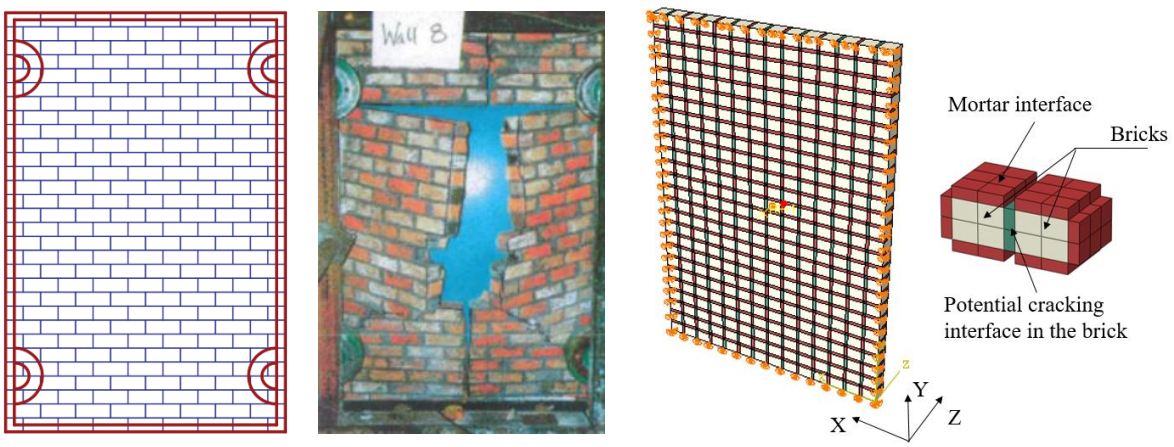

(a) A steel frame for supporting the wall at four sides

(b) Out-of-plane failure mode of the wall (experimental from Chee Liang, 1996)

(c) FE model of the wall

Fig. 4-13 A masonry wall supported at its edges and subjected to out-of-plane pressure

.

Table 4-5 Material properties of the interfaces (walls with out-of-plane loading)

	Kn (N/mm3)	Ks (N/mm3)	χ_0 (MPa)	C_0 (MPa)	tanϕ	C_Q (MPa)	tanϕ_Q	G_{ft} (N/mm)	G_{fs} (N/mm)
Interface (mortar)	230	105	1	1.2	0.57	120	0.01	0.036	0.25
Interface (brick joints)	500	500	2	2.8	1	280	0.01	0.1	0.5

Table 4-6 Material properties of brick (walls with out-of-plane loading)

Uniaxial tensile behaviour		Uniaxial compressive behaviour		Other relevant parameters for brick material	
Stress (MPa)	Inelastic strain	Stress* (MPa)	Inelastic strain	E = 16700 MPa	[b] e = 0.1
3.5	0	6	0	ν = 0.18	[c] f_{b0}/f_{c0} = 1.12
0.3	0.002	6.5	0.001	$\rho = 1.9\times10^{-9}$ tonne/mm^3	[d] K = 0.667
		0.6	0.007	Viscosity = 0.0002	[e] $\psi = 10^0$

[b] eccentricity, [c] bi-axial ratio, [d] ratio of stress invariant on meridian, [e] dilation angle– needed by material model (CDP)

The numerical simulation satisfactorily captured the failure mode of the wall as observed in the experimental investigation of Chee Liang (1996). A vertical central crack is first observed by breaking the mortar head joints and the corresponding artificial brick joints before reaching the peak load carrying capacity i.e point A on the load-displacement curve. With further loading, diagonal cracks are generated from the two ends of the vertical crack and they propagated towards the corners of the wall panel. This clearly demonstrated a two-way bending failure of the wall. The plastic strain (PEMAG) used as an indicator of brick crushing failure is presented in **Fig. 4-14**, which shows crushing failure near the corners of the wall caused by restraints provided by the steel frame.

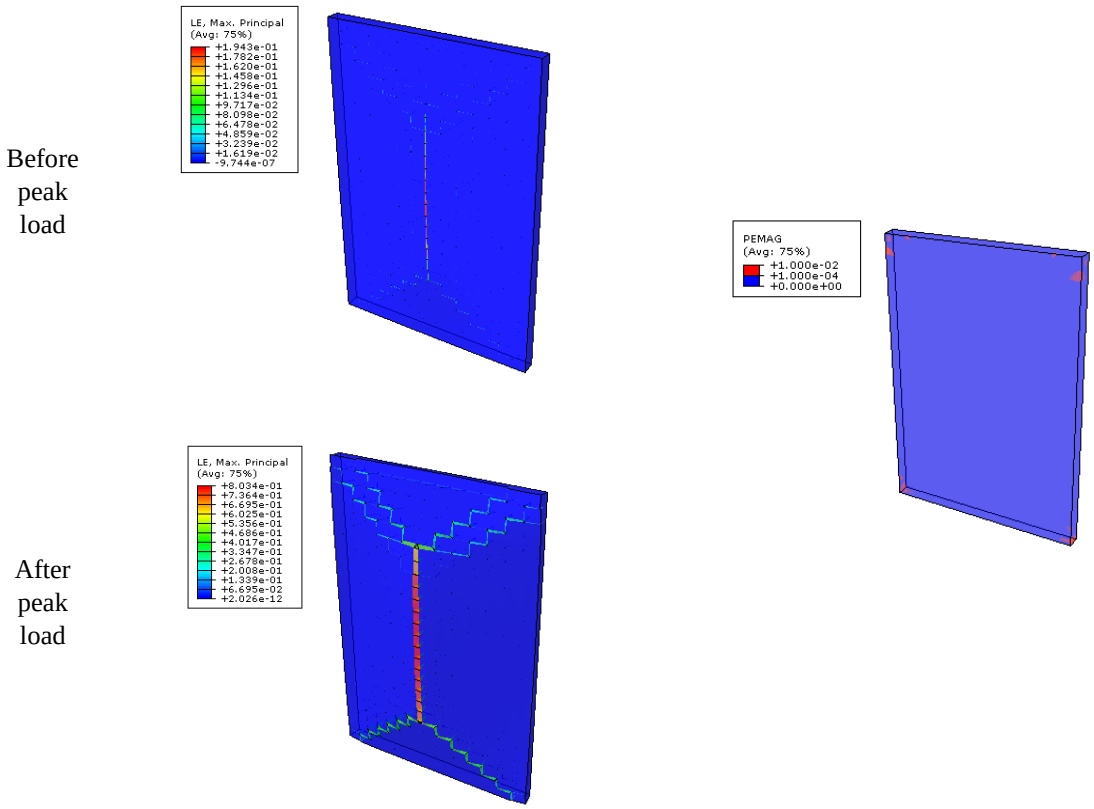

(a) Cracking pattern (b) Brick crushing indicator (PEMAG)

Fig. 4-14 Failure modes of the walls under out-of-plane loading predicted by the FE model

The load-displacement response obtained from the RP used in the present analysis is plotted in **Fig. 4-15** along with the experimental response measured by Chee Liang (1996). The linear variable differential transformer (LVDT) used to measure the displacement during the experiment was unfortunately damaged before reaching the peak load (**Fig. 4-15Error! Reference source not found.**). Thus the full load-displacement response could not be measured but fortunately the ultimate/collapse load carrying capacity (around 0.026MPa) of the wall was recorded, which is shown in **Fig. 4-15**. The simulated result is consistent with the results that could measure experimentally.

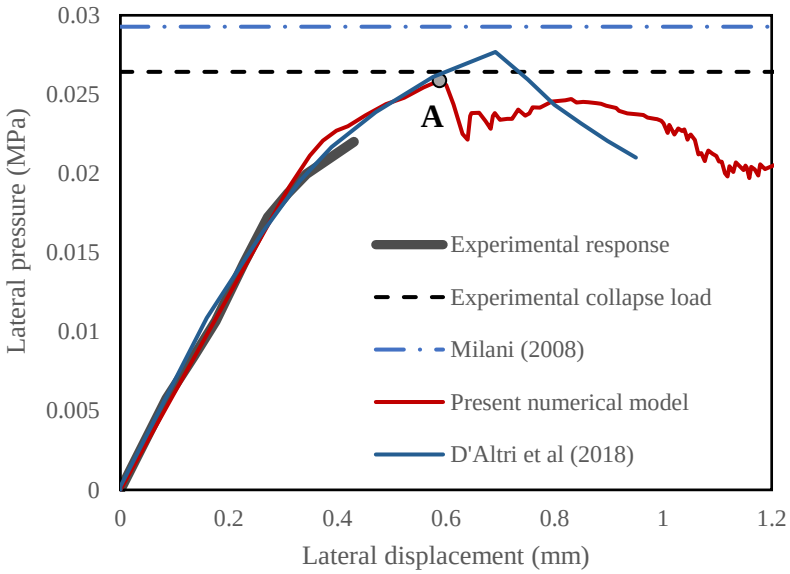

Fig. 4-15 Experimental validation of the load-displacement response of the wall under out-of-plane loading

4.7.5 Masonry walls supported at three sides with/without window under out-of-plane loading

The performance of the proposed model under a 3D state of stress is investigated further taking more realistic masonry walls of Graziotti et al. (2019) who conducted shake table tests of walls under out-of-plane actions. The experimental results of these tests were simulated by Sharma et al. (2021) who simulated their response by idealising the out-of-plane dynamic action as monotonic static pushover load following the recommendation of Bertolesi et.al (2019) and represented the contribution of supporting walls in the perpendicular direction as simple supports to simplify the analysis. From these studies, two sample walls, one wall with a window (CSW-000-RF) and another without a window (CS-000-RF), as shown in **Fig. 4-16** Error! R eference source not found.are chosen for the present investigation. Both walls have same supports (three sides are supported while top side is free) and dimensions (3.98m × 2.75m) while the size of the unsymmetrically placed window (CSW-000-RF) is 1.79m×1.63m (around 25% opening). These walls are constructed with Calcium Silicate (CS) brick (212mm×71mm×102mm) and 10mm mortar joints.

Table 4-7 Material properties of the interfaces (walls under out-of-plane loading)

	K_n (N/mm^3)	K_s (N/mm^3)	χ_0 (MPa)	C_0 (MPa)	$\tan\phi$	C_Q (MPa)	$\tan\phi_Q$	G_{ft} (N/mm)	G_{fs} (N/mm)
Bed-joint	40	20	0.62	0.81	0.46	81	0.36	0.03	0.05
Head-joint	20	10	0.31	0.4	0.46	40	0.36	0.03	0.05

Artificial-joint	100	100	2.2	1.5	0.46	150	0.36	0.03	0.05

.

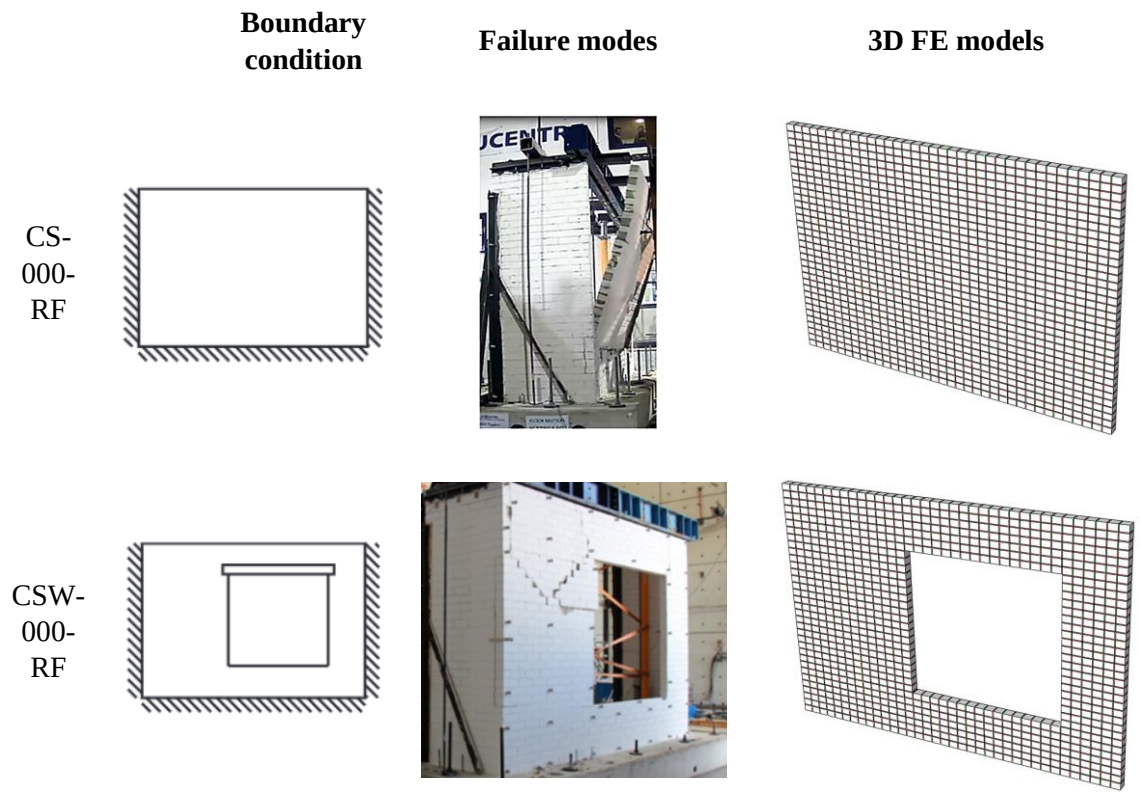

Fig. 4-16 Geometry, boundary conditions, failure modes, and FE models of walls (out-of-plane loading from Graziotti et al. 2019)

.

Similar to the FE model introduced in previous section (S**ection 4.7.4**), bricks are modelled with 3D solid element (C3D8R) where a mesh size of 2×1×1 is adopted for a full size brick. Mortar and artificial joints follow the same meshing arrangement and they are modelled using cohesive element (COH3D8). Since no compressive crushing is reported in the experimental investigation Graziotti et al. (2019), all bricks are simulated with elastic behaviour (E = 5000MPa, ν = 0.25). Interface properties are listed in **Table 4-7**Error! Reference source not found.. In this FE simulation, no vertical pre-pressure is applied and the out-of-plane load is applied as a monotonic pressure following the procedure introduced in the previous section.

Initial cracking

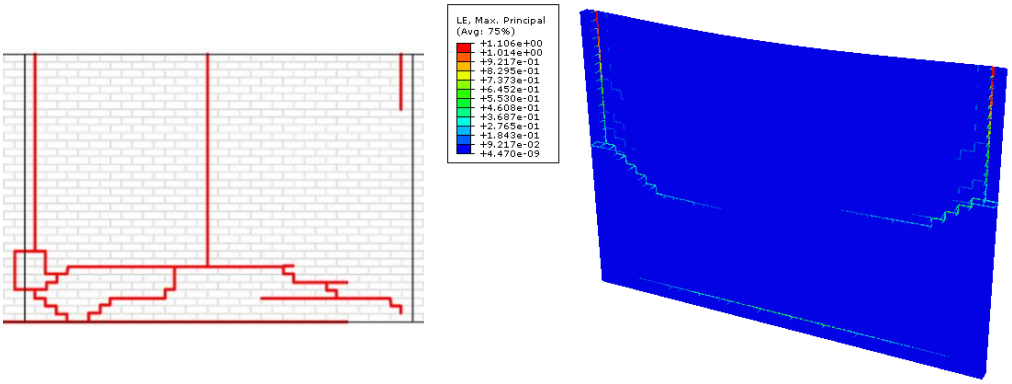

Post-failure cracking

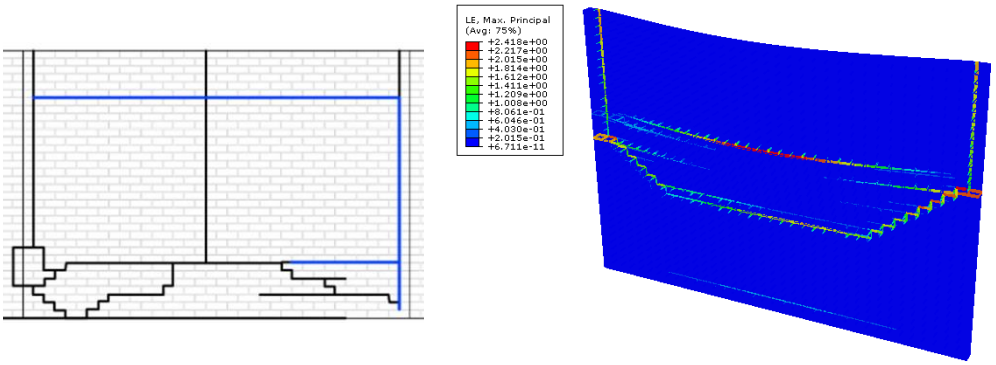

(a) CS-000-RF

Initial cracking

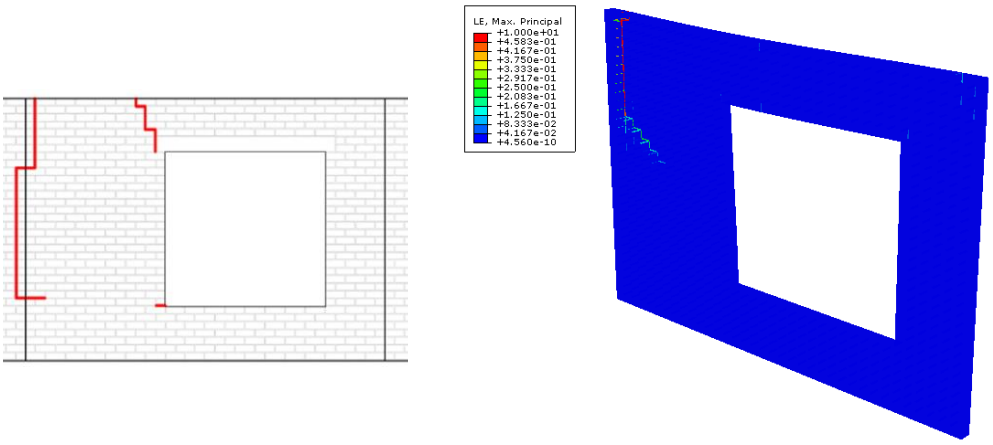

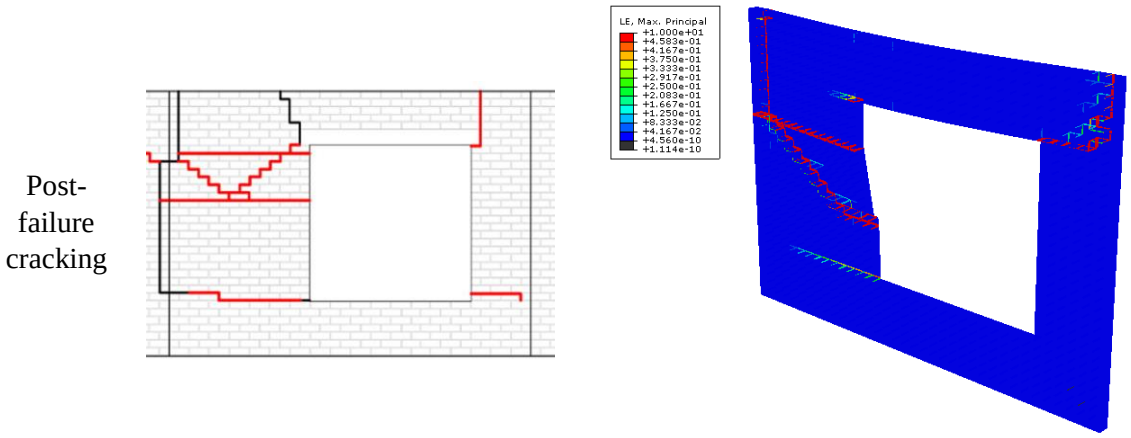

(b) CSW-000-RF

Fig. 4-17 Failure modes of the walls under out-of-plane loading from experiment and present FE simulation

The failure modes of the masonry walls are presented in **Fig. 4-17** where the cracks obtained from the FE simulation are characterised in terms of opening displacement (resultant) of interface elements are used to compare with experimental cracking patterns. The wall with no opening (CS-000-RP) has a typical out-of-plane overturning collapse (**Fig. 4-17 a**), which is well predicted by the numerical model. In the FE simulation, two vertical cracks developed along the vertical edges and jointed with a horizontal crack, which leads to overturning failure of the wall in the out-of-plane direction. The other wall with window (CSW-000-RF) has an initial vertical crack found near the returning wall (**Fig. 4-17 b**), which is also predicted by the model. In the final stage, horizontal and diagonal cracks are observed in both experiment and simulation on the left hand side of the wall.

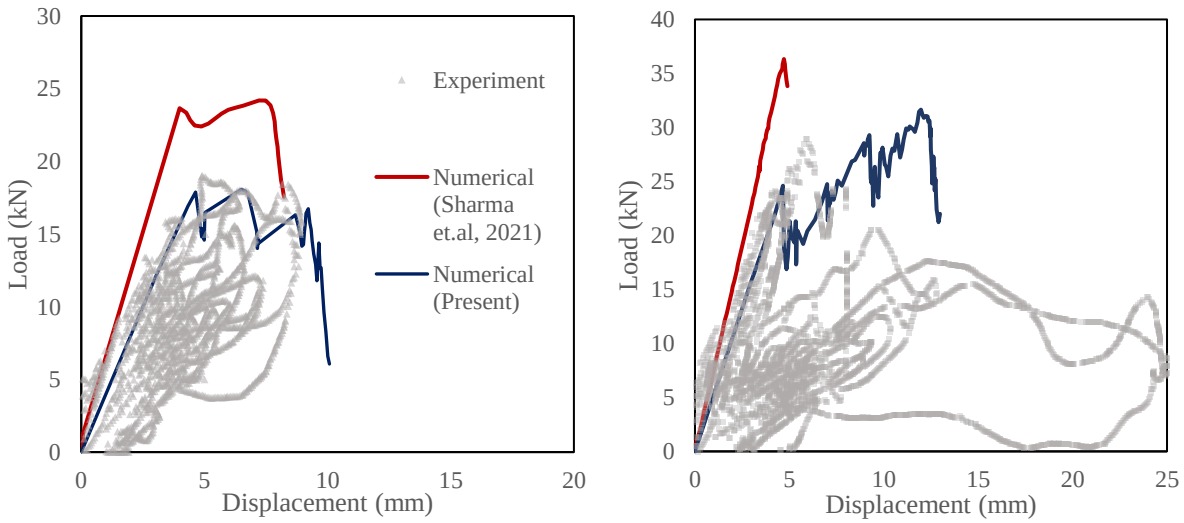

(a) CSW-000-RF

(b) CW-000-RF

Fig. 4-18 Experimental validation of the load-displacement response of the walls under out-of-plane loading

The load-displacement response obtained from the present analysis is compared in **Fig. 4-18** with the simulated static response of Sharma et al. (2021) and experimental dynamic response of Graziotti et al. (2019) expressed as an equivalent static response as represented by Sharma et al. (2021). In our simulation, the displacement is captured at the centre of the free edge as observed in the experimental response. The results (**Fig. 4-18**) show that the proposed model performed much better than the model of Sharma et al. (2021). Moreover, it is reported by Sharma et al. (2021) that their model encounter numerical convergence difficulties when trying to capture the post-failure behaviour, while the proposed model shows a robust performance.

4.7.6 In-plane cyclic response of a masonry wall

For experimental validation of the proposed model under cyclic loading, test results of a sample wall (TUD-COMP-4) reported by Messali et al. (2020) is used in this section. The wall as shown in **Fig. 4-19a** has wall a dimension of 4m×2.76m, and is constructed of calcium-silicate bricks (210mm×71mm×102mm) and mortar joints of 12mm thickness. The wall is clamped at the horizontal edges and free at the vertical edges. Under a fixed pre-pressure of 0.5MPa in the vertical direction, the wall is subjected cyclic horizontal displacement at the top edge maintaining no in-plane rotation of this edge. The wall shows a pure shear failure with diagonal cracks connected by a horizontal crack (**Fig. 4-19a**) in the experimental investigation. The FE simulation along with the meshing in this section followed the same procedure used in **Section 4.7.5**. Similarly, the bricks are treated as elastic (E = 9000MPa, ν = 0.14) as no compressive crushing of bricks is found in experiment. The nonlinear material properties of interfaces are listed in **Table 4-8**, which are picked up from Xie et al. (2021) who attempted to simulate this masonry wall.

Table 4-8 Material properties of the interfaces (walls under in-plane cyclic loading)

	K_n (N/mm^3)	K_s (N/mm^3)	χ_0 (MPa)	C_0 (MPa)	$\tan\phi$	C_Q (MPa)	$\tan\phi_Q$	G_{ft} (N/mm)	G_{fs} (N/mm)
Bed-joint	100	40	0.1	0.14	0.46	14	0.01	0.05	3
Head-joint	10	16	0.01	0.02	0.43	2	0.01	0.025	0.05
Artificial-joint	100	100	2.2	1.5	0.46	150	0.36	0.03	0.05

The propagation of crack simulated by the FE model is presented in **Fig. 4-19b** and **4-19c** by characterising the crack in terms of opening displacement (resultant) of interface elements. In the FE simulation, a diagonal crack with minor horizontal cracking (**Fig. 4-19b**) is initially predicted when the applied horizontal displacement reaches around 2 mm while a perpendicular cracking in the opposite direction (**Fig. 4-19c**) is formed when a similar amount

of displacement in the reverse direction is applied. It show that the final failure mode captured by the FE model (**Fig. 4-19c**) agreed closely with the cracking pattern observed in experiment (**Fig. 4-19a**). In **Fig. 4-19d**, the simulated in-plane load-displacement response of the wall for around three complete cycles is presented with the experimentally measured response. It shows that both ultimate load bearing capacity and deformation hysteresis are well reproduced by the FE model during the cyclic loading process. Our results also correlated with the simulated results of Xie et al. (2021) reasonably though the details are not provided.

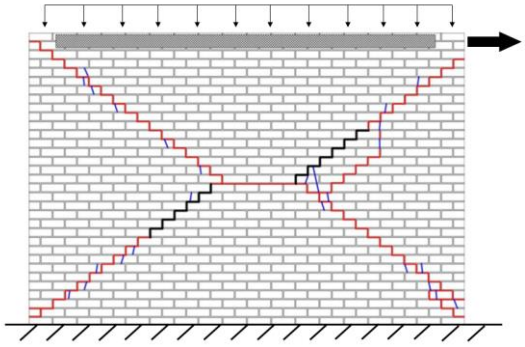

(a) Boundary conditions, loading and cracking mode of the wall [56]

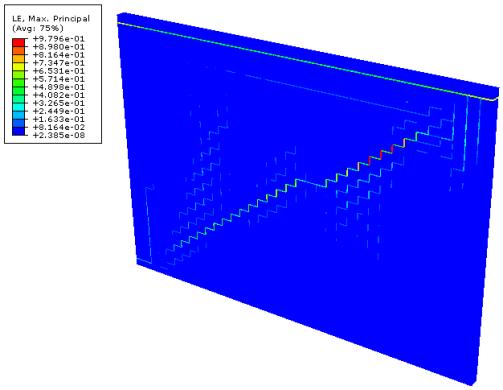

(b) initial cracking

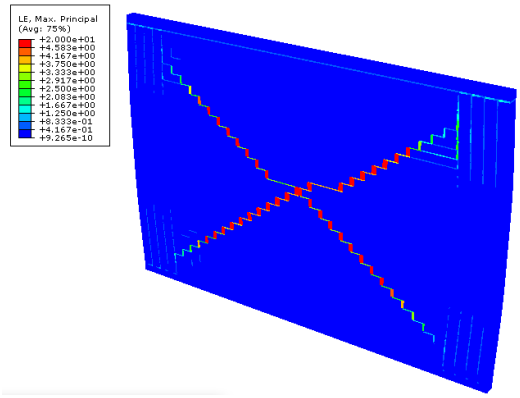

(c) final failure

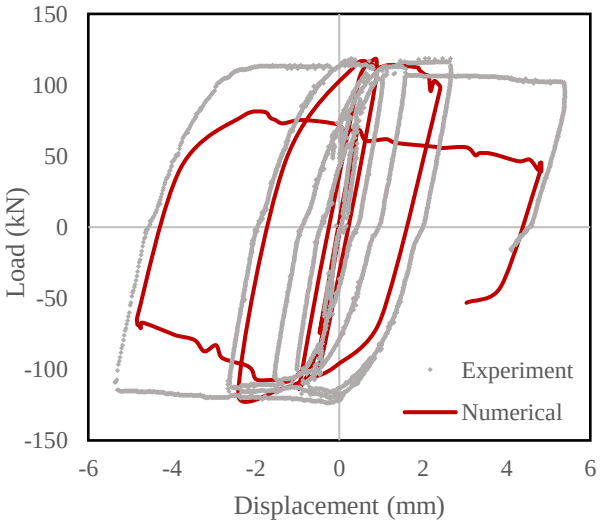

(d) load-displacement response

Fig. 4-19 Experimental validation of failure modes and load-displacement response of a masonry wall under in-plane cyclic loading

.

4.8 Conclusions

A FE based computational modelling technique is developed in this study to accurately simulate the nonlinear behaviour and cracking patterns of masonry structures subjected to in-plane and out-of-plane loading. One of the key contributions is the development of an interface model considering damage, plastic deformations and their coupling. The softening behaviour of an interface under different modes of failure is simulated by the shrinkage of the yield surface, which is controlled by the damage parameters that provides for coupling between damage and plasticity. In this model, the damage variables are related to the plastic work, which is a measure of dissipated fracture energy. The influence of the crack closure is accommodated by switching off the damage parameter used for stiffness degradation in a 'crack opening' (tension) scenario to restore the full stiffness of mortar joints that represents a realistic physical scenario of crack closure (compression). The model has the capability of having residual frictional resistance found in masonry joints. A smooth hyperbolic yield surface used in this model helps to minimise convergence issue due to discontinuities in sharp corners found in a multi-surfaces model. Similarly, a smooth curve is used for the evolution of damage parameters in the form of a cosine function.

An attempt has been made in this study to have an efficient numerical implementation of the developed model in order to have a stable simulation of large scale masonry structures having multiple joints, which can undergo complex loading conditions. For this purpose, a fully implicit backward Euler integration strategy is used and implemented through a Newton-Raphson iteration technique for the stress return mapping at an integration/material point. Furthermore, an adaptive sub-stepping scheme is implemented to improve the robustness for closed point projection return mapping process so that a full-scale masonry structure can be successfully analysed where the displacement increment at some locations can be significantly larger than at other locations. In order to achieve quadratic convergence at the global/elemental level solution, the consistent tangent stiffness matrix for the proposed damage-plastic model is derived following a recursive updating approach for the sub-stepping integration scheme.

The performance of the proposed numerical model is validated by applying the model to simulate masonry structures under different loading and the results obtained are compared with experimental results available in literature. This include 1) a single interface element for testing the constitutive behaviour of the cohesive elements under different loading conditions, 2) a shear couplet for testing its cyclic behaviour under shear-compression loading, 3) a masonry wall panel subjected to in-plane loading and finally 4) a masonry wall under out-of-plane loads, 5) two full-size masonry walls under push-over out-of-plane load, 6) a full-scale masonry wall under cyclic in-plane load. Comparison of the simulated load-displacement response as well as failure patterns produced by the proposed FE model with the experimental results demonstrates a very good capability of proposed interface model in predicting nonlinear behaviour of masonry structures properly. Thus, the model has potential application for practical engineering projects involving design of strategic new buildings and retrofit of historic buildings.

4.9 Reference

Vaculik J, Visintin P, Burton N, Griffith M, Seracino R. State-of-the-art review and future research directions for FRP-to-masonry bond research: Test methods and techniques for extraction of bond-slip behaviour. Construction and Building Materials 2018;183:325-45.

Griffith MC, Vaculik J, Lam N, Wilson J, Lumantarna E. Cyclic testing of unreinforced masonry walls in two - way bending. Earthquake Engineering & Structural Dynamics 2007;36:801-21.

Vaculik J, Griffith MC. Out-of-plane load–displacement model for two-way spanning masonry walls. Engineering Structures 2017;141:328-43.

Milani G, Lourenço PB. 3D non-linear behavior of masonry arch bridges. Computers & Structures 2012;110:133-50.

Su Y, Wu C, Griffth MC. Modelling of the bond–slip behavior in FRP reinforced masonry. Construction and Building Materials 2011;25:328-34.

Systèmes D. ABAQUS 6.14 analysis user's manual. Dassault Systems Inc Waltham, USA; 2014.

Lourenço PB, Rots JG. Multisurface interface model for analysis of masonry structures. Journal of engineering mechanics 1997;123:660-8.

Camanho PP, Dávila CG. Mixed-mode decohesion finite elements for the simulation of delamination in composite materials. 2002.

Alfano G, Sacco E. Combining interface damage and friction in a cohesive - zone model. International Journal for Numerical Methods in Engineering 2006;68:542-82.

Citto C. Two-dimensional interface model applied to masonry structures: University of Colorado at Boulder; 2008.

Kumar N, Amirtham R, Pandey M. Plasticity based approach for failure modelling of unreinforced masonry. Engineering structures 2014;80:40-52.

Kumar N, Barbato M. New constitutive model for interface elements in finite-element modeling of masonry. Journal of Engineering Mechanics 2019;145:04019022.

Giambanco G, Rizzo S, Spallino R. Numerical analysis of masonry structures via interface models. Computer methods in applied mechanics and engineering 2001;190:6493-511.

Macorini L, Izzuddin B. A non - linear interface element for 3D mesoscale analysis of brick - masonry structures. International Journal for numerical methods in Engineering 2011;85:1584-608.

Milani G. Simple homogenization model for the non-linear analysis of in-plane loaded masonry walls. Computers & Structures 2011;89:1586-601.

Nazir S, Dhanasekar M. A non-linear interface element model for thin layer high adhesive mortared masonry. Computers & Structures 2014;144:23-39.

Abdulla KF, Cunningham LS, Gillie M. Simulating masonry wall behaviour using a simplified micro-model approach. Engineering Structures 2017;151:349-65.

D'Altri AM, de Miranda S, Castellazzi G, Sarhosis V. A 3D detailed micro-model for the in-plane and out-of-plane numerical analysis of masonry panels. Computers & Structures 2018;206:18-30.

D'Altri AM, Messali F, Rots J, Castellazzi G, de Miranda S. A damaging block-based model for the analysis of the cyclic behaviour of full-scale masonry structures. Engineering Fracture Mechanics 2019;209:423-48.

Lotfi HR, Shing PB. Interface model applied to fracture of masonry structures. Journal of structural engineering 1994;120:63-80.

Parrinello F, Failla B, Borino G. Cohesive–frictional interface constitutive model. International Journal of Solids and Structures 2009;46:2680-92.

Sacco E, Lebon F. A damage–friction interface model derived from micromechanical approach. International Journal of Solids and Structures 2012;49:3666-80.

Smoljanović H, Nikolić Ž, Živaljić N. A combined finite–discrete numerical model for analysis of masonry structures. Engineering fracture mechanics 2015;136:1-14.

Andreotti G, Graziotti F, Magenes G. Expansion of mortar joints in direct shear tests of masonry samples: implications on shear strength and experimental characterization of dilatancy. Materials and Structures 2019;52:1-16.

Aref AJ, Dolatshahi KM. A three-dimensional cyclic meso-scale numerical procedure for simulation of unreinforced masonry structures. Computers & Structures 2013;120:9-23.

Chaimoon K, Attard MM. Modeling of unreinforced masonry walls under shear and compression. Engineering structures 2007;29:2056-68.

Simo JC, Hughes TJ. Computational inelasticity: Springer Science & Business Media; 2006.

Adhikary DP, Jayasundara CT, Podgorney RK, Wilkins AH. A robust return‐map algorithm for general multisurface plasticity. International Journal for Numerical Methods in Engineering 2017;109:218-34.

Pech S, Lukacevic M, Füssl J. A robust multisurface return-mapping algorithm and its implementation in Abaqus. Finite Elements in Analysis and Design 2021;190:103531.

Abreu R, Mejia C, Roehl D. A comprehensive implicit substepping integration scheme for multisurface plasticity. International Journal for Numerical Methods in Engineering. 2021 Sep 27.

Minga E, Macorini L, Izzuddin BA. A 3D mesoscale damage-plasticity approach for masonry structures under cyclic loading. Meccanica 2018;53:1591-611.

Spada A, Giambanco G, Rizzo P. Damage and plasticity at the interfaces in composite materials and structures. Computer Methods in Applied Mechanics and Engineering 2009;198:3884-901.

Yuen TY, Deb T, Zhang H, Liu Y. A fracture energy based damage-plasticity interfacial constitutive law for discrete finite element modelling of masonry structures. Computers & Structures 2019;220:92-113.

Caballero A, López C, Carol I. 3D meso-structural analysis of concrete specimens under uniaxial tension. Computer Methods in Applied Mechanics and Engineering 2006;195:7182-95.

Caballero A, Willam K, Carol I. Consistent tangent formulation for 3D interface modeling of cracking/fracture in quasi-brittle materials. Computer Methods in Applied Mechanics and Engineering 2008;197:2804-22.

Carol I, López CM, Roa O. Micromechanical analysis of quasi-brittle materials using fracture-based interface elements. International Journal for Numerical Methods in Engineering 2001;52:193-215.

Nguyen NH, Bui HH, Nguyen GD, Kodikara J. A cohesive damage-plasticity model for DEM and its application for numerical investigation of soft rock fracture properties. International Journal of Plasticity 2017;98:175-96.

Le LA, Nguyen GD, Bui HH, Sheikh AH, Kotousov A. Localised failure mechanism as the basis for constitutive modelling of geomaterials. International Journal of Engineering Science 2018;133:284-310.

Le LA, Nguyen GD, Bui HH, Sheikh AH, Kotousov A, Khanna A. Modelling jointed rock mass as a continuum with an embedded cohesive-frictional model. Engineering Geology 2017;228:107-20.

Pérez-Foguet A, Rodríguez-Ferran A, Huerta A. Consistent tangent matrices for substepping schemes. Computer methods in applied mechanics and engineering 2001;190:4627-47.

Bićanić N, Pearce C. Computational aspects of a softening plasticity model for plain concrete. Mechanics of Cohesive - frictional Materials: An International Journal on Experiments, Modelling and Computation of Materials and Structures 1996;1:75-94.

Armero F, Pérez-Foguet A. On the formulation of closest-point projection algorithms in elastoplasticity—part I: The variational structure. International Journal for Numerical Methods in Engineering 2002;53:297-329.

Pérez-Foguet A, Armero F. On the formulation of closest-point projection algorithms in elastoplasticity—part II: Globally convergent schemes. International Journal for numerical Methods in Engineering 2002;53:331-74.

Abbo AJ, Sloan S. An automatic load stepping algorithm with error control. International journal for numerical methods in engineering 1996;39:1737-59.

Sloan SW. Substepping schemes for the numerical integration of elastoplastic stress–strain relations. International journal for numerical methods in engineering 1987;24:893-911.

Hassanzadeh M. Determination of fracture zone properties in mixed mode I and II. Engineering Fracture Mechanics 1990;35:845-53.

Van der Pluijm R. Material properties of masonry and its components under tension and shear. 1992.

Van der Pluijm R. Shear behaviour of bed joints. 1993.

Atkinson R, Amadei B, Saeb S, Sture S. Response of masonry bed joints in direct shear. Journal of Structural Engineering 1989;115:2276-96.

Vermeltfoort AT, Raijmakers T, Janssen H. Shear tests on masonry walls. 1993.

Ng CL. Experimental and theoretical investigation of the behaviour of brickwork cladding panel subjected to lateral loading: University of Edinburgh; 1996.

Milani G. 3D upper bound limit analysis of multi-leaf masonry walls. International Journal of Mechanical Sciences 2008;50:817-36.

Graziotti F, Tomassetti U, Sharma S, Grottoli L, Magenes G. Experimental response of URM single leaf and cavity walls in out-of-plane two-way bending generated by seismic excitation. Construction and Building Materials 2019;195:650-70.

Sharma S, Silva L, Graziotti F, Magenes G, Milani G. Modelling the experimental seismic out-of-plane two-way bending response of unreinforced periodic masonry panels using a non-linear discrete homogenized strategy. Engineering Structures 2021;242:112524.

Bertolesi E, Silva LC, Milani G. Validation of a two-step simplified compatible homogenisation approach extended to out-plane loaded masonries. International Journal of Masonry Research and Innovation 2019;4:265-96.

Messali F, Esposito R, Ravenshorst G, Rots J. Experimental investigation of the in-plane cyclic behaviour of calcium silicate brick masonry walls. Bulletin of Earthquake Engineering 2020;18:3963-94.

Xie Z, Sousamli M, Messali F, Rots J. A sub-stepping iterative constitutive model for cyclic cracking-crushing-shearing in masonry interface elements. Computers & Structures 2021;257:106654.

Chapter 5: An effective stress based coupled damage-plasticity model

Nie Y, Sheikh A, Visintin P, Griffith M. An interfacial damage-plastic model for the simulation of masonry structures under monotonic and cyclic loadings. Submitted to Engineering Fracture Mechanism (under review).

Statement of Authorship

Title of Paper	An interfacial damage-plastic model for the simulation of masonry structures under monotonic and cyclic loadings
Publication Status	☐ Published ☐ Accepted for Publication ☑ Submitted for Publication ☐ Unpublished and Unsubmitted work written in manuscript style
Publication Details	Nie Y, Sheikh A, Visintin P, Griffith M. An interfacial damage-plastic model for the simulation of masonry structures under monotonic and cyclic loadings. Submitted to Engineering Fracture Mechanism (under review).

Principal Author

Name of Principal Author (Candidate)	Yu Nie		
Contribution to the Paper	Proposed the constitutive model and implement it by numerical method. Validate the proposed model by comparing numerical models with experimental results. Write and modify the manuscript.		
Overall percentage (%)	70%		
Certification:	This paper reports on original research I conducted during the period of my Higher Degree by Research candidature and is not subject to any obligations or contractual agreements with a third party that would constrain its inclusion in this thesis. I am the primary author of this paper.		
Signature		Date	10 May 2022

Co-Author Contributions

By signing the Statement of Authorship, each author certifies that:

i. the candidate's stated contribution to the publication is accurate (as detailed above);
ii. permission is granted for the candidate in include the publication in the thesis; and
iii. the sum of all co-author contributions is equal to 100% less the candidate's stated contribution.

Name of Co-Author	Abdul Sheikh		
Contribution to the Paper	Proposed the general concept and gave guidance of the methodology Supervised the technical development. Evaluate and revised the manuscript.		
Signature		Date	10 May 2022

Name of Co-Author	Phillip Visintin		
Contribution to the Paper	Supervised the technical development. Evaluate and revised the manuscript.		
Signature		Date	10 May 2022

Name of Co-Author	Michael Griffith		
Contribution to the Paper	Supervised the technical development. Evaluate and revised the manuscript.		
Signature		Date	10 May 2022

Please cut and paste additional co-author

Chapter 5: An effective stress based coupled damage-plasticity model

Abstract

A damage plasticity based interface constitutive model for simulating complex mixed behaviour of masonry joints is proposed in this paper. To improve the computational efficiency and robustness of the interface model, a novel modelling strategy is adopted to algorithmically decouple the damage and plastic deformations, which are treated separately in two stages. This approach helps to simulate elastic-perfectly-plastic behaviour in effective stress space and provides a non-evolving yield surface in first stage which significantly improves the convergence of stress return mapping. In second stage, a separate function is employed to model the evolution of damage used to quantify stress softening. The interface model is implemented within a finite element code used to analyse masonry structures of different scales/sizes under monotonic and cyclic loads. The experimental validation of the simulated results demonstrates good performance of the model in terms of accuracy and robustness. Moreover, the effects of different parameters on the model performance are investigated. One of the key parameters is the degradation of dilation angle incorporated through an energy based evolution function, which is observed to have importance in improving physical response and numerical performance.

5.1 Introduction

Masonry construction is common amongst residential and major public buildings and structures of significant architectural heritage. Masonry structures usually exhibit high compressive strength, but are susceptible to damage from tensile and shear stress, which are commonly generally caused by lateral loads such as those from seismic action (Benedetti et al. 2001). To improve the resistance of masonry structures under all possible loading conditions, the prediction of failure modes is essential; predictions help identify vulnerable regions in a structure, and enable the design of effective retrofits (De Lorenzis and Teng, 2007; Malena et al. 2019; Vaculik et al. 2018).

Masonry structures are typically designed using codified approaches based on empirical formulae or analytical models derived using simplified hypothesis (Griffith et al. 2007; Vaculik and Griffith, 2017). While convenient and reliable when applied to simple structures, these simplified approaches may be inadequate when considering nonlinear behaviour of structures with complex geometry or loading conditions. Compared with simplified analytical modelling approaches, detailed finite element (FE) based numerical modelling approaches are more capable of simulating the inelastic response of structures and behaviour such as the location of cracking in joints and crushing/cracking in brick units (Milani and Lourenço, 2012), all of which are significant in building repair and remediation (D'Altri et al. 2018).

To realise these benefits, the development of numerical modelling techniques (Baraldi and Cecchi, 2016; Ferrante et al. 2020; Ferrante et al. 2021; Iannuzzo et al. 2021; Malomo and DeJong 2021a, b; Sarhosis and Lemos, 2018; Serpieri et al. 2017; Valente et al. 2019) have drawn considerable research interest, and a number of models have been proposed. These models, which have different degrees of sophistication, have been broadly categorised by Lourenço (1997) into three modelling strategies: detailed micro-modelling (e.g. D'Altri et al. 2018; Andreotti et al. 2018), simplified micro-modelling (e.g. D'Altri et al. 2019; Lourenço and Rots, 1997) and macro-modelling (e.g. Milani et al. 2006). The primary focus of the examples of existing research referred to here is development of material models and their

implementation within a reliable Finite Element (FE) code, such as Abaqus (2014), or other in-house/commercial codes. Among these three modelling strategies, the simplified micro-modelling technique has become most popular because of its balance between predictive ability and computational efficiency. Simplified micro-modelling requires a continuum based model for bricks and an interface model for mortar joints which is based on a traction-separation law charactering tensile (Mode I) and shear (Mode II) failures (Camanho and Dávila, 2002). Brick units are usually assumed to have elastic behaviour, which helps to reduce computational cost, while mortar joints are taken to be inelastic to allow for simulation of cracking and failure. Interface models for mortar joints can be further characterized based on modelling frameworks. That is, Abdulla et al (2017) and Alfano and Sacco (2006) developed interface models based on pure damage mechanics, and similar interface models are also available in Abaqus, but are limited by the exclusion of frictional resistance, which is important in the simulation of mortar joints subjected to sliding (Mode II) displacements. Abdulla et al. (2017) addressed this issue by simply adding the frictional contact model (Abaqus, 2014) to the interface model (Camanho and Dávila, 2002) for their simulation. This approach appears to provide a simple and straightforward solution, but the determination of the damage parameter and its correlation with other quantities in a mixed-mode fracture scenario is problematic. To address these limitations, Alfano and Sacco (2006) developed a new interface model combing damage and frictional components. However, this approach did not consider the effect of several critical characteristics of mortar joint that have been observed in experimental studies, such as permanent plastic deformation and dilation (Andreotti et al. 2006).

Interface models for masonry joints have also been proposed based on the plasticity framework considering non-associated flow rules to allow for representation of dilation and the Coulomb frictional criterion (Nazir and Dhanasekar, 2014). An initial attempt was made by Lotfi and Shing (1994) who represented the mixed mode (Mode I and Mode II) behaviour of interface by a smooth hyperbolic curve. Subsequently, Lourenco and Rots (1997) proposed a multi-surface interface model consisting of a Mohr-Coulomb type friction surface with tension cut-off and a compression cap to indirectly simulate brick crushing failure. This model has become popular and has been used/modified by other researchers, e.g. Chaimoon and Attard (2007) who simplified the elliptic shape of the compressive cap into a diagonal flat surface for more convenient numerical implementation. Although the multi-surface yield function provides an improved physical representation, numerical implementation is challenging because stress return mapping can encounter convergence issues near corners produced by the intersection of multiple surfaces. This issue can be avoided by replacing corner regions with smooth curves or using a smooth closed yield surface (without corners) for modelling all failure modes (tension, shear and compression). Such attempts were made by (Citto 2008; Kumar and Amirtham, 2014) to simulate masonry joints using a tear drop shaped yield surface. However, the formulation of these closed yield surfaces are usually complicated and may result in serious numerical divergence problems (Kumar and Barbato, 2019) due to their cumbersome derivatives. A pure plasticity model does not consider stiffness degradation caused by the damage forms in mortar joints, which is important especially when the material is under cyclic loading conditions with an unloading-reloading scenario.

An interface model that considers both damage and plasticity, and their interaction should be capable of capturing a more realistic response of masonry joints. Thus, attempts such as those by (Minga et al. 2018; Spada et al. 2009; Yuen et al. 2019) have been made to develop coupled

damage-plasticity based models for the mortar joints, but the number of such models is limited and existing approaches have limitations. For example, the models proposed by Minga et al. (2018) and Spada et al. (2009) used multi-surface yield functions, with flat surfaces that produced sharp corners with discontinuities. This is avoided in the work of Yuen et al. (2019) by taking a smooth hyperbolic yield surface, but the implementation of the model is restricted to the forward Euler integration technique, which requires very small load steps, leading to high computational costs in large scale structural simulation, and potential divergence since this integration technique is not unconditionally stable. There is, therefore, a need for the development of an interface model for masonry joints considering the effects of damage, plasticity and their coupling, the development of which is presented here.

A damage-plasticity based model can be derived using two different formulations: one within nominal stress space, and the other within effective stress space. In the nominal stress based formulation, the evolution of plastic deformations and damage are taken simultaneously, and both are incorporated in the yield function, where all variables related to damage and plasticity are updated within a load increment using a single stage of analysis. This approach is followed by Spada et al. (2009) for masonry and others such as Nguyen et al. (2017) for applications such as geo-mechanics interface problems. In the other approaches based on effective stress, the coupled damage-plasticity model is decoupled algorithmically (not physical decoupling) in two stages: the plasticity component in first stage of analysis, and damage component in second stage of analysis. The yield function used in first stage does not include damage and a separate function for damage is applied in the second stage. The major benefit of this approach is that the plasticity formulation is simplified, and in the present case since, because the interface possesses only a softening response, becomes elastic-perfectly plastic. This approach is followed by Minga et al. (2018) for interface modelling as well as others for continuum modelling (e.g. Caballero et al. 2008; Grassl and Jirásek, 2006; Valentini and Hofstetter, 2013). The interface model developed in this study is based on effective stresses, and employs a smooth hyperbolic yield surface as introduced by Caballero et al. (2008) for simulating the concrete cracking. This is in contrary to the multi-surface yield function comprising flat surfaces used by Minga et al. (2018). In addition, a new generic formulation is presented in this paper which includes key improvements related to degradation of the dilation coefficient, which is incorporated using an energy based evolution equation. This inclusion is significant as it both captures physical behaviour and improves convergence stability as demonstrated with numerical examples.

5.2 Formulation of the constitutive model

The mechanism of crack formation and widening in masonry joints and other quasi-brittle materials such as concrete is presented in **Fig. 5-1**. At the initial stage of loading, micro-cracks develop in the mortar (or cement) matrix (**Fig. 5-1b**) and de-bonding of aggregate-cement interfaces (for concrete). Here the loading is represented by relative displacement (u) of the mortar joint (rather than strain) because a traction-separation relationship is commonly used for interface modelling. With further loading, these micro-cracks propagate and combine together to form macro-cracks (**Fig. 5-1c**). The degree of cracking can be conveniently characterised with a damage parameter D, which is the ratio of damaged area A_d (**Fig. 5-1c**) and the initial intact area A_0 (**Fig. 5-1a**) i.e. $D = A_d/A_0$. For a damaged joint under the action

of a force F (**Fig. 5-1c**), the stress on the undamaged area $A_u = A_0 - A_d$ is defined as effective stress $\bar{\sigma} = F/A_u$, while the stress on the gross area A_0 is defined as nominal stress $\sigma = F/A_0$, and they can be related with the damage parameter D as $\sigma = (1 - D)\bar{\sigma}$. Experimental tests (Van der Pluijm 1993; Van der Pluijm 1997) show a predominantly softening response (σ vs u) of mortar joints with negligible hardening behaviour (**Fig. 5-1d**) under tension and shear, which are the primary failure modes. In this scenario, it can therefore be assumed that the softening of nominal stress σ is entirely produced by the damage D while the effective stress $\bar{\sigma}$ remains constant (**Fig. 5-1d**). This assumption is beneficial when the effective stress space is used for constitutive modelling because the effective stress-displacement (relative) relationship is elastic-perfectly-plastic leading to no expansion/contraction of the yield surface. The formulation developed here will be based on this concept, and includes two algorithmically uncoupled steps: a plasticity based modelling stage followed by a damage based modelling stage.

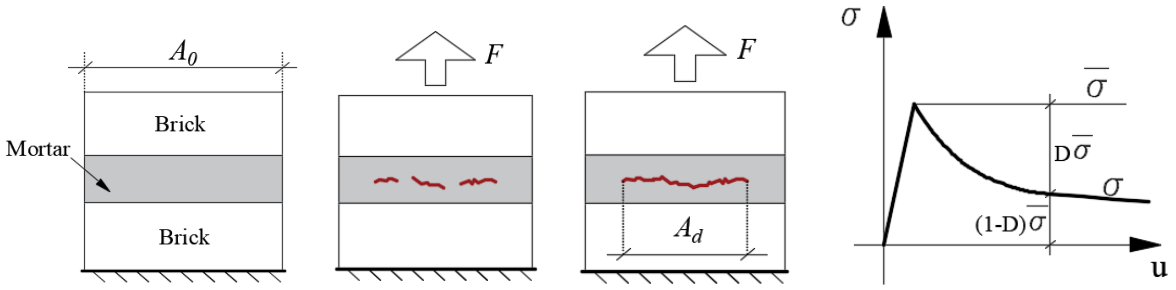

(a) intact masonry specimen

(b) micro-cracks (initial stage of loading)

(c) macro crack (further loading)

(d) stress (σ or $\bar{\sigma}$) – relative displacement (u) relation

Fig. 5-1 Cracking mechanism in masonry joints and definition of nominal/effective stress

For 3D modelling, the interface possesses three stress/traction components (one normal and two shear), which can be defined as nominal and effective stresses. As before, each component can be described based on a uniaxial loading scenario as follows.

$$\begin{Bmatrix} \sigma_n \\ \sigma_{s1} \\ \sigma_{s2} \end{Bmatrix} = \begin{bmatrix} 1 - D_n & 0 & 0 \\ 0 & 1 - D_s & 0 \\ 0 & 0 & 1 - D_s \end{bmatrix} \begin{Bmatrix} \overline{\sigma}_n \\ \overline{\sigma}_{s1} \\ \overline{\sigma}_{s2} \end{Bmatrix} \tag{5.1}$$

$$\{\sigma\} = ([I] - [D])\{\bar{\sigma}\}$$

where $[I]$ is the unit matrix and the subscripts are used to indicate normal (n) and shear ($s1$ and $s2$) components.

The traction-separation relationship (in elastic range) for a 3D interface is written in the effective stress space as:

$$\begin{Bmatrix} \overline{\sigma}_n \\ \overline{\sigma}_{s1} \\ \overline{\sigma}_{s2} \end{Bmatrix} = \begin{bmatrix} K_n^0 & 0 & 0 \\ 0 & K_s^0 & 0 \\ 0 & 0 & K_s^0 \end{bmatrix} \begin{Bmatrix} u_n \\ u_{s1} \\ u_{s2} \end{Bmatrix}; \quad \{\bar{\sigma}\} = [K^0]\{u\} \tag{5.2}$$

where K_n^0 and K_s^0 are elastic stiffness components of the interface in normal and shear directions.

5.2.1 Plasticity formulation of the interface

The constitutive model of a masonry joint/interface with a smooth hyperbolic yield surface *F* (**Fig. 5-2**) can be described as:

$$F = -(C - \overline{\sigma}_n tan\phi) + \sqrt{(\overline{\sigma}_{s1})^2 + (\overline{\sigma}_{s2})^2 + (C - \chi tan\phi)^2} \tag{5.3}$$

where *C* is the cohesive shear strength, $tan\phi$ is the frictional coefficient, and χ is the cohesive tensile strength of the interface. This yield surface is adopted from Caballero et al. (2008) who developed an accurate and robust interface model, but followed a different formulation to that developed here in that they implemented a pure plasticity based model with no damage. Additionally, the yield surface of Caballero et al. (2008) is expressed in nominal stress space in which the strength parameters (*C,* $tan\phi$, andχ) degrade, in the present formulation these parameters remain constant because the effective stresses are elastic-perfectly-plastic.

In order to avoid overestimation of the dilation angle, a non-associate flow rule is adopted by taking a plastic potential Q (**Fig. 5-2**) that is different from the yield surface. The expression of the potential surface is given in **Eq. (5.4)**, which is similar to the yield surface (hyperbolic), but in which the dilation angle ϕ_Q is different from friction angle ϕ.

$$Q = -\left(C_Q - \overline{\sigma}_n tan\phi_Q\right) + \sqrt{(\overline{\sigma}_{s1})^2 + (\overline{\sigma}_{s2})^2 + (C_Q - \chi tan\phi_Q)^2} \tag{5.4}$$

Similar to the yield function, the strength parameters of the plastic potential are constant except for the dilation angle ϕ_Q. This outcome is based on experimental observation of shear couplets under compression by Chaimoon (2007), who classified the evolution of dilation ($tan\phi_Q = du_n^p/du_s^p$) into two forms (**Fig. 5-3**): one with a constant residual dilation angle and the other with zero dilation angle.

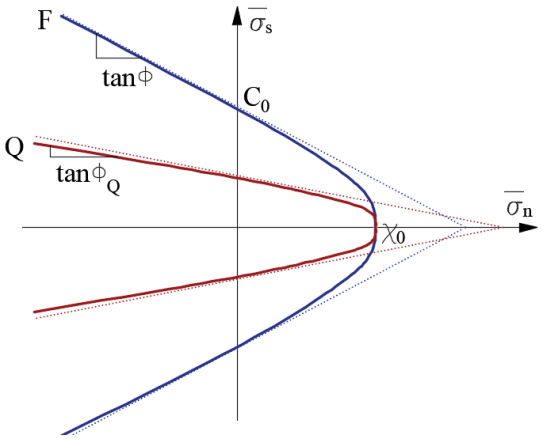

Fig. 5-2 Yield and potential surfaces ($\bar{\sigma}_s = \sqrt{(\bar{\sigma}_{s1})^2 + (\bar{\sigma}_{s1})^2}$)

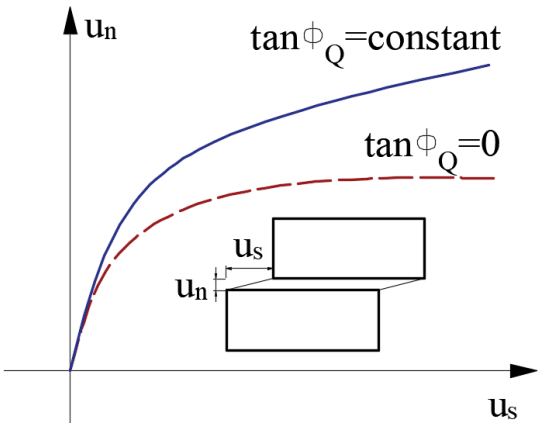

Fig. 5-3 Variation of dilation coefficient in masonry joints (Chainmoon 2007)

The variation of dilation coefficient $tan\phi_Q$ plays an important role in the stress return mapping procedure during numerical implementation because the potential surface (**Fig. 5-2**) controls the direction of plastic flow $\{m\} = \partial Q/\partial\{\bar{\sigma}\}$, which is followed to return the stress (plastic corrector) from its trial point (elastic predictor) to the yield surface. In many existing interface models [31, 38, 44], the dilation coefficient $tan\phi_Q$ is kept constant and assigned a small value close to zero, which is reasonable for masonry joints. The non-physical parameter C_Q is typically assigned a value around 10~100 times of the value of C (as listed in below table) because if taken to be too small, when combined with the very small value of the dilation angle ϕ_Q, the potential surface becomes extremely narrow leading to convergence difficulties. This issue is not encountered in the model developed by Lourenco and Rots (1997) who used same value for C_Q and C, with the difference being that Lourenco and Rots (1997) is a multi-surface model with a flat Coulomb type frictional surface.

	$tan\phi$	$tan\phi_Q$	C (MPa)	C_Q (MPa)
Caballero et al. (2008)	0.2	0.002	7	84
Macorini and Izzuddin (2013)	0.75	0.001	0.375	37.5
Kumar and Barbato (2019)	0.75	0.001	0.3625	18.125

The model proposed here has the benefit of using same value for C_Q and C, and this is achieved by taking a higher dilation angle ϕ_Q at the beginning and gradually degrading its value with the progression of shear sliding. This strategy is motivated by the physical observation from the testing conducted by Chaimoon (2007) (**Fig. 5-3**). The evolution of the dilation coefficient $tan\phi_Q$ is taken in the following form:

$$tan\phi_Q = \begin{cases} tan\phi_{Q0} & W^p < 0 \\ tan\phi_{Q0} - \left(tan\phi_{Q0} - tan\phi_{Qr}\right)\left(\frac{1}{2} - \frac{1}{2}\cos\left(\frac{\pi W^p}{G_{fs}}\right)\right) & 0 \le W^p \le G_{fs} \\ tan\phi_{Qr} & W^p > G_{fs} \end{cases} \quad (5.5)$$

where $tan\phi_{Q0}$ and $tan\phi_{Qr}$ are initial and residual dilation coefficients respectively, and G_{fs} is the fracture energy of the mortar joint under shear. The above equation provides a smooth degradation of the dilation coefficient maintain slope continuity at the ends, which also helped to improve convergence performance in Caballero et al. (2008).

Due to the elastic-perfectly-plasticity behaviour of the effective stresses, the shape of the yield surface will not be changed (no hardening/softening) but the potential surface can be changed due to evolution of the dilation angle ϕ_Q, which is determined by using an internal variable. For this purpose, the energy dissipation due to plastic work ($W^p = \int dW^p$) is used, and this is also required to determine the damage parameter used for the second stage of modelling presented in next section. The plastic work increment is calculated using effective stresses and plastic displacement (relative) increments of the interface:

$$dW^p = \begin{cases} \overline{\sigma}_n du_n^p + \overline{\sigma}_{s1} du_{s1}^p + \overline{\sigma}_{s2} du_{s2}^p & \overline{\sigma}_n \ge 0 \\ \sqrt{\left(du_{s1}^p\right)^2 + \left(du_{s2}^p\right)^2}\left(\sqrt{(\overline{\sigma}_{s1})^2 + (\overline{\sigma}_{s2})^2} + \overline{\sigma}_n tan\phi\right) & \overline{\sigma}_n < 0 \end{cases} \quad (5.6)$$

The calculation of plastic work is different if the direction of normal stress on the interface is reversed. That is, for tensile normal stress ($\overline{\sigma}_n \ge 0$), the plastic work includes energy dissipations by both normal and shear stresses. However, if the interface is under compression ($\overline{\sigma}_n < 0$), the normal stress will not contribute because of crack closure, but the energy dissipated by the frictional effect ($\overline{\sigma}_n tan\phi\sqrt{\left(du_{s1}^p\right)^2 + \left(du_{s2}^p\right)^2}$) should be included, in addition to usual contributions by the shear stresses.

5.2.2 Damage formulation of the interface

The damage of the interface is characterised using three damage parameters, corresponding to the three modes of failure. These consist of the tensile mode and two shear modes considering elastic behaviour under compressive loading. Thus the model is not based on a unified scalar damage parameter, but the two shear modes have the same damage parameter $D_s = D_{s1} = D_{s2}$ while a different damage parameter D_n ($\neq D_s$) is used for loading in the normal direction. The use of different damage parameters provides a more realistic representation than that achieved using a scalar damage based model such as those often used for isotropic materials. The use of multiple damage parameters is motivated by the experimental observations of Pluijm (1993, 1997), which showed that the fracture energy of mortar joints in tensile mode G_{ft} is much lower

than its fracture energy in shear mode G_{fs}. The idea of using different damage parameters is reinforced further by considering the damage behaviour of orthotropic materials such as wood (Pech et al. 2021), concrete (Meschke et al. 1998) and composites (Sheikh et al. 2009), where it is observed that the damage scenario is more complex due to different material properties in different directions.

The plastic work W^p computed in the previous plasticity stage of the modelling is used to define the evolution of damage parameters of mortar joints. The damage parameters for uniaxial tension (d_n) and shear (d_s) are expressed as follows:

$$d_n = \begin{cases} 0 & W^p < 0 \\ \frac{1}{2} - \frac{1}{2}\cos\left(\frac{\pi W^p}{G_{ft}}\right) & 0 \le W^p \le G_{ft} \\ 1 & W^p > G_{ft} \end{cases} \quad (5.7) \qquad d_s = \begin{cases} 0 & W^p < 0 \\ \frac{1}{2} - \frac{1}{2}\cos\left(\frac{\pi W^p}{G_{fs}}\right) & 0 \le W^p \le G_{fs} \\ 1 & W^p > G_{fs} \end{cases} \quad (5.8)$$

Fig. 5-4 shows a gradual smooth evolution process of the damage parameters; this arises due to the use of a cosine function (**Eqs. (5.7) and (5.8)**) and benefits convergence stability.

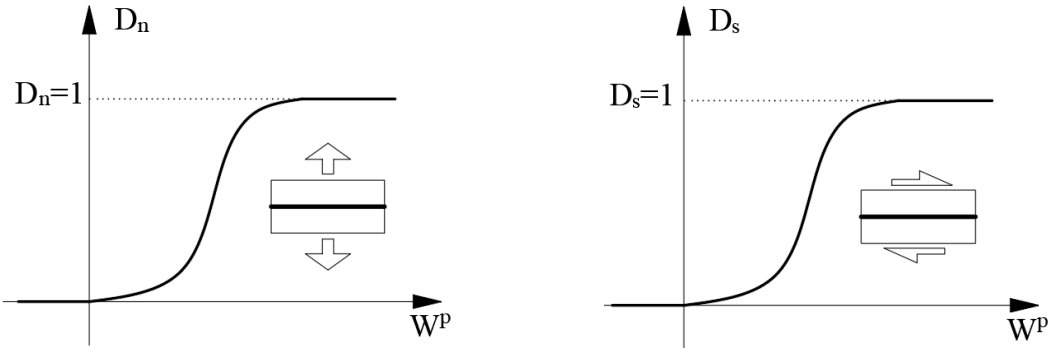

(a) uniaxial tensile damage (b) uniaxial shear damage

Fig. 5-4 Damage evolution of masonry joints under uniaxial a) tension and b) shear

The expression for the damage parameter d_n (**Eq. (5.7)**) is also applicable for masonry joints under mixed mode loading that includes tension and shear ($D_n = d_n$), but is not suitable for compressive loading. Similarly, the expression for d_s (**Eq. (5.8)**) is applicable for an interface under shear and tension ($D_s = d_s$) but is not be applicable for shear with compression. In cases involving compression, the damage corresponding to normal direction will be zero ($D_n = 0$) since the compressive behaviour is elastic due to crack closure, while the damage corresponding to shear D_s will not reach 1 because of frictional resistance caused by the lateral compression. This outcome is demonstrated in **Fig**. 5-5, where **Fig**. 5-5**a** shows the degradation of the shear resistance up to its frictional resistance ($-\overline{\sigma}_n tan\phi$), and **Fig**. 5-5**b** shows the

evolution of D_s, which is capped by its maximum value $D_{s,max}$ (<1). **Fig**. 5-5**c** helps to quantify the maximum value $D_{s,max} = \frac{C}{\overline{\sigma}_s} = \frac{C}{C-\sigma_n tan\phi} = \frac{C}{C+|\overline{\sigma}_n|\ tan\phi}$. It is to be noted that the effective normal stress is the same as the nominal normal stress under compression ($\overline{\sigma}_n = \sigma_n$). Also, the frictional coefficient $\tan\phi$ is assumed to be constant with no degradation in any situation, which is based on the study of Yuen et al. (2019) who compiled a series of shear test results of masonry specimens under pre-compression. Thus, the damage parameters for all loading scenarios can be expresses as

$$D_n = \begin{cases} d_n & \overline{\sigma}_n \geq 0 \\ 0 & \overline{\sigma}_n < 0 \end{cases} \qquad (5.9)$$

$$D_s = \begin{cases} d_s & \overline{\sigma}_n \geq 0 \\ \dfrac{C}{C + |\overline{\sigma}_n|\ tan\phi} d_s & \overline{\sigma}_n < 0 \end{cases} \qquad (5.10)$$

Finally, the damage parameter matrix as presented in **Eq. (5.9)** can be determined, which is utilised to compute nominal stresses from effective stresses with the help of **Eq. (5.1)**.

$$[D] = \begin{bmatrix} D_n & 0 & 0 \\ 0 & D_s & 0 \\ 0 & 0 & D_s \end{bmatrix} \qquad (5.11)$$

.

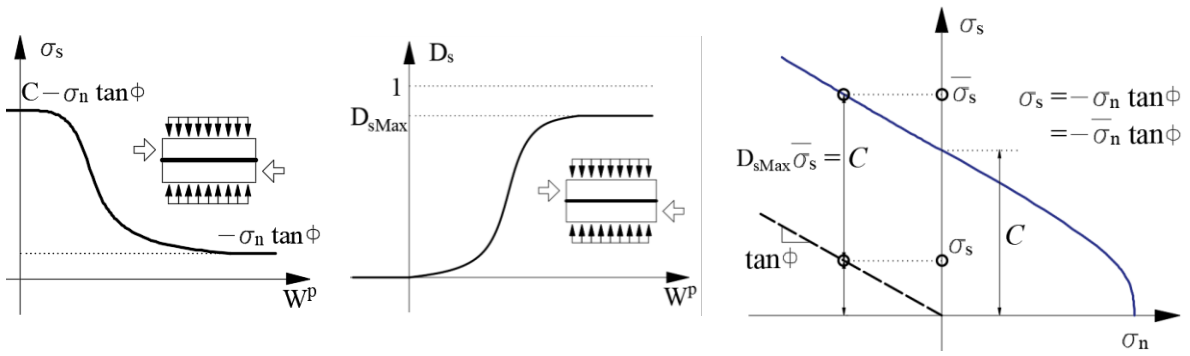

(a) degradation of shear resistance

(b) evolution of damage in shear

(c) yield surfaces during frictional sliding

Fig. 5-5 Cohesive-frictional behaviour of masonry joints under compression and shear

.

5.3 Numerical implementation

In a damage-plasticity model where damage and plasticity are decoupled algorithmically (not physically), numerical implementation involves two main phases:

1) Transfer of nominal stresses (converged) from the previous load step $\{\sigma\}^t$ to effective stresses $\{\bar{\sigma}\}^t$. These nominal stresses are then updated using an elastic predictor-plastic corrector strategy to compute effective stress of the current step $\{\bar{\sigma}\}^{t+1}$;

2) In the second phase the damage parameters $[D]^{t+1}$ are updated using the plastic work $W^{p,t+1}$ computed in previous phase. Effective stresses $\{\bar{\sigma}\}^{t+1}$ are then transferred to the nominal stresses of the current time step $\{\sigma\}^{t+1}$. Finally, the updated quantities are used to compute the consistent tangent operator (CTO) needed for global level FE analysis of the masonry structure.

Fig. 5-6 provides a simple demonstration of the procedure where parameters with superscripts "*t*" and "*t+1*" represent values at the end of previous and current time steps, respectively. Though time step is a common terminology in nonlinear analysis, it is to be noted that they are load steps in the present study dealing with nonlinear static analysis of masonry structures.

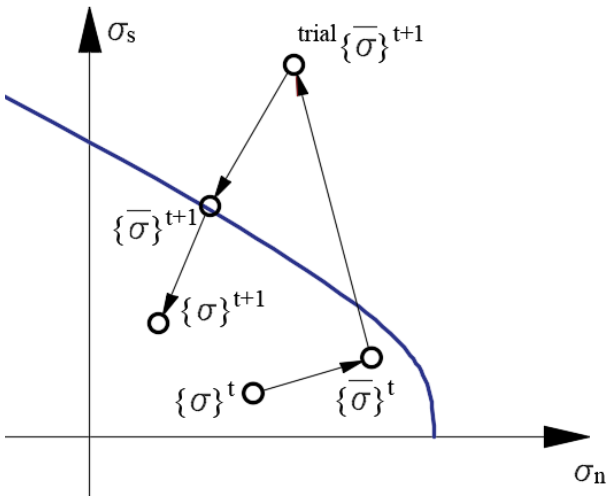

Fig. 5-6 Procedure for the numerical implementation

The procedure for updating effective stresses at the current step can be nonlinear if the elastic predictor providing the trial stress ${}^{trial}\{\bar{\sigma}\}^{t+1}$ moves outside of the elastic domain ($F\left({}^{trial}\{\bar{\sigma}\}^{t+1}, W^p\right) > 0$) and involve plastic deformations. In this case, a fully implicit backward Euler method is applied to integrate the nonlinear constitutive model using a closest point projection method (CPPM) iteratively with the aid of Newton-Raphson (NR) iteration technique. The maximum value of a damage parameter is restricted to 0.999 (not 1.0) in order to avoid numerical issues in estimating the effective stress $\{\bar{\sigma}\}^t$ (**Eq. (5.1)**) that will drift the elastic trial stress ${}^{trial}\{\bar{\sigma}\}^{t+1}$ far away from the yield surface.

5.3.1 Backward Euler Integration scheme

The incremental displacement (relative) of the current time step $\{du\}^{t+1}$ can be split into elastic and plastic components according to $\{du\}^{t+1} = \{du^e\}^{t+1} + \{du^p\}^{t+1}$. The elastic

displacement increment can be written as $\{du^e\}^{t+1} = \{du\}^{t+1} - \{du^p\}^{t+1}$, which is utilized to express the stress at time *t*+1 according to backward Euler integration technique:

$$\{\bar{\sigma}\}^{t+1} = \{\bar{\sigma}\}^{t} + \{d\bar{\sigma}\}^{t+1} = \{\bar{\sigma}\}^{t} + [K^0](\{du\}^{t+1} - \{du^p\}^{t+1}) \tag{5.12}$$

Eq. (5.12) can also be expressed in terms of elastic predictor and plastic corrector as:

$$\{\bar{\sigma}\}^{t+1} = (\{\bar{\sigma}\}^{t} + [K^0]\{du\}^{t+1}) - [K^0]\{du^p\}^{t+1} \tag{5.13}$$

where the first part of the equation gives the trial stress ${}^{trial}\{\bar{\sigma}\}^{t+1}$=$(\{\bar{\sigma}\}^{t} + [K^0]\{du\}^{t+1})$ as an elastic predictor, and the last part $-[K^0]\{du^p\}^{t+1}$ is the plastic corrector. The plastic displacement increment $\{du^p\}^{t+1}$ can be determined using the potential function Q (**Eq. (5.4)**) as follows:

$$\{du^p\}^{t+1} = d\lambda \frac{\partial Q}{\partial \{\bar{\sigma}\}} = d\lambda \{m\}^{t+1}$$

$$\{m\}^{t+1} = \begin{Bmatrix} m_n \\ m_{s1} \\ m_{s2} \end{Bmatrix}^{t+1} = \begin{Bmatrix} \dfrac{tan\phi_Q}{\sqrt{(\overline{\sigma}_{s1})^2 + (\overline{\sigma}_{s2})^2 + \left(C_Q - \chi_0 tan\phi_Q\right)^2}} \\ \dfrac{\overline{\sigma}_{s1}}{\sqrt{(\overline{\sigma}_{s1})^2 + (\overline{\sigma}_{s2})^2 + \left(C_Q - \chi_0 tan\phi_Q\right)^2}} \\ \dfrac{\overline{\sigma}_{s2}}{\sqrt{(\overline{\sigma}_{s1})^2 + (\overline{\sigma}_{s2})^2 + \left(C_Q - \chi_0 tan\phi_Q\right)^2}} \end{Bmatrix}^{t+1} \tag{5.14}$$

Substitution of **Eq. (5.14)** in **Eq. (5.13)** gives the key equation for stress return mapping:

$$\{\bar{\sigma}\}^{t+1} = {}^{trial}\{\bar{\sigma}\}^{t+1} - d\lambda^{t+1}[K^0]\{m\}^{t+1} \tag{5.15}$$

In addition to the three equations in **Eq. (5.15)** which correspond to the three stress components, the full consistency condition of the yield function presented in **Eq. (5.16)** is used to obtain the fourth equation needed to solve the four unknowns (three stresses and the incremental plastic multiplier $d\lambda^{t+1}$).

$$F(\{\bar{\sigma}\}^{t+1}) = 0 \text{ with } d\lambda^{t+1} \geq 0 \tag{5.16}$$

In **Eq. (5.15)** and **(5.16)**, the unknown variables ($\{\bar{\sigma}\}^{t+1}$, $d\lambda^{t+1}$) are implicit within the backward Euler integration system. Thus, the solution of this system requires an iterative process, which is realized using the Newton-Raphson (NR) technique. For this purpose, **Eqs. (15) and (16)** are expressed in residual form $\{r\}^j$:

$$\{r\}^j = \begin{Bmatrix} \{r_\sigma\} \\ r_{d\lambda} \end{Bmatrix}^j = \begin{Bmatrix} \{\bar{\sigma}\}^j - {}^{trial}\{\bar{\sigma}\}^{t+1} + d\lambda^j [K^0]\{m\}^j \\ F(\{\bar{\sigma}\}^j) \end{Bmatrix} \tag{5.17}$$

where *j* indicates the iteration number and all unknowns of the current time step *t*+1 will be iteratively updated. Thus the superscript *t*+1 of these unknown variables (**Eqs. (15) and (16)**) are replaced with *j*. The known converged values of the variables obtained at the end of previous time step *t* remain constant during the iteration. The iterative process is continued until the variables at the current time step are converged. Convergence is checked by calculating the maximum value of the norm using residuals for stress components and the absolute value of the incremental plastic multiplier, and comparing it with a predefined small tolerance value (*TOL*) as follows:

$$\|r\|_\infty = Max(\|\{r_\sigma\}\|, |r_{d\lambda}|) < TOL \tag{5.18}$$

Once the above condition is satisfied for a specific value of *j*, the NR iteration stops and all unknown variables $\{\sigma\}^j$, $d\lambda^j$ are replaced with $\{\sigma\}^{t+1}$, $d\lambda^{t+1}$ and the process is stepped forward to the next time step. If convergence is not achieved, the known variables are updated using **Eq. (5.19)**.

$$\begin{bmatrix} \{\bar{\sigma}\} \\ d\lambda \end{bmatrix}^{j+1} = \begin{bmatrix} \{\bar{\sigma}\} \\ d\lambda \end{bmatrix}^j + \begin{bmatrix} \delta\{\bar{\sigma}\} \\ \delta d\lambda \end{bmatrix}^{j+1} = \begin{bmatrix} \{\bar{\sigma}\} \\ d\lambda \end{bmatrix}^j - \left([\mathrm{J}]^j\right)^{-1}\{r\}^j \tag{5.19}$$

The Jacobian [J] used in the above equation (superscript *j* is omitted for simplicity) is the gradient of the residual vector:

$$[\mathrm{J}] = \frac{\partial\{r\}(\{\bar{\sigma}\}, d\lambda)}{\partial(\{\bar{\sigma}\}, d\lambda)} = \begin{bmatrix} [I] + d\lambda[K^0]\dfrac{\partial\{m\}}{\partial\{\bar{\sigma}\}} & [K^0]\{m\} \\ \dfrac{\partial F}{\partial\{\bar{\sigma}\}} & 0 \end{bmatrix} \tag{5.20}$$

where

$$\{n\} = \frac{\partial F}{\partial\{\overline{\sigma}\}} = \begin{Bmatrix} tan\phi \\ \dfrac{\overline{\sigma}_{s1}}{\sqrt{(\overline{\sigma}_{s1})^2 + (\overline{\sigma}_{s2})^2 + (C_0 - \chi_0 tan\phi)^2}} \\ \dfrac{\overline{\sigma}_{s2}}{\sqrt{(\overline{\sigma}_{s1})^2 + (\overline{\sigma}_{s2})^2 + (C_0 - \chi_0 tan\phi)^2}} \end{Bmatrix} \tag{5.21}$$

$$\left[\frac{\partial\{m\}}{\partial\{\overline{\sigma}\}}\right] = \begin{bmatrix} 0 & 0 & 0 \\ 0 & \dfrac{\overline{\sigma}_{s2}{}^2 + \left(C_Q - \chi_0 tan\phi_Q\right)^2}{\left(\overline{\sigma}_{s1}{}^2 + \overline{\sigma}_{s2}{}^2 + \left(C_Q - \chi_0 tan\phi_Q\right)^2\right)} & \dfrac{-\overline{\sigma}_{s1}\overline{\sigma}_{s2}}{\left(\overline{\sigma}_{s1}{}^2 + \overline{\sigma}_{s2}{}^2 + \left(C_Q - \chi_0 tan\phi_Q\right)^2\right)} \\ 0 & \dfrac{-\overline{\sigma}_{s1}\overline{\sigma}_{s2}}{\left(\overline{\sigma}_{s1}{}^2 + \overline{\sigma}_{s2}{}^2 + \left(C_Q - \chi_0 tan\phi_Q\right)^2\right)} & \dfrac{\overline{\sigma}_{s1}{}^2 + \left(C_Q - \chi_0 tan\phi_Q\right)^2}{\left(\overline{\sigma}_{s1}{}^2 + \overline{\sigma}_{s2}{}^2 + \left(C_Q - \chi_0 tan\phi_Q\right)^2\right)} \end{bmatrix} \tag{5.22}$$

Once the convergence is achieved ($\|r\|_\infty < TOL$), the incremental plastic work for the current time step is calculated using **Eq. (5.6)**:

$$dW^p = \begin{cases} d\lambda(\overline{\sigma}_n m_n + \overline{\sigma}_{s1} m_{s1} + \overline{\sigma}_{s2} m_{s2}) & \overline{\sigma}_n \geq 0 \\ d\lambda\sqrt{(m_{s1})^2 + (m_{s2})^2}\left(\sqrt{(\overline{\sigma}_{s1})^2 + (\overline{\sigma}_{s2})^2} + \overline{\sigma}_n tan\phi\right) & \overline{\sigma}_n < 0 \end{cases} \tag{5.23}$$

It is to be noted that the converged values of $\{\bar{\sigma}\}^{t+1}, \{m\}^{t+1}, d\lambda^{t+1}$ are used in **Eq. (5.23)** to calculate $dW^p = dW^{p,t+1}$, which is used to update of plastic work:

$$W^{p,t+1} = W^{p,t} + dW^{p,t+1} \tag{5.24}$$

5.3.2 Consistent tangent operator (CTO) of the damage-plastic model

The use of a consistent tangent stiffness operator (CTO) is critical for improving the computational efficiency when a full Newton Raphson technique is applied at the global (structural) level. For the proposed damage-plastic based interface model, the CTO is written in terms of effective stress and damage parameter using **Eq. (5.1)**:

$$\frac{\partial\{\sigma\}^{t+1}}{\partial\{du\}^{t+1}} = \frac{\partial\left(([I]-[D]^{t+1})\{\bar{\sigma}\}^{t+1}\right)}{\partial\{du\}^{t+1}} = ([I]-[D]^{t+1})\frac{\partial\{\bar{\sigma}\}^{t+1}}{\partial\{du\}^{t+1}} - \left(\frac{\partial[D]^{t+1}}{\partial\{du\}^{t+1}}\right)^{\mathrm{T}}\{\bar{\sigma}\}^{t+1} \quad (5.25)$$

where $\frac{\partial\{\bar{\sigma}\}^{t+1}}{\partial\{du\}^{t+1}}$ can be regarded as the CTO of the plasticity component of the model expressed in effective stress space $\{\bar{\sigma}\}^{t+1}$. This can be derived by taking derivative of **Eqs. (5.15) and (5.16)** with respect to the displacement increment $\{du\}^{t+1}$ and their re-arrangement in the following form:

$$\frac{\partial}{\partial\{du\}^{t+1}}\begin{bmatrix}\{\bar{\sigma}\}^{t+1} + d\lambda^{t+1}[K^0]\{m\} \\ F(\{\bar{\sigma}\}^{t+1})\end{bmatrix} = \frac{\partial}{\partial\{du\}^{t+1}}\begin{bmatrix}\{\bar{\sigma}\}^{t} + [K^0]\{du\}^{t+1} \\ 0\end{bmatrix} \quad (5.26)$$

The derivative on the left hand side (LHS) of the above equation is expressed in terms of $\{\bar{\sigma}\}^{t+1}$ and λ^{t+1} using chain rule, while the right hand side (RHS) will retain elastic stiffness matrix $[K^0]$ only as $\{\bar{\sigma}\}^{t}$ is constant at current time step:

$$\frac{\partial}{\partial(\{\bar{\sigma}\}^{t+1}, d\lambda^{t+1})}\begin{bmatrix}\{\bar{\sigma}\}^{t+1} + d\lambda^{t+1}[K^0]\{m\} \\ F(\{\bar{\sigma}\}^{t+1})\end{bmatrix}\frac{\partial(\{\bar{\sigma}\}^{t+1}, d\lambda^{t+1})}{\partial\{du\}^{t+1}} = \begin{bmatrix}[K^0] \\ [0]\end{bmatrix} \quad (5.27)$$

Following **Eq. (5.20)**, the left hand side (LHS) of the above equation is modified further and is expressed in terms of Jacobian:

$$[\mathrm{J}]^{t+1}\begin{bmatrix}\left[\frac{\partial\{\bar{\sigma}\}^{t+1}}{\partial\{du\}^{t+1}}\right] \\ \left[\frac{\partial d\lambda}{\partial\{du\}^{t+1}}\right]\end{bmatrix} = \begin{bmatrix}[K^0] \\ [0]\end{bmatrix} \quad (5.28)$$

Now the CTO for the plasticity component is written using a projection matrix $[P] = \begin{bmatrix}1 & 0 & 0 & 0 \\ 0 & 1 & 0 & 0\end{bmatrix}^T$:

$$\left[\frac{\partial\{\bar{\sigma}\}^{t+1}}{\partial\{du\}^{t+1}}\right] = [P]^T([\mathrm{J}]^{t+1})^{-1}[P][K^0] \quad (5.29)$$

The derivative of the damage parameter with respect to the increment of displacement $\frac{\partial[D]^{t+1}}{\partial\{du\}^{t+1}}$ in **Eq. (5.25)** is expressed using chain rule in the following form:

$$\frac{\partial[D]^{t+1}}{\partial\{du\}^{t+1}} = \frac{\partial[D]^{t+1}}{\partial W^{p,t+1}} \frac{\partial W^{p,t+1}}{\partial d\lambda^{t+1}} \frac{\partial d\lambda^{t+1}}{\partial\{du\}^{t+1}} \tag{5.30}$$

The last term of **Eq. (5.30)** $\frac{\partial d\lambda^{t+1}}{\partial\{du\}^{t+1}}$ is readily available from **Eq. (5.28)**, and the second term can be derived using **Eqs. (5.23) and (5.24)**:

$$\frac{\partial W^{p,t+1}}{\partial d\lambda^{t+1}} = \frac{\partial(W^{p,t} + dW^{p,t+1})}{\partial d\lambda^{t+1}} = \frac{\partial(dW^{p,t+1})}{\partial d\lambda^{t+1}}$$

$$\frac{\partial W^{p,t+1}}{\partial d\lambda^{t+1}} = \begin{cases} \overline{\sigma}_n m_n + \overline{\sigma}_{s1} m_{s1} + \overline{\sigma}_{s2} m_{s2} & \overline{\sigma}_n \geq 0 \\ \sqrt{(m_{s1})^2 + (m_{s2})^2}\left(\sqrt{(\overline{\sigma}_{s1})^2 + (\overline{\sigma}_{s2})^2} + \overline{\sigma}_n tan\phi\right) & \overline{\sigma}_n < 0 \end{cases} \tag{5.31}$$

Finally, **Eq.** (11) along with **Eqs. (5.7)-(5.10)** are used to determine the first term of **Eq. (5.30)**:

$$\frac{\partial[D]}{\partial W^p} = \begin{bmatrix} \frac{\partial D_n}{\partial W^p} & 0 & 0 \\ 0 & \frac{\partial D_s}{\partial W^p} & 0 \\ 0 & 0 & \frac{\partial D_s}{\partial W^p} \end{bmatrix} \tag{5.32}$$

where

$$\frac{\partial D_n}{\partial W^p} = \begin{cases} \frac{\partial d_n}{\partial W^p} & \overline{\sigma}_n \geq 0 \\ 0 & \overline{\sigma}_n < 0 \end{cases} \tag{5.33}$$

$$\frac{\partial D_s}{\partial W^p} = \begin{cases} \frac{\partial d_s}{\partial W^p} & \overline{\sigma}_n \geq 0 \\ \frac{C}{C + |\overline{\sigma}_n| \, tan\phi} \frac{\partial d_s}{\partial W^p} & \overline{\sigma}_n < 0 \end{cases} \tag{5.34}$$

$$\frac{\partial d_n}{\partial W^p} = \begin{cases} \frac{1}{2}\frac{\pi}{G_{ft}} \sin\left(\frac{\pi W^p}{G_{ft}}\right) & 0 \leq W^p \leq G_{ft} \\ 0 & W^p > G_{ft} \end{cases} \tag{5.35}$$

$$\frac{\partial d_s}{\partial W^p} = \begin{cases} \frac{1}{2}\frac{\pi}{G_{fs}} \sin\left(\frac{\pi W^p}{G_{fs}}\right) & 0 \leq W^p \leq G_{fs} \\ 0 & W^p > G_{fs} \end{cases} \tag{5.36}$$

Now the individual components of **Eq. (5.25)** are all obtained, which will be used to get the CTO for the damage plasticity based model proposed in this study. The tangent stiffness (CTO) usually does not affect the solution accuracy, but it improves the computational efficiency and robustness.

Numerical implementation procedure is summarized in below algorithm.

Algorithm for numerical implementation of interface model

1: Known converged variables from previous step: $W^{p,t}$; $\{\sigma\}^t$; $\{du\}^{t+1}$; $[D]^t$; $[K^0]$

2: Compute effective stress (current step - initial value): $\{\overline{\sigma}\}^t = \left\{\frac{\sigma_n^t}{1-D_n^t} \quad \frac{\sigma_{s1}^t}{1-D_S^t} \quad \frac{\sigma_{s2}^t}{1-D_S^t}\right\}$

3: Compute trial stress of the current step: ${}^{trial}\{\overline{\sigma}\}^{t+1} = \{\overline{\sigma}\}^t + [K^0]\{du\}^{t+1}$

4: Check for plastic yielding: ${}^{trial}F = F({}^{trial}\{\overline{\sigma}\}^{t+1}, \chi_0, C_0, tan\phi)$

5: Elastic status:

IF $\left({}^{trial}F \leq 0\right)$ **THEN**

Update current step variables: $\{\overline{\sigma}\}^{t+1} = {}^{trial}\{\overline{\sigma}\}^{t+1}$; $W^{p,t+1} = W^{p,t}$; $[K^{tan}] = [K^0]$; $[D]^{t+1} = [D]^t$

Compute nominal stress (current step – final value): $\{\sigma\}^{t+1} = ([I] - [D]^t)\{\overline{\sigma}\}^{t+1}$

6: Plastic status:

ELSE

$\{\overline{\sigma}\}^{j=0} = {}^{trial}\{\overline{\sigma}\}^{t+1}$; $\|r\|^{j=0} = 1$; $d\lambda^{j=0} = 0$

7: NR Loop

DO WHILE ($\|r\|^j >$ TOL)

8: Compute: $\{n\}^j; \{m\}^j; \left[\frac{\partial\{m\}}{\partial\{\overline{\sigma}\}}\right]; F^j$

9: Compute Jacobian $[\mathrm{J}]^j$ and its inverse matrix $\left([\mathrm{J}]^j\right)^{-1}$

10: Compute residual vector and its norm: $\{r\}^j$; $\|r\|^j$

11: Compute: $\begin{Bmatrix}\{\overline{\sigma}\}^{j+1} \\ d\lambda^{j+1}\end{Bmatrix} = \begin{Bmatrix}\{\overline{\sigma}\}^{j} \\ d\lambda^{j}\end{Bmatrix} - \left([\mathrm{J}]^j\right)^{-1}\{r\}^j$

$j = j + 1$

ENDDO

12: Compute: $dW^{p,t+1} = dW^p(\{\overline{\sigma}\}^j, \{m\}^j, d\lambda^j)$

Update current step variables: $\{\overline{\sigma}\}^{t+1} = \{\overline{\sigma}\}^j$; $W^{p,t+1} = W^{p,t} + dW^{p,t+1}$; $[D]^{t+1} = [D](W^{p,t+1})$

13: Compute CTO and nominal stress:

$[K^{tan}] = ([I] - [D])\frac{\partial\{\overline{\sigma}\}}{\partial\{du\}} - \left(\frac{\partial[D]}{\partial W^p}\frac{\partial W^p}{\partial d\lambda}\frac{\partial d\lambda}{\partial\{du\}}\right)^T\{\overline{\sigma}\}$; $\{\sigma\}^{t+1} = ([I] - [D]^{t+1})\{\overline{\sigma}\}^{t+1}$

ENDIF

.

5.4 Behaviour of the constitutive model using a single cohesive element

The constitutive model is implemented using an 8-node three-dimensional cohesive element (COH3D8) shown in **Fig. 5-7**. The element is fully supported at its bottom surface by restraining all degrees of freedom of the four nodes (bottom surface), while the top surface is subjected to different modes of loading by imposing displacements along 1) *n* (tensile mode), 2) s_1 and s_2 (shear modes), and 3) *n*, s_1 and s_2 (tension-shear mixed mode). In order to have the same displacement at each of the four top surface nodes, displacements are imposed to a reference point (RP) created for this purpose and the RP is kinematically coupled (connected) to these four nodes. This approach also helps to conveniently capture the total force applied to

the top surface in the form of reaction force of the RP. The size of the element is taken as 100mm×100mm with a thickness of 10mm, the value of thickness does not influence the traction-separation constitutive relationship but thickness is needed for creating the geometry. The implementation of the constitutive model is programmed (Fortran) as an user defined material (UMAT) subroutine for the FE code ABAQUS. Interfacial properties used for the single cohesive element tests under different loading conditions are listed in **Table 5-1**. The tolerance used to check convergence in **Eq. (5.18)** is defined as 0.0001 for all models.

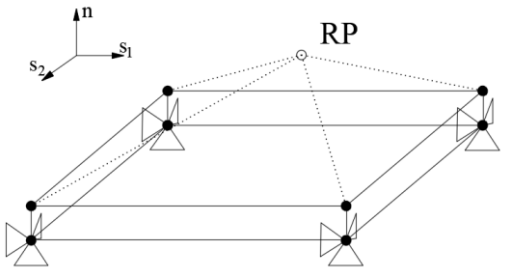

Fig. **5-7** Single cohesive element (COH3D8) with boundary conditions and RP

.

Table 5-1. Material properties used for the single element tests

Loading	K_n^0 (N/mm^3)	K_s^0 (N/mm^3)	χ_0 (N/mm^2)	C_0/C_Q (N/mm^2)	G_{ft} (N/mm)	G_{fs} (N/mm)	$tan\phi$	$tan\phi_{Q0}$	$tan\phi_{Qr}$
Monotonic tension	82	36	0.3	0.87	0.012	0.071	1	0.01	0
Un/Re-load tension	82	36	0.3	0.87	0.012	0.071	1	0.01	0
Monotonic shear	82	36	0.3	0.87	0.012	0.058	1	0.01	0
Un/Re-load shear	82	36	0.3	0.87	0.012	0.058	1	0.01	0
Mono shear with pre-compression (Pv = 0.1MPa)	82	36	0.3	0.87	0.012	0.071	1	0.01	0
Cycle shear with pre-compression (Pv = 0.1MPa)	82	36	0.3	0.87	0.012	0.071	1	0.01	0
Mono shear with pre-compression (Pv = 1MPa)	82	36	0.3	0.87	0.012	0.188	1	0.01	0
Cycle shear with pre-compression (Pv = 1MPa)	82	36	0.3	0.87	0.012	0.188	1	0.01	0
Cycle shear with pre-compression (Pv=1MPa) - partial softening	82	36	0.3	0.87	0.012	0.188	1	0.01	0

Tension-shear mixed mode with variation of $tan\phi_Q$	82	36	0.3	0.87	0.012	0.058	1	0 0.1 0.2 1 1	0 0.1 0.2 1 0
Cycle shear with pre-compression (Pv = 1MPa) and variation of $tan\phi_{Q0}$	82	36	0.3	0.87	0.012	0.188	1	0.2 0.1 0.01	0

The behaviour of the model is first tested under uniaxial monotonic (M) and unloading-reloading (U-R) tension using displacement control. The predicted response is plotted in **Fig**. 5-8**a**, which shows an expected response with gradual stiffness degradation due to damage evolution demonstrated by the unloading paths. A similar test under uniaxial shear is conducted and the response is presented in **Fig**. 5-8**b**. In the next attempt, the behaviour under cyclic shear with a constant pre-compression is tested by taking two cases with two different values of the pre-compression (Pv), where the unloading/reloading is done when the interface is fully degraded under shear and has only frictional resistance. The results produced by the model are shown in **Fig**. 5-8**c**, and as expected, exhibit an increase of peak load and frictional resistance with higher pre-compression. The figure also shows the effect of different fracture energy in shear $G_{fs} = 0.058 - 0.13\sigma_n$ for different pre-compressions, which follow the recommendation of Pluijm (1993) based on experimental observations. **Fig**. 5-8**d** shows the cyclic response predicted by the interface model under cyclic shear with pre-compression (Pv = 1.0MPa) where the unloading/reloading is done when the interface is not fully degraded and has some cohesive resistance (i.e. partially softening). The amplitude of shear displacement is progressively increased in subsequent cycles until full degradation of the interface occurs. The figure also includes the monotonic response of the interface in order to compare with the cyclic response. For any cycle, the segment of the curve after peak stress and before unloading is similar to the monotonic response with a lag of shear displacement.

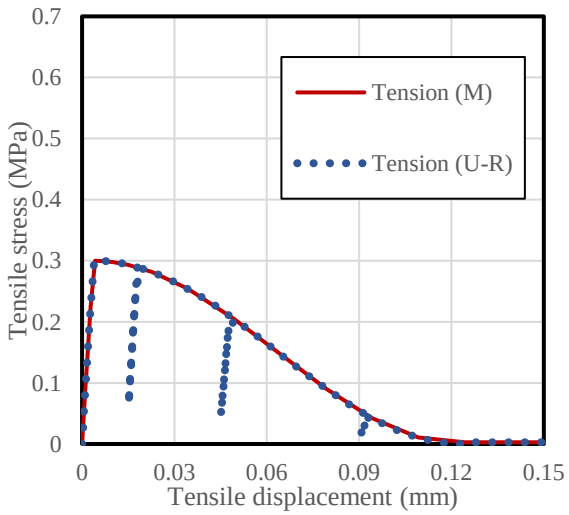

(a) uniaxial tension

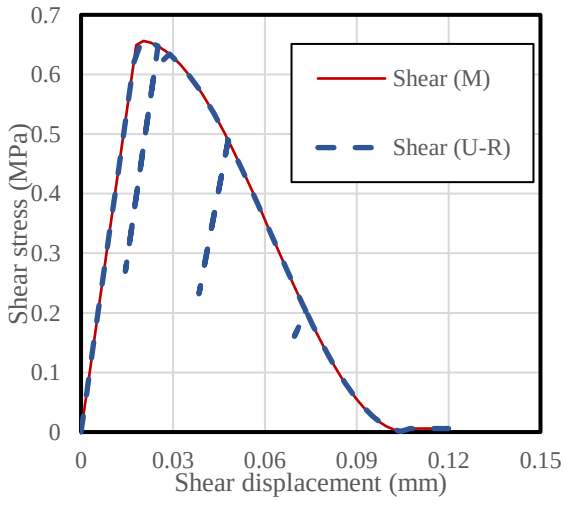

(b) uniaxial shear

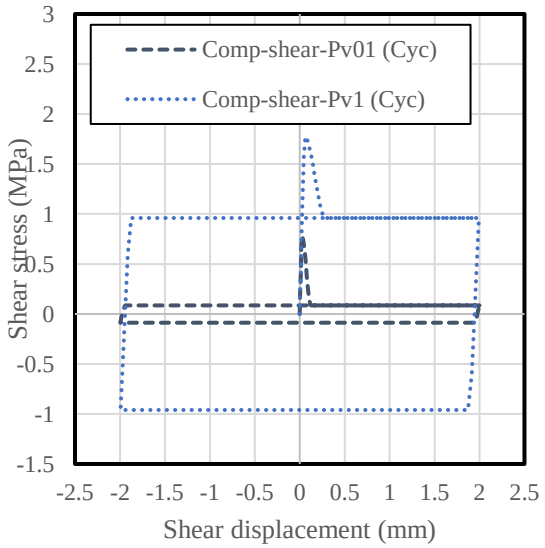

(c) Cyclic shear under pre-compression

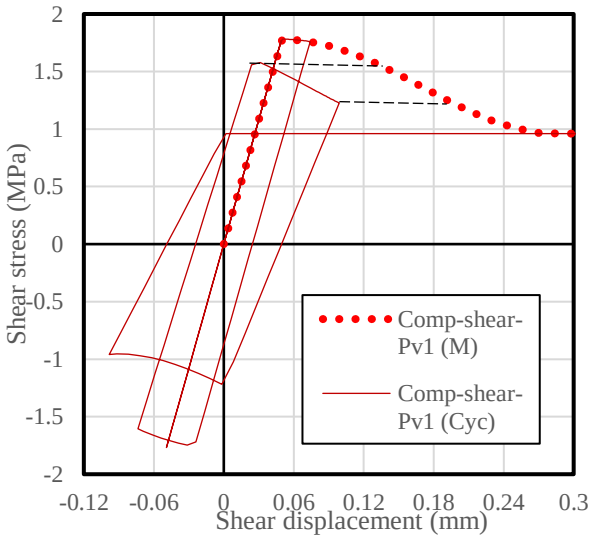

(d) Cyclic shear under pre-compression

Fig. 5-8 Behaviour of the interface model under different uniaxial loading scenarios

The interface model is now tested under tension-shear mixed mode loading, where both normal and shear displacements are gradually increased and have the same value at any time ($u_n = u_s$), such that a 45^0 loading path is induced. The results of this simulation are presented in **Fig. 5-9a** and **Fig. 5-9b**. The effect of the dilation coefficient ($\tan\phi_Q$) on the stress-displacement response is shown in **Fig. 5-9a** where the value of the dilation angle (ϕ_Q) for any specific case is not changed during loading ($\phi_{Q0} = \phi_{Qr}$). These results (**Fig. 5-9a**) show that with the increase of the dilation angle (ϕ_Q), the normal stress decreases but shear stress increases in spite of the constant fracture energy. This typical behaviour can be justified with the plastic return of the stress to the yield surface (F) but normal to the potential surface (Q) as illustrated in **Fig. 5-9c**. Similar results are presented in **Fig. 5-9b** but with focus on the effect of degradation of the dilation angle ($\phi_{Q0} \neq \phi_{Qr}$). The initial value used for the dilation angle ($\phi_{Q0} = 1.0$) may not be realistic (too high) for mortar joints, but it is common for simulating a potential crack surface in bricks using artificial joints. **Fig. 5-9b** also show that the normal stress becomes negative (compressive) when the dilation angle is not degraded ($\phi_{Q0} = \phi_{Qr}$), and this is not expected in reality (compression caused by tension-shear loading). Figure 9d, does however provide justification for this result in terms of plastic return of the stress. Thus the degradation of the dilation angle should be considered specifically for a high initial value of dilation angle and this is followed in the present study according to **Eq. (5.5)**.

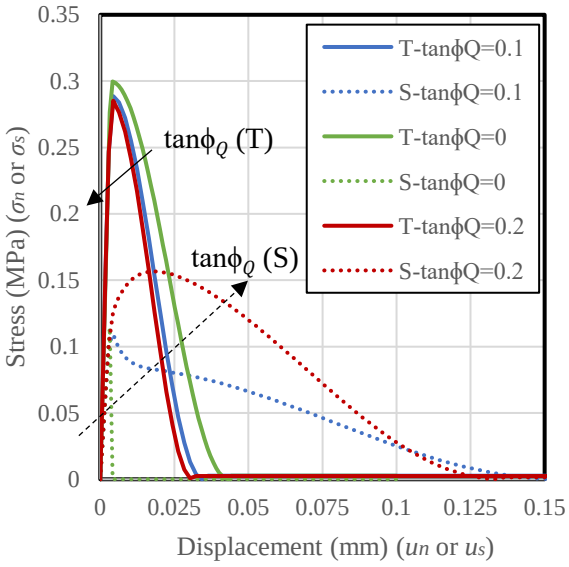

(a) Different dilation coefficient

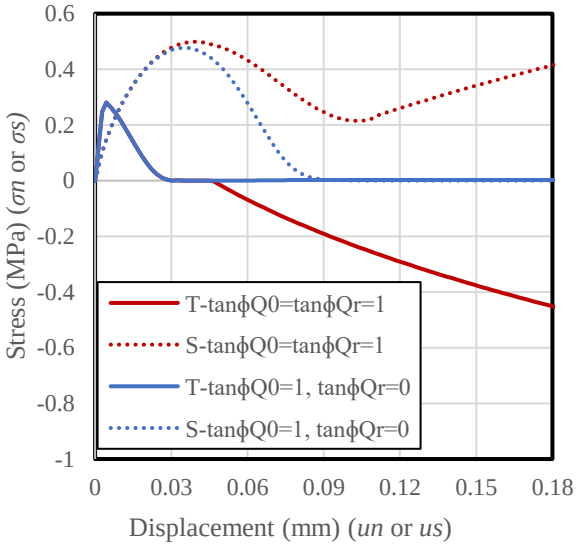

(b) Incorrect stress-displacement relation due to improper dilation coefficient and its calibration

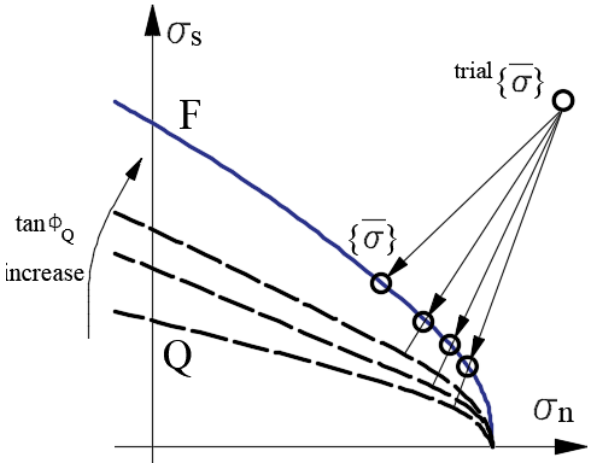

(c) dilation coefficient is zero

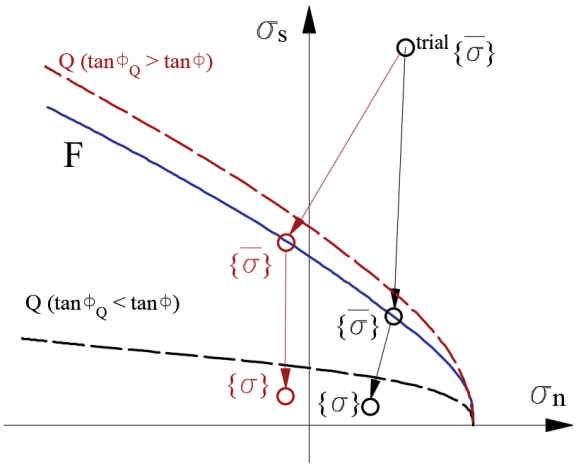

(d) dilation coefficient is larger than friction coefficient

Fig. 9 Stress-displacement relation under mix-mode loading and the influence of dilation coefficient on the modelling results

Finally, the interface model is tested under shear with constant pre-compression (Pv = 1.0MPa) considering degradation of the dilation angle. For this testing, three different initial values ($tan\phi_{Q0}$ = 0.01, 0.1, 0.2) are used and they are all degraded to zero ($tan\phi_{Qr}$ = 0). The variation of opening/normal displacement with respect to the applied shear displacement is presented in **Fig**. 5-**10a**, which shows a gradual increase of the opening displacement before it becomes

constant when the cohesive strength is exhausted, and the resistance arises only from friction. The opening displacement is obviously higher (**Fig**. 5-**10a**) for higher values of dilation angle (ϕ_{Q0}), but the shear stress is not affected by the change of dilation angles as demonstrated in **Fig**. 5-**10b**.

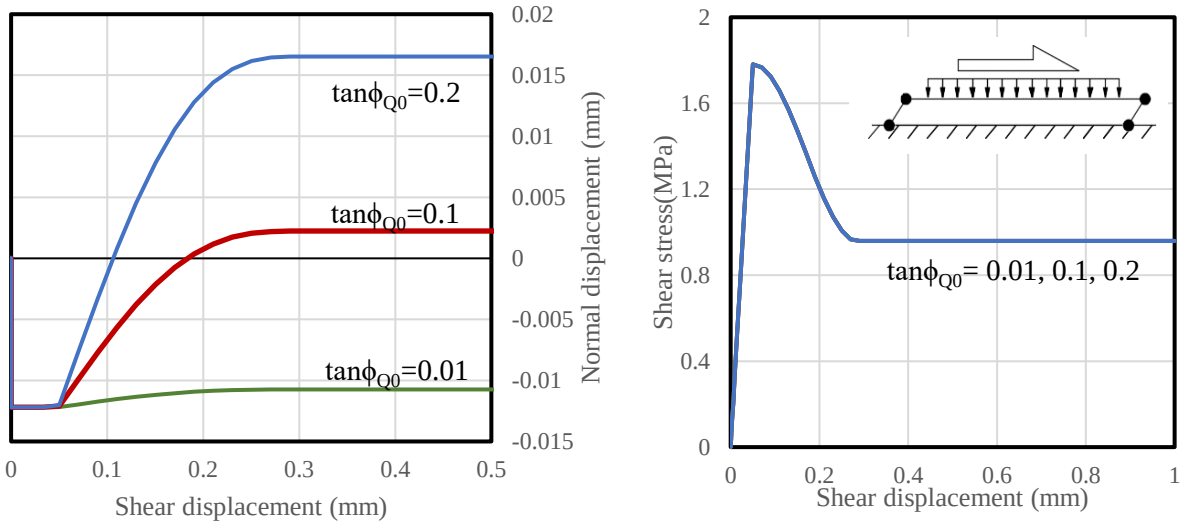

(a) normal displacement vs. shear displacement (b) shear stress vs. shear displacement

Fig. 5-**10** Effect of dilation on shear response of the interface under constant pre-compression

5.5 Numerical examples of masonry structures to validate the model

In this section, the structural level validation of the interface model is conducted by implementing the model within a FE code (Abaqus 6.14), which is used for simulation different sizes of masonry structures under monotonic and cyclic loading. The mortar joints are simulated with the 8 node hexahedral cohesive element (COH3D8), which accommodates the proposed traction-separation based constitutive model. The bricks are simulated using the 8 node 3D hexahedral solid element (C3D8R) with reduced integration as well as the cohesive element (COH3D8) for modelling potential crack planes within brick units as artificial joints if needed. While a static-implicit solver was used for single element testing in last section, here, a dynamic-implicit solver with the option of quasi-static analysis is used for analysing to all masonry structures to avoid potential convergence issues in large scale modelling. In the following simulations, the density of both bricks and mortar joints is taken as 1900 kg/m^3 = 1.9e-9 ton/mm^3.

5.5.1 Masonry couplets under different loading

For the validation of the model for small scale masonry system, the following test results of masonry couplets under different loading are used: 1) uniaxial monotonic tensile tests by Van

der Pluijm (1997), 2) cyclic shear tests with constant pre-compression (Pv) by Atkinson et al. (1989), and 3) shear tests with unloading-reloading taking pre-compression (Pv) by Chaimoon (2007). The nonlinear material properties used for simulating the interfaces are provided in **Table 5-2**. The bricks are assumed to be elastic since the failure occurred in the specimens through cracking of mortar joints and no brick failure as observed experimentally in any of the three cases. The elastic material properties used for simulating bricks are calibrated as: elastic modulus E = 16700MPa and Poisson's ratio v = 0.15 for the tension test, E = 16700MPa and v = 0.2 for cyclic shear test, and E = 14700MPa and v = 0.2 for the shear test with loading and unloading.

Table 5-2 Interface material properties of the masonry couplet

Test	K_n^0	K_s^0	χ_0	C_0 or C_Q	G_{ft}	G_{fs}	$tan\phi$	$tan\phi_{Q0}$	$tan\phi_{Qr}$
	N/mm^3	N/mm^3	N/mm^2	N/mm^2	N/mm	N/mm			
Monotonic tension test, Pluijm (1997)	82	36	0.25	0.87	0.015	0.058	1	0.01	0.01
Cyclic shear test (Pv = 1.34MPa, 4.31MPa), Atkinson et.al (1989)	82	36	0.65	1.2	0.278	2.78	0.67	0.01	0
Shear test with unload-reload (Pv = 0.28MPa), Chaimoon (2007)	82	10	0.1	0.07	0.012	0.062	0.82	0.15	0.05
Unload-reload shear test (Pv = 0.51MPa), Chaimoon (2007)	82	4.25	0.1	0.3	0.012	0.071	0.76	0.25	0.001

Tension test of a masonry couplet

The masonry couplet tested under uniaxial monotonic tensile loading is made of two full size clay bricks (210 mm×80 mm×100 mm) joined by a 10 mm thick mortar layer (210 mm×10 mm×100 mm). A mesh size of 5×2×3 was used for modelling a brick unit (**Fig**. 5-11**a**), while the mortar joint followed the meshing system of the bricks (5×3). The bottom surface of the specimen was fully restrained and the top surface was subjected to tensile/vertical displacement using a reference point (RP). The results (tensile stress vs opening displacement) predicted by the model are presented in **Fig**. 5-11**b** along with the experimental results obtained by Pluijm (1997), which are shown in terms of their upper and lower bounds. In addition to the cosine function based damage evolution presented in **Eq. (5.7)**, the performance of the model is tested using two alternative functions: an exponential function (**Eq. (5.37)**) and a polynomial function (**Eq. (5.37)**). The parameter α_1 and α_2 used in **Eq. (5.37)** and **Eq. (5.38)** help to control the damage evolution, which is taken as 1.0 in the simulation presented. The polynomial function (**Eq. (5.38)**) satisfies zero slope at the two ends ($W^p = 0$ and G_{ft}) to enable a smooth transition similar to the cosine function and helps to improve convergence stability. The cosine function (**Eq. (5.7)**) is used in all other examples. The predicted response of the interface using these functions is also included in **Fig. 5-11b,** which shows that the simulated results are within the range of experimental results. The von-Mises stress contour corresponding to 0.15mm opening displacement is also shown in **Fig. 5-11a**.

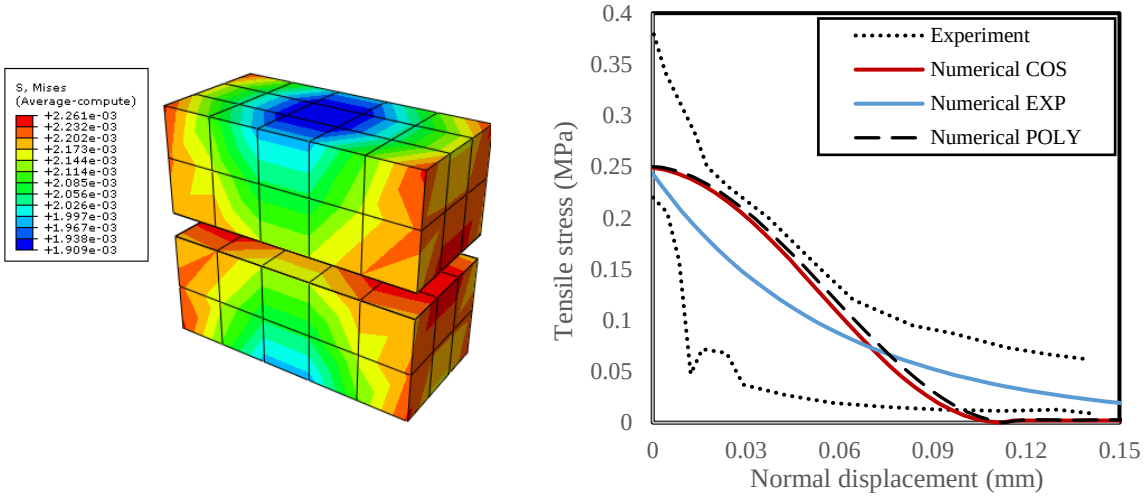

(a) Meshing and stress contour (b) Stress vs displacement in tension

Fig. 5-11 A masonry couplet under tension

$$d_n = 1 - e^{-\frac{\alpha_1 W^p}{G_{ft}}} \quad (37) \qquad d_n = \begin{cases} 0 & W^p < 0 \\ \alpha_2 \left[3\left(\frac{W^p}{G_{ft}}\right)^2 - 2\left(\frac{W^p}{G_{ft}}\right)^3 \right] & 0 \le W^p \le G_{ft} \\ 1 & W^p > G_{ft} \end{cases} \quad (38)$$

Cyclic shear tests of a masonry couplet

Fig. 5-12**a** shows the masonry couplet (one leaf) tested by Atkinson et.al [48] under cyclic shear with pre-pressures (Pv). The couplet is simulated by taking a mesh of 6×2×3 to discretise a full size brick unit (193 mm × 55 mm × 100 mm), the interface elements follow the same discretization system of bricks. The bottom surface of the shear couplet specimen is fully restrained (**Fig**. 5-12**a**), and the top surface is subjected to cyclic shear/horizontal displacement using a reference point (RP). In Fig. 12b, the results of two simulations are presented (Pv = 1.34MPa and 4.31MPa). For simulation the pre-pressure is first applied and kept constant (1.34MPa or 4.31MPa) before imposing the shear displacement, each simulation is continued up to one and a quarter cycles of the applied shear displacement. The modelled response in **Fig**. 5-12**b** shows satisfactory agreement with the experimental and demonstrates that the softening of shear strength starts after the peak strength is reached at the end of the linear elastic region. This is followed by a gradual degradation until a constant frictional resistance is reached when the fracture energy is fully consumed with no cohesive strength. The results also show, as expected, that both peak shear strength and frictional resistance are higher for a larger value of the pre-pressure.

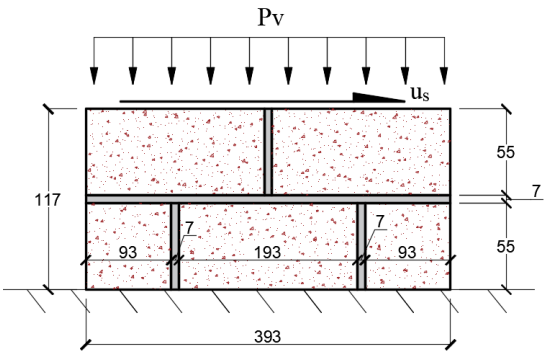

(a) Geometry and boundary conditions of the specimen

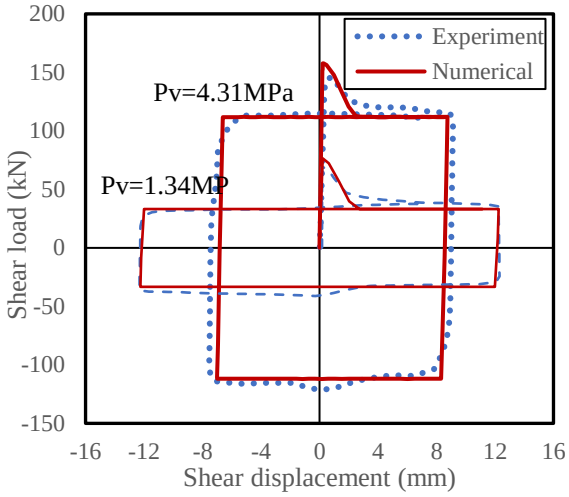

(b) Shear load vs shear displacement

Fig. 5-12 A masonry couplet under cyclic shear with constant pre-compressions

Shear tests of masonry couplets with unloading and reloading

To investigate the behaviour of masonry joints in shear including the impact of dilation, two masonry couplets tested by Chaimoon (2007) under shear with unloading and reloading conditions are considered. Each couplet, which is subjected to a different pre-compression (**Table 5-2**) consists of two full size bricks (each brick: 230 mm ×51 mm×110 mm) joined with a 10mm thick mortar layer. **Fig. 5-13a** shows the meshing system used for modelling the couplets, where a mesh size of 8×2×4 is used for a brick and the mortar joint follows that meshing arrangement. Similar to the previous example, after imposing a constant pre-compression (Pv), the bottom surface is fully fixed and the top surface is subjected to shear displacement with the help of a reference point (RP). Before reaching their maximum displacement (1.5mm for both specimens), the shear displacement is unloaded and reloaded three times for the first specimen S_1 (Pv = 0.28MPa) and four times for the second specimen S_2 (Pv = 0.51MPa). The simulated response of the mortar (shear load vs shear displacement) is compared with the experimental results (Chaimoon 2007) in **Fig**. 5-13**b**, and a good correlation between numerical and experimental results is observed. The simulated results show visible stiffness degradation, especially for the second specimen with a higher pre-compression, but interestingly, the experimental results did not show similar prominent stiffness degradation. To investigate dilation behaviour of the masonry joint, the variation of irreversible (plastic) opening displacement with respect to the irreversible shear displacement is plotted in **Fig**. 5-13**c** for both specimens. The figure also includes the experimental results (Chaimoon 2007), and a satisfactory validation of the numerical results is observed. The von Mises stress contour corresponding to 1.5mm shear displacement is also shown in **Fig**. 5-13**a**.

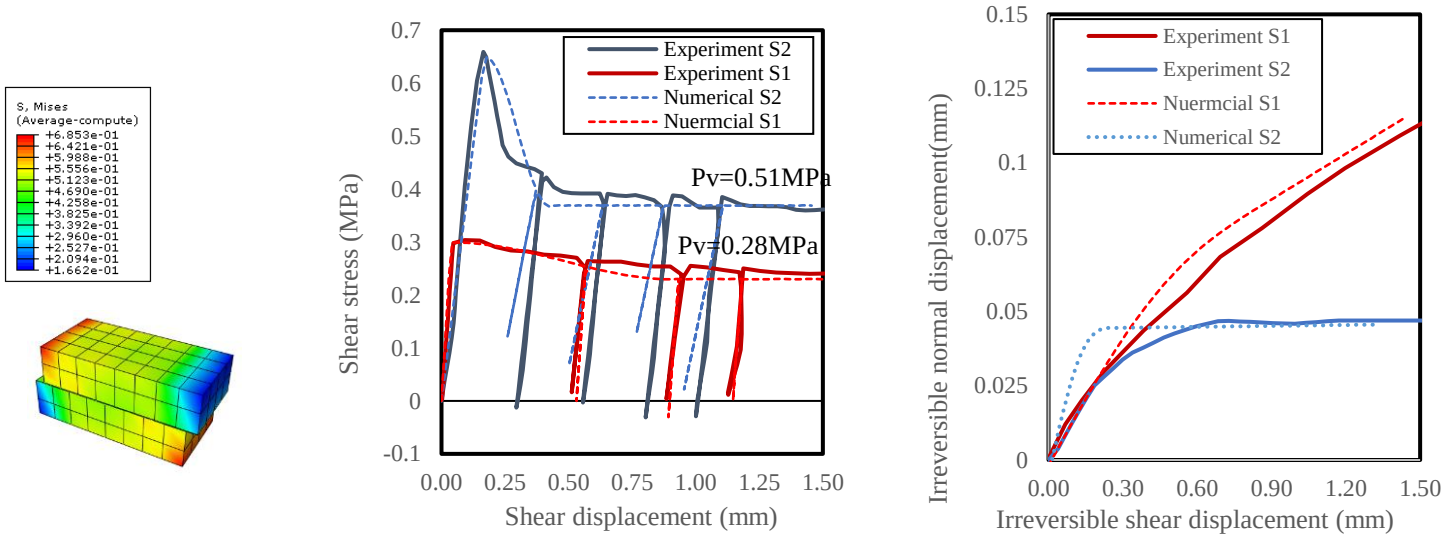

(a) Meshing and stress contour

(b) Shear stress vs shear displacement

(c) normal displacement vs shear displacement

Fig. 5-13 A masonry couplet under shear with unloading and reloading

5.5.2 Three point bending test of a masonry beam

Before attempting the modelling of full structural walls, in this section, the results of modelling of a single leaf masonry beam are presented. For the purpose of validation, modelling results are compared to the experimental observations of Chaimoon (2007), who tested a masonry beam under three point bending with several cycles of loading and unloading. The beam geometry along with the central load point and two roller supports is shown in **Fig. 5-14**. The beam is composed of 4 courses of bricks (each full size brick: 230 mm × 76 mm × 110 mm) where both bed and head joints are 10 mm thick, giving the beam overall dimensions 1430 mm × 334 mm × 110 mm. Also shown in **Fig**. **5-14a** is the final crack pattern, which is observed to pass through the mortar joints at the middle-span through to the top surface.

The nonlinear material properties used for the mortar joints are: K_n^0 = 100 N/mm^3, K_s^0 = 50 N/mm^3, χ_0 = 0.08 N/mm^2, $C_0 = C_Q$ = 0.35 N/mm^2, G_{ft} = 0.006 N/mm, G_{fs} = 0.025 N/mm, $tan\phi$ = 1.0, $tan\phi_{Q0} = tan\phi_{Qr}$ = 0.1, while properties for the artificial brick joints are: K_n^0 = 100 N/mm^3, K_s^0 = 100 N/mm^3, χ_0 = 2.0 N/mm^2, $C_0 = C_Q$ = 2.8 N/mm^2, G_{ft} = 0.08 N/mm, G_{fs} = 0.5 N/mm, $tan\phi = tan\phi_{Q0} = tan\phi_{Qr}$ = 0.1. Since no compression failure of bricks observed in the test, bricks are assumed to be elastic and the material properties used for their modelling are: E = 16700MPa and ν = 0.2. Although tensile cracking of bricks was not observed in this specific case, a full-size brick often experiences cracking along its vertical mid-plane aligned with the head joint of adjacent course of bricks. Thus an artificial joint is inserted at that plane and are also modelled with the interface element shown in **Fig**. **5-14b** with different colour. A full size brick is modelled with a mesh division of 4×2×2 and the mortar joints follow the same meshing arrangement as the bricks. Though both supports are roller in the experimental setup, for

modelling, one is taken as a roller and the other as a pin to avoid any singularity. The point load is applied through vertical displacement of a reference point (RP) kinematic coupled with a narrow strip assigned at the top surface of the beam at its mid-span.

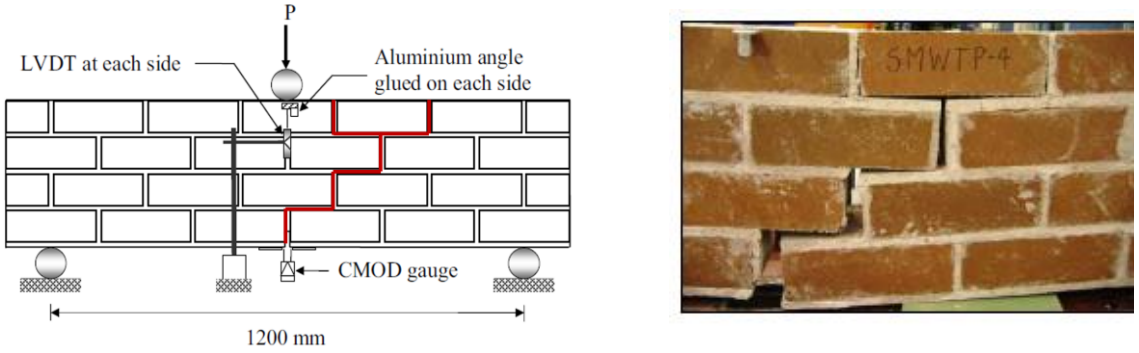

(a) Geometry and failure modes of the beam specimen under three point bending

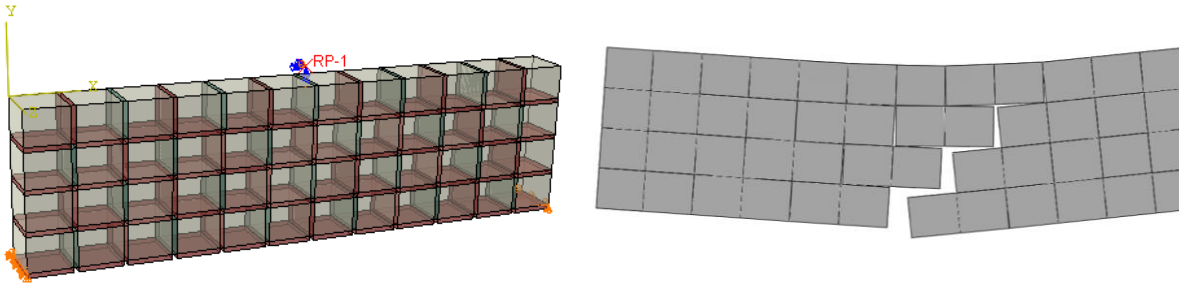

(b) FE model (red region: mortar joints, green region: artificial joints) and its cracking pattern

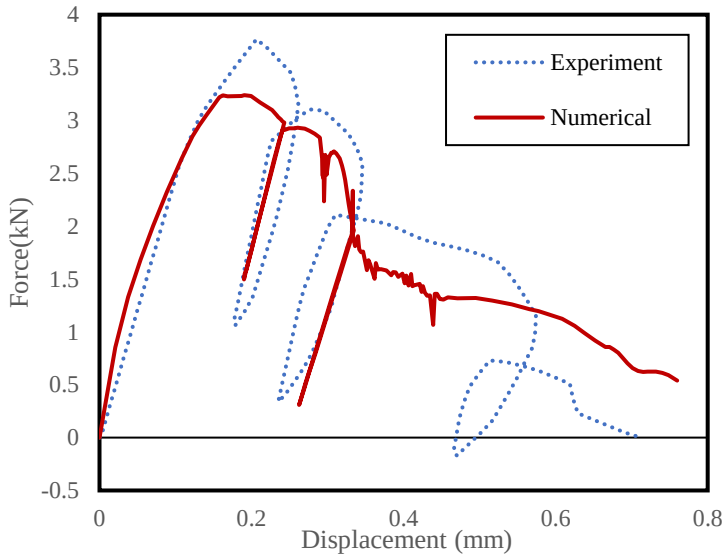

(c) Force vs vertical displacement

Fig. **5-14** A masonry beam under three point bending with unloading and reloading

The variation of point load with respect to the mid-span vertical displacement captured from RP is plotted in **Fig**. **5-14c** along with the experimental results given by Chaimoon (2007). The figures shows that the proposed model could capture the response of first two cycles reasonably well. The unloading in the third cycle is not captured since the physical system is very close to instability because there is no reinforcement in the tensile zone. **Fig**. **5-14b** shows the crack pattern simulated by the model, which strongly correlates with the experimentally observed crack pattern.

5.5.3 Masonry wall under monotonic shear with pre-compression

In this section, experimental results of masonry walls tested under monotonic shear by Raijmakers and Vermeltfoort (1993) are used to study the performance of the model in simulating realistic masonry structures. For this purpose, three typical specimens from the experiments conducted by Raijmakers and Vermeltfoort (1993) are chosen, each of which have the same geometry (**Fig. 5-15a**) but different pre-compression and material properties. The dimensions of the single leaf masonry panels is: 990 mm × 1000 mm × 100 mm, and consists of 18 courses of solid clay bricks (full size brick: 210 mm × 52 mm × 100 mm) with 10 mm thick mortar head and bed joints. The walls are fully supported at the bases and a horizontal shear displacement is applied through a steel beam connected at the top surface of the walls. Before application of the shear, the walls are subjected to a constant pre-pressure (Pv) of 0.3MPa for the first two specimens (J4D and J5D designated here as S1 and S2 separately) and 2.12MPa for the third specimen (J7D designated as S3).

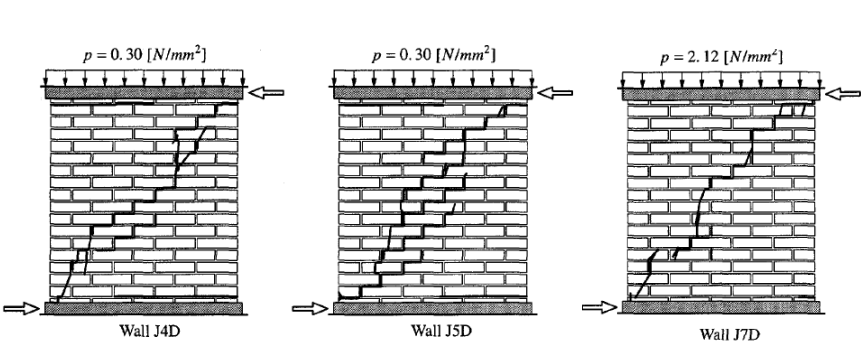

(a) Masonry walls and their failure modes (Raijmakers and Vermeltfoort, 1993)

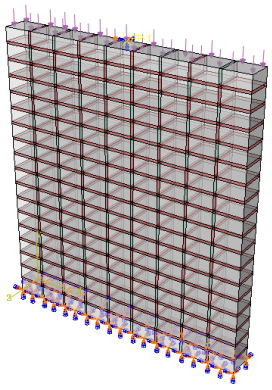

(b) FE model before meshing (artificial joints are in green)

Fig. 5-15 Masonry walls under monotonic loading

Similar to the FE model used for simulating the beam problem in the previous section, artificial joints are inserted at the vertical mid-plane of bricks for simulating potential tensile cracks. **Fig**.

5-15**b** shows the division of bricks and joints used in the FE modelling before meshing is applied. A mesh division of 6×2×3 is used for a full size brick while the mortar and artificial (brick) joints follow the meshing arrangement of the brick units. The figure (**Fig**. 5-15**b**) also shows restraint at the bottom surface and pre-compression applied on the top surface, which is applied before the application of the shear displacement using a reference point (RP) coupled with all nodes at the top surface. In addition to the nonlinear behaviour of joints, in a larger scale structure, the brick units may have inelastic response due to micro-cracking and crushing failure under compression. Thus the concrete damage-plasticity (CDP) material model available in Abaqus for modelling quasi-brittle materials is employed in the simulation of bricks. For this purpose, the material properties used are: E = 16700MPa, ν = 0.18, dilation angle $\psi = 10^0$, bi-axial strength ratio f_{b0}/f_{c0} = 1.12, eccentricity used in potential function e = 0.1, ratio of radial distances in deviatoric plane along tension and compression meridians K = 0.667, viscosity parameter for regularisation μ = 0.0002. This modelling also required the stress-strain diagram which is given in a tabular form (**Table 5-3**). The inelastic material properties used for simulation of mortar and artificial (brick) joints are provided in **Table 5-4**.

Table 5-3 Uniaxial stress-strain relations of bricks (walls under monotonic shear)

Uniaxial tensile behaviour		Uniaxial compressive behaviour		
Stress (MPa)	Inelastic strain	Stress* (MPa)		Inelastic strain
3.5	0	6	11	0
0.3	0.002	6.5	11.5	0.001
		0.6	0.6	0.007

* First column of stress correspond to S1 and S2, second column corresponds to S3

Table 5-4 Material properties of joints (walls with monotonic loading, M: Mortar, A: Artificial joints)

Test			K_n^0	K_s^0	χ_0	C_0 or C_ζ	G_{ft}	G_{fs}	$tan\phi$	$tan\phi_{Q0}$	$tan\phi_{Qr}$
			N/mm^3	N/mm^3	N/mm^2	N/mm^2	N/mm	N/mm			
Monotonic loaded wall Raijmakers & Vermeltfoort (1993)		M Pv=0.3MPa	82	36	0.3	0.45	0.072	0.15	0.75	0.01	0.01
		M Pv=2.12MPa	82	36	0.16	0.224	0.012	0.1	0.75	0.01	0.01
		A	100	100	2	2.8	0.08	0.5	1	1	1

Cracking patterns predicted by the FE model are shown in **Fig**. **5-16**, where it is observed that significant diagonal cracks form across the section and horizontal cracks form near the corners. The diagonal cracks are found to be initially developed near the central portion of the walls and propagate in zigzag pattern towards the corners with the increase of horizontal displacement. Vertical cracks not only develop in the head joints (mortar) but also propagate in the artificial joint of bricks. **Fig**. **5-16** also demonstrates that the magnitude of the pre-pressure has significant effect on the development of cracks and their propagation. For instance, horizontal cracks adjacent to the top left corner and bottom right corner of the wall are clearly

visible under lower pressure (0.3MPa), while these horizontal cracks are negligible for the walls with higher pre-compression (2.12MPa). This is because higher vertical compression resist the opening of bed joints in vicinity of wall corners.

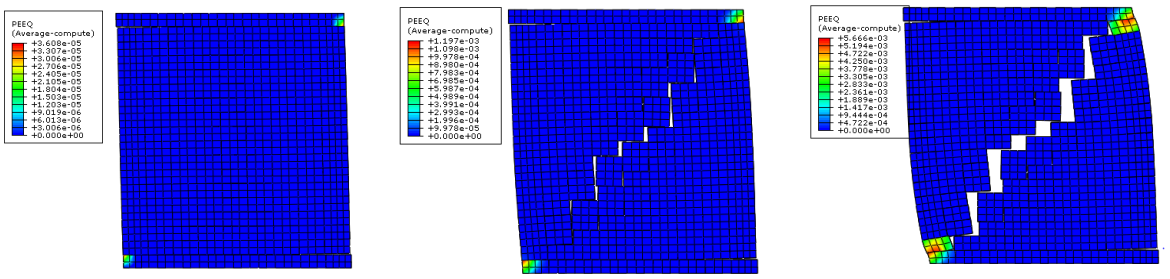

1.08mm 2.1mm 3.8mm

Wall under 0.3MPa pre-pressure

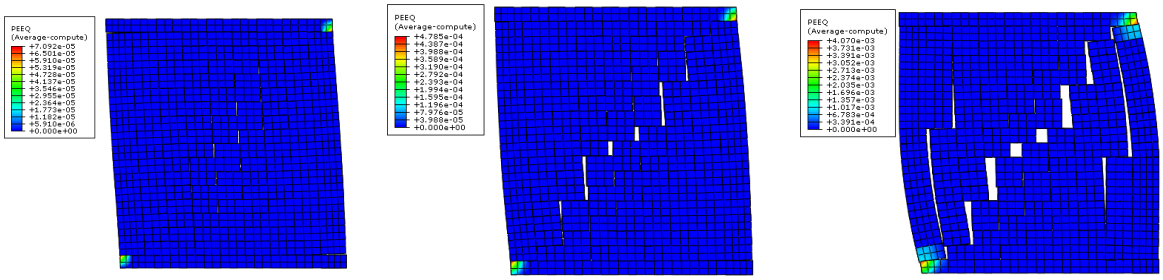

2.08mm 2.1mm 3.1mm

Wall under 2.12MPa pre-pressure

Fig. **5-16** Failure modes of the walls under in-plane loading predicted by the FE model

(PEEQ: plastic equivalent strain magnitude to quantify crushing)

The variation of the shear load with respect to the applied horizontal displacement captured from the reference point (RP) are compared with the experimental results reported by Raijmakers and Vermeltfoort, (1993) in **Fig**. **5-17,** and demonstrate that the numerical results are well correlated with experimental results. The figure also shows that the wall under 0.3MPa compression has predicted a peak load of around 50kN with no significant drop up to 4mm displacement as the experimental results of walls S1 and S2. The predicted load capacity of the wall under 2.12MPa has a sharp drop after reaching its peak load (around 100kN) and then it experience a more significant load reduction until to the final collapse load 60kN, whilst the experimental results of the wall S3 show a softening response until the load capacity reduces to its final collapse.

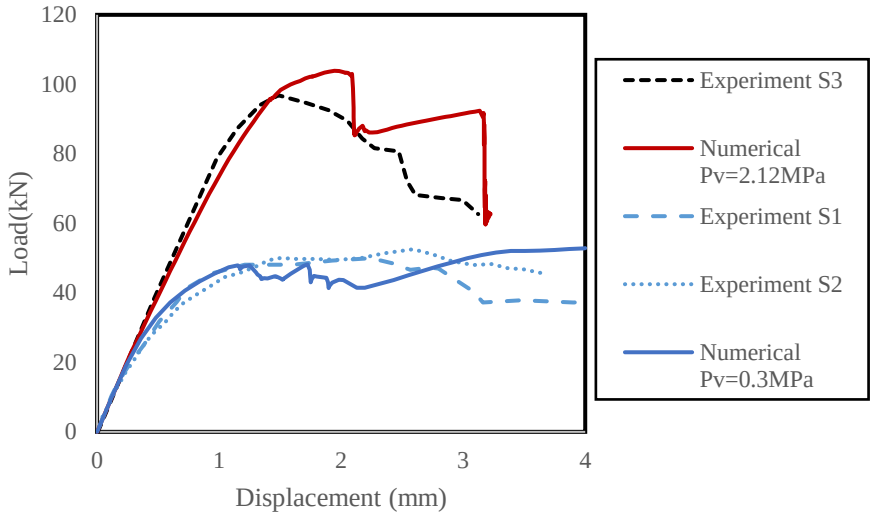

Fig. 5-17 Experimental validation of the load-displacement response of the walls under monotonic shear

5.5.4 Masonry wall under cyclic shear with pre-compression

The performance of the model in simulating behaviours of masonry walls under cyclic loading is investigated in this section. For this purposes, the experimental results of two masonry wall specimens tested under cyclic shear with constant pre-compressions by Salmanpour et.al (2015) are considered. The wall specimens studied here are subjected to the same pre-pressure (Pv) but they have different geometries and materials. The first wall specimen is built using calcium silicate brick units (P4 [50]designated as S1 here) where the wall (**Fig. 5-18a**) have a dimension of 1590 mm × 1550 mm × 150 mm composed of 8 courses of bricks (each: 250 mm × 190 mm × 150 mm). The second specimen (**Fig. 5-18a**) is built using clay bricks (T3 [50]designated as S2) with a larger wall dimension of 2600 mm × 2690 mm × 150 mm and is comprised of 13 courses of bricks (each: 290 mm × 190 mm × 150 mm). The mortar joints used in both walls are estimated to have 10mm thickness. The walls are fully supported at their bases and a steel beam is connected on the top surface of the walls to provide horizontal shear displacement after imposing a pre-pressure (Pv = 1.16MPa).

Table 5-5 Uniaxial stress-strain relations of bricks (walls under cyclic shear)

Uniaxial tensile behaviour		Uniaxial compressive behaviour		
Stress (MPa)	Inelastic strain	Stress* (MPa)		Inelastic strain
3.5	0	11	9	0
0.3	0.002	11.5	9.5	0.001
		0.6	0.6	0.007

* First column of stress correspond to S1, second column corresponds to S2

Table 5-6 Material properties of joints (walls under cyclic loading, M: Mortar joint, A: Artificial joints)

Test		K_n^0	K_s^0	χ_0	C_0 or C_i	G_{ft}	G_{fs}	$tan\phi$	$tan\phi_{Q0}$	$tan\phi_{Qr}$
		N/mm^3	N/mm^3	N/mm^2	N/mm^2	N/mm	N/mm			
Cyclic loaded wall Salmanpour et.al (2015)	M-S1	50	25	0.2	0.3	0.2	0.35	0.75	0.01	1e-6
	M-S2	50	25	0.2	0.24	0.1	0.125	0.48	0.01	1e-6
	A	100	100	2	2.8	1	2	1	1	1

P4 (S1) T3 (S2)

(a) Geometry and failure modes of the walls (b) Loading cycles for FE model

Fig. **5-18** Masonry walls under cyclic shear with constant pre-compression (Salmanpour et.al 2015)

.

Similar to the previous section, for modelling, artificial joints were inserted at the vertical mid-plane of bricks for simulating potential tensile cracks. The cyclic shear load used in the simulation of two walls is shown in **Fig**. **5-18b** where the value of time (horizontal axis) can be arbitrary as it has no influence on predicted results since the analysis is based quasi static modelling. As the computational demand is significantly higher for simulating the response of walls under a large number of loading cycles, a relatively course mesh (compared to that used for monotonically loaded walls in the previous section) is used here, which has a mesh division of 2×2×1 for a full brick and this is followed by the interfaces. The constant pre-compression is first applied on the top surface of the wall and it is then subjected to cyclic loading by imposing horizontal displacement (**Fig**. **5-18b**) to an assigned RP, which is coupled with all nodes at the top surface of wall. For modelling the inelastic response of bricks, the CDP model is employed. The elastic modulus (E) and Poisson's ratio (v) used are: E = 6000MPa, v = 0.2 for the wall specimen S1, and E = 16700MPa, v = 0.2 for S2. The other parameters needed by the CDP model are the same as those used in the previous section for simulating monotonic loaded walls except the uniaxial stress-strain relations, which are listed in **Table 5-5**. The nonlinear material properties used for modelling mortar and artificial (brick) joints are presented in **Table 5-6.**

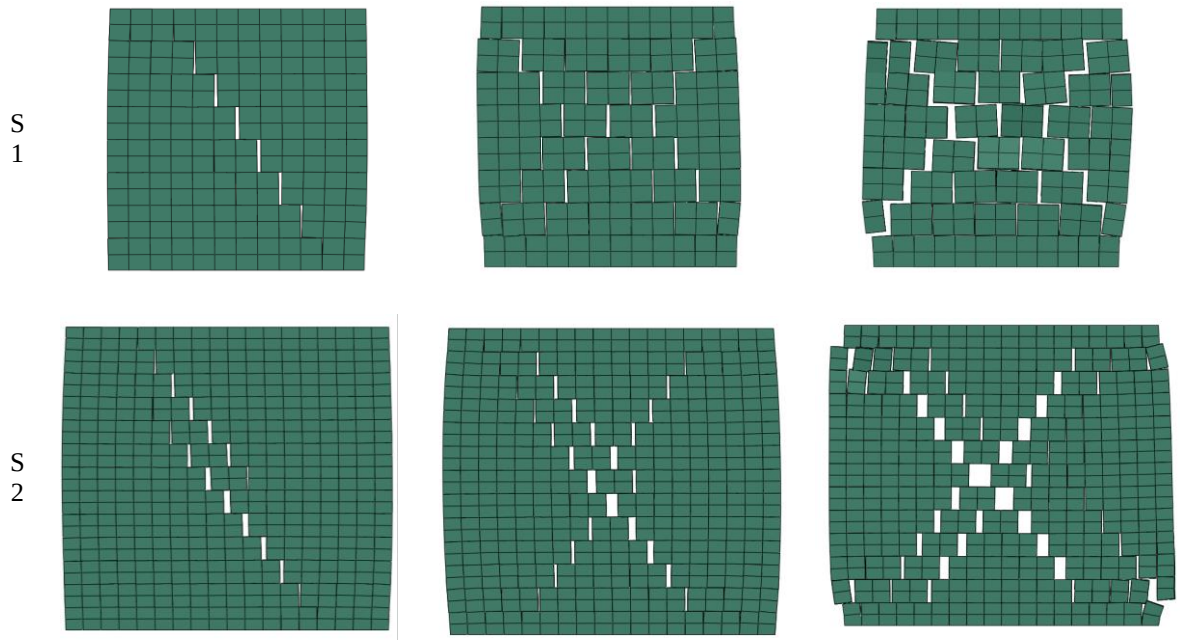

(a) Stage-1: Formation of one sided diagonal cracking

(b) Stage-2: Formation of two sided diagonal cracking (X shaped cracking pattern)

(c) Stage-3: Widening of cracks leading to separation of wall segments horizontally

Fig. 5-19 Failure modes of the walls under cyclic loading (FE model prediction)

.

The propagation of predicted cracks within the two masonry walls is shown in **Fig**. **5-19**, which provided cracking patterns at three different stages of loading. In the initial stage (**Fig**. **5-19a**), one sided diagonal cracking near the central portion of the wall is predicted after few cycles of low amplitude of shear displacement and no horizontal cracks near the corners. Followed by several cycles after that, the model simulated two sided diagonal cracking and giving an X shaped cracking pattern (**Fig**. **5-19b**), which is a typical failure mode of masonry walls subjected to in-plane cyclic shear load with pre-pressure. In the final loading stage (**Fig**. **5-19c**), the model shows lateral swelling of the walls by widening the X shape cracks and leading to separation of wedge shaped wall segments horizontally under the cyclic shaking movements. It also associates horizontal sliding and cracking of bed joints near the wall corners. The load-displacement response obtained from FE models are compared with experimental results reported by Salmanpour et al. (2015) in **Fig**. **5-20**, which shows a satisfactory correlation in terms of the prediction of load capacity and stiffness deterioration.

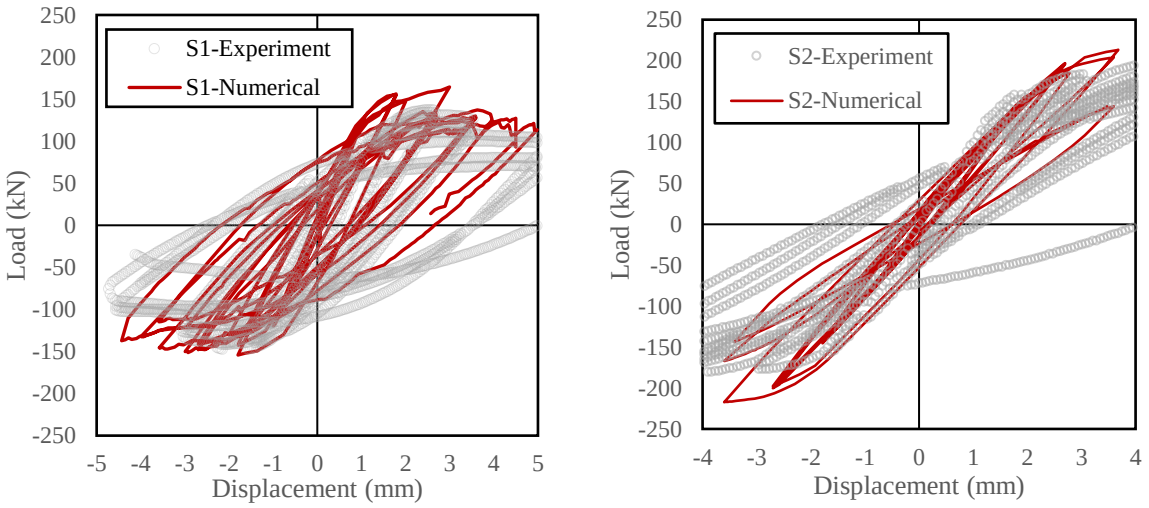

Fig. 5-20 Experimental validation of the load-displacement response of the walls under cyclic loading

.

The experimental investigation (**Fig. 5-18a**) shows major damage at both the central and corner regions of the wall. In order to have better insight of the damage process, the energy dissipation contour of the mortar joints and artificial brick joints are presented in **Fig**. 5-**21**. The mortar joints show maximum energy dissipation near the central region of the wall, i.e. the failure of mortar joints that may be the possible reason for removal of the portion of brick near the central portion. In contrary, the artificial brick joints dissipated maximum energy near the corners, which is responsible for cracking of brick that may cause the failure of walls near the corners. The position of these joints within the masonry wall is also shown to visualise the possible scenario of failure.

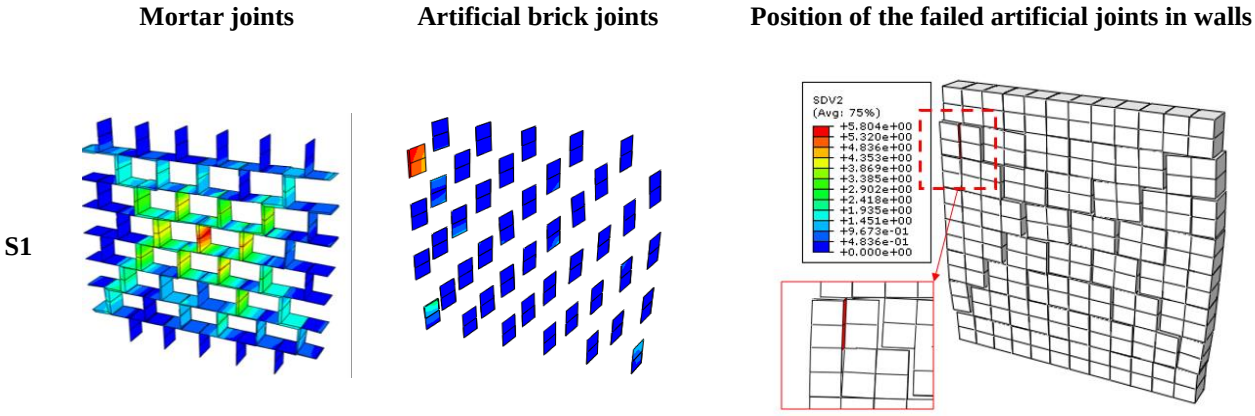

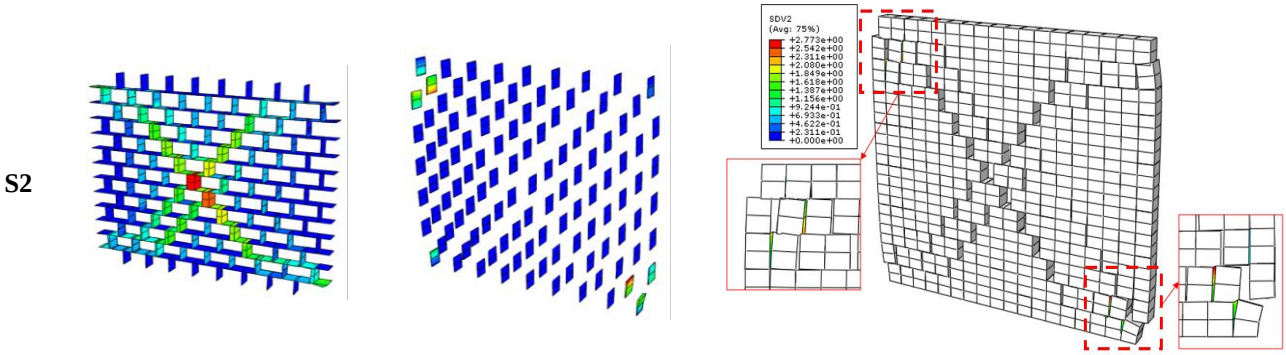

Fig. 5-21 Plastic energy dissipation (W^p) of the joints (SDV2 in FE model)

5.6 Conclusion

In this study, a numerical modelling technique is developed to simulate the nonlinear response and failure modes of the masonry structures subjected to monotonic and cyclic loadings. The key innovation of this study is the development of an interface model considering damage, plasticity and their interactions. The modelling of plasticity and damage are undertaken in the two separate stages: 1) computation of effective stress and plastic work using a yield surface having no expansion/shrinkage due to elastic-perfectly-plastic materiel behaviour in effective stress space; 2) computation of damage parameter using plastic work obtained in first stage and the determination of nominal stress by using the damage parameter to soft the constant post-yield effective stress. A smooth hyperbolic yield surface is used in this model to help minimise convergence issue usually found in multi-surfaces plasticity models with discontinuities at sharp corners. A generic formulation of the model is provided with some improvements over existing models. The incorporation of the degradation of dilation angle via an energy based evolution function is found to be important in improving physical behaviour and numerical stability.

In order to simulate large scale masonry structures subjected to complex loading scenarios without convergence issue, the interface model is implemented by using a fully implicit backward Euler integration (BEI) technique for stress updating because BEI technique provides unconditional stability of solution. The resulting nonlinear equations provided by the BEI are solved using full Newton-Raphson iteration technique. To achieve quadratic convergence at the global/elemental level solution using Newton-Raphson iteration technique, the consistent tangent stiffness matrix for the proposed damage-plastic based model is derived.

The interface model is implemented within a FE code Abaqus, for analysing masonry structures of different scales under monotonic and cyclic loading. Before experimental validation of the model, a single element test is conducted under different loading conditions for verification of the interface model to access its overall prediction capability in terms of expected trends. The FE model is then applied to the analysis a number of masonry structures of different sizes subjected to monotonic and cyclic loads for experimental validation of the proposed model to access its performance in terms of accuracy and robustness of solution along with range of applicability. This includes: 1) a masonry couplet tested under uniaxial tension, 2) a masonry

couplet tested under cyclic shear with constant pre-compression, 3) a masonry couplet tested under shear displacement with unloading-reloading scenarios along with constant pre-compression to investigate damage and dilation behaviours, 4) a masonry beam tested under three point bending with unloading-reloading, 5) two masonry walls panel subjected to monotonic shear loading under different pre-compressions, and 6) two masonry walls panel subjected to cyclic loading under same pre-compression but different geometries. The force-displacement responses as well as failure modes predicted by the proposed model are found to be consistent with the experimental results within satisfaction level in most cases, which ensures the capability of the proposed interface model in simulating masonry structures having varied geometries and loading.

5.7 Reference

Abaqus User M. Abaqus Theory Guide. Version 6.14. USA: Dassault Systems Simulia Corp. 2014.

Abdulla KF, Cunningham LS, Gillie M. Simulating masonry wall behaviour using a simplified micro-model approach. Engineering Structures. 2017;151:349-65.

Alfano G, Sacco E. Combining interface damage and friction in a cohesive - zone model. International Journal for Numerical Methods in Engineering. 2006;68:542-82.

Andreotti G, Graziotti F, Magenes G. Detailed micro-modelling of the direct shear tests of brick masonry specimens: the role of dilatancy. Engineering Structures. 2018;168:929-49.

Andreotti G, Graziotti F, Magenes G. Expansion of mortar joints in direct shear tests of masonry samples: implications on shear strength and experimental characterization of dilatancy. Materials and Structures. 2019;52:1-16.

Atkinson R, Amadei B, Saeb S, Sture S. Response of masonry bed joints in direct shear. Journal of Structural Engineering. 1989;115:2276-96.

Baraldi D, Cecchi A. Discrete approaches for the nonlinear analysis of in plane loaded masonry walls: Molecular dynamic and static algorithm solutions. European Journal of Mechanics-A/Solids. 2016;57:165-77.

Benedetti D, Carydis P, Limongelli M. Evaluation of the seismic response of masonry buildings based on energy functions. Earthquake engineering & structural dynamics. 2001;30:1061-81.

Caballero A, Willam K, Carol I. Consistent tangent formulation for 3D interface modeling of cracking/fracture in quasi-brittle materials. Computer Methods in Applied Mechanics and Engineering. 2008;197:2804-22.

Camanho PP, Dávila CG. Mixed-mode decohesion finite elements for the simulation of delamination in composite materials. 2002.

Chaimoon K, Attard MM. Modeling of unreinforced masonry walls under shear and compression. Engineering structures. 2007;29:2056-68.

Chaimoon K. Numerical simulation of fracture in unreinforced masonry: Ph. D thesis; 2007.

Citto C. Two-dimensional interface model applied to masonry structures: University of Colorado at Boulder; 2008.

D'Altri AM, de Miranda S, Castellazzi G, Sarhosis V. A 3D detailed micro-model for the in-plane and out-of-plane numerical analysis of masonry panels. Computers & Structures. 2018;206:18-30.

D'Altri AM, Messali F, Rots J, Castellazzi G, de Miranda S. A damaging block-based model for the analysis of the cyclic behaviour of full-scale masonry structures. Engineering Fracture Mechanics. 2019;209:423-48.

De Lorenzis L, Teng J-G. Near-surface mounted FRP reinforcement: An emerging technique for strengthening structures. Composites Part B: Engineering. 2007;38:119-43.

Ferrante A, Clementi F, Milani G. Advanced numerical analyses by the Non-Smooth Contact Dynamics method of an ancient masonry bell tower. Mathematical Methods in the Applied Sciences. 2020;43:7706-25.

Ferrante A, Loverdos D, Clementi F, Milani G, Formisano A, Lenci S et al. Discontinuous approaches for nonlinear dynamic analyses of an ancient masonry tower. Engineering Structures. 2021;230:111626.

Grassl P, Jirásek M. Damage-plastic model for concrete failure. International journal of solids and structures. 2006;43:7166-96.

Griffith MC, Vaculik J, Lam N, Wilson J, Lumantarna E. Cyclic testing of unreinforced masonry walls in two - way bending. Earthquake Engineering & Structural Dynamics. 2007;36:801-21.

Hofstetter BV, G. Review and enhancement of 3D concrete models for large-scale numerical simulations of concrete structures. International Journal for numerical and analytical Methods in Geomechanics. 2013;37:221-46.

Iannuzzo A, Dell'Endice A, Van Mele T, Block P. Numerical limit analysis-based modelling of masonry structures subjected to large displacements. Computers & Structures. 2021;242:106372.

Kumar N, Amirtham R, Pandey M. Plasticity based approach for failure modelling of unreinforced masonry. Engineering structures. 2014;80:40-52.

Kumar N, Barbato M. New constitutive model for interface elements in finite-element modeling of masonry. Journal of Engineering Mechanics. 2019;145:04019022.

Lotfi HR, Shing PB. Interface model applied to fracture of masonry structures. Journal of structural engineering. 1994;120:63-80.

Lourenço PB, Rots JG. Multisurface interface model for analysis of masonry structures. Journal of engineering mechanics. 1997;123:660-8.

Lourenço PJBB. Computational strategies for masonry structures. 1997.

Macorini L, Izzuddin B. A non-linear interface element for 3D mesoscale analysis of brick-masonry structures. International Journal for numerical methods in Engineering. 2011;85:1584-608.

Malena M, Portioli F, Gagliardo R, Tomaselli G, Cascini L, de Felice G. Collapse mechanism analysis of historic masonry structures subjected to lateral loads: A comparison between continuous and discrete models. Computers & Structures. 2019;220:14-31.

Malomo D, DeJong M. A Macro-Distinct Element Model (M-DEM) for out-of-plane analysis of unreinforced masonry structures. Engineering Structures. 2021;244:112754.

Malomo D, DeJong MJ. A Macro-Distinct Element Model (M-DEM) for simulating the in-plane cyclic behavior of URM structures. Engineering Structures. 2021;227:111428.

Meschke G, Lackner R, Mang HA. An anisotropic elastoplastic‐damage model for plain concrete. International journal for numerical methods in engineering. 1998;42:703-27.

Milani G, Lourenço PB, Tralli A. Homogenised limit analysis of masonry walls, Part I: Failure surfaces. Computers & structures. 2006;84:166-80.

Milani G, Lourenço PB. 3D non-linear behavior of masonry arch bridges. Computers & Structures. 2012;110:133-50.

Minga E, Macorini L, Izzuddin BA. A 3D mesoscale damage-plasticity approach for masonry structures under cyclic loading. Meccanica. 2018;53:1591-611.

Nazir S, Dhanasekar M. A non-linear interface element model for thin layer high adhesive mortared masonry. Computers & Structures. 2014;144:23-39.

Nguyen NH, Bui HH, Nguyen GD, Kodikara J. A cohesive damage-plasticity model for DEM and its application for numerical investigation of soft rock fracture properties. International Journal of Plasticity. 2017;98:175-96.

Pech S, Lukacevic M, Füssl J. A robust multisurface return-mapping algorithm and its implementation in Abaqus. Finite Elements in Analysis and Design. 2021;190:103531.

Salmanpour AH, Mojsilović N, Schwartz J. Displacement capacity of contemporary unreinforced masonry walls: an experimental study. Engineering Structures. 2015;89:1-16.

Sarhosis V, Lemos J. A detailed micro-modelling approach for the structural analysis of masonry assemblages. Computers & Structures. 2018;206:66-81.

Serpieri R, Albarella M, Sacco E. A 3D microstructured cohesive–frictional interface model and its rational calibration for the analysis of masonry panels. International Journal of Solids and Structures. 2017;122:110-27.

Sheikh AH, Bull PH, Kepler JA. Behaviour of multiple composite plates subjected to ballistic impact. Composites Science and Technology. 2009;69:704-10.

Spada A, Giambanco G, Rizzo P. Damage and plasticity at the interfaces in composite materials and structures. Computer Methods in Applied Mechanics and Engineering. 2009;198:3884-901.

Vaculik J, Griffith MC. Out-of-plane load–displacement model for two-way spanning masonry walls. Engineering Structures. 2017;141:328-43.

Vaculik J, Visintin P, Burton N, Griffith M, Seracino R. State-of-the-art review and future research directions for FRP-to-masonry bond research: Test methods and techniques for extraction of bond-slip behaviour. Construction and Building Materials. 2018;183:325-45.

Valente M, Milani G, Grande E, Formisano A. Historical masonry building aggregates: advanced numerical insight for an effective seismic assessment on two row housing compounds. Engineering Structures. 2019;190:360-79.

Van der Pluijm R. Non-linear behaviour of masonry under tension. HERON-ENGLISH EDITION-. 1997;42:25-54.

Van der Pluijm R. Shear behaviour of bed joints. 1993.

Vermeltfoort AT, Raijmakers T, Janssen H. Shear tests on masonry walls. 1993.

Yuen TY, Deb T, Zhang H, Liu Y. A fracture energy based damage-plasticity interfacial constitutive law for discrete finite element modelling of masonry structures. Computers & Structures. 2019;220:92-113.

Chapter 6: A damage-plasticity based model for compressive cap

Nie, Y, Sheikh, A., Griffith, M., Visintin, P. and Vaculik, J. (2021, Nov 25 - 26). Interface based damage-plasticity model for predicting the compressive failure of masonry under monotonic and cyclic loads. Australian Earthquake Engineering Society Virtual Conference

Chapter 6: A damage-plasticity based model for compressive cap

Abstract

In this chapter, the compressive behaviour of masonry structures is predicted by proposed interfacial constitutive model which contains plasticity and damage mechanism to model the nonlinear response of masonry mortar joints. The interfacial model has an elliptical yield surface in the plasticity framework and its hardening/softening strength along the variation of plastic energy dissipation is controlled by the damage parameter. Based on the traction-separation law, the proposed interfacial model is defined into the cohesive element in the finite element model to simulate the compressive of masonry under both monotonic and cyclic compressive loading conditions. Compared with plasticity models and pure damage models, the proposed damage-plasticity model can better simulate the response of masonry in terms of its stiffness degradation and inelastic deformation. The unloading-reloading mechanical characteristics of masonry structures is modelled by the interface model which has well consistency with experimental results from literature.

6.1 Introduction

Masonry structures, which are widely used in residential and public buildings, are especially vulnerable to cyclic loads when earthquake occurs. Based on the research reported by Ingham and Griffith (2011), the vast majority of damage was happen in unreinforced brick masonry (URM) buildings in the 2010 Christchurch earthquake. In recent years, the prediction of cyclic response for masonry structures has aroused widespread interest in seismic engineering (Griffith et.al, 2007; Derakhshan et.al, 2013; Vaculik and Griffith et.al, 2018) in terms of the macro-behaviour of masonry structures by using analytical models. Similar macro concepts are adopted by studies (Milani et.al, 2007; Di Nino and Luongo, 2019) focus on numerical techniques which aim to simulate masonry structures by homogenising bricks and mortar joints into a continuum solid which is called representative volume element (RVE). Although the homogenisation approach has advantages with regard to computational efficiency and the accuracy of load-displacement response, it is limited in predicting the failure modes and post-failure deformation of masonry structures, which is vital in providing guideline for the masonry retrofitting (Su et.al, 2011; Burton et.al, 2021).

Detailed micro-modelling method (Sarhosis and Lemos, 2018; Greco et.al, 2020; Calderón et.al, 2019; Andreotti et.al, 2018) is another modelling strategy which include all components in the model, including the brick, mortar and the interface between brick-mortar. This modelling approach can simulate precisely the cracking patterns and their propagation in mortar joints and bricks. However, the application of this approach is restrained in small size structures (such as masonry couplets or prisms) as well as simply loading conditions (monotonic load within small deformation) due to its extremely high computation costs. Therefore, a more practical modelling strategy, which is called simplified micro-method (Lotfi and Shing, 1994; Lourenço and Rots, 1997), is commonly accepted in simulating the real size masonry structures under complex loading conditions (Minga et.al, 2018; D'Altri et.al, 2019; Tubaldi et.al, 2020). The mortar joint in the simplified micro-model is lumped into an interface/cohesive element which represents all nonlinear response of the masonry while the bricks are simulated by using solid elements. In this way, both computational efficiency and modelling accuracy of the finite element (FE) models are considered, and this simplified

method is also extended to the application of discrete element models (Bui et.al, 2021) and finite discrete element models (Smoljanović et.al, 2018).

In previous studies related to simplified micro-modelling (Lotfi and Shing, 1994; D'Altri et.al, 2019), the compressive behaviour in the interface model is often ignored and assuming the compressive failure is all subjected to brick elements having nonlinear continuum constitutive behaviour, which reduces the computational efficiency since finer meshing is required for solid elements. Therefore, in this study the compressive behaviour of masonry is investigated and simulated by using an interface based model within damage-plasticity framework.

6.2 Constitutive model

The interface based constitutive model, as shown in Figure 1, follows the traction-separation law behaviour in a 2D space where 'n' and 's' denote the normal and shear directions respectively. The elastic behaviour of the interface can be represented by **Eq. (6.1)** with the elastic stiffness matrix $[K^0]$, nominal stress vector $\{\sigma\}$ and relative displacement vector $\{u\}$.

$$\{\sigma\} = [K^0]\{u\}; \quad \begin{Bmatrix}\sigma_n \\ \sigma_s\end{Bmatrix} = \begin{bmatrix}K_n^0 & 0 \\ 0 & K_s^0\end{bmatrix}\begin{Bmatrix}u_n \\ u_s\end{Bmatrix} \tag{6.1}$$

.

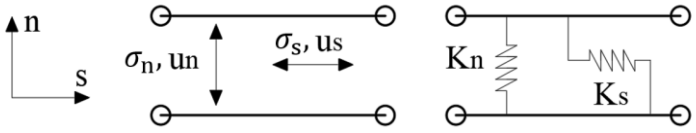

Fig. 6-1 Elastic behaviour of the interface in 2D space

To define the strength/stiffness softening behaviour of mortar joints, a damage matrix $[D]$ is induced for the transformation between nominal stress $\{\sigma\}$ and effective stress $\{\bar{\sigma}\}$.

$$\{\sigma\} = ([I] - [D])\{\bar{\sigma}\}; \quad \begin{Bmatrix}\sigma_n \\ \sigma_s\end{Bmatrix} = \begin{bmatrix}1 - D_n & 0 \\ 0 & 1 - D_s\end{bmatrix}\begin{Bmatrix}\bar{\sigma}_n \\ \bar{\sigma}_s\end{Bmatrix} \tag{6.2}$$

where $[I]$ is the unit matrix.

An elliptical yield surface (**Fig. 6-2a**) is adopted here to determine the elastic domain, which can be written as:

$$F_c\left(\{\bar{\sigma}\}, W_c^p\right) = C_{nn}\bar{\sigma}_n^2 + C_{ss}\bar{\sigma}_s^2 + C_n\bar{\sigma}_n - \left(f_c(W_c^p)\right)^2 \tag{6.3}$$

where C_{nn} and C_{ss} are parameters for controlling the configuration of the yield surface in normal and shear directions, and C_n is used to adjust the central position of the ellipse. W_c^p is the plastic work of the interface under compression and its increment can be calculated as:

$$dW_c^p = \left|\bar{\sigma}_n du_n^p\right| + \left|\bar{\sigma}_s du_s^p\right| \tag{6.4}$$

.

.

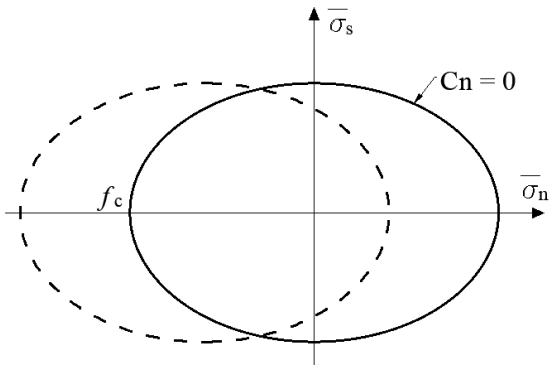

(a) Yield surface of the compressive cap

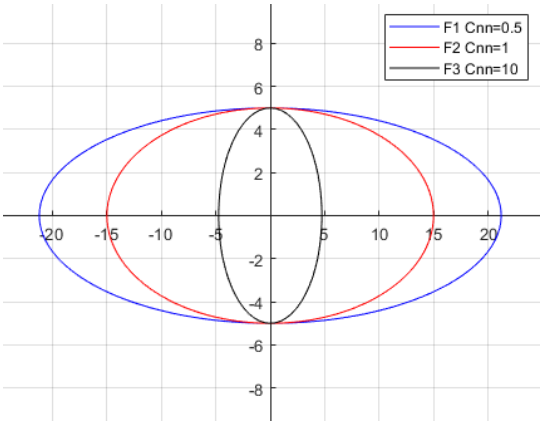

(b) Cnn changes; Css = 9; Cn = 0

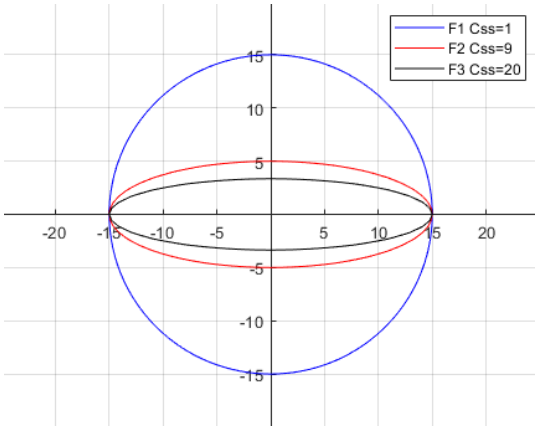

(c) Cnn = 1; Css changes; Cn = 0

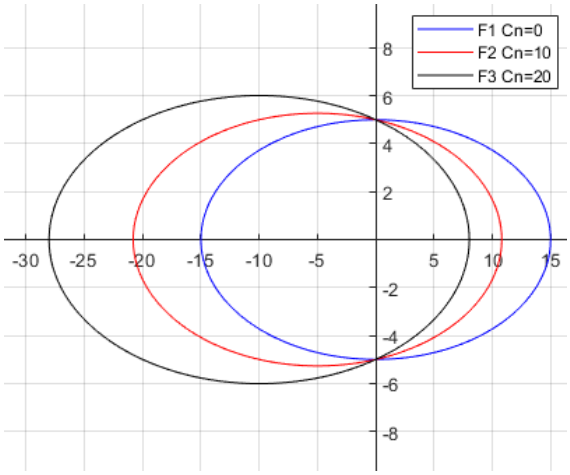

(d) Cnn = 1; Css = 9; Cn changes

Fig. 6-2 Elliptical shape yield surface

The incremental plastic displacement $\{du^p\} = \begin{Bmatrix} du_n^p \\ du_s^p \end{Bmatrix}$ in current model is computed based on the associated flow rule, namely, potential surface is the same as yield surface, $Q_c = F_c$.

$$\{du^p\} = d\lambda \frac{\partial Q_c}{\partial \{\bar{\sigma}\}} = d\lambda \frac{\partial F_c}{\partial \{\bar{\sigma}\}} \tag{6.5}$$

where $d\lambda$ is the increment of plastic multiplier.

Typically, the compressive failure of masonry prism includes hardening and softening behaviours in terms of the variation of compressive strength f_c along with the plastic work (or equivalent displacement). For the sake of numerical implementation by using damage parameters, in some literature (Minga et.al, 2018) the hardening component is ignored and only

softening behaviour remained, as shown in **Fig. 6-3a**. In this study, the hardening evolution is considered incorporating with the softening response (**Fig. 6-3b**) which is determined by a damage parameter D_c.

In the **Fig. 6-3b**, the strength evolution can be expressed by using a piecewise function:

$$f_c = \begin{cases} f_{ci} + (f_{cu} - f_{ci})\left(\dfrac{2W_c^p}{G_{fch}} - \left(\dfrac{W_c^p}{G_{fch}}\right)^2\right), & W_c^p \le G_{fch} \\ f_{cu} - (f_{cu} - f_{cr})\left[\alpha\left(\dfrac{W_c^p - G_{fch}}{G_{fcs}}\right)^{\alpha-1} - (\alpha-1)\left(\dfrac{W_c^p - G_{fch}}{G_{fcs}}\right)^{\alpha}\right], & G_{fch} < W_c^p \le G_{fc} \\ f_{cr}, & W_c^p > G_{fc} \end{cases} \quad (6.6)$$

where f_{ci}, f_{cu} and f_{cr} are initial, ultimate and residual compressive strength respectively; G_{fch}, G_{fcs} and G_{fc} $(= G_{fch} + G_{fcs})$ are hardening, softening and total compressive fracture energy respectively. α is the configure parameter for the softening part of stress-plastic work curve.

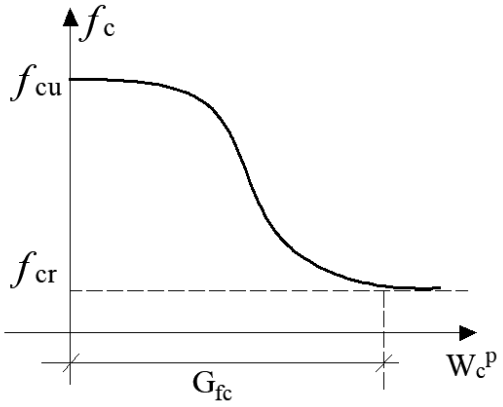

(a) softening

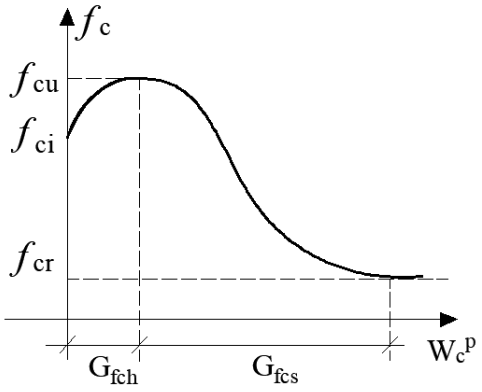

(b) hardening-softening

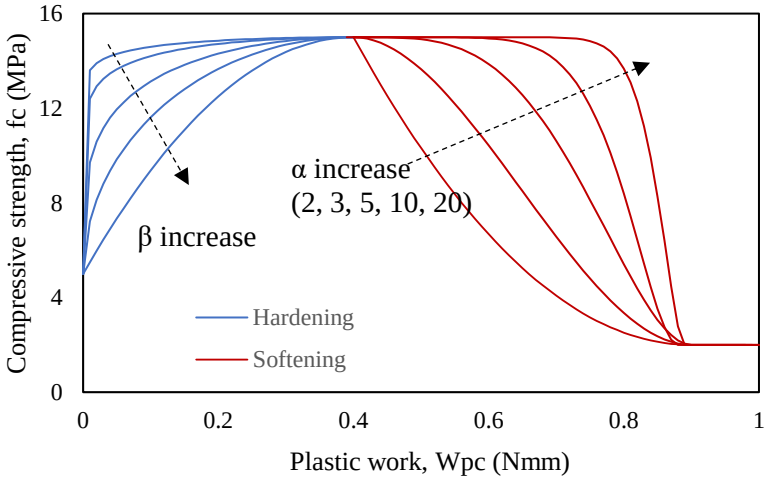

(c) Variation of compressive strength with the plastic work

$(f_{ci} = 5\ MPa, f_{cu} = 15\ MPa,\ f_{cr} = 2\ MPa,\ G_{fch} = 0.4\ Nmm, G_{fcs} = 0.5\ Nmm)$

Fig. 6-3 Strength evolution in compression

.

Based on **Eq. (6.6)**, the ratio of plastic work to fracture energies r_w can be written as:

$$r_w = \begin{cases} r_{ch} = \dfrac{W_c^p}{G_{fch}}, & W_c^p \le G_{fch} \\ r_{cs} = \begin{cases} \dfrac{W_c^p - G_{fch}}{G_{fcs}}, & G_{fch} < W_c^p \le G_{fc} \\ 1, & W_c^p > G_{fc} \end{cases} \end{cases} \tag{6.7}$$

Besides, the ratio of initial and residual strength to the ultimate strength are defined as:

$$\beta_i = \frac{f_{ci}}{f_{cu}}; \quad \beta_r = \frac{f_{cr}}{f_{cu}} \tag{6.8}$$

Substituting **Eqs (6.7)** and **(6.8)** into **Eq. (6.6)**, a damage parameter for the compressive failure can be expressed as:

$$D_c = \begin{cases} D_{ch} = (1-\beta_i)(1-2r_w + {r_w}^2), & W_c^p \le G_{fch} \\ D_{cs} = (1-\beta_r)[\alpha {r_w}^{\alpha-1} - (\alpha-1){r_w}^{\alpha}], & W_c^p > G_{fch} \end{cases} \tag{6.9}$$

And finally the strength is a function of damage parameters,

$$f_c = (1 - D_c) f_{cu} \tag{6.10}$$

In above equations, the softening damage parameter D_{cs} is controlled by the configure parameter α which helps to calibrate the geometry of polynomial curves as shown in **Fig. 6-4** where $f_{cu} = 20\ MPa,\ f_{cr} = 5\ MPa,\ G_{fc} = 0.5\ Nmm.$

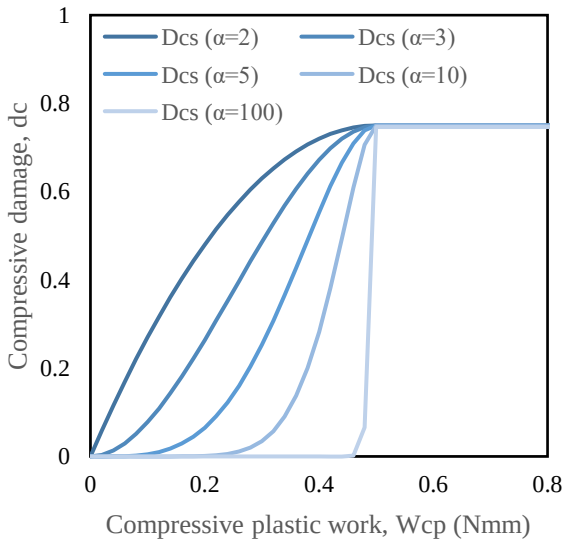

(a) damage parameter D_{cs}

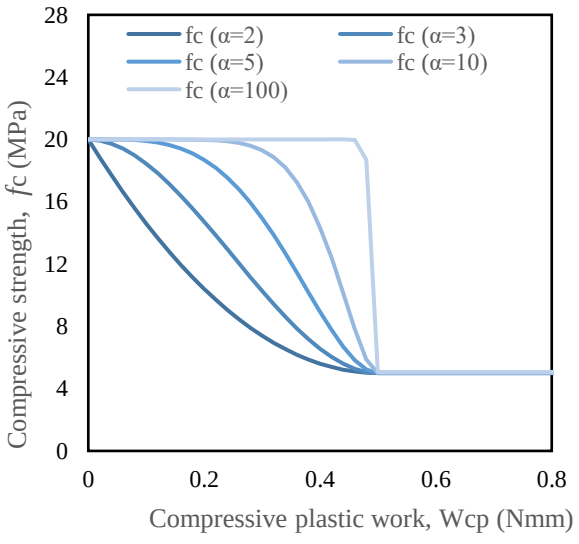

(b) compressive strength f_c

Fig. 6-4 Evolution of softening

It should be noted that α should be no more than 2 to keep as a polynomial function.

For the sake of numerical implementation, separating above equation to two new formula based on hardening and softening behaviour respectively, where the hardening expression is:

$$f_{ch} = \begin{cases} f_{ci} + (f_{cu} - f_{ci})\left(\dfrac{2W_c^p}{G_{fch}} - \left(\dfrac{W_c^p}{G_{fch}}\right)^2\right)^{\beta}, & W_c^p \le G_{fch} \\ f_{cu}, & W_c^p > G_{fch} \end{cases} \tag{6.11}$$

And the softening can be expressed by using damage parameter D_{nc}

$$D_{nc} = \begin{cases} 0, & W_c^p \le G_{fch} \\ \left(1 - \dfrac{f_{cr}}{f_{cu}}\right)\left[\alpha\left(\dfrac{W_c^p - G_{fch}}{G_{fcs}}\right)^{\alpha-1} - (\alpha - 1)\left(\dfrac{W_c^p - G_{fch}}{G_{fcs}}\right)^{\alpha}\right], & G_{fch} < W_c^p \le G_{fc} \\ \left(1 - \dfrac{f_{cr}}{f_{cu}}\right), & W_c^p > G_{fc} \end{cases} \tag{6.12}$$

$$f_{cs} = (1 - D_{nc}) f_{cu} \tag{6.13}$$

6.3 Numerical implementation

Hardening-plasticity is written as:

$$[\mathrm{J}] = \frac{\partial\{r\}}{\partial(\{\bar{\sigma}\}, d\lambda)} = \begin{bmatrix} [\mathrm{I}] + d\lambda[K^0]\dfrac{\partial\{m_c\}}{\partial\{\bar{\sigma}\}} & [K^0]\{m_c\} \\ \{n_c\}^{\mathrm{T}} & \dfrac{\partial F}{\partial d\lambda} \end{bmatrix} \tag{6.14}$$

where

$$\frac{\partial F}{\partial d\lambda} = \frac{\partial F}{\partial W^p}\frac{\partial W^p}{\partial d\lambda} = \frac{\partial F}{\partial W^p}\frac{\partial dW^p}{\partial d\lambda} \tag{6.15}$$

Considering the plastic work is an incremental accumulated state variable:

$$W_c^{p,t+1} = W_c^{p,t} + dW_c^{p,t+1} \tag{6.16}$$

where

$$dW_c^{p,t+1} = d\lambda(|\bar{\sigma}_n m_n| + |\bar{\sigma}_s m_s|) \tag{6.17}$$

And known variable $W_c^{p,t}$ is independent on the $d\lambda$, therefore,

$$\frac{\partial F}{\partial d\lambda} = \frac{\partial F}{\partial W^p}\frac{\partial dW^p}{\partial d\lambda} \tag{6.18}$$

where

$$\frac{\partial F}{\partial W^p} = -2f_{ch}\frac{\partial f_{ch}}{\partial W^p} \tag{6.19}$$

And the gradient of f_{ch} to W^p is derived based on (6.11) as:

$$\frac{\partial f_{ch}}{\partial W^p} = \begin{cases} \left(f_{cu} - f_{ci}\right)\left(\frac{2}{G_{fch}} - \frac{2W_c^p}{{G_{fch}}^2}\right)\beta\left(\frac{2W_c^p}{G_{fch}} - \left(\frac{W_c^p}{G_{fch}}\right)^2\right)^{\beta-1}, & W_c^p \le G_{fch} \\ 0, & W_c^p > G_{fch} \end{cases} \tag{6.20}$$

It should be noted that $\frac{\partial f_{ch}}{\partial W^p}$ is not the slope of $f_{ch} - u_n$ curve. In elastoplastic model, the hardening modulus $\frac{\partial f_{ch}}{\partial u_n}$ should be smaller than the elastic stiffness K^0 to avoid the diverge issue.

Algorithm. 2.1 Damage-(hardening) plasticity interface model for the compressive cap model

1: Given variables: $W^{p,t}$; $\{\sigma\}^t$; $\{du\}^{t+1}$; $[D]^t$; $[K^0]$; α; β

2: Effective stress: $\{\overline{\sigma}\}^t = ([I] - [D]^t)^{-1}\{\sigma\}^t$
Trial stress: ${}^{trial}\{\overline{\sigma}\}^{t+1} = \{\overline{\sigma}\}^t + [K^0]\{du\}^{t+1}$

3: Compute: ${f_{ch}}^t = f_{ch}(W^{p,t})$; $\frac{\partial f_{ch}}{\partial W^p}(W^{p,t})$

4: Yield surface: ${}^{trial}F = F({}^{trial}\{\overline{\sigma}\}^{t+1}, {f_{ch}}^t)$

5: Elastic status:
IF $\left({}^{trial}F \le 0\right)$ **THEN**
$\{\overline{\sigma}\}^{t+1} = {}^{trial}\{\overline{\sigma}\}^{t+1}$; $W^{p,t+1} = W^{p,t}$; $[D]^{t+1} = [D]^t$

6: Plastic status:
ELSE
$\{\overline{\sigma}\}^{j=0} = {}^{trial}\{\overline{\sigma}\}^{t+1}$; $W^{p,j=0} = W^{p,t}$; $\|r\|^{j=0} = 1$; $d\lambda^{j=0} = 0$

7: NR Loop
DO WHILE ($\|r\|^j >$ TOL)

8: Compute: $\{n\}^j$; $\{m\}^j$; $\left[\frac{\partial\{m\}}{\partial\{\overline{\sigma}\}}\right]$; ${f_{ch}}^j = f_{ch}(W^{p,j})$; F^j

9: Assembly Jacobian $[\mathrm{J}]^j$ and its inverse matrix $\left([\mathrm{J}]^j\right)^{-1}$

10: Compute residual vector and its norm: $\{r\}^j$; $\|r\|^j$

IF$\left(\|r\|^{j} \leq \mathrm{TOL}\right)$ $Converge!$ **EXIT** $NR\ Loop$

$W_c^{p,j} = W_c^{p,t} + dW_c^{p,j}$

11: Compute $\begin{Bmatrix}\delta\{\overline{\sigma}\}^{j+1} \\ \delta d\lambda^{j+1}\end{Bmatrix} = -\left([\mathrm{J}]^{j}\right)^{-1}\{r\}^{j}$; $\begin{Bmatrix}\{\overline{\sigma}\}^{j+1} \\ d\lambda^{j+1}\end{Bmatrix} = \begin{Bmatrix}\{\overline{\sigma}\}^{j} \\ d\lambda^{j}\end{Bmatrix} + \begin{Bmatrix}\delta\{\overline{\sigma}\}^{j+1} \\ \delta d\lambda^{j+1}\end{Bmatrix}$

IF$\left(d\lambda^{j+1} < 0\right)$ $d\lambda^{j+1} = 0$

$j = j + 1$;

IF$(j > jMax)$ **THEN**

$'Diverge!'$; $\Delta^{t+1} = \frac{\Delta^{t+1}}{2}$; redo computation at $t+1$; **EXIT** $NR\ Loop$

ENDDO

12: Compute $dW^{p,t+1} = dW^{p}(\{\overline{\sigma}\}^{j}, \{m\}^{j}, d\lambda^{j})$ and update plastic variables

$\{\overline{\sigma}\}^{t+1} = \{\overline{\sigma}\}^{j}$; $W^{p,t+1} = W^{p,j}$; $[D]^{t+1} = [D](W^{p,t+1})$

ENDIF

13: Update nominal stress: $\{\sigma\}^{t+1} = ([I] - [D]^{t+1})\{\overline{\sigma}\}^{t+1}$

6.4 Numerical validation

To validate the proposed constitutive model in **Section 6.2**, the implementation algorithm in **Section 6.3** is programmed as a user defined material subroutine (UMAT) for the finite element (FE) code Abaqus (version 6.14) which is powerful in analysing nonlinear problems. The interface model is implemented by using a 4-node cohesive element (COH2D4) which is fully restrained on the bottom edge and a displacement controlled load is applied vertically on the top edge. Modelling results are compared with the monotonic experimental result (specimen named as *strong mortar*) from Kaushik et al (2007) and cyclic experimental result (specimen named as *B1*) from Oliveira et al (2006). Prisms with 5 clay bricks and 4 layer 10 mm thickness mortar joints tested by Kaushik et al (2007) and Oliveira et al (2006) are 400 mm and 280 mm height respectively. Material properties for the interface model are listed in **Table 6-1**. Others material parameters of all models are the same, including $C_{nn} = 1$, $C_{ss} = 9$ and $C_n = 0$. The convergence tolerance of the NR iteration is defined as 0.00001 with a maximum loop number 999 to avoid the endless iteration.

Table 6-1. Interface properties of the uniaxial compressive test

Test units	K_n^0 N/mm^3	K_s^0 N/mm^3	G_{fch} N/mm	G_{fcs} N/mm	f_{ci} MPa	f_{cu} MPa	f_{cr} MPa	β	α
Monotonic Kaushik et al (2007)	50	25	4	10	1	7.5	1.5	0.8	3.5
Cyclic Oliveira et al (2006)	50	40	50	65	5	29	2	0.55	3.5

In **Fig. 6-5**, the modelling results predicted by the model with hardening/softening evolution have better consistency with the experimental results in terms of both strength variation and stiffness reduction. In the initial loading stage, the masonry prism has a high elastic stiffness that will gradually decrease during the loading process. To meet the good correlation in elastic-hardening stage, the normal elastic stiffness K_n^0 in model only with softening response has to

be calibrated much lower than that in model with hardening/softening response, as listed in **Table 6-1**.

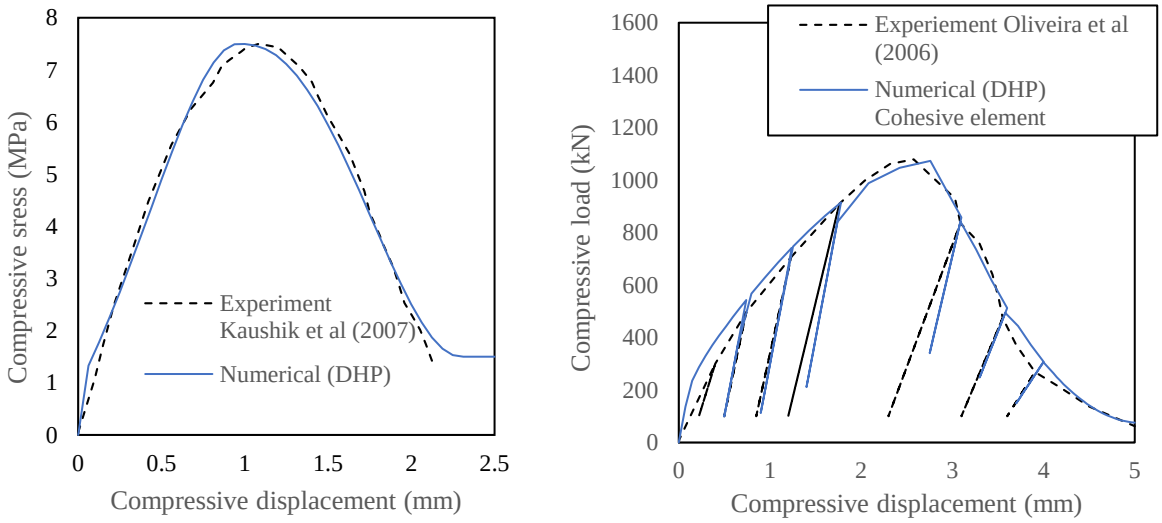

(a) monotonic (b) cyclic

Fig. 6-5 Uniaxial compressive experimental/modelling result comparison

6.5 Conclusion

A damage-plasticity model is proposed for predicting the nonlinear response of masonry under monotonic and cyclic compressive loadings. The constitutive behaviour of the interface model is developed based on the traction-separation law in a 2D space which is commonly used in simplified micro-model for simulating the nonlinear behaviour of masonry structures. Compared with the plasticity model, the proposed model considering the effect of damage has capability to predict the stiffness degradation of masonry under the cyclic loading. Besides, the computational efficiency and robustness is greatly improved by introducing the damage parameter to control the softening response of the stress-displacement (relative) relations. Compared with the damage model, the inelastic deformation in present model can be calculated efficiently by using implicit integration method to prevent the overestimation of the stiffness degradation, which is an inevitable disadvantage existing in the pure damage model. To simplify the numerical implementation, damage and plasticity are decoupled algorithmically in nominal and effective stress spaces separately.

The evolution of the damage parameter along with the plastic work can be determined as either softening or hardening/softening expressions. All variables used in the proposed damage parameter equation have physical meanings except the configure coefficient α which is proposed to calibrate the shape of strength softening. In comparison with previous analytical equations from literatures, the proposed polynomial expression is a continuous curve which can be differentiated or integrated conveniently.

6.6 References

Andreotti, G., Graziotti, F., & Magenes, G. (2018). Detailed micro-modelling of the direct shear tests of brick masonry specimens: the role of dilatancy. Engineering Structures, 168, 929-949.

Bui, T. T., Limam, A., & Sarhosis, V. (2021). Failure analysis of masonry wall panels subjected to in-plane and out-of-plane loading using the discrete element method. European Journal of Environmental and Civil Engineering, 25(5), 876-892.

Burton, C., Visintin, P., Griffith, M., & Vaculik, J. (2021, December). Laboratory investigation of pull-out capacity of chemical anchors in individual new and vintage masonry units under quasi-static, cyclic and impact load. In Structures (Vol. 34, pp. 901-930). Elsevier.

Calderón, S., Arnau, O., & Sandoval, C. (2019). Detailed micro-modeling approach and solution strategy for laterally loaded reinforced masonry shear walls. Engineering Structures, 201, 109786.

Derakhshan, H., Griffith, M. C., & Ingham, J. M. (2013). Out-of-plane behavior of one-way spanning unreinforced masonry walls. Journal of Engineering Mechanics, 139(4), 409-417.

Di Nino, S., & Luongo, A. (2019). A simple homogenized orthotropic model for in-plane analysis of regular masonry walls. International Journal of Solids and Structures, 167, 156-169.

Greco, F., Leonetti, L., Luciano, R., Pascuzzo, A., & Ronchei, C. (2020). A detailed micro-model for brick masonry structures based on a diffuse cohesive-frictional interface fracture approach. Procedia Structural Integrity, 25, 334-347.

Griffith, M. C., Vaculik, J., Lam, N. T. K., Wilson, J., & Lumantarna, E. (2007). Cyclic testing of unreinforced masonry walls in two‐way bending. Earthquake Engineering & Structural Dynamics, 36(6), 801-821.

Ingham, J., & Griffith, M. (2010). Performance of unreinforced masonry buildings during the 2010 Darfield (Christchurch, NZ) earthquake. Australian Journal of Structural Engineering, 11(3), 207-224.

Kaushik, H. B., Rai, D. C., & Jain, S. K. (2007). Stress-strain characteristics of clay brick masonry under uniaxial compression. Journal of materials in Civil Engineering, 19(9), 728-739.

Lotfi, H. R., and Shing, P. B. (1994). Interface model applied to fracture of masonry structures. Journal of structural engineering, 120(1), 63-80.

Lourenço, P. B., and Rots, J. G. (1997). Multisurface interface model for analysis of masonry structures. Journal of engineering mechanics, 123(7), 660-668.

Milani, G., Lourenço, P., & Tralli, A. (2007). 3D homogenized limit analysis of masonry buildings under horizontal loads. Engineering Structures, 29(11), 3134-3148.

Oliveira, D. V., Lourenço, P. B., & Roca, P. (2006). Cyclic behaviour of stone and brick masonry under uniaxial compressive loading. Materials and structures, 39(2), 247-257.

Sarhosis, V., & Lemos, J. V. (2018). A detailed micro-modelling approach for the structural analysis of masonry assemblages. Computers & Structures, 206, 66-81.

Smoljanović, H., Živaljić, N., Nikolić, Ž., & Munjiza, A. (2018). Numerical analysis of 3D dry-stone masonry structures by combined finite-discrete element method. International Journal of Solids and Structures, 136, 150-167.

Su, Y., Wu, C., & Griffth, M. C. (2011). Modelling of the bond–slip behavior in FRP reinforced masonry. Construction and Building Materials, 25(1), 328-334.

Vaculik, J., & Griffith, M. C. (2018). Out-of-plane shaketable testing of unreinforced masonry walls in two-way bending. Bulletin of Earthquake Engineering, 16(7), 2839-2876.

Chapter 7: A comprehensive multi-surface damage-plasticity based model

Nie Y, Sheikh A, Visintin P, Griffith M. Simulation of masonry structures under monotonic/cyclic loading conditions with an interfacial based multi-surface damage-plastic model. Submitted to Computer Methods in Applied Mechanics and Engineering (submitted).

Statement of Authorship

Title of Paper	Simulation of masonry structures under monotonic/cyclic loading conditions with an interfacial based multi-surface damage-plastic model
Publication Status	☐ Published ☐ Accepted for Publication ☑ Submitted for Publication ☐ Unpublished and Unsubmitted w ork w ritten in manuscript style
Publication Details	Nie Y, Sheikh A, Visintin P, Griffith M. Simulation of masonry structures under monotonic/cyclic loading conditions with an interfacial based multi-surface damage-plastic model. (submitted to Computer Method of Applied Mechanism and Engineering).

Principal Author

Name of Principal Author (Candidate)	Yu Nie		
Contribution to the Paper	Proposed the constitutive model and implement it by numerical method. Validate the proposed model by comparing numerical models with experimental results. Write and modify the manuscript.		
Overall percentage (%)	70%		
Certification:	This paper reports on original research I conducted during the period of my Higher Degree by Research candidature and is not subject to any obligations or contractual agreements with a third party that would constrain its inclusion in this thesis. I am the primary author of this paper.		
Signature		Date	10 May 2022

Co-Author Contributions

By signing the Statement of Authorship, each author certifies that:

i. the candidate's stated contribution to the publication is accurate (as detailed above);
ii. permission is granted for the candidate in include the publication in the thesis; and
iii. the sum of all co-author contributions is equal to 100% less the candidate's stated contribution.

Name of Co-Author	Abdul Sheikh		
Contribution to the Paper	Proposed the general concept and gave guidance of the methodology Supervised the technical development. Evaluate and revised the manuscript.		
Signature		Date	10 May 2022

Name of Co-Author	Phillip Visintin		
Contribution to the Paper	Supervised the technical development. Evaluate and revised the manuscript.		
Signature		Date	10 May 2022

Name of Co-Author	Michael Griffith		
Contribution to the Paper	Supervised the technical development. Evaluate and revised the manuscript.		
Signature		Date	10 May 2022

Please cut and paste additional co-author panels here as required.

Abstract

In this chapter, a new traction-separation based constitutive model for use in finite element simulation of masonry joints under complex loading conditions, is developed for cohesive elements. The proposed model is formulated using damage parameters and plastic deformation with mutual couplings, and can accurately simulate the complex nonlinear behaviours of masonry joints considering hardening or softening of strength and stiffens degradation. To enhance the numerical stability of the model, plasticity and damage are separated algorithmically and implemented in two phases. In the first phase, the plastic deformations are treated using a multi-surface plasticity model composed of a smooth hyperbolic yield surface for tension-shear mixed-mode failure and an elliptical cap primarily for the compressive failure. This is implemented in effective stress space and helps restrict the evolution of yield surfaces with no softening, significantly enhancing the efficiency of stress return mapping by the closed point projection method. In addition, an adaptive sub-stepping scheme is adopted to further improve the robustness of the numerical implementation. In the second phase, nominal stresses are computed from the effective stresses using damage parameters. The evolution of these damage parameters is defined in terms of plastic work with is defined by a polynomial forms, and is recommended in this study for a better calibration capability. Improvements are made in the formulation of compressive cap including incorporation of hardening of strength and stiffness degradations as these are ignored in existing interface models. This approach helped improve simulation of the masonry under cyclic loads with tension-compression transitions. For the structural level applications, the interface model is implemented within a finite element program, which is utilised to simulate failure of a number of masonry specimens under in-plane/out-of-plane monotonic/cyclic loading. The simulated results are rigorously validated with existing experimental data that shows a good potential in modelling masonry structures.

7.1 Introduction

Investigation of the behaviour of masonry structures is an important work in the area of structural engineering that benefits the maintenance of significant heritage buildings and the design of new architectural buildings [1]. However, the prediction of behaviours of masonry structures is challenging due to inhomogeneity in the system and complex nonlinear material response. Though empirical based approaches [2] can provide an easy solution of this problem, they only give an approximate solution that may not be adequate to assess the safety of large masonry buildings with complex architectural forms. Thus, there is a growing trend towards the use of precise numerical modelling approaches for simulating masonry structures because they are ideal for solving complex nonlinear problems [3-10]. In this context, Lourenco[11] has classified the modelling strategies of masonry structures into three groups: 1) Detailed Micro-Modelling [12], where bricks and mortars are discretely modelled using continuum elements and brick-mortar interfaces are modelled with zero thickness cohesive elements; 2) Macro-Modelling [13, 14], where bricks and mortars are homogenized as a single continuum utilising a representative volume element (RVE); 3) Simplified Micro-Modelling [15], where bricks are modelled using continuum elements, while cohesive elements are used for mortar joints (entire thickness) and artificial joints placed inside bricks to simulate the potential crack in bricks. Amongst the above modelling strategies, the simplified micro-modelling strategy

seems an optimum approach as it can provide a balance between computational efficiency and accuracy, and this approach is adopted in this study. As the nonlinear behaviour is predominantly localised in mortar joints, and it is insignificant in brick units, the primary challenge of a simplified micro model is to accurately define the nonlinear interfacial behaviour by developing a reliable constitutive model for the cohesive element.

Existing literature shows that damage mechanics and plasticity theory are commonly used for interface models. The use of damage mechanics based interface models have became popular in simulating masonry structures [16, 17], and this is likely due to the availability of such interface models in commercially available finite element (FE) program such as ABAQUS [18]. However, these interface models [18] do not have the option for frictional resistance which is always found in shear/mode II failure of masonry. Though the frictional contact feature can be used in combination with the interface model to address this issue, it is not a good option as the transition from the softening to the friction regions is not captured well. Moreover, the determination of mixed-mode parameters under complex loading scenarios is problematic due to the lack of experimental results. For mix-mode failure simulation, the Benzeggagh-Kenane fracture criterion [19] along with its default values are popularly used [16, 17], but these values are calibrated from testing of polymer based composite materials. To avoid such issues, Alfano and Sacco [20] developed an interface model incorporating the frictional component in their formulation. However, a damage mechanics based model does not provide dilation characteristics of mortar bed joints, and this is an important feature observed in real experiments [21].

On the other hand, the use of plasticity based interface models is found to be more popular in modelling masonry structures, which may be due their better representation of the mortar failure. One of the earlier models was developed by Lofti and Shing [22] who proposed a single hyperbolic yield surface that can successfully capture the tension-shear mixed mode region without using an addition yield surface for tension cut-off. A more traditional approach was adopted by Scimemi et al. [23], who used a Mohr-Column type flat surface and another flat surface for tension cut-off. The intersection of these two yield surfaces give a sharp corner, which needs special attention during numerical implementation since it can lead to convergence problems or incorrect stress returns. As this model [23] does not have provision for checking compression failure, the model was extended further by adding another flat yield surface as a compression cap [24, 25] parallel to the surface for tension cut-off. A similar model was introduced by Sutcliffe et al. [10] and Chaimoon and Attard [26] where the flat compression cap was replaced with a conical surface. A further improvement was made by Lourenco and Rots [15] who used an elliptical surface for the compression-cap that lead to a very popular model in masonry modelling. But these models [10, 15, 24-26] gives two corners (problematic regions) produced by the three surfaces. The number of corners was reduced to one by taking two hyperbolic surfaces [7], where one was used as a compression cap. To avoid any corners without sacrificing the compression failure, single closed smooth surface having a tear-drop type shape was proposed [27, 28] but the performance of the model was not satisfactory.

In general, plasticity based models appear to be much better but they do not have the provision of stiffness degradation, which is important in masonry structured subjected to cyclic loading due to load reversal. This limitation has motivated researchers in recent years to develop interface elements considering damage, irreversible plastic deformations, and their possible

couplings to have a realistic modelling of masonry joints. One such attempts was made by Spada et al. [9] who used yield surfaces similar to that of [23] in addition a similar failure envelopes for defining damage by extend the concept of plasticity to damage. However, linking these two failure envelops with corners made numerical implementation very cumbersome as it needs checking of sixteen different cases during integration of their model at every material point. Minga et al. [24] extended the plasticity model to incorporate damage, but model does not allow for the hardening that can be observed in compression. Also, [24] did not clarify how the problems associated with stress return near the corners. The hardening of the compression cap was considered by Xie et al [25] who developed an interface model, where the formulation is primarily governed by the damage to have a total deformation based simulation that substituted the return mapping. Yuen et al. [29] proposed a relatively simple model by using a single yield surface similar to that of [22] along with the forward Euler techniques for explicit integration of their model but did little modifications to accommodate sub-stepping.

In addition to the capabilities of the constitutive models, numerical implementation is another important aspect for the overall modelling success, but this is always is challenging because the convergence issues of the iterative solution process is often experienced in solving real complex problems. A fully implicit integration technique with closed point projection method (CPPM) is a preferred option in a plasticity based formulation as this technique is the unconditionally stable [30] and provides accurate solution [31]. However, this approach usually involves a Newton-Raphson iterative technique for the stress return mapping procedure, which can be divergent if the deformation increment in a time step is large [32] or there is a sharp region in a yield surface with high curvatures [33]. Furthermore, multi-surface models with corners introduces additional difficulties in achieving convergence since the active yield surfaces need to be updated during iterations and an improper strategy adopted in subsequent steps can led to an incorrect stress update[34]. To address these numerical issues, researchers have adopted different strategies such as line search method [35-37] for improving the convergence stability and accuracy for larger step size and exact/optimized/brute force [35, 38, 39] for detecting the correct active surfaces near corners of multi-surface plasticity models. Similar to line search method, the sub-stepping technique was adopted by some researchers [40, 41] because this technique has a generic character and it is more powerful than the line search method. Sloan [41] implemented this technique for forward Euler integration scheme while Pérez-Foguet et al. [40] did it for backward Euler integration scheme.

Though a number of models possessing different degrees of limitations and capabilities exist in literature, some issues are still unresolved and there is a need for development of a comprehensive interface model for accurate and robust failure modelling of masonry structures with computational efficiency. Such an attempt has been made in this study, by developing a coupled damage-plasticity based interfacial model for masonry joints subjected to mixed mode loading comprising of tensile, shear and compression. For this purpose, a multi-surface plasticity model is adopted that includes a smooth hyperbolic yield surface as recommended by Caballero et al. [42] and a compression cap as recommended by Lourenco and Rots [15]. A fully implicit backward Euler integration technique is used along with an adaptive sub-stepping scheme to achieve our aim. The evolution of damage parameters is defined in terms of plastic work using three newly proposed polynomial expressions for effective representation of their variations. We separated the damage and plasticity components algorithmically and

they are implemented independently that helped to improve the robustness of numerical simulation. This is achieved by using an effective stress based formulation, which helped to eliminate any softening of yield surfaces. For a better representation of the tension-compression transition encountered in cyclic loading, the hardening effect is incorporated with the compression cap. The interface model is implemented within a reliable finite element program (ABAQUS) for simulation of a number of masonry structures under monotonic and cyclic loads applied in the form of in-plane and out-of-plane mode. Finally, a through experimental validation of the simulated results is conducted using test data available in literature, which demonstrated a very good performance of the model in analysing a wide range of masonry structures.

7.2. Formulation of the interfacial constitutive model

The cracking failure progression in masonry joints (similarly applicable to other quasi-brittle type materials) can be characterised by the stress-relative displacement response at the crack interface as shown in **Fig. 7-1**. Experimental tests [43, 44] under uniaxial tension and simple shear indicate that the inelastic behaviour of mortar joints is predominantly a strain softening response, as shown in **Fig. 7-1b**. The test under uniaxial compression [45] shows a visible strain hardening region before the softening response (**Fig. 7-1c**). As the failure of masonry mortar joints is simulated by an interface model, in this study, the stress is expressed in terms of separation of mortar joints i.e., the relative displacement (u) rather than strain commonly used for continuum models.

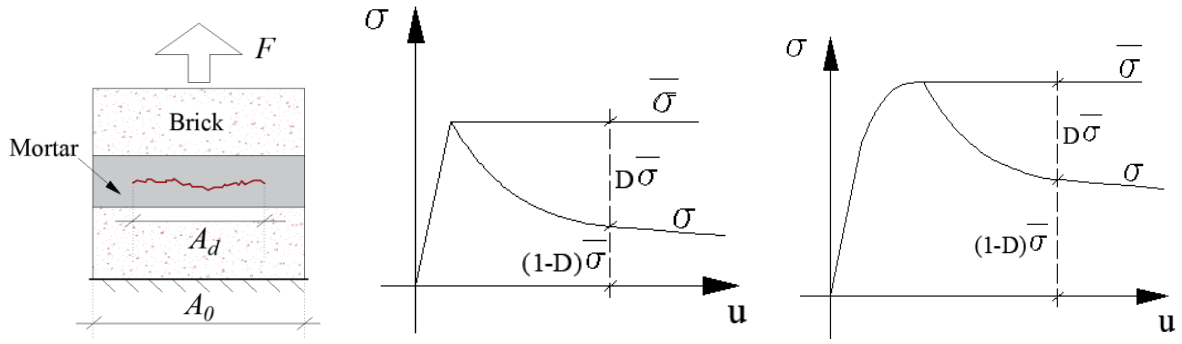

(a) a masonry couplet specimen

(b) nominal/effective ($\sigma/\bar{\sigma}$) stress vs relative displacement between crack faces (u) under uniaxial tension/shear

(c) nominal/effective ($\sigma/\bar{\sigma}$) stress vs relative displacement between crack faces (u) under uniaxial compression

Fig. 7-1. Characterization of masonry joint failure with nominal and effective stresses

During the initial stage of loading after yielding, some micro-cracks are formed in masonry mortar joints or cement matrix as well as interface between coarse aggregates and cement paste of concrete structures. With the gradual increase of loading F, micro-cracks grow, propagate and joined together to form a macro-crack (see **Fig. 7-1a**). The degree of failure can be defined using the damage parameter D, which is the ratio of damaged area of the mortar

interface A_d to its initial gross area A_0 (**Fig. 7-1a**). For a damaged joint, the nominal stress and effective stress are defined as $\sigma = F/A_0$ and $\bar{\sigma} = F/(A_0 - A_d)$ respectively, and they can be related using the damage parameter as $\sigma = (1 - D)\bar{\sigma}$. It is to be noted that the value of nominal stress (σ) changes with the change of load (F) only as A_0 is constant while the effective stress ($\bar{\sigma}$) depends on the current load as well as current undamaged area. The formation of micro-cracks degrades the additional load resisting capability that shows strain hardening behaviour, which is prominent for compressive loading (**Fig. 7-1c**). Once the macro-cracks are formed, the load resistance of the material/mortar is dropped that shows a strain softening response (**Fig. 7-1b, c**). For the tensile and shear loading, the delay between the formations of micro- and macro-cracks is not significant and leads to a negligible strain hardening region. Unlike the nominal stress (that follows the variation pattern of load F), the effective stress remains constant without any drop after the peak load, and this helps to improve the robustness in numerical modelling.

To achieve an accurate solution, the proposed constitutive model is integrated using a fully implicit/ backward Euler method because it is unconditionally stable if the time step size (load increment in the present case) is not too big. However, to enhance the robustness of the solution involving a Newton-Raphson iterative technique, an effective stress based formulation is adopted as effective stress remains constant after the peak point with no apparent softening (analogues to elastic-perfectly plastic scenario). The real softening of the material in nominal stress space can be obtained from the post peak constant effective stress using the damage parameters. This is beneficial as most of the convergence problems are associated with the tracking of the softening branch found in nominal stress space. Moreover, an adaptive sub-stepping scheme is adopted for further improvement of the robustness of solution. This has provided added benefit for smoothly tracing the hardening branch found under compressive loading. The interfacial constitutive model has two stress components and their representations in nominal and effective stress spaces can be related as:

$$\begin{Bmatrix}\sigma_n\\ \sigma_s\end{Bmatrix} = \begin{bmatrix}1-D_n & 0\\ 0 & 1-D_s\end{bmatrix}\begin{Bmatrix}\bar{\sigma}_n\\ \bar{\sigma}_s\end{Bmatrix}; \quad \{\sigma\} = ([I] - [D])\{\bar{\sigma}\} \tag{7.1}$$

where $[I] = diag\{1,1\}$ is a unit matrix; subscripts n and s are used to denote the normal and shear components respectively; and other notations follow the previous descriptions.

In the elastic range of the interface, the traction-separation ($\{\bar{\sigma}\} - \{u\}$) relationship in effective stress space can be expressed as:

$$\begin{Bmatrix}\bar{\sigma}_n\\ \bar{\sigma}_s\end{Bmatrix} = \begin{bmatrix}K_n^0 & 0\\ 0 & K_s^0\end{bmatrix}\begin{Bmatrix}u_n\\ u_s\end{Bmatrix}; \qquad \{\bar{\sigma}\} = [K^0]\{u\} \tag{7.2}$$

where K_n^0 and K_s^0 are elastic stiffness of the interfacial in normal and shear mode of deformations.

The formulation for the inelastic response of the proposed interface model involves two stages: plasticity in first stage and damage evolution in second stage, which are presented in the following sections.

7.2.1 Plasticity formulation of the interface

A multi-surface plasticity models as shown in **Fig. 7-2** is used for the proposed interface model. The yield surface of the model consists of a smooth hyperbolic curve F_1 for simulating the behavior under tension-shear mixed mode of loading and an elliptical curve F_2 to simulate the behavior under compression (**Fig. 7-2**). In the effective stress space, these yield surfaces (F_1 and F_2) can be expressed as:

$$F_1 = -(f_s - \bar{\sigma}_n tan\phi) + \sqrt{\bar{\sigma}_s{}^2 + (f_s - f_t \cdot tan\phi)^2} \tag{7.3}$$

$$F_2 = C_{nn}\bar{\sigma}_n{}^2 + C_{ss}\bar{\sigma}_s{}^2 + C_n\bar{\sigma}_n - f_c{}^2 \tag{7.4}$$

where f_t, f_c, f_s and $tan\phi$ are tensile strength, compressive strength, shear strength and frictional coefficient of the interface; C_{nn} and C_{ss} are configuration parameters that control the size of the ellipse (F_2) in normal and shear directions, while C_n determine the positon of the elliptic center on $\bar{\sigma}_n$ axis.

.

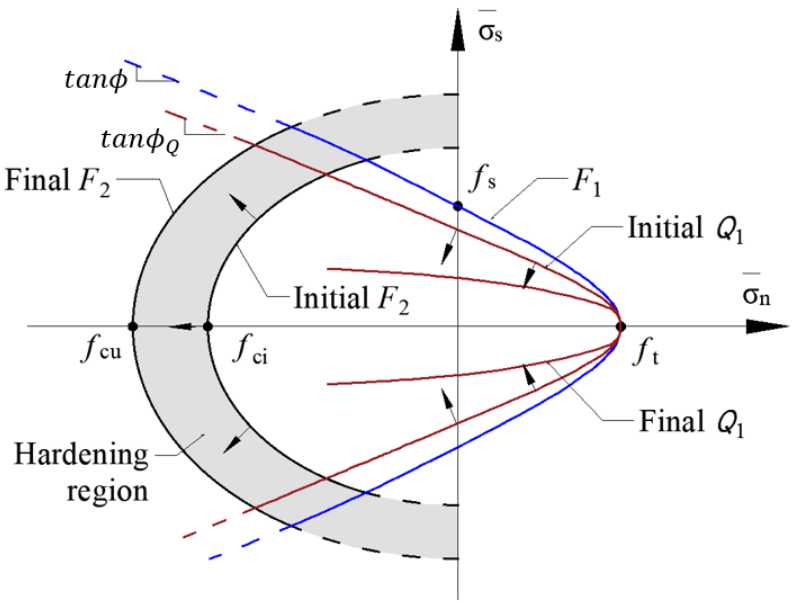

Fig. 7-2. Yield and potential surfaces in effective stress space and their possible evolutions

.

The hyperbolic curve F_1 is adopted from Caballero et al. [42] who proposed a tension-shear mixed-mode interface model within a pure plasticity framework to simulate the cracking failure of concrete materials. In their work, which is based on nominal stress space, the yield surface has a hyperbolic curve and contracts gradually as the material softens, and finally reduces to a conical surface with a sharp corner that can be a source of convergence problems during the stress return mapping. As the present work is based on the effective stress space, the curve F_1 does not contract as its parameters (f_t, f_s and $tan\phi$) remain constant and its behaviour is similar to an elastic-perfectly plastic model. The elliptic surface F_2 is used for the compressive cap, which is adopted from Lourenco and Rots [15] who proposed a pure plasticity based interface model having Mohr-Column type yield surface with tension cut-off along with the compressive cap. As the model of [15] is based on nominal stress space, F_2 will shrink after peak load due the material softening, which can cause numerical instability during the stress return mapping procedure [36]. Grassl and Rempling [46] proposed a model using a single yield surface having a full elliptical shape and formulated their model in effective stress space which helped to minimize the convergence problem due to this numerical instability. This has motivated us to formulate our model in effective stress space that will restrict the evolution of F_2 (present model) in the hardening region only ($f_{ci} \leq f_c \leq f_{cu}$) in the form of expansion (**Fig. 7-2**) with no further change or shrinking during the strain softening region after peak load (f_{cu}). The evolution of F_2 in the hardening region only and no evolution of F_1 has helped to enhance the robustness of our numerical implementation.

A typical non-associated behavior is observed in the post elastic deformation of quasi-brittle materials such as mortar joints or masonry bricks since their dilation angle ϕ_Q controlling the direction of plastic deformation is much smaller than the frictional angle ϕ defining the yield surface. This needs a plastic potential surface Q_1 (**Fig. 7-2**), different from F_1 (non-associated), where Q_1 is dependent on dilation coefficient $tan\phi_Q$ for estimating plastic deformations. However, the compressive cap in present work follows the associated flow rule, thus its potential surface Q_2 is the same as the yield surface F_2 as it does not involve a frictional component of the material response. The expression of the potential surfaces are as follows, where Q_1 is obtained from F_1 (**Eq. 7.3**) by replacing ϕ with ϕ_Q.

$$Q_1 = -\left(f_s - \bar{\sigma}_n tan\phi_Q\right) + \sqrt{\bar{\sigma_s}^2 + (f_s - f_t \cdot tan\phi_Q)^2} \tag{7.5}$$

$$Q_2 = F_2 \tag{7.6}$$

During hardening of the compression cap, the evolution of the compressive strength f_c needed to define F_2 or Q_2 (**Eq. 7.4**) is expressed in terms of accumulated plastic work W^p used as internal variable (see **Section 7.2.2**). The same internal variable is used to define the evolution of damage parameter needed to estimate the nominal stress of the compression cap from its effective stress in the strain softening range. Similarly, plastic work (dissipated energy) is used to define the evolution of the damage parameter for tension-shear mixed-mode deformation characterized by F_1. In numerical implementation, the integral form of plastic work is computed incrementally as $W^p = \int dW^p = \sum dW^p$ by updating its value after convergence of every load increment. The increment of plastic work dW_1^p and dW_2^p corresponding to the two yield surfaces F_1 and F_2 can be defined as:

$$dW_1^p = \begin{cases} \bar{\sigma}_n du_n^{p1} + \bar{\sigma}_s du_s^{p1}, & \bar{\sigma}_n \geq 0 \\ \left|du_s^{p1}\right|(|\bar{\sigma}_s| + \bar{\sigma}_n tan\phi), & \bar{\sigma}_n < 0 \end{cases} \tag{2.7}$$

$$dW_2^p = \bar{\sigma}_n du_n^{p2} + \bar{\sigma}_s du_s^{p2} \tag{2.8}$$

The estimation of dW_1^p depends on the nature of normal stress σ_n i.e., tension or compression. If the interface is under tension ($\bar{\sigma}_n \geq 0$), the dissipated energy is produced by both normal and shear deformations, while the effect of shear deformation is only considered under compression ($\bar{\sigma}_n < 0$) with a deduction for the frictional component $\left(\left|du_s^{p1}\right| \cdot \bar{\sigma}_n tan\phi\right)$ since it is not included in characterize the cohesive behavior and related fracture energy in shear. On other hand, the determination of dW_2^p depends on normal and shear modes of deformation and it is not affected by the nature of normal stress. The 2D cohesive model presented above can be easily extended to 3D model by incorporating another shear component and the resulting formulation of the 3D model is presented in.

7.2.2 Evolution of damage parameters and nominal stresses

Due to heterogeneity in the behavior of mortar-brick joints under different modes of deformation, the degradation of interface strengths during material softening is determined by using three different damage parameters corresponding to tensile (d_t), shear (d_s) and compressive (d_c) modes of failures. A single scale damage parameter may be conveniently used for continuum models for isotropic material [47,48], but multiple damage parameters are needed for interfacial based constitutive models [49] or continuum models for anisotropic materials such as wood [39] or composites [50]. The experimental testing of masonry couplet/prism specimens under uniaxial tension [44], uniaxial shear [43] and uniaxial compression [45] show dissimilar response in terms of their strengths and fracture energies. The damage parameters used in the present model are expressed in terms of plastic work, fracture energies, material strength parameters, and some additional parameters controlling the shape of damage evolution (shape parameters) as:

$$d_t = \begin{cases} \alpha_t \left(\frac{W_1^p}{G_{ft}}\right)^{\alpha_t - 1} - (\alpha_t - 1)\left(\frac{W_1^p}{G_{ft}}\right)^{\alpha_t}, & W_1^p < G_{ft} \\ 1, & W_1^p \geq G_{ft} \end{cases} \tag{2.9}$$

$$d_s = \begin{cases} \alpha_s \left(\frac{W_1^p}{G_{fs}}\right)^{\alpha_s - 1} - (\alpha_s - 1)\left(\frac{W_1^p}{G_{fs}}\right)^{\alpha_s}, & W_1^p < G_{fs} \\ 1 & W_1^p \geq G_{fs} \end{cases} \tag{2.10}$$

$$d_c = \begin{cases} 0, & W_2^p \le G_{fch} \\ \left(1-\frac{f_{cr}}{f_{cu}}\right)\left[\alpha_c\left(\frac{W_2^p - G_{fch}}{G_{fcs}}\right)^{\alpha_c - 1} - (\alpha_c - 1)\left(\frac{W_2^p - G_{fch}}{G_{fcs}}\right)^{\alpha_c}\right], & G_{fch} < W_2^p \le G_{fc} \\ \left(1-\frac{f_{cr}}{f_{cu}}\right), & W_2^p > G_{fc} \end{cases} \quad (2.11)$$

where G_{ft}, G_{fs} and G_{fc} are fracture energies for tensile, shear and compressive modes of deformation; α_t, α_s and α_c are shape parameters for tensile, shear and compressive mode of damage evolution; f_{cu} and f_{cr} are ultimate and residual compressive strengths. It is to be noted that the hardening component G_{fch} and the softening component G_{fcs} of G_{fc}(= G_{fch}+G_{fcs}) are needed separately to express the damage parameter under compression d_c.

With these damage parameters, the damage matrix appeared in **Eq. (7.1)** can be formed as:

$$[D] = \begin{bmatrix} D_n & 0 \\ 0 & D_s \end{bmatrix} \quad (7.12)$$

where

$$D_n = \begin{cases} d_t, & \sigma_n \ge 0 \\ d_c, & \sigma_n < 0 \end{cases} \quad \text{and} \quad D_s = \begin{cases} d_s, & \sigma_n \ge 0 \\ d_s \dfrac{f_{s0}}{f_{s0} + |\sigma_n| tan\phi}, & \sigma_n < 0 \end{cases} \quad (7.13)$$

With the damage parameters, the nominal stress components (normal and shear) under opening and closing modes of deformation are expressed as:

$$\sigma_n = \begin{cases} f_t = (1-d_t) f_{t0} & \textbf{Opening mode} \\ f_c = \begin{cases} f_{ci} + (f_{cu} - f_{ci})\left(\dfrac{2W_2^p}{G_{fch}} - \left(\dfrac{W_2^p}{G_{fch}}\right)^2\right)^{\beta}, & W_2^p \le G_{fch} \\ (1-d_c) f_{cu}, & W_2^p > G_{fch} \end{cases} & \textbf{Closing mode} \end{cases} \quad (7.14)$$

$$\sigma_s = f_s = \begin{cases} (1-d_s) f_{s0}, & \textbf{Opening mode} \\ \left(1 - d_s \dfrac{f_{s0}}{f_{s0} + |\sigma_n| tan\phi}\right) f_{s0}, & \textbf{Closing mode} \end{cases} \quad (7.15)$$

where f_{ci} is the initial compressive strength at the onset of yielding; β is the shape parameter for the evolution of compressive strength during hardening. It should be noted that, unlike other strength parameters, the evolution of compressive strength during hardening is not dependent on damage parameters, but it needs plastic work and hardening part of the fracture energy apart from the initial and ultimate compressive strengths.

The variations of damage parameters and strengths with respect to plastic works under different modes of uniaxial loading are plotted in **Fig. 7-3**. The strength parameters are degraded gradually with the increase of damage parameters, which are in turn dependent on the plastic work (W_1^p and W_2^p). For tensile loading, the influence of the shape parameter α_t on the variation of strength is shown in **Fig. 7-3a** where the rate of strength degradation at the initial stage (lower value of W_1^p) is found to be very small for a higher value α_t. This is absolutely negligible as the curve became initially flat for α_t > 3 and the flat region extends with the increase of α_t. This is similarly observed in **Fig. 7-3b** and **Fig. 7-3c**, which demonstrate that shape parameters (α_t, α_s and α_c) can efficiently help to calibrate the strength parameters in terms of plastic works. **Fig. 7-3b** shows that the shear strength of the interface decrease to zero when the interface is subjected to tension or no normal loading, while the interface has a residual strength due to frictional resistance ($|\sigma_n| \cdot tan\phi$) if the interface is under compression.

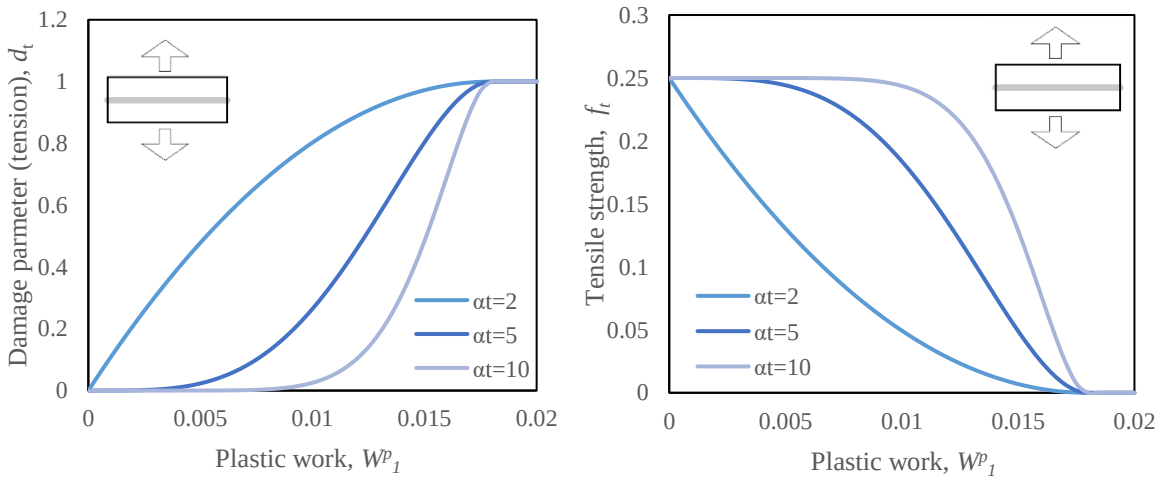

(a) evolution of damage and strength under tension

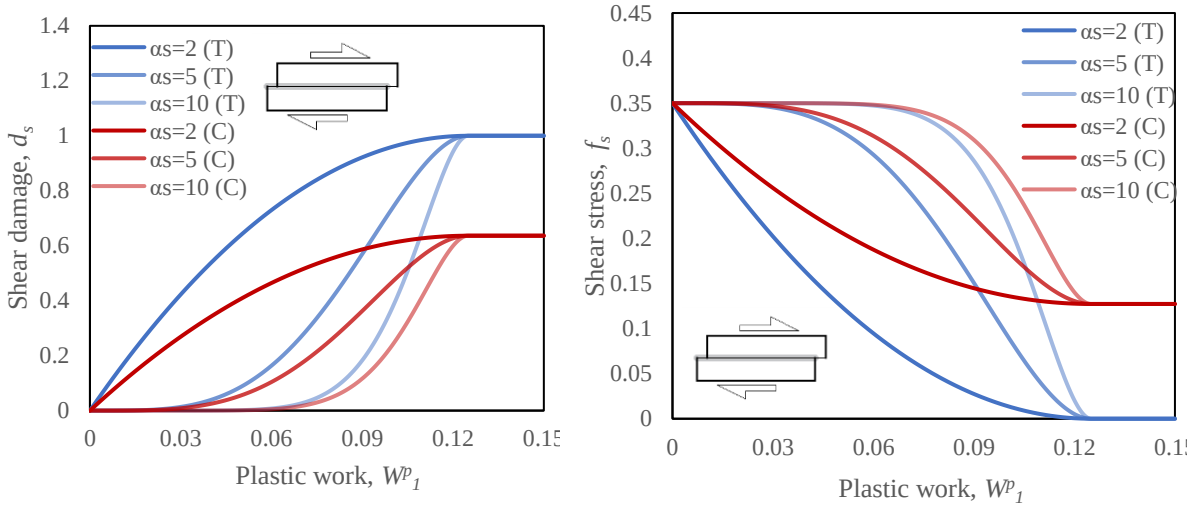

(b) uniaxial shear damage and strength

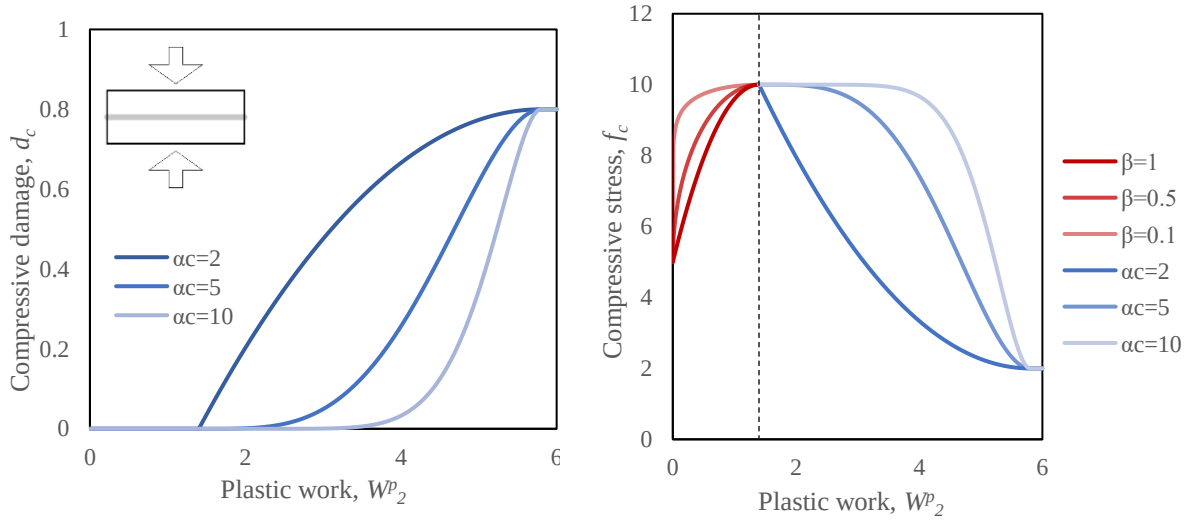

(c) uniaxial compressive damage and strength

Fig. 7-3 Evolution of damage and strength of masonry joints under different modes of uniaxial loading

.

Fig. 7-3c shows the behavior of the interface under compression, where the curves for the strength evolution are divided into hardening and softening regions at the same point (indicated by the vertical dashed line) when the plastic work W_2^p reaches the value of G_{fch} (portion of the fracture energy under compression corresponds to the hardening part). Also, the hardening curve becomes stiffer with the decrease of hardening shape parameter β.

It should be noted that, the value of hardening shape parameter β should be 1 or less (not negative) while the softening shape parameters α_t, α_s and α_c should be 2 and more (may be $+\infty$).

7.2.3 Evolution of dilation coefficient

The direct shear tests conducted by Chainmoon [51] on masonry couplets show that the normal displacement of joints caused by the dilation effects was gradually reduced with the shear loading to a small constant value that may be close to zero in some scenarios (**Fig. 4**). This experimental observation indicates that the dilation coefficient $tan\phi_Q (= du_n^p/du_s^p)$ has softening characteristics with the progression of shear loading. This effect is incorporated in the present model through a parameter $d_{\phi Q}$ which is used to simulate the degradation of the dilation coefficient $tan\phi_Q$ from its initial and residual values $tan\phi_{Q0}$ and $tan\phi_{Qr}$, respectively, as recommended in **Eq. (7.16)**.

$$tan\phi_Q = \begin{cases} tan\phi_{Q0} - (tan\phi_{Q0} - tan\phi_{Qr})d_{\phi_Q}, & W_1^p < G_{fs} \\ tan\phi_{Qr}, & W_1^p \geq G_{fs} \end{cases} \tag{7.16}$$

where

$$d_{\phi_Q} = \left[\alpha_{\phi Q}\left(\frac{W_1^p}{G_{fs}}\right)^{\alpha_{\phi Q}-1} - (\alpha_{\phi Q} - 1)\left(\frac{W_1^p}{G_{fs}}\right)^{\alpha_{\phi Q}}\right]$$

The above parameter $d_{\phi Q}$ is expressed in terms of plastic work W_1^p, fracture energy under shear G_{fs}, and a shape parameter $\alpha_{\phi Q}$ in the form of a polynomial as recommend in **Eq. (7.16)**. The concept behind the proposed expression for $d_{\phi Q}$ is extracted from the formats used for defining the damage parameters. The variation of $tan\phi_{Qr}$ with respect to W_1^p is plotted in **Fig. 7-5**, which shows a similar pattern as found for the damage parameter i.e., the curve becomes more flat in the initial stage with the increase of $\alpha_{\phi Q}$.

.

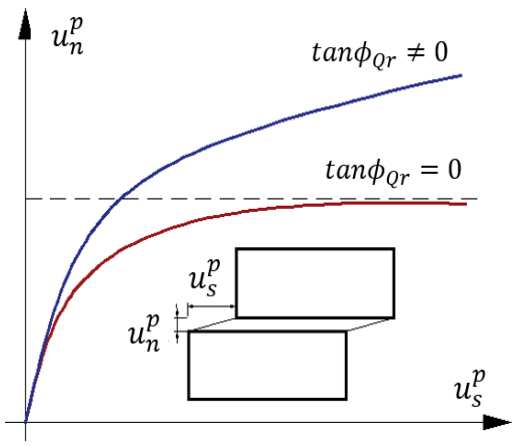

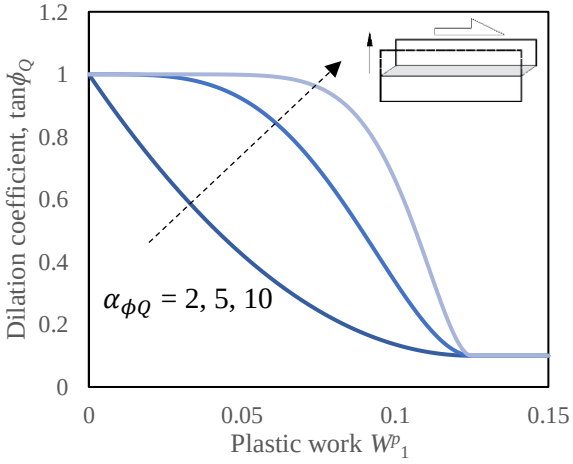

Fig. 7-4. Variation of normal displacement vs shear displacment (relative) under shear loading [51]

Fig.7-5. Evolution of dilation coefficient with respect to plastic work under shear loading

.

7.3. Numerical implementation

The effective stress based formulation used for the proposed model facilitates the separation of damage and plasticity components algorithmically, as mentioned earlier, which helps to improve the computational efficiency and robustness in the implementation of the constitutive model in an incremental-iterative scheme. The main steps associated with its numerical implementation for a load step/increment are listed below and the flow of operation is shown in **Fig. 7-6**.

1) Transferring nominal stress $\{\sigma^t\}$ from the converged previous load/time step " t " to effective stress $\{\bar{\sigma}^t\}$ by using the damage matrix $[D^t]$;
2) From $\{\bar{\sigma}^t\}$, the effective stress $\{\bar{\sigma}^{t+1}\}$ and plastic work $W^{p,t+1}$ in the current load/time step "t+1" are iteratively computed by using an elastic predictor-plastic corrector strategy until the converged is attained;
3) Using $W^{p,t+1}$, the damage matrix $[D^{t+1}]$ is updated and it is used to calculate the nominal stress $\{\sigma^{t+1}\}$ for the time step "t+1".

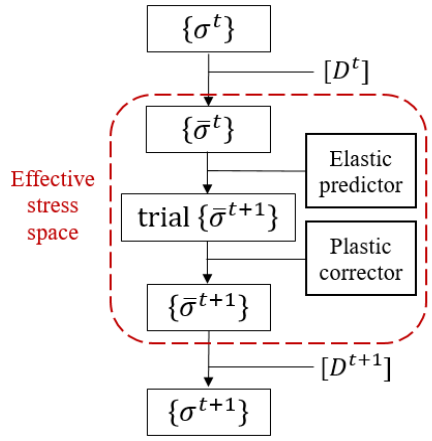

Fig. 7-6 Overall process for stress update

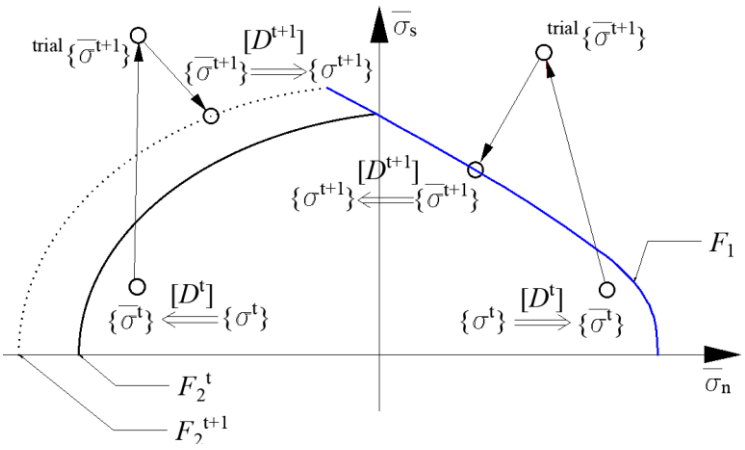

Fig. 7-7 Stress return mapping progress

Fig. 7-7 shows the stress return mapping procedure in the effective stress space for a typical load step. First the trail stress ${}^{trial}\{\bar{\sigma}^{t+1}\}$ is calculated as elastic predictor from $\{\bar{\sigma}^t\}$, and it is found outside of the yield surface i.e., $F\left({}^{trial}\{\bar{\sigma}\}^{t+1}\right) > 0$, the material is in inelastic stage and a fully implicit backward Euler integration scheme is utilized for the stress return mapping procedure to calculate $\{\bar{\sigma}^{t+1}\}$. For the tension-shear mixed mode loading scenario, the trail stress ${}^{trial}\{\bar{\sigma}^{t+1}\}$ returns back to the fixed (non-evolving) hyperbolic yield surface F_1

following the closet point projection method (CPPM) introduced by Simo and Hughes [34]. In case of compression or compression-shear mode of loading, ${}^{trial}\{\bar{\sigma}^{t+1}\}$ returns back to the yield surface F_2 (compressive cap), which can expand (evolve) during hardening stage but remains fixed (not moving) after peak load (see **Fig. 7-2**).

7.3.1 Determination of the correct active surface

For multi-surface plasticity models, a complex scenario is commonly encountered when the trial stress is located near a corner i.e., interaction of multiple yield surfaces, which can lead to wrong stress return mapping due to selection of incorrect yield surface. A typical region near a corner is shown in **Fig. 7-8** where the region of the effective stress space can be divided into 6 sub-regions (**E**$_L$, **B**$_1$, **B**$_2$, **C**$_1$, **C**$_2$, **A**) produced by the yield surfaces F_i (F_1 and F_2 in our model) and their normal (i.e., plastic flow) directions $\partial F_i/\partial\{\sigma\}$. If the trial stress is located within **E**$_L$, which is enveloped by the yield surfaces, the stress point is in the elastic domain of the stress space and no stress return mapping is needed and the trial stress (elastic predictor) is the final stress. If the trial stress point is located in region **B**$_2$ ($F_1 < 0$, $F_2 > 0$) or region **C**$_2$ ($F_1 > 0$, $F_2 < 0$), the correct yield surface will be F_2 or F_1, respectively that will be used for the stress return. However, both yield surfaces are active in terms of violating yield condition i.e., $F_1 > 0$ and $F_2 > 0$, if the trial stress point is in region **B**$_1$, **C**$_1$ and **A**. For a general case of multi-surface plasticity models having any number of yield surfaces, the active set of yield surfaces for a trial set can be expressed as:

$$\{\mathbb{J}_{act}\} = \{i \in \{1, 2 \dots \dots\} \mid F_i > 0\} \tag{7.17}$$

.

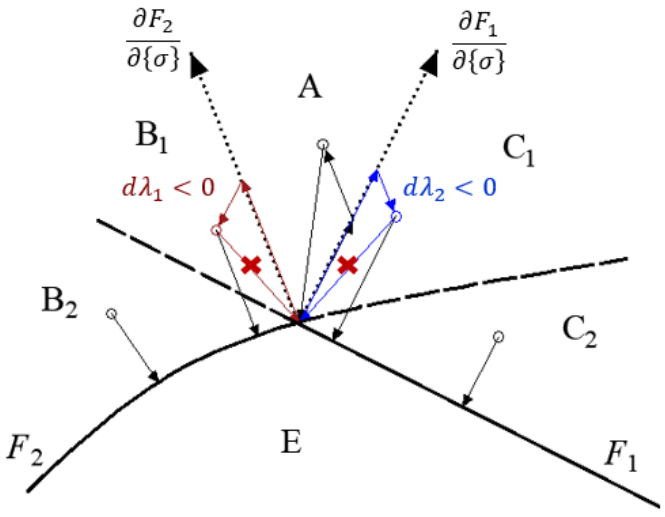

Fig. 7-8. Return mapping path of the multi-surface plasticity model

In this scenario, we need to identify the correct yield surface from this set of active surfaces for stress return. A simple solution of this problem has been adopted in some studies (e.g., [7]) where the trial stress point belong to all these regions (**B**$_1$, **C**$_1$ and **A**) predicted by **Eq. (7.17)** is returned back to the corner. However, this may lead to incorrect stress return that

may be significant in some occasions. For example, the trial stress in **B₁** should return back to F_2 but not F_1 (see **Fig. 7-8**). Thus the stress return from the trial stress point belonging to different regions (**B₁**, **C₁** and **A**) should be treated separately to avoid any issue, which needs identification of the correct region (**B₁**, **C₁** or **A**).

Therefore, the stress return mapping procedure of multi-surface plasticity models is more challenging than that of single surface plasticity model because the difference of region (**B₁**, **C₁** and **A**) cannot be distinguished by checking the yield conditions $F_i > 0$ only i.e., **Eq. (7.17)**. Simo and Hughes [34] recommended a generic solution that needs checking of yield conditions $F_i > 0$ as well as plastic multipliers ($d\lambda_i > 0$), which provides a more precise set of active surfaces that can be represented as:

$$\{\mathbb{J}_{act}\} = \{i \in \{1, 2 \dots \dots\} \,|F_i > 0 \text{ and } d\lambda_i > 0\} \tag{7.18}$$

Table 7-1 Stress return mapping path around corner regions

Region	F_1	F_2	$d\lambda_1$	$d\lambda_2$	$\{\mathbb{J}_{act}\}$ based on **Eq (3.1)**	$\{\mathbb{J}_{act}\}$ based on **Eq (3.2)**
A	>0	>0	>0	>0	$\{1, 2\}$	$\{1, 2\}$
B₁	>0	>0	<0	>0	$\{1, 2\}$	$\{2\}$
C₁	>0	>0	>0	<0	$\{1, 2\}$	$\{1\}$
B₂	<0	>0	=0	>0	$\{2\}$	$\{2\}$
C₂	>0	<0	>0	=0	$\{1\}$	$\{1\}$
E_L	<0	<0	=0	=0	$\{\emptyset\}$	$\{\emptyset\}$

Table 7-1 shows the possible sets of active surfaces $\{\mathbb{J}_{act}\}$ along with the values of F_i and $d\lambda_i$ for the different sub-regions shown in **Fig. 7-8**. The table shows that the set contains one active surface for sub-region **B₁** and **C₁**, which is the correct yield surface for stress return. However, the set contains two active surfaces (both F_1 and F_2) for sub-region **A** when the stress will be returned back to the corner. As the stress return is based Newton-Raphson (NR) iterative technique, different strategies may be adopted for determination of $\{\mathbb{J}_{act}\}$ and these are broadly classified by Pech et al. [39] as follows:

- Exact method: remove a yield surface F_i from the set of active surfaces $\{\mathbb{J}_{act}\}$ if $d\lambda_i < 0$ but do the checking ($d\lambda_i < 0$) and deactivate F_i only after the convergence of NR iterative method.
- Optimized method: check $d\lambda_i$ after every iteration of the NR iterative method, and update $\{\mathbb{J}_{act}\}$ by deactivating F_i once $d\lambda_i < 0$ is found.

Another method was proposed by Adhikary et al. [35] that considers all possible combinations of active surfaces. They defined this method as "dumb" as it is not efficient but found it useful in solving a complex scenario with large number of yield surfaces when the above two method did not worked.

There might be a concern with the exact and the above method since they can violate the condition ($d\lambda_i > 0$), but that should be a necessary requirement for feasible solution of a general constrained problem [52]. However, all numerical simulations in this study are solved by the optimized method that worked successfully without facing such issue.

7.3.2 Fully implicit backward Euler integration

The increment of relative displacement $\{du^{t+1}\}$ in current time/load step consists of elastic and plastic components as $\{du^{t+1}\} = \{du^{e,t+1}\} + \{du^{p,t+1}\}$ and it can be used to update the stress as:

$$\begin{aligned} \{\bar{\sigma}^{t+1}\} = \{\bar{\sigma}^{t}\} + \{d\bar{\sigma}^{t+1}\} &= \{\bar{\sigma}^{t}\} + [K^0](\{du^{t+1}\} - \{du^{p,t+1}\}) \\ &= (\{\bar{\sigma}^{t}\} + [K^0]\{du^{t+1}\}) - [K^0]\{du^{p,t+1}\} \end{aligned} \tag{7.19}$$

where the first part of the above equation provides the trial stress ${}^{trial}\{\bar{\sigma}^{t+1}\} = \{\bar{\sigma}^{t}\} + [K^0]\{du^{t+1}\}$, which is the elastic predictor, while the second part $-[K^0]\{du^{p,t+1}\}$ is the plastic corrector. Using the plastic potential functions Q_i, the increment of plastic displacement resultant for multi-surface plasticity model [53] can be determined as:

$$\{du^{p}\} = \sum_{i \in \{\mathbb{J}_{act}\}} d\lambda_i \frac{\partial Q_i}{\partial \{\bar{\sigma}\}} \tag{7.20}$$

where the subscript " i " in above equation corresponds to the set of active yield surface $\{\mathbb{J}_{act}\}$ which is defined in **Eq. (3.2)**. Substituting **Eq**. **(3.4)** into **Eq**. **(3.3)**, it can be rewritten as:

$$\{\bar{\sigma}^{t+1}\} = \left\{{}^{trial}\bar{\sigma}^{t+1}\right\} - \sum_{i \in \{\mathbb{J}_{act}\}} {d\lambda_i}^{t+1}[K^0]\left(\frac{\partial Q_i}{\partial \{\bar{\sigma}\}}\right)^{t+1} \tag{7.21}$$

The above equation cannot be solved directly due to nonlinearity, and will be solved iteratively using the NR method that will need updated stress within an iteration as well as updated yield functions or plastic multipliers within that iteration. For the implementation of the iterative technique, the full consistency condition for the yield functions are used and it is expressed as:

$$F_i = 0, \qquad i \in \{\mathbb{J}_{act}\} \tag{7.22}$$

where $F_1(\{\bar{\sigma}^{t+1}\})$ is dependent on effective stress only whilst $F_2\left(\{\bar{\sigma}^{t+1}\}, {f_c}^{t+1}\right)$ depends on both effective stress and compressive strength.

To facilitate the iterative solution scheme of **Eq. (7.21)** along with **Eq. (7.22)**, the residual vector $\{r^k\}$ for *k*-th iteration can be written as:

$$\{r^k\} = \begin{Bmatrix} \{r_\sigma^k\} \\ r_F^k \end{Bmatrix} = \begin{Bmatrix} \{\bar{\sigma}^k\} - \{^{trial}\bar{\sigma}^{t+1}\} + \sum_i d\lambda_i^k [K^0] \left(\dfrac{\partial Q_i}{\partial \{\bar{\sigma}\}}\right)^k \\ F_i^k \end{Bmatrix}, \qquad i \in \{\mathbb{J}_{act}^k\} \tag{7.23}$$

where a maximum number of iterative " $k_{\max}$ " should be pre-defined to avoid unlimited loops in case of divergence. The converging criteria used in the present study to stop the iteration is defined as:

$$\|r\| = Max(\|\{r_\sigma\}\|, |r_F|) < TOL \tag{7.24}$$

where $\|r\|$ is the norm of residual vector but it is calculated for the two components separately corresponding to **Eq. (7.21)** and **Eq. (7.22)** and the larger value is adopted. A small value of the tolerances (*TOL*) is predefined to stop the iteration with an acceptable level of solution accuracy. The increments of the effective stress vector $\{\delta\bar{\sigma}^k\}$ and the incremental plastic multipliers $\delta {d\lambda_i}^k$ (may be a vector but written in the form of index for simplicity in the presentation) within an iteration (*k*) is written as:

$$\{\delta^k\} = \begin{Bmatrix} \{\delta\bar{\sigma}^k\} \\ \delta {d\lambda_i}^k \end{Bmatrix} = [J^k]^{-1}\{r^k\}, \quad i \in \{\mathbb{J}_{act}^k\} \tag{7.25}$$

where the Jacobian matrix $[J^k]$ is the gradient of the residual vector (**Eq. 7.23**) with respect to $\{\bar{\sigma}\}$ and $d\lambda_i$ (the iteration number *k* is not written for simplicity in the presentation) and it can be expressed as:

$$[J] = \frac{\partial\{r\}}{\partial(\{\bar{\sigma}\}, d\lambda)} = \begin{bmatrix} [I] + \sum_i d\lambda_i [K^0] \dfrac{\partial^2 Q_i}{\partial \{\bar{\sigma}\}^2} & [K^0] \dfrac{\partial Q_i}{\partial \{\bar{\sigma}\}} \\ \left(\dfrac{\partial F_i}{\partial \{\bar{\sigma}\}}\right)^T & \dfrac{\partial F_i}{\partial d\lambda_i} \end{bmatrix}, \quad i \in \{\mathbb{J}_{act}^k\} \tag{7.26}$$

Using **Eq (7.25)**, the incremental plastic multiplier and the set of active yield surfaces can be updated as:

$$d\lambda_i{}^{k+1} = d\lambda_i{}^{k} + \delta d\lambda_i{}^{k}, \qquad i \in \{\mathbb{J}_{act}^{k}\} \tag{7.27}$$

$$\{\mathbb{J}_{act}^{k+1}\} = \{i \in \{1, 2 \dots \dots\} \mid \ d\lambda_i^{k+1} > 0\} \tag{7.28}$$

In some situations, $\{\mathbb{J}_{act}^{k+1}\}$ may be changed from its previous iteration $\{\mathbb{J}_{act}^{k}\}$ if one of the incremental plastic multipliers $d\lambda_i^{k+1}$ becomes negative. In that scenario, the new set of active yield surfaces is use and the iteration process is restarted from the beginning of the load step. Otherwise, proceed further after updating the effective stress and the plastic work as:

$$\{\bar{\sigma}^{k+1}\} = \{\bar{\sigma}^{k}\} + \{\delta\bar{\sigma}^{k}\} \tag{7.29}$$

$$W^{p,k+1} = W_i^{p,k} + dW_i^{p,k}, \quad i \in \{\mathbb{J}_{act}^{k}\} \tag{7.30}$$

The plastic work increment dW_i^p in the above equation can be determined by substituting **Eq. (7.20)** into **Eqs. (7.7)** and **(7.8)** is formulated as (iteration number *k* again omitted for simplicity of presentation):

$$dW_1^p = \begin{cases} d\lambda_1 \left(\sigma_n \dfrac{\partial Q_1}{\partial \sigma_n} + \sigma_s \dfrac{\partial Q_1}{\partial \sigma_s}\right), & \sigma_n \geq 0 \\ d\lambda_1 (|\sigma_s| + \sigma_n tan\phi) \left|\dfrac{\partial Q_1}{\partial \sigma_s}\right|, & \sigma_n < 0 \end{cases} \tag{7.31}$$

$$dW_2^p = d\lambda_2 \left(\sigma_n \frac{\partial Q_2}{\partial \sigma_n} + \sigma_s \frac{\partial Q_2}{\partial \sigma_s}\right) \tag{7.32}$$

.

3.3 Adaptive sub-stepping scheme for the implicit integration

Even though the implicit integration technique is unconditionally stable, theoretically, for load increments of any size [30], convergence may be an issue in reality if the integration point is subjected to a complex loading scenario due to some reason such as large curvatures of the yield surface at the tension apex [54] or the size of load step is large. The solution of this problem is the reduction of the load increment size. Though some high-end FE software [18, 55] can automatically reduce the load increment, if needed, this is applied globally i.e., all integration points of the whole structure, which significantly affects the computation efficiency. A more efficient and economic strategy is use of sub-stepping scheme in local (material model) level where the reduction of load increment is applied to severely affected integration points only.

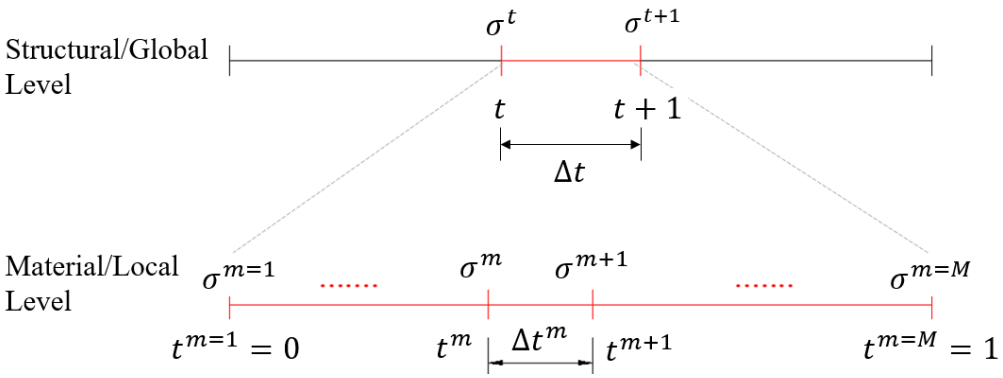

Fig. 7-9 Time steps in global (structural) and local (material) levels

As shown in **Fig. 7-9**, the time step size Δt at global level is sub-divided into a number of sub-steps, which are denoted by $t^m \in [0,1]$ and the corresponding stresses are denoted as σ^m. The size of a sub-step Δt^m is adaptively adjusted based on the performance of the NR iteration in the previous sub-step using a multiplier δ^m based on the concept of [38], which is defined as:

$$\delta^m = \max(\sqrt{k_d/k}, \zeta) \tag{7.33}$$

where k_d is a pre-defined value which is the desirable number of maximum iterations to achieve convergence and k is the number of iterations utilised in the previous sub-step. If $k < k_d$, the step size adjustment multiplier δ_m will be larger than 1, which indicates that the size of next sub-step will be larger than previous step and vice versa. Another pre-defined multiplier ζ $(0 < \zeta < 1)$ is used to control the minimum size of a sub-step. This multiplier ζ is directly used to reduce the sub-step size when the NR iteration scheme is failed in addition to calculate δ_m. For the last sub-step, t^m should not exceed 1 and this is achieved by restricting the maximum value of the sub-stepping size as:

$$\Delta t^{m+1} = \min(\delta^m \Delta t^m, 1 - t^m) \tag{7.34}$$

Fig. 7-10 shows a flowchart to demonstrate the overview of the adaptive sub-stepping procedure.

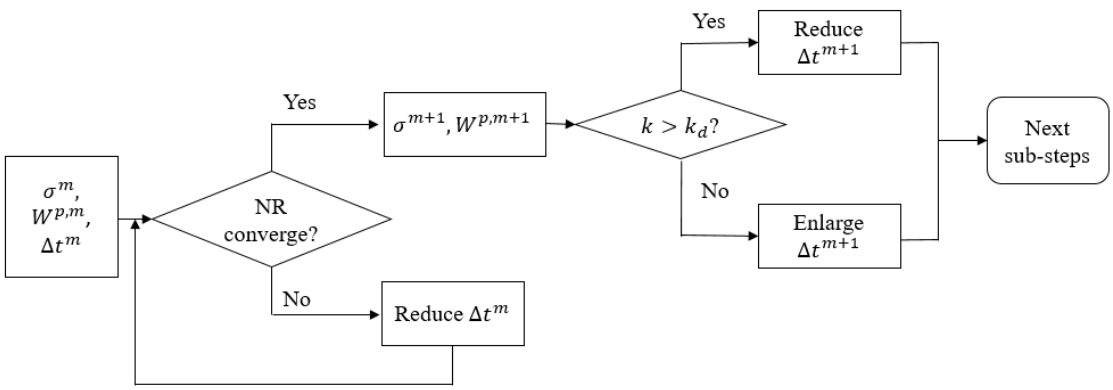

Fig. 7-10 Flow-chart for the adaptive sub-stepping procedure

7.4. Numerical analysis

7.4.1 Performance of stress return mapping technique

Before application of the proposed model at the structural scale to problems such as masonry walls, the performance of the model is scrutinized at different levels (material point, single element, and specimen) to have a thorough understanding of its performance. In this section, the numerical performance of the model at a material/integration point (i.e., stress return mapping process) is evaluated in terms of efficiency of convergence. A number of stress return mapping tests are numerically conducted with/without sub-stepping to show the importance of sub-stepping. For this purpose, both yield surfaces are assumed to be non-evolving. In this section, the results are presented in schematic form to explain the process. The stress return mapping technique is implemented numerically by writing a stand-alone program in FORTRAN

Figure 7-11 illustrates the different scenarios of stress return mapping process of a trial stress point to the yield surface F_1 where the stress point is located in the region **C2** (see **Fig. 7-8**) and bit far from F_1. For the first two cases (**Fig. 7-11a** and **Fig. 7-11b**), the sub-stepping option is not be activated, which leads to no convergence in **Fig. 7-11a** as the stress point oscillated between **N1** and **N2** with no exit while a convergence is somehow attained in **Fig. 7-11b** (trial stress point distance is relatively less) but it took a very large number of iterations.

Fig. 7-11c shows the use of sub-stepping option for the trial stress in first case (**Fig. 7-11a**) where a quick convergence is achieved with no numerical trouble. For one of its sub-steps, the return mapping process is illustrated in **Fig. 7-11d**.

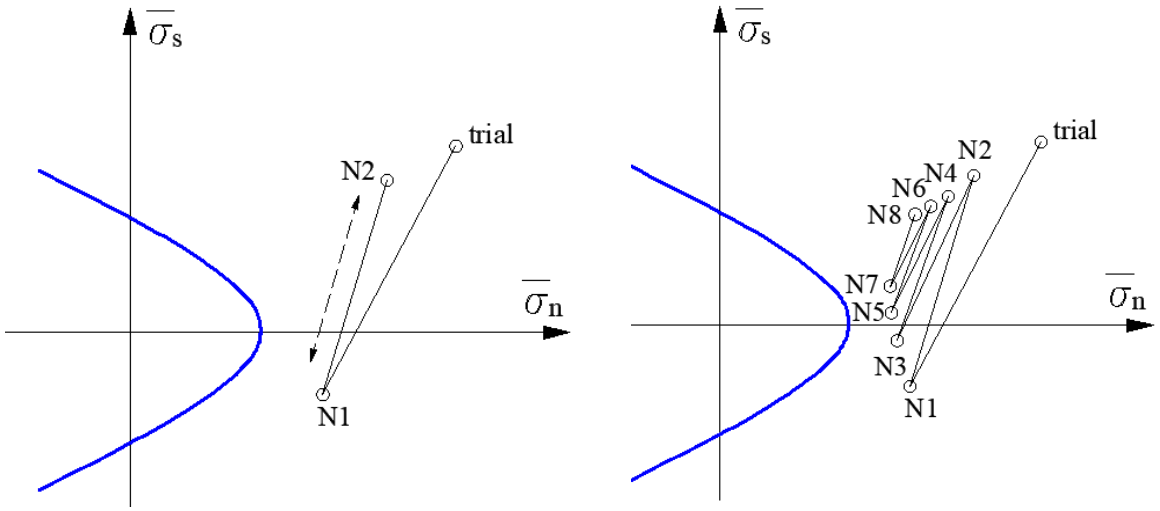

(a) infinite iteration (no convergence)

(b) converged with a large number iterations

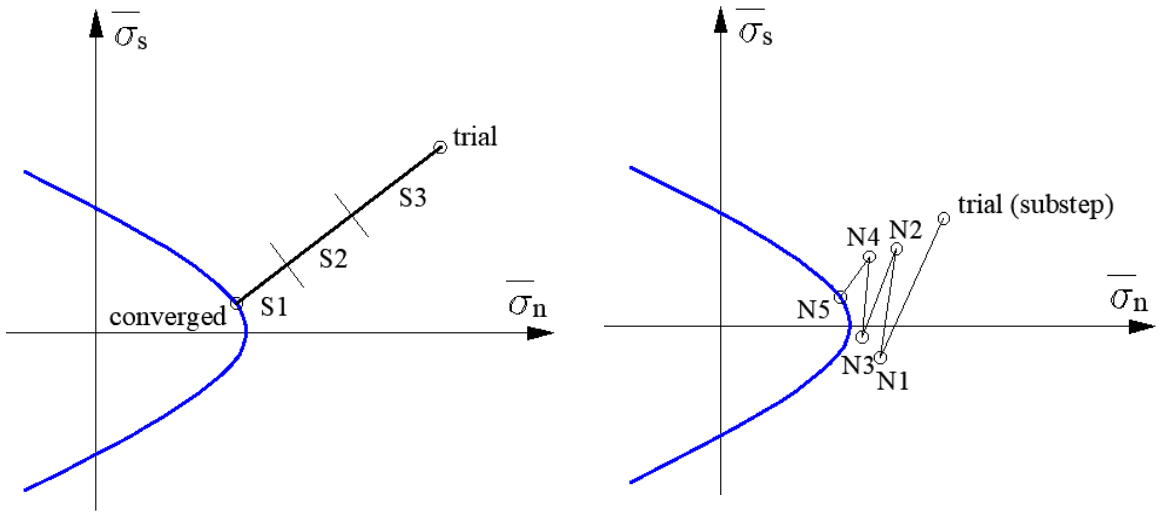

(c) sub-stepping scheme

(d) convergence within a sub-step

Fig. 7-11 Stress return mapping paths corresponding to yield surface F_1

.

Similarly, the stress return of a trial stress point located in the region $\mathbf{B_2}$ (see **Fig. 7-8**) is conducted for returning the stress point to the yield surface F_2. In this case, the stress return process performed relatively better that the previous case (**Fig. 7-11**), which is due to a gentle curvature of F_2 (elliptical curve) while the hyperbolic curve has a high curvature (sharp change) near its tip. However this took a large number of iterations that may be an issue for solving a large scale problem. The sub-stepping option is used for the same problem that has shown a significant improvement of the convergence efficiency.

Fig. 7-12 illustrates the stress return paths of a trial stress point located in the region **A** (see **Fig. 7-8**) when the sub-stepping option is not used. The stress should go back the corner point but it can drift since the stress point may be moved from region **A** to $\mathbf{B_1}$ or $\mathbf{C_1}$ (see **Fig. 7-8**) during the iterative process. This drifting can be avoided by using the sub-stepping option that helps to bring the stress point exactly at the corner. Though the deviation is small, it may be accumulated in a large size complex structural problem.

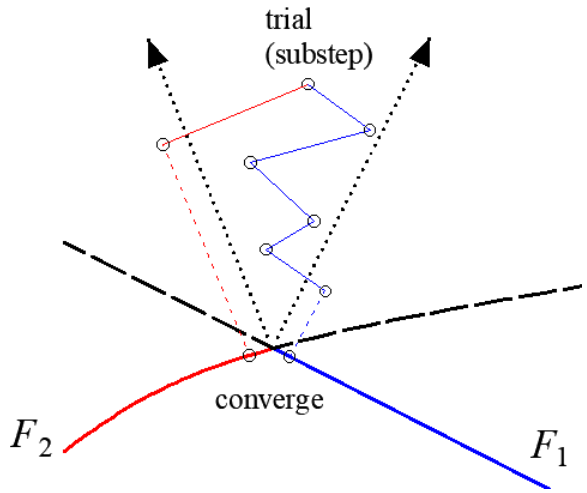

Fig. 7-12 Stress return mapping paths for the corner region

7.4.2 Single element tests for cohesive model

The proposed interfacial model is implemented in a 3D cohesive element (**Fig. 7-13**) COH3D8 which is a built-in element within the finite element (FE) program Abaqus 6.14 [18]. The 4 nodes at the bottom surface of the element are fully restrained (fixed), while the 4 nodes at its top surface are kinematically coupled with a reference point (RP), which is used as a controlling point to apply various loads on the cohesive element. The size of the cohesive element is taken as 100mm×100mm×10mm, where the 10mm thickness is used for geometric visualization only and it has no influence on the traction-separation based constitutive relationship. The numerical implementation of the interfacial model is done by writing a subroutine in FORTRAN and connected with Abaqus 6.14 as a user defined material (UMAT) model.

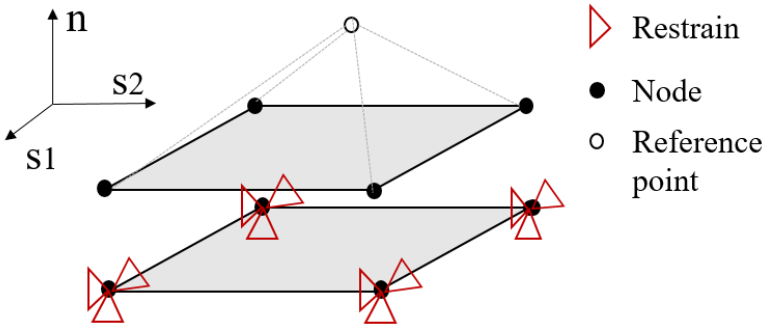

Fig. 7-13 Cohesive element with boundary conditions and reference point

.

Table 7-2 Material properties for single element test (cohesive model)

Material Properties	unit	T or T-UR	C or C-UR	T-C-Cyc	S or S-UR or S-Cyc	T-S-Mix

K_n	N/mm^3	82	82	82	-	82
K_s	N/mm^3	-	-	36	36	36
f_{t0}	MPa	0.25	-	1	-	0.25
G_{ft}	N/mm	0.018	-	0.09	-	0.018
f_{s0}	MPa	-	-	-	0.35	0.35
$tan\phi$		-	-	-	0.75	0.75
G_{fs}	N/mm	-	-	-	0.125	0.125
f_{ci}	MPa	-	2.5	2.5	-	-
f_{cu}	MPa	-	5	5	-	-
f_{cr}	MPa	-	1	1	-	-
G_{fch}	N/mm	-	0.4	0.4	-	-
G_{fcs}	N/mm	-	4.4	4.4	-	-

Hardening/softening material/shape parameters

β	α_c	α_t	α_s	$\alpha_{\phi Q}$
1	3	2	2	2

For the single element tests, the material properties and the shape parameters related to hardening/softening curves are listed in **Table 7-2** where T, C, S denotes uniaxial tension, compression and shear mode of monotonic loading, UR represent unloading/reloading, while Cyc and Mix indicates cyclic and mixed-mode loading, respectively. The response of the element under uniaxial tensile loading is plotted in **Fig. 7-14a** in the form of stress-displacement (relative) curve, which shows that model has well captured the strain softening behavior as well as stiffness degradation during unloading-reloading conditions. **Fig. 7-14b** shows the response of the element under uniaxial compression where the stiffness remains intact during strain hardening stage but stiffness degradation is found during strain softening region. A slightly more complex loading scenario is simulated by loading the element in tension beyond the elastic range but before the failure, and it is then loaded in compression as shown in **Fig. 7-14c**. The response shown in this figure indicates that the stiffness, degraded due to tensile softening, is restored to its intact value K_n^0 when the interface entered into the compressive loading region ($\sigma_n < 0$) due to crack closure in the masonry joint. **Fig. 7-14c** also included the response of the element under pure tension and pure compression for comparison.

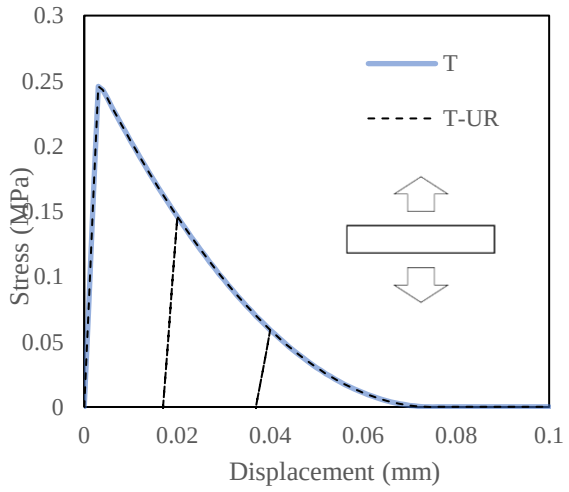

(a) Uniaxial tension

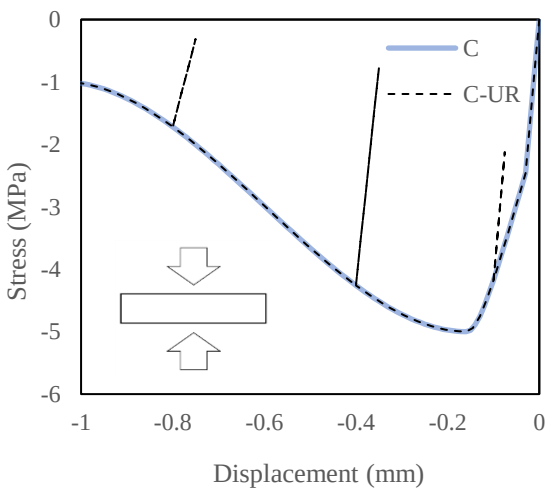

(b) Uniaxial compression

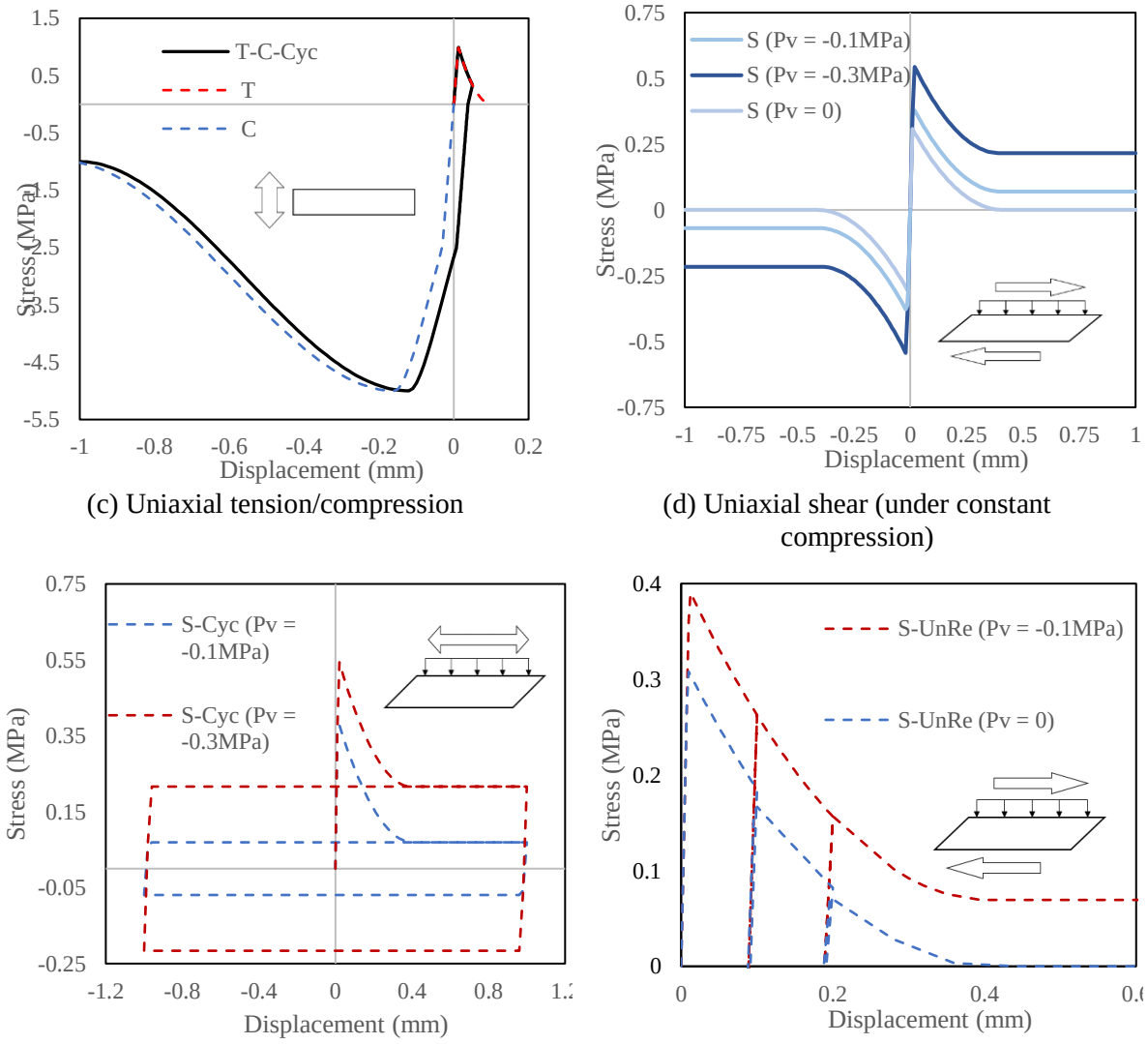

(c) Uniaxial tension/compression

(d) Uniaxial shear (under constant compression)

(e) Cyclic uniaxial shear (under constant compression)

(f) Uniaxial shear (under constant compression) with unloading and reloading

Fig. 7-14 Response of the cohesive element under different mode of loading

.

To investigate the fractional behavior of the interface, the element is subjected to shear loading with a constant pre-pressure and the response predicted by the model is plotted in in **Fig. 7-14d**. The simulation is conducted taking three different values of the pre-pressure (0, -0.1MPa, and -0.3MPa), and shows that a higher pre-pressure increases peak shear strength as well as residual frictional resistance. The shear responses are also symmetrical with respect to both forward and reverse directions of loading (u_s and $-u_s$). **Fig. 7-14e** shows the shear response of the interface under cyclic shear loading with two different level of constant pre-pressures (-0.1MPa and -0.3MPa) where the response is presented for a full cycle. After dissipation of the mode II (shear) fracture energy during the softening region, the frictional component plays an important role as the residual shear resistance still helps to contribute in the load carrying process. This is beneficial for structures subjected to dynamic loading such as earthquake by absorbing more energy. In **Fig. 7-14f**, the stiffness degradation of the interface under shear loading with a constant pre-pressure is shown by unloading and reloading of the

shear load, which shows a similar characteristics as found in the first case (**Fig. 7-14a**) under uniaxial tension.

As the normal displacement is influenced by the shear response due to dilation of the interface (see **Section 7.2**), a mixed-mode of loading scenario is investigated taking 45^0 loading path (i.e., equal shear and tensile displacements) and different dilation coefficients. The simulated response presented in **Fig. 7-15a** (tension) and 7-**15b** (shear) reveals that the dilation angle influences the peak load and softening response. A higher value of dilation coefficient $\tan\phi_Q$ is found to deteriorate the tensile response (**Fig. 7-15a**) while it helps to improve the shear response (**Fig. 7-15b**).

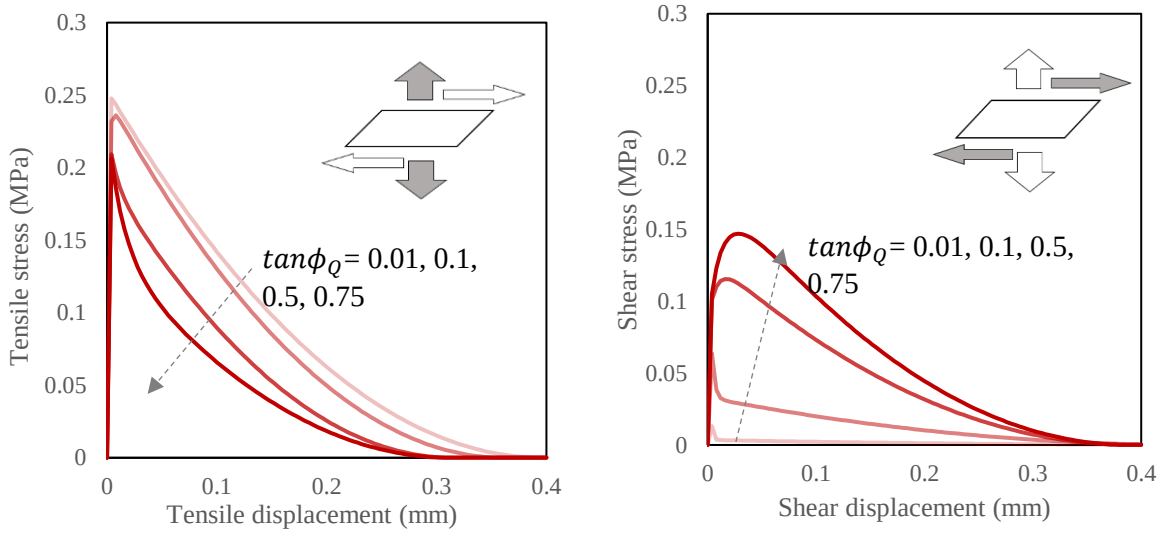

(a) Tensile behaviour (b) Shear behaviour

Fig. 7-15 Effect of dilation coefficient on the interface subjected mixed-mode loading

.

7.4.3 Specimen (Couplet/prism) level validation

In this section, the proposed model is validated using couplets and prismatic specimens made of a few bricks, which are subjected to monotonic and cyclic loadings. A brick unit is modelled with solid element (C3D8R) using meshing size of 4×2×2 while the cohesive elements (COH3D8) is used for mortar joints that followed the meshing arrangement of the bricks. The cohesive elements used the coupled damage-plasticity based constitutive model developed in this study while the bricks are assumed to be elastic. Though the implicit static solver has been used for the single element test, the implicit dynamic solver with a quasi-static mode is adopted from this section to minimize the convergent issue at global/structural level (FE analysis) as the complexity of the problems, need to be simulated, will be increased. For the numerical modelling conduced in this section, the material properties used for the interface are listed in **Table 7-3**. The density used for the mortar joints as well as brick and are 2000 kg/m^3 but it is appropriately scaled internally by the quasistatic option of the ABAQUS solver.

Table 7-3 Material properties of the mortar joints for couplet/prismatic specimens

Material Parameters	unit	Uniaxial tension (T)	Uniaxial shear (S)	Cyclic shear (S-Cyc)	Compression (un/re-loading) (C-UR)	Shear (un/re-loading) S-UR, Pv = -0.28MPa	Shear (un/re-loading) S-UR, Pv = -0.51MPa
K_n	N/mm^3	82	-	-	300	-	-
K_s	N/mm^3	-	400	36	-	10	4.25
f_{t0}	MPa	0.3	-	-	-	-	-
G_{ft}	N/mm	0.035	-	-	-	-	-
α_t		2	-	-	-	-	-
f_{s0}	MPa	-	1.2	1.2	-	0.07	0.3
$tan\phi$		-	1	0.67	-	0.82	0.76
G_{fs}	N/mm	-	0.25	3.78	-	0.082	0.14
α_s		-	2	2	-	2	2
f_{ci}	MPa	-	-	-	2	-	-
f_{cu}	MPa	-	-	-	29	-	-
f_{cr}	MPa	-	-	-	2	-	-
G_{fch}	N/mm	-	-	-	8	-	-
G_{fcs}	N/mm	-	-	-	20	-	-
β		-	-	-	0.5	-	-
α_c		-	-	-	3	-	-
$tan\phi_{Q0}$		-	1	0.1	-	0.15	0.15
$tan\phi_{Qr}$		-	0.1	0.01	-	0.065	0.001
$\alpha_{\phi Q}$		-	2	2	-	2	4

A displacement controlled tension test was carried out by Pluijm [44] on clay brick masonry couplets each made of two brick units (size of a unit: 210 mm×80 mm×100 mm) and a 10mm thick mortar joint between the units (**Fig. 7-16a**) where 80mm is the height. The experimental results (post elastic softening response) reported by them Pluijm [44] are presented in **Fig. 7-16a** for the validation of numerical results predicted by the proposed model for the same problem (uniaxial tension test of the masonry couplet). The numerical results are mostly enveloped within the measured test data set. Similarly, the direct shear tests was conducted by Pluijm [43] on masonry couplets having same geometry and materials by imposing three different levels of constant pre-pressure (0.1MPa, 0.5MPa, and 1.0MPa) applied vertically. The couples under this loading scenario are simulated with the prosed model and the predicted results are presented with the test results [43] in **Fig. 7-16b** for experimental validation. The variation of shear stress with respect to the inelastic displacement (**Fig. 7-16b**) shows an exponential softening followed by a constant residual friction. In the numerical modelling, the values of the shape parameters α_t and α_s are taken as 2 to simulate the exponential softening as observed in the experiment. **Fig. 7-16b** shows a good correlation between the numerical and experimental results.

Atkinso et al. [56] carried out cyclic shear tests on masonry couplets having a different size and configuration as shown in **Fig. 7-16c** using two levels of constant pre-pressure (1.34MPa and 4.31MPa) for a complete cycle. The numerical sumulation of these speciments

is conduced by the proposed model, and the predicted results (shear stress-relative displacement variation) are validated with the experimental results [56] in **Fig. 7-16c**. Modelling results have a good agreement with experiments in terms of peak load and residual frictional resistance.

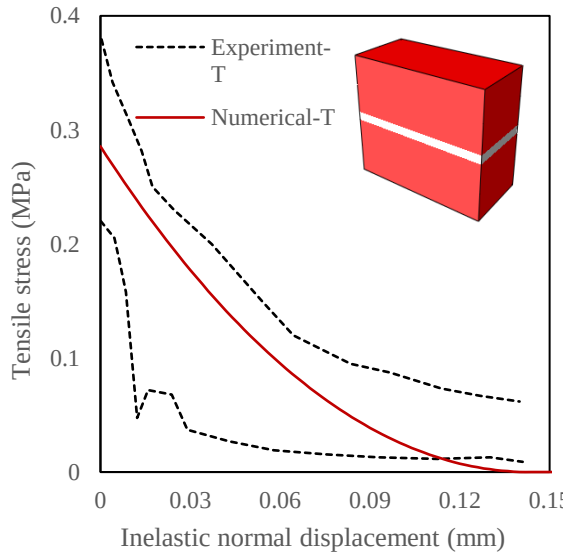

(a) Uniaxial Tension

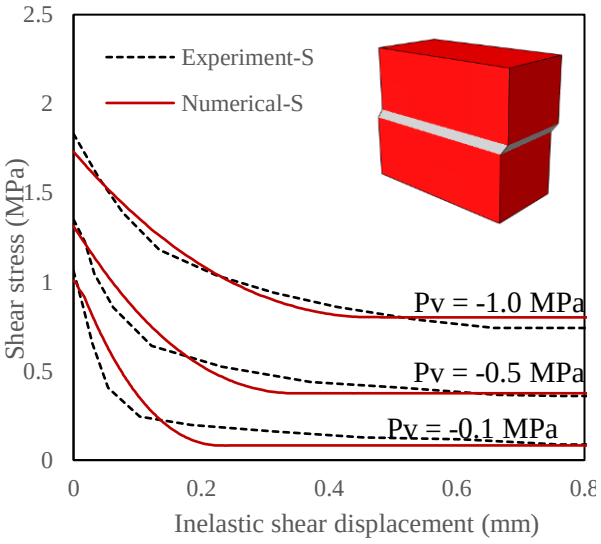

(b) Uniaxial Shear

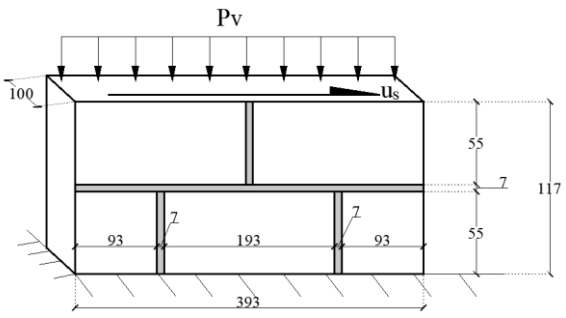

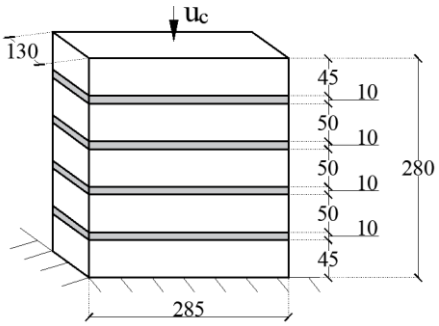

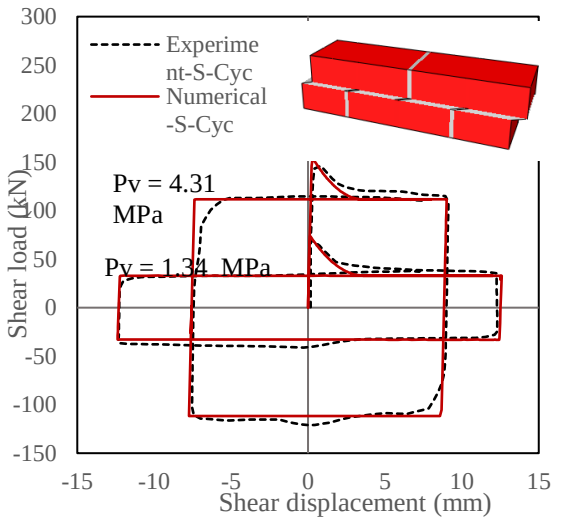

(c) Cyclic Shear

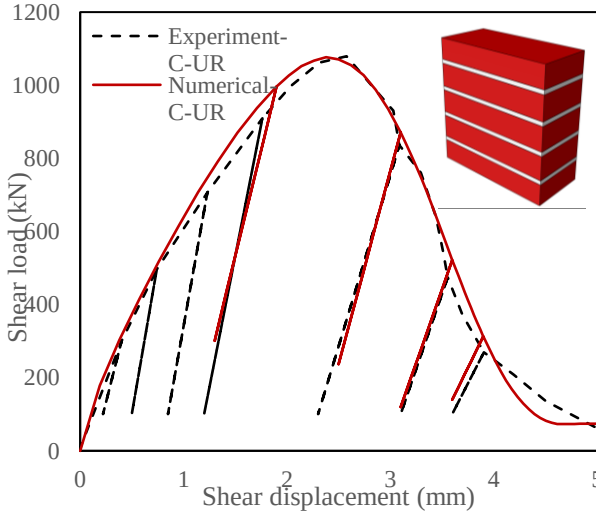

(d) Compression

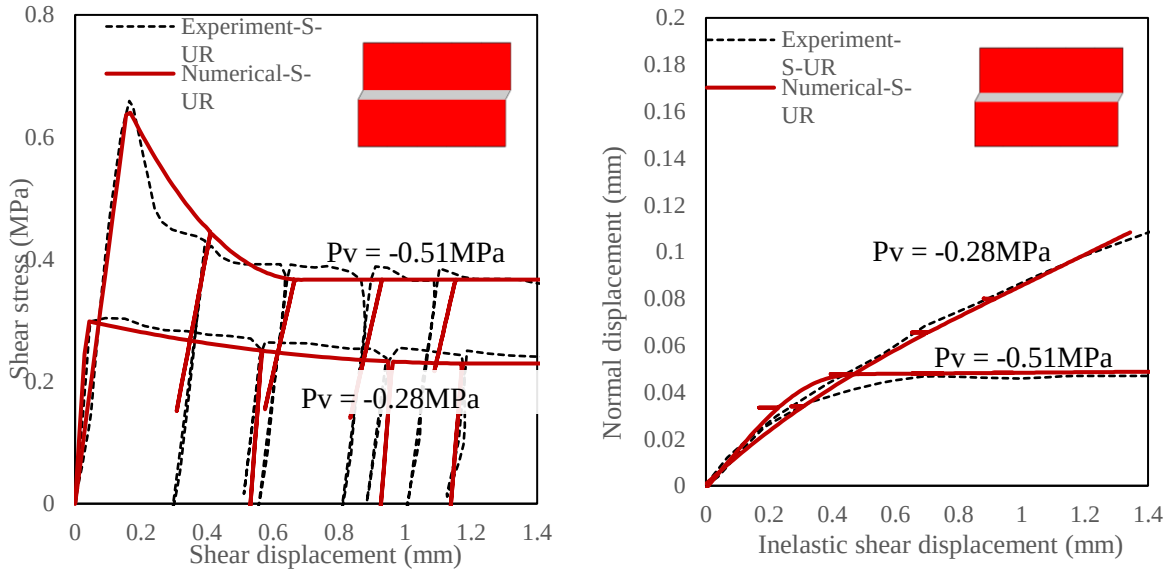

(e) Shear stress vs Shear displacement (f) Normal displacement vs Shear displacement

Fig. 7-16 Masonry couplet tests

The performance of the interface model under uniaxial compression with unloading/reloading scenarios for estimating stiffness degradation is validated with the experiment results of [57]. A prismatic specimen consists of 5 bricks as shown in **Fig. 7-16d** was subjected to vertical compressive load by using a steel plate bonded to the top surface of the specimen that was resting at its bottom surface on a fixed plate [57]. The numerical resulted produced by the proposed model are compared with the experimental results in **Fig. 7-16d**. Since the stiffness degradation is not observed experimentally during strain hardening region, the unloading-reloading scenario is simulated by the proposed model for one time only before the peak load which has shown the expected behaviour of no stiffness degradation. In the softening phase, the unloading/reloading scenario is simulated by the model for three cycles, as was done in experiment, and the results show a stiffness reduction consistent with the experimental response.

The dilation of a masonry joint is now studied by the proposed model that followed the experimental investigation of [51]. They applied shear loading on masonry couplets, made of two full size clay bricks (each: 230mm ×51mm×110mm) connected by a 10 mm thick mortar joint, keeping the couplets under constant pre-pressure having two different values of (0.28 MPa and 0.51 Mpa), which show a distinct variation of dilation behaviours. For the specimen under lower confining pressure (0.28 MPa), the peak shear strength was marginally higher than the residual frictional resistance (**Fig. 7-16e**) while the normal displacement increased steadily with the tangential shear deformation (**Fig. 7-16f**). In case of higher pre-pressure (0.51 MPa), the peak strength was visibly higher than the frictional resistance (**Fig. 7-16e**) while the variation of normal displacement stopped quickly and became nearly flat once the fractional resistance was reached (**Fig. 7-16f**). The numerical results simulated by the proposed model are compared with the experimental results in **Fig. 7-16**, and show that the model is capable of capturing all these features with a satisfactory agreement with experiments results. The

unloading-reloading scenarios are also simulated as done in the experiment [51] but it shows no stiffness degradation under this mode of loading.

7.4.4 Masonry walls under monotonic in-plane and out-of-plane loads

The testing of masonry wall specimens under monotonic in-plane loading, conducted by [58], is widely used as a benchmark example for experimental validations of numerical models and such an attempt is made in this section to assess the performance of our model. For this purpose, three masonry wall specimens, as shown **Fig. 7-17a**, are adopted from this study [58] who designated them as J4D, J5D and J7D. These three single leaf wall panels have a geometry (990 mm width × 1000 mm height × 100 mm thickness) composed by 18 courses of solid clay bricks (each: 210 mm × 52 mm × 100 mm) and 10 mm thick mortar joints. The bottom surface of these walls is fully restrained at the ground and the top surface (connected with a steel beam) is subjected to a constant confining pressure (Pv = 0.3MPa for J4D and J5D; Pv = 2.12MPa for J7D) and a horizontal load imposed through the steel beam in the form of displacement control.

In our FE modelling of the masonry walls, artificial joints/interfaces are placed through vertical planes of full size bricks at their middle lengths to simulate the potential cracks of brick units as shown in **Fig. 7-17b** apart from the real mortar joints. For both type of joints, the material properties used for the numerical modelling are listed in **Table 7-4**. Similar to the previous section, all nonlinear inelastic behaviors of the masonry walls are simulated by the interface model while the bricks are treated as elastic with Young's modulus E = 16700 MPa and Poisson's ratio v = 0.18. Though the results presented in the previous section corresponds to a mesh size based on 4×2×2 for single brick unit, it was observed from a mesh convergence study that a relatively less refined meshing can be adequate for getting good results. Therefore, a meshing arrangement based on 2×1×1 for a single brick unit is adopted in this section for analyzing bigger size problems (walls) with a good degree of computational efficiency.

Table 7-4 Interfacial material properties of the masonry walls under monotonic loading

Material Parameters	unit	In-plane loading (Pv = -0.3MPa)		In-plane loading (Pv = -2.12MPa)		Out-of-plane loading	
Joints		Mortar	Artificial	Mortar	Artificial	Mortar	Artificial
K_n	N/mm^3	82	100	82	100	220	280
K_s	N/mm^3	36	100	36	100	105	280
f_{t0}	MPa	0.3	2	0.16	2	1	2
G_{ft}	N/mm	0.072	0.12	0.012	0.25	0.072	0.25
α_t		2	2	2	2	2	2
f_{s0}	MPa	0.45	2.8	0.224	4	1.2	2.8
$tan\phi$		1	1	0.75	1	0.5	1
G_{fs}	N/mm	0.15	0.5	0.05	1	0.25	0.5
α_s		2	2	2	2	2	2
f_{ci}	MPa	2	10	6.5	30	5	30
f_{cu}	MPa	5.5	20	10.5	50	10	50
f_{cr}	MPa	1	5	1	5	2	10
G_{fch}	N/mm	0.8	10.5	2	20.5	10.5	25
G_{fcs}	N/mm	4.2	10.5	3	20.5	10.5	25
β		1	1	1	1	1	1

α_c	2	2	2	2	2	2
$tan\phi_{Q0}$	0.01	1	0.01	1	0.5	1
$tan\phi_{Qr}$	0.01	1	0.01	1	0.1	1
$\alpha_{\phi Q}$	2	2	2	2	2	2

Numerical results for the load-displacement response at the wall top surface (horizontal direction) simulated by the model are compared with the experimental results in **Fig. 7-17c**, which shows a good predictive capability of the model for such complex problems. For walls under lower confining pressure (0.3MPa), the peak load is around 50 kN with a long flat plateau proving a good degree of durability, while the wall under higher confining pressure (2.12MPa) resisted a higher peak load of around 100kN but it was reduced rapidly in the post-peak region. Cracking patterns produced by the numerical models (**Fig. 7-17d**) show typical diagonal cracks go through the entire walls with small horizontal cracks near the corners. Cracks produced by the FE models include failure of mortar (bed and head) joints as well as splitting of bricks though the artificial joints, which helped to simulate the real failure patterns of the walls well.

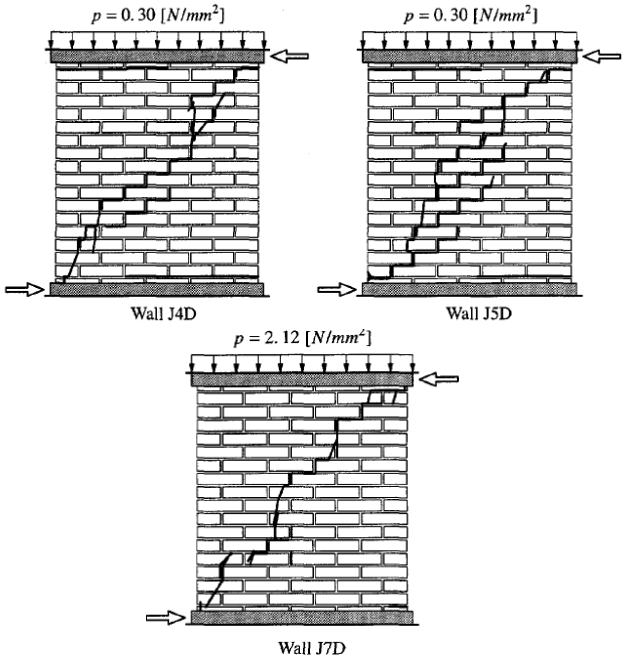

(a) Masonry wall panels and their failure modes from experiment (Raijmakers and Vermeltfoort 1993)

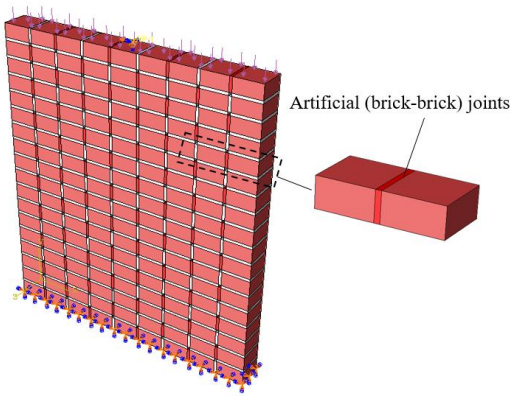

(b) FE model

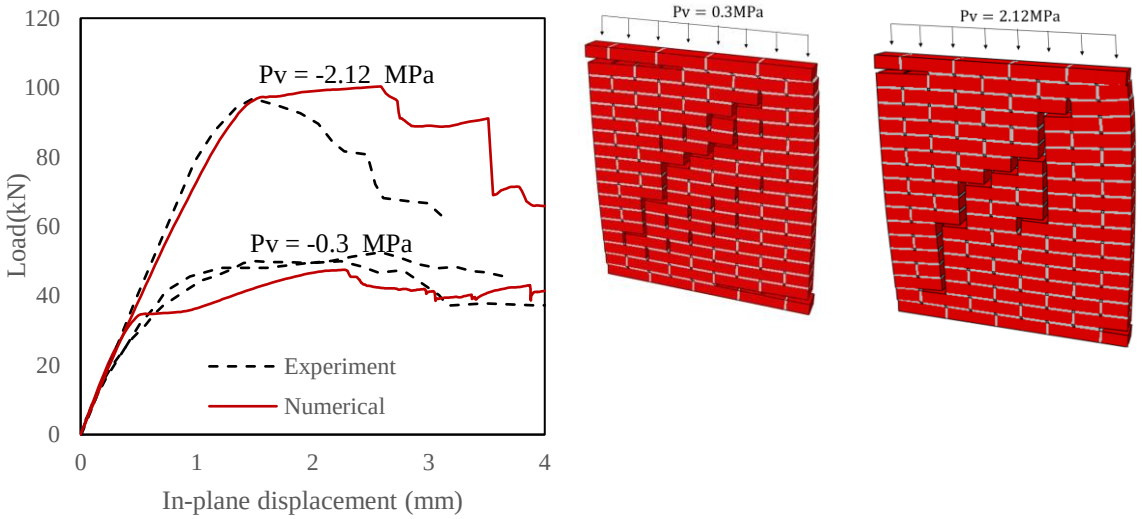

(c) load-displacement response (d) simulated cracking patterns

Fig. 7-17 Masonry wall panels under monotonic in-plane loading

The capability of the model to simulate the response of masonry walls subjected to out-of-plane monotonic loading is now assessed. For this purpose, a masonry wall panel tested by Ng [59] is adopted. The single leaf wall specimen has 795 mm width, 1190 mm height and 53 mm thickness and it built with solid clay bricks (each: 112mm × 36mm × 53mm) and 10 mm thick mortar joints. In the experimental set-up, an airbag was placed between the masonry wall (back surface) and a stiff support (concrete wall) to provide lateral (out-of-plane) pressure on the back surface of the panel. Four edges of the masonry wall were firmly supported by using a steel frame (**Fig. 7-18a**) that cause deformation of the wall under two-way bending (**Fig. 7-18b**). The meshing pattern used for the FE modelling of the wall is identical to that used in the previous case (**Fig. 7-17**). To simulate the uniform pressure exerted by the air-bag on the wall, a reference point (RP) is used and it is coupled with the loading surface of the panel using the feature "structural distributing" of ABAQUS (**Fig. 7-18c**). A displacement control technique is applied to the RP that helped to develop pressure on the panel surface but the pressure will be automatically increased or decreased depending on the load resisting capability of the panel during its entire loading range with both hardening and softening behaviors. The material used for the interfaces are same as provided in **Table 7-4** while the bricks are taken as elastic with elastic modulus E = 16700 MPa and Poisson's ratio ν = 0.15.

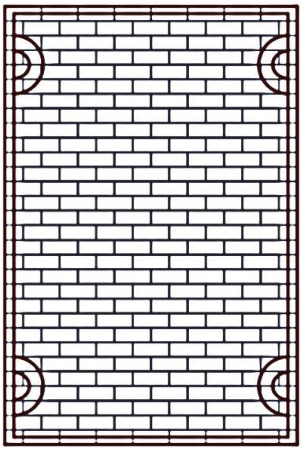

(a) a steel frame to support the panel at four edges

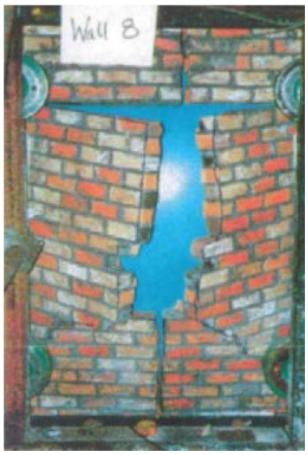

(b) failure mode of the wall

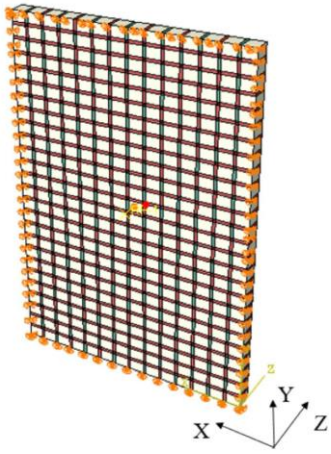

(c) FE model of the wall with boundary conditions and RP

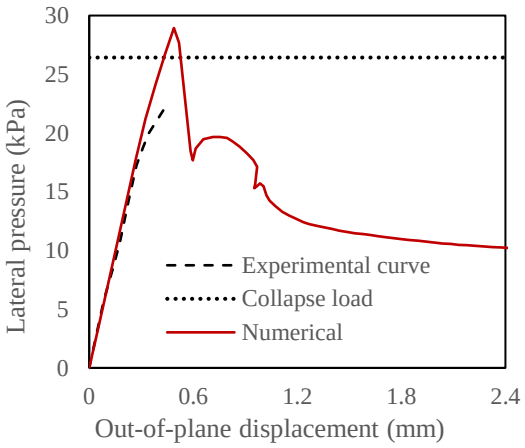

(d) load-displacement response

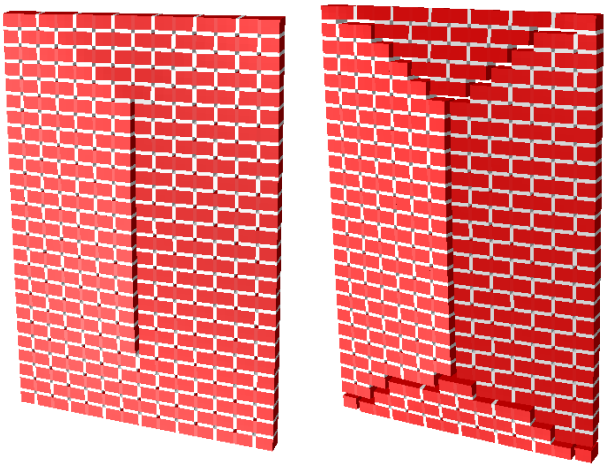

(e) cracking patterns

Fig.7-18 A masonry wall panel subjected monotonic out-of-plane loading

The load-displacement response (deflection at the panel central vs uniform pressure) predicted by the model is plotted in **Fig. 7-18d**. For its experimental validation, the measured response as reported by [59] is included in **Fig. 7-18d**. However, the entire range of the panel response could not be measured experimentally due to unexpected sudden failure of the LVDT before reaching the peak load. Ng [59] could however measure the peak load which is also included in **Fig. 7-18d**. The figure shows that the numerical results have a satisfactory correlation with the peak load and the load-displacement response that could be measured. **Fig. 7-18e** shows the failure modes simulated by the model at two different stages of loading. First the straight vertical crack along the longitudinal central line of the panel is produced, and it is then propagated diagonally in four branches from the vertical crack tips to the four corners of the wall.

7.4.5 Masonry walls under in-plane cyclic loading

In this section, two single leaf masonry wall specimens subjected to cyclic in-plane loading are selected from literature for experimental validation of the proposed model. **Fig. 7-19a** shows one of these specimens that was tested by Salmanpour et al. [60] in Swiss Federal Institute of Technology (ETH) Zurich under constant pre-pressure of 1.16MPa. The wall designated as T3 [60] had a dimension of 1590 mm×1550 mm×150 mm that was made of 13 courses of clay bricks (each: 250 mm × 190 mm × 150 mm) and 10 mm thick mortar joints. The other wall specimen as shown in **Fig. 7-19b** was tested under 0.5 MPa pre-pressure by Messali et al. [61] in the Delft University of Technology (TUD). This wall (designated as COMP4) had a dimension of 4000 mm×2760 mm×102 mm that was made by 34 courses of calcium silicate bricks (210 mm × 71 mm × 102 mm) and 12 mm mortar joints. Both walls were firmly supported at their bases and subjected to horizontal reversible displacements through a steel beam perfectly bonded at their upper surfaces.

Table 7-5 Interfacial material properties of the walls subjected to in-plane cyclic loading

Material Parameters	unit	IP-Cyc-ETH (Pv = -1.16MPa)			IP-Cyc-DUT (Pv = -0.5MPa)		
Joints		Mortar-head	Mortar-bed	Artificial	Mortar-head	Mortar-bed	Artificial
K_n	N/mm^3	50	20	100	100	10	100
K_s	N/mm^3	25	10	100	40	16	100
f_{t0}	MPa	0.2	0.2	2	0.1	0.01	2.2
G_{ft}	N/mm	0.1	0.1	1	0.05	0.025	0.03
α_t		2	2	2	2	2	2
f_{s0}	MPa	0.45	0.24	2.8	0.14	0.02	1.5
$tan\phi$		0.3	0.48	1	0.46	0.43	0.46
G_{fs}	N/mm	1.5	1.5	2	3	0.05	0.05
α_s		5	5	2	2	2	2
f_{ci}	MPa	5	2	30	4	6	30
f_{cu}	MPa	9.5	5	50	6	8	50
f_{cr}	MPa	1	1	10	2	2	10
G_{fch}	N/mm	2.5	0.8	25	7.5	17	10.5
G_{fcs}	N/mm	2.5	2	25	7.5	17	10.5
β		1	1	1	1	1	1
α_c		2	2	2	2	2	2
$tan\phi_{Q0}$		0.1	0.1	1	0.1	0.02	0.36
$tan\phi_{Qr}$		0.01	0.01	1	0.01	0.01	0.01
$\alpha_{\phi Q}$		2	2	2	2	2	2

For the FE modelling of these two walls, the meshing system followed the same strategy used in the previous example (**Section 7.4.4**). The material properties used for the interface modelling are listed in **Table 7-5** while the elastic properties taken for the bricks are: E = 3000 MPa and ν = 0.2 for the ETH wall; E = 9000 MPa and ν = 0.14 for the DUT wall. Based on the suggestion of [25], different interfacial properties are taken for head and bed joints (mortar) in the present case of cyclic loading.

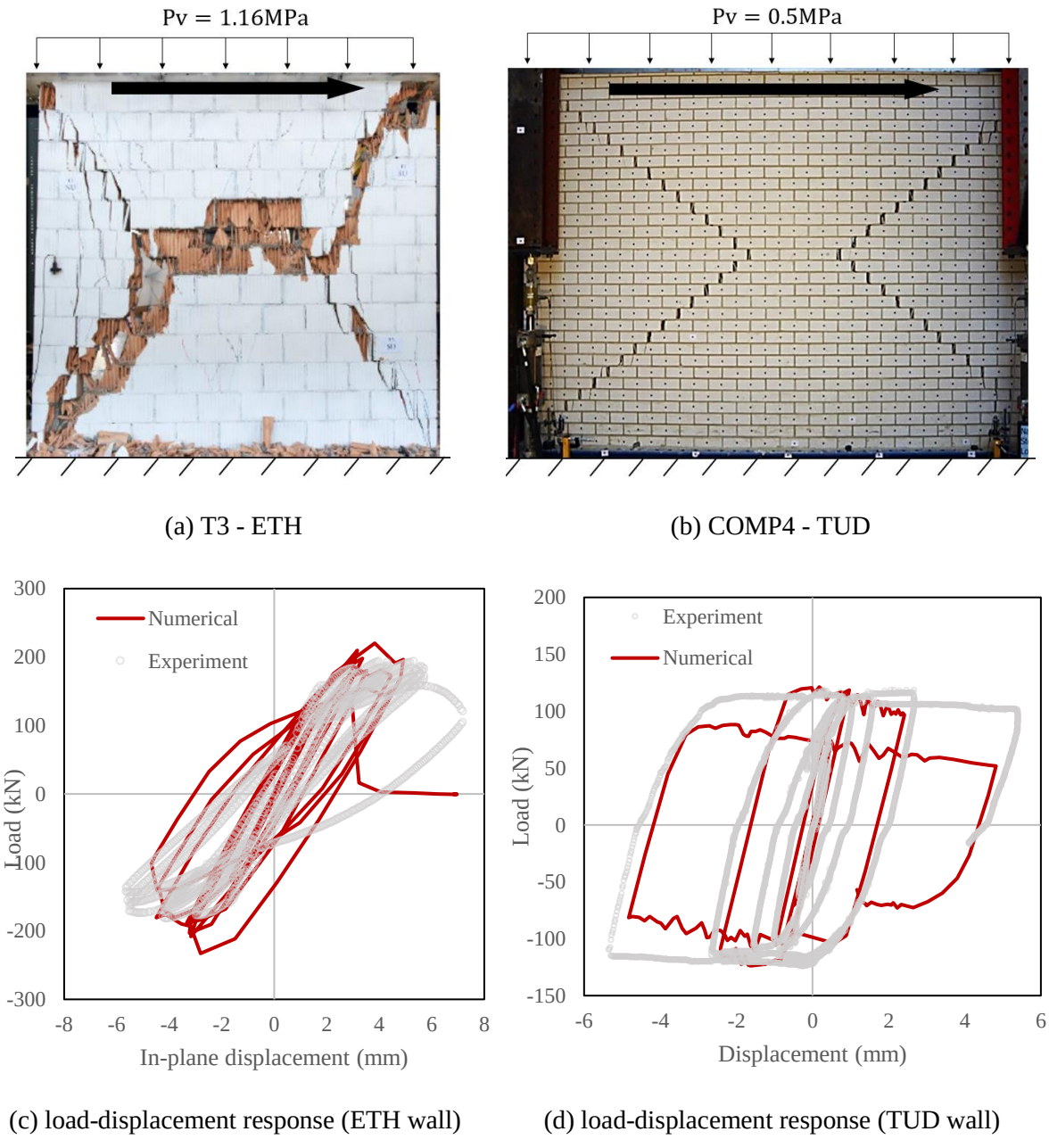

(a) T3 - ETH

(b) COMP4 - TUD

(c) load-displacement response (ETH wall)

(d) load-displacement response (TUD wall)

Fig. 7-19 Masonry walls under cyclic in-plane loading

.

The cyclic response (horizontal displacement at top surface vs load) of the two walls predicted by the proposed model is compared with the experimental results in **Fig. 7-19c** and **7-19d**, which show a reasonable consistency between them in terms of peak load and overall hysteretic behavior for such a complex loading scenario. The gradual degradation of stiffness with the increase of cycles was observed in the ETH masonry panel during experiment, which was due to the compressive crushing failure of mortar bed joints near the bottom edge. This has been successfully captured by the numerical model. The failure modes of the two walls predicted by the FE model are presented in **Fig. 7-20**. **Fig. 7-20a** clearly shows a completed crushing of mortar joints near the bottom edge that lead to drop the load resting capacity to

zero (see **Fig. 7-19c**). In contrast, the experiment as well as the FE modelling (**Fig. 7-19d**) show insignificant stiffness degradation of the TUD masonry wall probably due to lower pre-compression. The simulation shows a typical shear failure mode of the wall (TUD) with two symmetric localized diagonal cracks up to the final stage of loading (**Fig. 7-20b**), which is similarly observed in experiment (**Fig. 7-19b**).

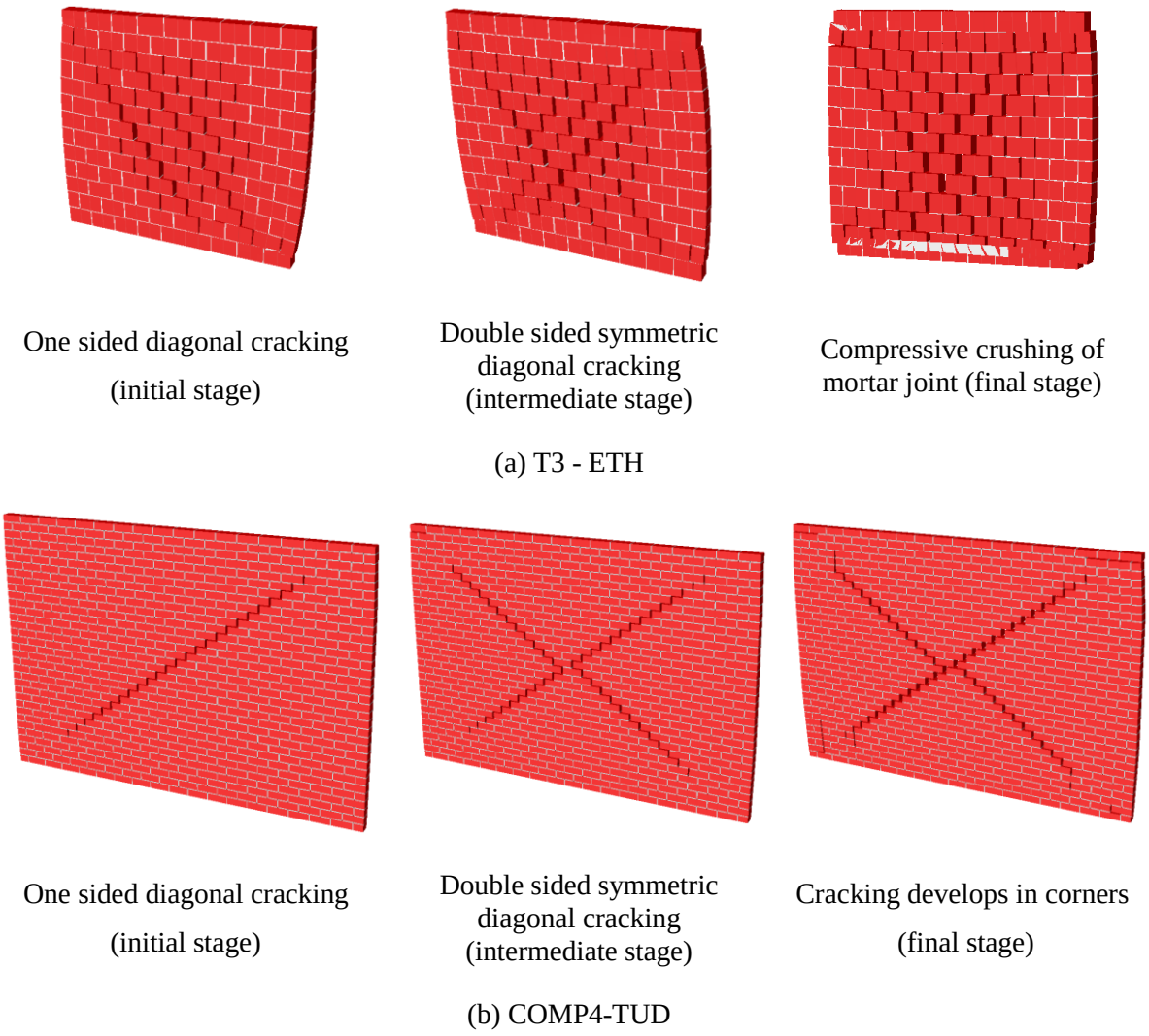

Fig. 7-20 Cracking patterns of FE models under cyclic in-plane load

.

7.4.6 A masonry wall under out-of-plane cyclic loading

To investigate the performance of the proposed model in simulating masonry walls under out-of-plane cyclic loading, a wall specimen tested by Messali et al. [62] under such loading is chosen. The wall (designated as COMP11) had a dimension of 3874 mm×2765 mm×102mm (**Fig. 7-21a**), which was built in the Delft University of Technology (TUD) using calcium silicate bricks (210 mm × 71 mm × 102 mm) and 12 mm mortar joints. To apply the out-of-plane cyclic load on the wall, two airbags were used at the two sides of the wall. The pressure

exerted by one of these airbags was varied (active side) while the pressure of other airbag was kept constant (passive side)

Table 7-6 Interfacial material properties of the wall subjected to out-of-plane cyclic loading

Material Parameters	K_n	K_s	f_{t0}	G_{ft}	α_t	f_{s0}	$tan\phi$	G_{fs}	α_s	
unit	N/mm^3	N/mm^3	MPa	N/mm		MPa		N/mm		
Mortar	28	14	0.2	0.3	2	0.35	0.4	0.45	2	
Artificial	100	100	1	0.25	2	1.4	1	0.5	2	
Material Parameters	f_{ci}	f_{cu}	f_{cr}	G_{fch}	G_{fcs}	β	α_c	$tan\phi_{Q0}$	$tan\phi_{Qr}$	$\alpha_{\phi Q}$
unit	MPa	MPa	MPa	N/mm	N/mm					
Mortar	3	6	1	15	15	1	2	0.5	0.01	2
Artificial	30	50	10	25	25	1	2	1	1	2

.

The computational demand for FE simulation of this problem is expected to be higher than previous examples due to the complexity of out-of-plane response (e.g., tension-shear mixed mode failures in joints) which requires higher computing cost. Thus, to reduce the computational time, one quarter of the wall panel (**Fig. 21b**) is modelled in the FE simulation utilizing the structural symmetry. Boundary conditions are also shown in **Fig. 21b**. The meshing arrangement is same as that used in the previous example. This specimen is subjected to 0.05 MPa pre-pressure on its top surface before the lateral cyclic load is applied. The material properties used of modelling the bricks are: E = 6800 MPa and ν = 0.15, while the nonlinear material properties used for the interface model are listed in **Table 6.**

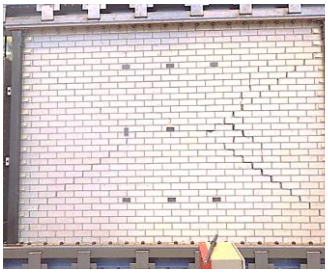

(a) Wall specimen with failure modes

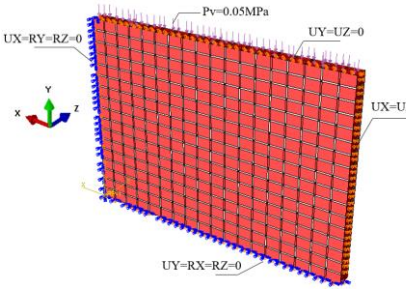

(b) FE model (one quarter)

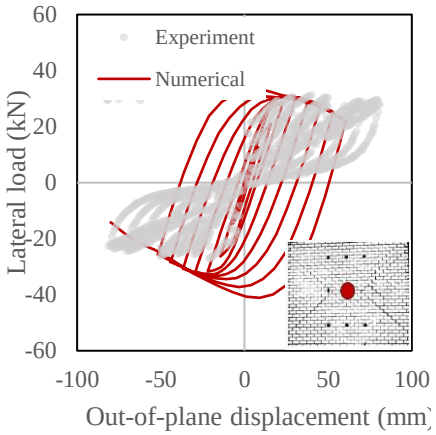

(c) Load-displacement response

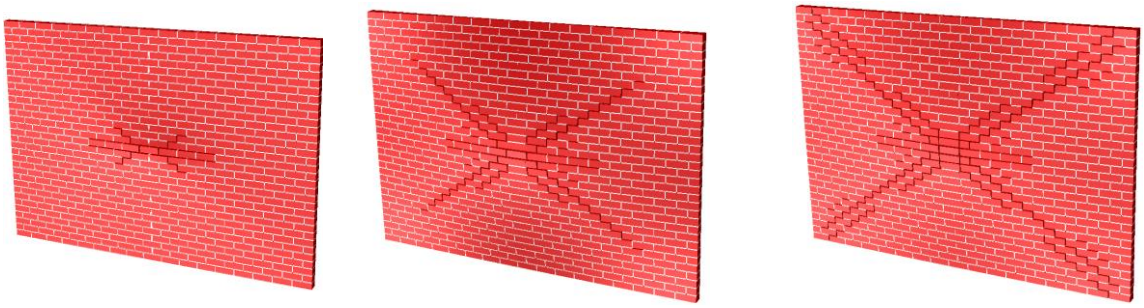

Initial stage of cracking Intermediate stage of Cracking Final stage of cracking

(d) Simulated failure modes

Fig.7-21 Masonry wall (TUD, COMP11) under out-of-plane cyclic loading

The response (out-of-plane displacement vs load) at the panel center captured by the FE model is presented in **Fig. 7-21c** along with the experimentally measured response. **Fig. 7-21c** shows that FE model predicted the peak load resting capacity reasonably well but the shape of hysteresis deviated from the experimental result. This is probably due to the complex loading scenario produced by the two airbags apart from the challenge associated with the measurement of displacements in experiment. The failure modes of the wall simulated by the model at different stage of loading are presented in **Fig. 7-21d**, which shows a good correlation with the cracking pattern observed in experiment (**Fig. 7-21a**). In the FE simulation, horizontal and small diagonal cracks are initially observed in the central region of the wall and these diagonal cracks are subsequently propagated towards the corners of the wall (**Fig. 7-21d**). At the final stage, a typical two-way bending failure mode is formed that consists of a horizontal crack (around 1/3 length of the wall width) and 4 diagonal cracks.

7.5. Conclusions

The present study has developed an accurate and robust interfacial constitutive model for masonry joints for use in predicting the non-linear response of masonry walls subjected to monotonic and cyclic loads applied either in- or out-of-plane. The interface model is implemented within a reliable finite element program (ABAQUS) for failure modelling of structural level problems under complex loading scenarios. The major contributions of this work includes incorporation of damage within a multi-surfaces plasticity framework in a consistent manner to accommodate strength hardening/soften as well as stiffness degradation of masonry joints subjected to tension, shear, compression or a mixed mode of loading. A smooth hyperbolic yield surface is used to capture the tensile-shear mixed mode behavior. The other yield surface of the plasticity model is an elliptic cap for simulating the compression-shear mixed model scenarios. The interface model is formulated in effective stress space that helped to provide no softening of the yield surfaces and it leads to enhance the robustness of the model by improve the numerical stability.

In the numerical implementation of the interfacial model, a fully implicit backward Euler integration technique is used to achieve enhance accuracy and robustness in the NR iterative

process for the stress return mapping. For a multi-surface plasticity model, the strategy for selection of active yield surfaces and their updating within the iterative process is very important and it has been addressed carefully in this study. To improve the robustness of numerical implementation, an adaptive sub-stepping method is adopted here. Moreover, to enhance the computational efficiency and robustness, an adaptive sub-stepping scheme is implemented that can adjust the load increment size at local (material point) level automatically based on the performance of NR iteration in previous sub-steps.

The performance of the interface model is investigated by analyzing masonry structures in different scales and loading scenarios. This is facilitated with the Finite element (FE) modelling of these masonry structures that utilised solid elements for bricks, and cohesive elements for mortar joints as well as artificial joints within brick units. Apart for making some initial checking at material point and single element level, the different problems simulated by the FE model are: 1) masonry couplets/prismatic specimens under tension, compression and shear with constant pre-compression where these loads may be monotonic or cyclic and may have unloading-reloading scenarios; 2) masonry panels under in-plane and out-of-plane monotonic loads; 3) masonry walls under in-plane cyclic loads; and 4) masonry wall under out-of-plane cyclic loads. A thorough experimental validation of the load-deformation response and failure modes of these structures predicted by the model is conducted using benchmarking test results available in literature. The numerical analysis confirmed a very good performance of the model in solving such complex problems of masonry system in terms of accuracy, robustness, and computational efficiency.

7.6. Reference

[1] A. Tralli, C. Alessandri, G. Milani, Computational methods for masonry vaults: a review of recent results, (2014).

[2] D. Theodossopoulos, B. Sinha, A review of analytical methods in the current design processes and assessment of performance of masonry structures, Construction and Building Materials, 41 (2013) 990-1001.

[3] T. Deb, T.Y. Yuen, D. Lee, R. Halder, Y.C. You, Bi - directional collapse fragility assessment by DFEM of unreinforced masonry buildings with openings and different confinement configurations, Earthquake Engineering & Structural Dynamics, 50 (2021) 4097-4120.

[4] G. Giambanco, E. La Malfa Ribolla, A. Spada, Meshless meso-modeling of masonry in the computational homogenization framework, Meccanica, 53 (2018) 1673-1697.

[5] M. Kujawa, I. Lubowiecka, C. Szymczak, Finite element modelling of a historic church structure in the context of a masonry damage analysis, Engineering Failure Analysis, 107 (2020) 104233.

[6] P.B. Lourenço, Computations on historic masonry structures, Progress in Structural Engineering and Materials, 4 (2002) 301-319.

[7] L. Macorini, B. Izzuddin, A non-linear interface element for 3D mesoscale analysis of brick-masonry structures, International Journal for numerical methods in Engineering, 85 (2011) 1584-1608.

[8] D. Malomo, M. DeJong, A Macro-Distinct Element Model (M-DEM) for out-of-plane analysis of unreinforced masonry structures, Engineering Structures, 244 (2021) 112754.

[9] A. Spada, G. Giambanco, P. Rizzo, Damage and plasticity at the interfaces in composite materials and structures, Computer Methods in Applied Mechanics and Engineering, 198 (2009) 3884-3901.

[10] D. Sutcliffe, H. Yu, A. Page, Lower bound limit analysis of unreinforced masonry shear walls, Computers & Structures, 79 (2001) 1295-1312.

[11] P.J.B.B. Lourenço, Computational strategies for masonry structures, (1997).

[12] G. Andreotti, F. Graziotti, G. Magenes, Detailed micro-modelling of the direct shear tests of brick masonry specimens: the role of dilatancy, Engineering Structures, 168 (2018) 929-949.

[13] B. Panto, L. Silva, G. Vasconcelos, P.B. Lourenço, Macro-modelling approach for assessment of out-of-plane behavior of brick masonry infill walls, Engineering Structures, 181 (2019) 529-549.

[14] N. Ravichandran, D. Losanno, F. Parisi, Comparative assessment of finite element macro-modelling approaches for seismic analysis of non-engineered masonry constructions, Bulletin of Earthquake Engineering, 19 (2021) 5565-5607.

[15] P.B. Lourenço, J.G. Rots, Multisurface interface model for analysis of masonry structures, Journal of engineering mechanics, 123 (1997) 660-668.

[16] K.F. Abdulla, L.S. Cunningham, M. Gillie, Simulating masonry wall behaviour using a simplified micro-model approach, Engineering Structures, 151 (2017) 349-365.

[17] B. Zeng, Y. Li, C.C. Noguez, Modeling and parameter importance investigation for simulating in-plane and out-of-plane behaviors of un-reinforced masonry walls, Engineering Structures, 248 (2021) 113233.

[18] D. Systemes, Abaqus 6.14 documentation–theory guide, Providence, RI, (2015).

[19] M.L. Benzeggagh, M. Kenane, Measurement of mixed-mode delamination fracture toughness of unidirectional glass/epoxy composites with mixed-mode bending apparatus, Composites science and technology, 56 (1996) 439-449.

[20] G. Alfano, E. Sacco, Combining interface damage and friction in a cohesive-zone model, International Journal for Numerical Methods in Engineering, 68 (2006) 542-582.

[21] G. Andreotti, F. Graziotti, G. Magenes, Expansion of mortar joints in direct shear tests of masonry samples: implications on shear strength and experimental characterization of dilatancy, Materials and Structures, 52 (2019) 1-16.

[22] H.R. Lotfi, P.B. Shing, Interface model applied to fracture of masonry structures, Journal of structural engineering, 120 (1994) 63-80.

[23] G.F. Scimemi, G. Giambanco, A. Spada, The interphase model applied to the analysis of masonry structures, Computer Methods in Applied Mechanics and Engineering, 279 (2014) 66-85.

[24] E. Minga, L. Macorini, B.A. Izzuddin, A 3D mesoscale damage-plasticity approach for masonry structures under cyclic loading, Meccanica, 53 (2018) 1591-1611.

[25] Z. Xie, M. Sousamli, F. Messali, J. Rots, A sub-stepping iterative constitutive model for cyclic cracking-crushing-shearing in masonry interface elements, Computers & Structures, 257 (2021) 106654.

[26] K. Chaimoon, M.M. Attard, Modeling of unreinforced masonry walls under shear and compression, Engineering structures, 29 (2007) 2056-2068.

[27] C. Citto, Two-dimensional interface model applied to masonry structures. University of Colorado at Boulder, 2008.

[28] N. Kumar, R. Amirtham, M. Pandey, Plasticity based approach for failure modelling of unreinforced masonry, Engineering structures, 80 (2014) 40-52.

[29] T.Y. Yuen, T. Deb, H. Zhang, Y. Liu, A fracture energy based damage-plasticity interfacial constitutive law for discrete finite element modelling of masonry structures, Computers & Structures, 220 (2019) 92-113.

[30] M. Ortiz, E.P. Popov, Accuracy and stability of integration algorithms for elastoplastic constitutive relations, International journal for numerical methods in engineering, 21 (1985) 1561-1576.

[31] J. Chaboche, G. Cailletaud, Integration methods for complex plastic constitutive equations, Computer methods in applied mechanics and engineering, 133 (1996) 125-155.

[32] S.W. Sloan, A.J. Abbo, D. Sheng, Refined explicit integration of elastoplastic models with automatic error control, Engineering Computations, (2001).

[33] A. Wilkins, B.W. Spencer, A. Jain, B. Gencturk, A method for smoothing multiple yield functions, International Journal for Numerical Methods in Engineering, 121 (2020) 434-449.

[34] J.C. Simo, T.J. Hughes, Computational inelasticity, Springer Science & Business Media, 2006.

[35] D.P. Adhikary, C.T. Jayasundara, R.K. Podgorney, A.H. Wilkins, A robust return-map algorithm for general multisurface plasticity, International Journal for Numerical Methods in Engineering, 109 (2017) 218-234.

[36] J. Lee, H.J. Bong, M.-G. Lee, Return mapping with a line search method for integrating stress of the distortional hardening law with differential softening, Computers & Structures, 257 (2021) 106652.

[37] A. Pérez-Foguet, F. Armero, On the formulation of closest-point projection algorithms in elastoplasticity—part II: Globally convergent schemes, International Journal for Numerical Methods in Engineering, 53 (2002) 331-374.

[38] R. Abreu, C. Mejia, D. Roehl, A comprehensive implicit substepping integration scheme for multisurface plasticity, International Journal for Numerical Methods in Engineering, 123 (2022) 5-40.

[39] S. Pech, M. Lukacevic, J. Füssl, A robust multisurface return-mapping algorithm and its implementation in Abaqus, Finite Elements in Analysis and Design, 190 (2021) 103531.

[40] A. Pérez-Foguet, A. Rodríguez-Ferran, A. Huerta, Consistent tangent matrices for substepping schemes, Computer methods in applied mechanics and engineering, 190 (2001) 4627-4647.

[41] S. Sloan, Substepping schemes for the numerical integration of elastoplastic stress–strain relations, International journal for numerical methods in engineering, 24 (1987) 893-911.

[42] A. Caballero, K. Willam, I. Carol, Consistent tangent formulation for 3D interface modeling of cracking/fracture in quasi-brittle materials, Computer Methods in Applied Mechanics and Engineering, 197 (2008) 2804-2822.

[43] R. Van der Pluijm, Shear behaviour of bed joints, (1993).

[44] R. Van der Pluijm, Non-linear behaviour of masonry under tension, HERON-ENGLISH EDITION-, 42 (1997) 25-54.

[45] H.B. Kaushik, D.C. Rai, S.K. Jain, Stress-strain characteristics of clay brick masonry under uniaxial compression, Journal of materials in Civil Engineering, 19 (2007) 728-739.

[46] P. Grassl, R. Rempling, A damage-plasticity interface approach to the meso-scale modelling of concrete subjected to cyclic compressive loading, Engineering Fracture Mechanics, 75 (2008) 4804-4818.

[47] P. Grassl, D. Xenos, U. Nyström, R. Rempling, K. Gylltoft, CDPM2: A damage-plasticity approach to modelling the failure of concrete, International Journal of Solids and Structures, 50 (2013) 3805-3816.

[48] Y. Tao, J.-F. Chen, Concrete damage plasticity model for modeling FRP-to-concrete bond behavior, Journal of composites for construction, 19 (2015) 04014026.

[49] A.M. D'Altri, S. de Miranda, G. Castellazzi, V. Sarhosis, A 3D detailed micro-model for the in-plane and out-of-plane numerical analysis of masonry panels, Computers & Structures, 206 (2018) 18-30.

[50] A.H. Sheikh, P.H. Bull, J.A. Kepler, Behaviour of multiple composite plates subjected to ballistic impact, Composites Science and Technology, 69 (2009) 704-710.

[51] K. Chaimoon, Numerical simulation of fracture in unreinforced masonry. Ph. D thesis, 2007.

[52] F. Armero, A. Pérez-Foguet, On the formulation of closest-point projection algorithms in elastoplasticity—part I: The variational structure, International Journal for Numerical Methods in Engineering, 53 (2002) 297-329.

[53] W.T. Koiter, Stress-strain relations, uniqueness and variational theorems for elastic-plastic materials with a singular yield surface, Quarterly of applied mathematics, 11 (1953) 350-354.

[54] R.S. Crouch, H. Askes, T. Li, Analytical CPP in energy-mapped stress space: application to a modified Drucker–Prager yield surface, Computer methods in applied mechanics and engineering, 198 (2009) 853-859.

[55] T. Diana, Diana finite element analysis user's manual release 9.4. 4, Delft, The Netherlands, (2012).

[56] R. Atkinson, B. Amadei, S. Saeb, S. Sture, Response of masonry bed joints in direct shear, Journal of Structural Engineering, 115 (1989) 2276-2296.

[57] D.V. Oliveira, P.B. Lourenço, P. Roca, Cyclic behaviour of stone and brick masonry under uniaxial compressive loading, Materials and structures, 39 (2006) 247-257.

[58] A.T. Vermeltfoort, T. Raijmakers, H. Janssen, Shear tests on masonry walls, (1993).

[59] C.L. Ng, Experimental and theoretical investigation of the behaviour of brickwork cladding panel subjected to lateral loading. University of Edinburgh, 1996.

[60] A.H. Salmanpour, N. Mojsilović, J. Schwartz, Displacement capacity of contemporary unreinforced masonry walls: an experimental study, Engineering Structures, 89 (2015) 1-16.

[61] F. Messali, R. Esposito, G. Ravenshorst, J. Rots, Experimental investigation of the in-plane cyclic behaviour of calcium silicate brick masonry walls, Bulletin of Earthquake Engineering, 18 (2020) 3963-3994.

[62] F. Messali, G. Ravenshorst, R. Esposito, J. Rots, Large-scale testing program for the seismic characterization of Dutch masonry walls, in: Proceedings of 16th world conference on earthquake (WCEE), Santiago, Chile, 2017.

Chapter 8: Discussion and Conclusion

In this thesis, interface based constitutive models for masonry are developed, implemented and applied in simulating masonry walls under various loading conditions by using the finite element method. The target of this research is to propose an efficient and comprehensive constitutive model for modelling masonry structures in mesoscale level. A general procedure of this study is summarized in the flowchart presented in **Fig. 8-1**.

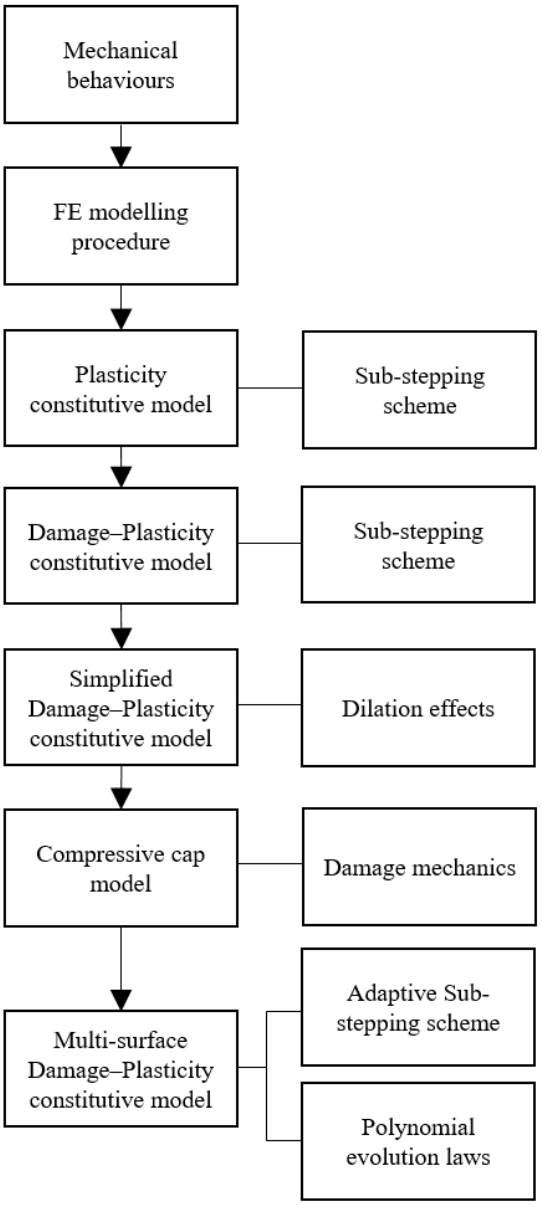

Fig. 8-1 Research scope

(1) Initially, mechanical behaviours of masonry, especially the brick-mortar joint, are investigated to determine the fundamentals of constitutive models. These characteristics includes: tensile/shear strength softening, compressive strength hardening-softening, fractional and dilation effects, stiffness degradation and irreversible deformation.

(2) The FE modelling procedure of masonry simulation is then studied with a focus on the block based model (also called as simplified micro-modelling). A surface based cohesive model built-in Abaqus is utilized to model the connection between continuum elements (bricks and mortars). Computational solvers are compared in terms of their efficiency and robustness.

(3) By using a user defined material subroutine, the first self-developed interfacial constitutive model is implemented in the cohesive element provided by the Abaqus element library. In the material subroutine, a sub-stepping scheme is applied to the algorithm to enhance the robustness of the stress return mapping progress. The constitutive model is proposed based on the plasticity framework which contains a tension-shear mixed mode hyperbolic yield surface.

(4) To properly reproduce the stiffness degradation of masonry joints under cyclic loads, energy/work determined damage parameters are induced into the plasticity framework to

replace the strength evolution. Sub-stepping scheme is also utilized to enhance the stability of numerical implementation in local level (user defined subroutine).

(5) A simplified damage-plasticity constitutive model is proposed to improve the computational efficiency. The transition between effective stress space and nominal stress space allows the algorithm conduct damage and plasticity separately, which significantly increase the computational productivity. Meanwhile, a new function is proposed to determine the variation of the dilation coefficient, which has an obvious influence on mechanical behaviour of the mortar joint and numerical results of stress return mapping.

(6) An elliptic cap formulation is adopted to illustrate the compressive failure of masonry joints conceptually. Based on above simplified damage-plasticity framework, the cap yield surface is only allowed to be expanded in a limited region (from initial to ultimate compressive strength). The hardening-softening variation of the compressive strength is defined by a segment function with hardening parameters and damage parameters in softening part.

(7) Finally, a comprehensive constitutive model for the masonry joint is proposed based on the damage-plasticity framework enhanced by an adaptive sub-stepping scheme. A tension-shear mixed mode hyperbolic yield surface is combined with a compressive cap yield surface in the effective stress space. The accuracy of stress return mapping is ensured by adopting the optimized method to update the set of active yield surface iteratively according to Karush–Kuhn–Tucker conditions. The model proposed in this chapter has the most appropriate performance compared with other models in previous chapters.

Disadvantages existing in this study are listed below and suggested improvements are also presented for further work:

- Both stiffness and strength reductions are depended on damage parameters. In the practical observation of experimental results, the shear stiffness degradation of masonry joints under compression is negligible and this phenomenon is defined as crack closure. Even though the crack closure is considered in the coupled damage-plasticity model which has no stiffness change in shear direction when the interface is under confined pressure, the shear stiffness degradation is unavoidable in the simplified damage-plasticity framework since strength softening is also controlled by the damage parameters. To distinguish the contribution of damage and plasticity, a more considerable theory, thermodynamic framework where plastic deformation and stiffness degradation are controlled by plastic yield surface and damage yield surface separately, could be attempted.
- Fully implicit (first order accurate Backward Euler) integration is the only integration algorithm in this study. A generalized midpoint rule with second order accuracy is recommended to deal with more complex stress updating procedures.
- Numerical enhanced method only has sub-stepping scheme. More advanced numerical stability tools could be adopted, such as linear search (cubic/quadratic/golden section), damped Newton method, quasi-Newton method and singular value decomposition (SVD).
- This study only focuses on investigating the constitutive aspect of interface model. More effort is required at the elemental level, including the integration technique of cohesive element (Gauss/Newton-Cotes), the number of integration points (linear/quadratic), viscosity parameters and co-rotational formulation.